Exploiting Shape Sensitive Interactions in Colloidal Suspensions— From Directed Self-assembly to the Structural Glass Transition

A Thesis

Submitted for the Degree of

DOCTOR OF PHILOSOPHY

by

CHANDAN KUMAR

CHEMISTRY AND PHYSICS OF MATERIALS UNIT
JAWAHARLAL NEHRU CENTRE FOR ADVANCED SCIENTIFIC RESEARCH
(A Deemed University)
Bangalore – 560 064

February 2017

asato mā sadgamaya
tamaso mā jyotirgamaya
mṛtyormā amṛtaṁ gamaya

असतो मा सद्गमय ।
तमसो मा ज्योतिर्गमय ।
मृत्योर्मा अमृतं गमय ॥

Lead us from unreal to Real.
Lead us from darkness to the Light.
Lead us from the fear of death,
To knowledge of Immortality.

asat: untrue, unreal, not existing
mā: not
sat: truth, existence, being
gamaya: lead me to
tamas: darkness, ignorance
mā: not
jyoti: light
mṛtyu: death
amṛta: immortality

Amma (Smt. Indu Devi) &
Papajee (Shri I C Vidyasagar)

DECLARATION

I hereby declare that the matter embodied in the thesis entitled "**Exploiting Shape Sensitive Interactions in Colloidal Suspensions– From Directed Self-assembly to the Structural Glass Transition**" is the result of investigations carried out by me at the Chemistry and Physics of Materials Unit, Jawaharlal Nehru Centre for Advanced Scientific Research, Bangalore, India under the supervision of **Prof. Rajesh Ganapathy** and that it has not been submitted elsewhere for the award of any degree or diploma.

In keeping with the general practice in reporting scientific observations, due acknowledgment has been made whenever the work described is based on the findings of other investigators. Any omission that might have occured by oversight or error of judgement is regretted.

Chandan Kumar

CERTIFICATE

I hereby certify that the matter embodied in this thesis entitled "**Exploiting Shape Sensitive Interactions in Colloidal Suspensions– From Directed Self-assembly to the Structural Glass Transition**" has been carried out by **Mr. Chandan Kumar** at the Chemistry and Physics of Materials Unit, Jawaharlal Nehru Centre for Advanced Scientific Research, Bangalore, India under my supervision and that it has not been submitted elsewhere for the award of any degree or diploma.

Prof. Rajesh Ganapathy
(Research Supervisor)

Acknowledgements

Though the face of the thesis carries my name, I mince no words in owning up that this document is an outcome of persistent encouragements, help, and kindness of many people, most of whom worked behind the scene to make it possible for me. This journey is best summed up in the words of the German theologist and the Nobel laureate Albert Schweitzer who said, *"At times, our own light goes out and is rekindled by a spark from another person. Each of us has cause to think with deep gratitude of those who have lighted the flame within us".* When I look back to my formative years in Sainik School Ghorakhal (SSGK), Nainital, I find that I was trained to lead the life like a soldier with science just as a usual subject, however, the last seven years of my stay in Soft Matter Lab has changed the way I perceive science, especially research in basic sciences. I express my deepest gratitude to Prof. Rajesh Ganapathy, my Ph.D. advisor, for bringing this change in me. His die hard attitude as an experimentalist, like he keeps saying, *"Chandan, if you bleed for an experiment, the experiment will bleed for you"*, has made a deep impact on me. He has given me freedom to plan and execute most part of the projects independently, but during the difficult phases, the brainstorming sessions, usually the post-midnight ones, always jump started an otherwise stalled work engine. He has routinely gone outside his duties to fire fight my concerns, anxieties, and worries.

I am grateful to Prof. A. K. Sood (FRS) from IISc, Bangalore in whose collaboration the project on site-specific colloidal crystallization was done. It actually started with a casual discussion on a Saturday afternoon. With his vast and diverse knowledge in science, especially physics, and crystal-clear basics, he can articulate complex problems in an unbelievably simple way as well as connect happenings in day-to-day life to various physics equations. His love and passion for science is a lifetime inspiration for people like us who want to pursue science in the future.

I am thankful to Prof. C. N. R. Rao (FRS) for providing world-class experimental facilities at our institute and also for being a constant source of inspiration. I would like to thank present and past chairmen of CPMU, Prof. G.U. Kulkarni, Prof. S.

Balasubramanian, and Prof. Chandrabhas Narayana. I am also thankful to Integrated Ph.D. coordinator, CPMU, Prof. S. Balasubramanian and Prof. Tapas Maji for their help, guidance, and support. I would always cherish the love and care which I received from Bala Sir during my stay at JNC.

With warm regards, I express my gratitude to all my course instructors for sharing their knowledge and teaching me various courses as part of my MS coursework, Prof. Bala, Prof. Ganapathy, Prof. K.S. Narayan, Prof. Chandrabhas, Prof. Sundaresan, Prof. Eswarmoorthy, Prof. R. Datta, Prof. Kulkarni, Prof. S.M. Shivprasad, Prof. S. Rajaram, Prof. H. Ila, Prof. Subir Das, Prof. Swapan Pati, Prof. Shobhana Narasimhan, Prof. Waghmare, Prof. Aloknath Chakraborty (IISc), Prof. Chandan Das Gupta (IISc), Prof. Jaydeep Basu (IISc). The encounters with Chandrabhas sir in the campus often turned into interesting and refreshing discussions, mostly on science and politics.

I thank all my past and present labmates, Dr. Manasa, Dr. Shreyas Gokhale (IISc), Dr. Vikram Rathee (IISc), Srishti, Amritha, Rajeev, Neelima, Manodeep, Srimayee, Niloyendu, Navneet, for being supportive and helping me as and when needed. My special thanks to Manasa for making me adapt to the lab and research environment, Srishti for making the lab-life enlivening and cheerful, Vikram Bhaiya and Amritha for a patient hearing of my blabbering whenever I went through a lean phase in life. Days spent with Manasa, Amritha and Srishti are the most memorable part of my stay at JNC.

I am thankful to my Integrated Ph.D. batchmates, Rajasekhar, Chandan De, Koushik, Sisir, Anirban, Arkamita, and Ram for creating wonderful memories. I also thank my other friends from JNC, Dr. Rajdeep, Dr. Mohit, Dr. Chidambar, Dr. Garmia, Dr. Shivani, Manjeet, Anshul, Devendra Negi, Sankalp, Sanjay, Rajib, Arjun, Raagesh, Palak, Ashwini, Baradraj, Shiney, Susheela, Swami (Sashi), Shivraman for standing with me in my happy and sad times. The countless dinner outings, often several in a single week, with Negi, Anshul, and Rajasekhar to share and vent our frustrations was refreshing and enabled us to get back to the lab with renewed vigour and energy. The company of Rajdeep *bhaiya*, Negi, Rajsekhar, Anshul and Ashutosh *bhaiya* to various trekking escapades have given me memories to reminisce for all my life. I am extremely thankful to Sankalp, a friend trained in engineering but tries to interpret the physics of my doubts; even the ones not limited to physics. Also, thanks to Manjeet, who got addicted to coffee like me, for all the chats over a cup of coffee when the clock struck 11 in the mornings.

My heartfelt thanks to my college and school friends, Dr. Ashutosh Singh, Adhip, Anurag, Rajesh, Nitya *bhaiya*, Maria, Dr. Punnet, Sumit Sati and friends of millennium batch (2000-07) of SSGK (esp. Lt. Cdr. Deepak, and Dr. Jeetendra Pandey) for being a constant support all these years. I must accept life without friends like Adhip in Bangalore would have been really challenging. He is a friend, a mentor, a sibling whom I can bank upon in all the rough weathers of my life. The encouraging words of Ashutosh *bhaiya* always boosted my moral to get back to the life with new *josh* and energy.

I would like to express my humble gratitude to my teachers from college and school, Mr. A. K Srivastava, Mr. Michael Beanland, Mr. K. N. Joshi, Mr. G. S Joshi, Dr. J. S. Bisht, Mr. A. C. Rai, Mr. Wesley Santraj, Mrs. Poonam Bhandari, Dr. Pragati Ashdir, Dr. V. P. Nagpal, Mr. S. V. Bakre, Dr. M. C. Jain, for shaping my life and teaching that I must take both happy and hard times in life with positive attitude, as they are just phase in life and not the life in totality. The excerpts from the book "Discover Your Destiny with The Monk Who Sold His Ferrari" that was penned by K. N. sir in my diary while I was departing from the school, *"We all are connected at an invisible level. As you do your healing, you aid to the healing of the world. As you let your brilliance shine, you silently invite those around you to do the same..."* continues to give me solace even after a decade.

I appreciate and thank the tireless efforts of JNC staffs - academic, administrative, library, technical, hostel, Dhanvantari and garden for creating a conducive environment for research at the institute.

Last but not the least, I am deeply grateful to my family, especially my parents and siblings (Mr. Rajeev Ranjan, Mr. Ranjan, and Mrs. Ragni), for their immense support. Quite often while I was bleeding away for the experiments, I was never there to support and/or listen to them. Yet they never shot back at my avoidance towards family duties. Even though they fumble to distinguish between a medical doctor and a Ph.D. and are never aware of what I am doing or what I aspire to become, they back me with all their heart and soul.

Synopsis

Research on colloidal suspensions has been at the forefront of soft matter research. In addition to their many uses in our day-to-day lives, for instance as shear thickening agents, in the purification of water, etc., colloidal crystals with well-controlled lattice parameters have been shown to have potential applications in optoelectronics and photonics. Moreover, since the phase behaviour of colloidal suspensions shares close similarity with the atomic systems, they are often used as model atoms to gain microscopic insights into a multitude of long-standing puzzles in condensed matter physics such as glass transition and crystal nucleation. Importantly, the anisotropies in the shape and/or interactions in colloidal suspensions can be tuned at the experimenters' will, which is otherwise impossible in atomic systems. In fact, here in this thesis, the geometrical nature of short-ranged depletion attraction has been exploited to address some key questions in colloids research, both from the perspective of future applications as well as our basic understanding of glass transition in systems with shape and/or interaction anisotropies. First, the short-ranged depletion attraction in colloids have been utilized to overcome the limitations in site-specific colloidal crystal nucleation and growth. Secondly, we introduced and investigated the role of anisotropic interactions in the physics of structural glass transition, testing some key predictions of various glass transition theories. This has also led to an advancement in our understanding of the underlying microscopic mechanism for the breakdown of Stokes-Einstein and Stokes-Einstein-Debye relations for supercooled liquids. The thesis has been organized as follows.

Chapter 1 provides the necessary background and motivation behind the experimental works presented in the thesis. It discusses the current approaches to realize colloidal crystals, challenges, and limitations of these techniques as well as ways to surmount them. It also contains introduction to supercooled liquids and glasses and shows how colloids have served as model atoms to gain microscopic insights of dynamics at single-particle resolution.

In Chapter 2, we have briefly described the protocols that have been followed to synthesize various colloidal particles. We have also discussed the soft lithographic techniques that have been used to realize templates with complex surface features (Moiré templates).

The deliberate positioning of nano- and microstructures on surfaces is often a prerequisite for fabricating functional devices. While template-assisted nucleation is a promising route to self-assemble these structures, its success hinges on particles reaching target sites prior to nucleation and for nano/microscale particles, this is hampered by their small surface mobilities. In Chapter 3, we show how we circumvent this fundamental limitation by designing templates with spatially varying feature sizes, in this case moiré patterns, which in the presence of short-range depletion attraction presented surface energy gradients for the diffusing colloids. The templates serve a dual purpose, firstly in directing the particles to target sites by enhancing their surface mean free paths and secondly in dictating the size and symmetry of the growing crystallites. Using optical microscopy, we directly followed the nucleation and growth kinetics of colloidal islands on these surfaces at the single-particle level. We demonstrate nucleation control, with high fidelity, in a regime that has remained inaccessible in theoretical, numerical and experimental studies on atoms and molecules as well. Our findings pave the way for fabricating non-trivial surface architectures composed of complex colloids and nanoparticles as well.

Anisotropy in shape and/or interactions is a feature of many molecular systems. In Chapter 4, we demonstrate experimentally the key role of particle shape and interaction anisotropy in reentrant glass phenomena. Our system comprised of colloidal ellipsoids, aspect ratio $\alpha = 2.1$, interacting via a short-range depletion interaction. Since the strength of the depletion interaction between particles also depends on their local curvature, for ellipsoidal particles this leads to an anisotropic attractive interaction. Using a combination of MCT scaling arguments and the size distribution and scaling of most-mobile particle clusters, we first show that, sans attraction, the orientational and translational glass transitions, ${\phi_g}^R$ and ${\phi_g}^T$ respectively, occur at the same area fraction ϕ. Remarkably, the onset of quasi-long-range ordering at intermediate attraction strengths results in a two-step glass transition with an intervening orientational glass regime. Most interestingly, within experimental certainty, we observe reentrant glass dynamics only in the translational degrees of freedom.

In Chapter 5, we have examined the influence of the shape of dynamical heterogeneities on the Stokes-Einstein (SE) and Stokes-Einstein-Debye (SED) relations from

data of previous chapter (Chapter 4) on quasi-two-dimensional suspensions of colloidal ellipsoids. For ellipsoids with repulsive interactions, both SE and SED relations are violated at all area fractions. On approaching the glass transition, however, the extent to which this violation occurs changes beyond a crossover area fraction. Quite remarkably, we find that it is not just the presence of dynamical heterogeneities but their change in the shape from string-like to compact that coincides with this crossover. On introducing a suitable short-range depletion attraction between the ellipsoids, associated with the lack of morphological evolution of dynamical heterogeneities, the extent to which the SE and SED relations are violated remain unchanged even for deep supercooling.

Chapter 6 contains the brief summary and outlook of the works presented in the thesis.

Table of contents

List of figures

List of tables

Chapter 1

Introduction

Colloids−dispersion of solid particles in a fluid−have played a key role in the survival of human civilization. Quite interestingly, the diverse material applications of colloids like in the making of Lycurgus cups (4^{th} century) or as a diagnostic therapy in the cure of dysentery, epilepsy and tumours (17^{th} century) [1] precede the coining of the word "colloid" in mid 19^{th} century. The word colloid originates from the Greek word "kolla" (glue) and "eiods" (appearance) and was coined by Thomas Graham, a Scottish chemist in 1861. Later, a comprehensive understanding of diverse and exotic properties of colloids led to their numerous applications in industries and day-to-day life. Examples include thickening agents, food products such as mayonnaise and ice creams, in the purification of water, paints, inks, electrical gadgets, photonic band gap materials etc. More recently, colloidal crystals as structural color filters are playing crucial roles in the development of next generation electronic gadgets [2–12]. Apart from their versatile material applications, colloids mimic the phase behavior of atomic systems and thus provide microscopic insights into complex, diverse and intensely debated phenomena in condensed matter physics [13–23]. The typical number density of colloidal particles in a suspension is of the order 10^{13}cm^{-3} and hence, the structure and dynamics of systems comprising of colloidal particles, like atomic systems, are governed by laws of classical statistical mechanics. Moreover, the effective interaction potential in colloids has a soft or hard repulsion which is usually followed by a strong or weak attraction and is qualitatively similar to Lennard-Jones (LJ) potential of atoms.

$$V_{\text{LJ}}(r) = 4\epsilon\left[\left(\frac{\sigma}{r}\right)^{12} - 2\left(\frac{\sigma}{r}\right)^{6}\right] \qquad \sigma : \text{size of the atom.} \tag{1.1}$$

In addition to the fact that colloids mimic atoms, the most appealing reason for the current surge in using colloids as model atoms is their slow dynamics. As the sizes of colloids are significantly larger than atoms, their Brownian diffusion time τ_B $(= \sigma^2/D)$ ranges from a few millisecond to seconds and hence they are large enough to be seen and slow enough to be followed at single-particle resolution using a conventional optical microscope. For instance, using ingenious experimental techniques, colloidal supercooled liquids and glasses have helped discern between the competing theories of the glass transition [14–16]. More importantly, unlike atomic systems, the shape and interactions in colloidal systems can be tuned at experimenters' will. In fact, over last two decades, there have been substantial advances in the synthesis of colloidal particles with tailored shape and interaction anisotropies [24]. These include colloidal rods and ellipsoids [25–29], dumb-bells [30], patterned particles like striped spheres [31], complex cluster like dimers, trimers, tetramers [32, 33], lock and key colloids [34], patchy spheres with well controlled valence [35–38], Janus spheres and ellipsoids [39–41], faceted polyhedra like cubes and tetrahedra [42–44] (Figure 1.1). Interestingly, studies over the last couple of years have revealed rich and exotic phase behaviour for particles with shape and/or interaction anisotropies [24, 41, 43, 45–50]. It is worth noting that complex colloids enable us to probe, in addition to translational degrees of freedom (DOF), the influence of orientational and vibrational DOF on the structure and dynamics of the system.

It is apparent from the preceding discussions that research on colloidal suspensions focuses in two broad directions. First, using them for prospective future applications and second as model atoms. This thesis addresses some questions in both these directions. First, in order to overcome the long-standing limitations of low surface mobilities of colloids in site-specific crystal nucleation and growth, we have designed substrates with complex surface features that allow remarkable control over both the size and symmetry of the colloidal crystallites. Second, we have investigated the role of anisotropic interactions in relaxation and transport properties of supercooled liquids and glasses of complex colloids. Coincidently, in all the problems probed here, the nature of interactions between colloids or colloids and the surface have been tuned to realize the desired effects. Thus, we begin our discussion with colloidal hard spheres, the simplest possible interaction in colloidal suspensions.

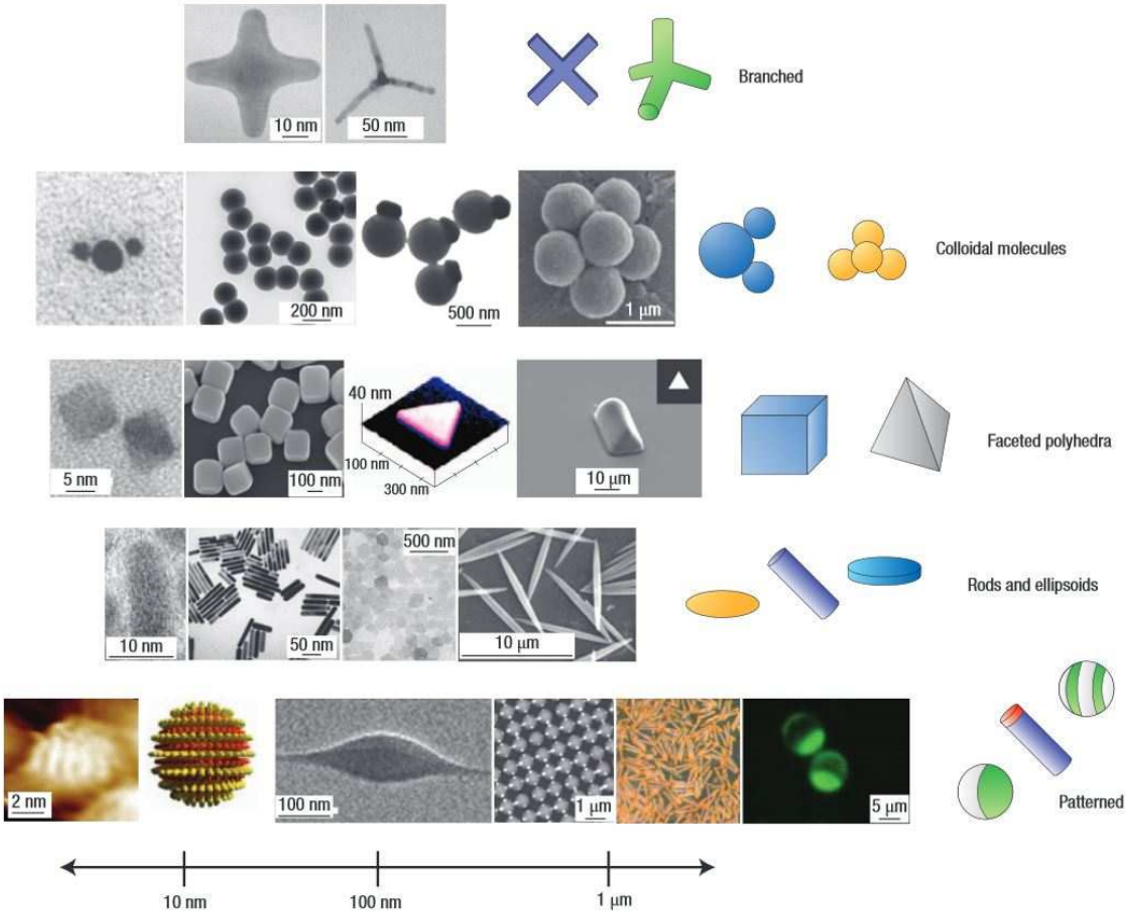

Figure 1.1 Typical examples of colloidal particles with diverse shapes and/or interactions. The first four rows correspond to particles with various shapes. The last row shows, from left to right, examples of patterned particles; striped spheres, biphasic rods, patchy spheres with valence, Au-Pt nanorods and Janus spheres. Adopted from [24].

1.1 Colloidal Hard Spheres

The hard sphere (HS) interaction potential is widely used for understanding the statistical mechanical phenomena of fluids and solids. It is simply described by impenetrable spheres that cannot overlap in space. Interestingly, the inter-particle interaction in hard colloids such as silica, polystyrene, etc. can be best characterized by the HS interaction (Figure 1.2). Mathematically, HS potential is expressed as

$$U_{HS}(r) = \begin{cases} \infty & \text{if} \quad 0 < r < \sigma \\ 0 & \text{if} \quad r > \sigma \end{cases}. \tag{1.2}$$

Here, σ is the size of the colloid. Now, from thermodynamics, the Helmholtz free

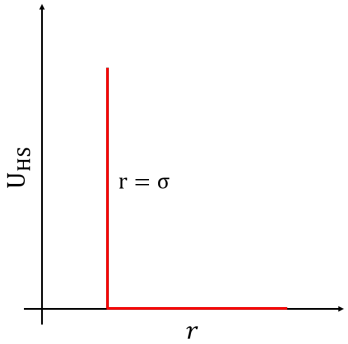

Figure 1.2 Hard sphere interaction potential as a function of radial distance r.

energy F of a system can be expressed as,

$$F = U - TS = -k_B T \ln Z. \tag{1.3}$$

Here, U and S denotes the internal energy and entropy of the system, respectively. Z is the partition function that can be mathematically expressed as,

$$Z = \sum_{config.} \exp\left(- \sum_{i,j\text{bonds}} \frac{U_{ij}}{k_B T} \right). \tag{1.4}$$

Since the inter-particle interaction potential is given by Eqn.1.2, the inner summation in Eqn.1.4 can be simplified as,

$$\exp\left(- \sum_{i,j\text{bonds}} \frac{U_{ij}}{k_B T} \right) = 0 \qquad \text{if } r \leq \sigma \tag{1.5}$$

$$\exp\left(-\sum_{i,j\text{bonds}}\frac{U_{ij}}{k_BT}\right)=1 \qquad \text{if } r>\sigma \tag{1.6}$$

Therefore Z is essentially a sum over all configurations and so, *only* entropy governs the phase behaviour of the particles with HS interactions. Moreover, volume fraction Φ is the lone parameter that controls the entropy of hard spheres and for monodisperse spheres of radius a, Φ can be written as,

$$\Phi=\frac{4}{3}\pi a^3\frac{N}{V} \tag{1.7}$$

where N is the total number of particles in a volume V. Thus, for colloids Φ acts like inverse of temperature of atomic system.

1.1.1 Phase Diagram of Hard Spheres

The first attempt to study the HS phase diagram was made by Wood & Jacobson [51] and Alder & Wainright [52] in 1957. Using analytical works and computer simulations to calculate the free energies of fluid and solid phases, they predicted the existence of a freezing transition for hard spheres. Later, Hoover and Ree reported the fluid-crystal coexistence and fluid-crystal transition in HS systems [53]. The HS phase diagram (pressure versus Φ) is shown in Figure 1.3. The four branches in the phase diagram

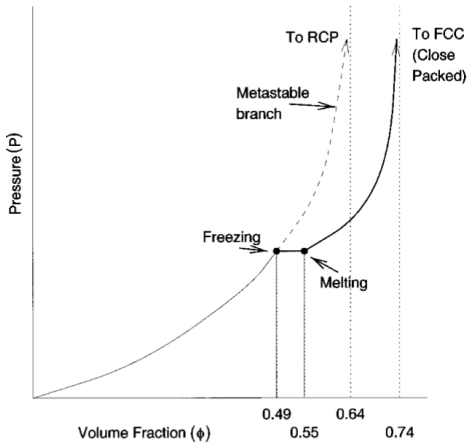

Figure 1.3 The phase diagram for hard spheres. Adopted from [54].

show the fluid phase ($\Phi<0.494$), fluid-crystal coexistence ($0.494<\Phi<0.545$), and the lines leading to random close packing ($\Phi_{\text{RCP}}=0.644$) and closed packed face-centred packing ($\Phi_{\text{fcc}}=0.74$). Further, theories and computer simulations have also predicted

that a rapid quench of the liquid can bypass the transition to the crystalline phase and consequently the HS system falls into a metastable state (supercooled liquids and glasses) [55, 56]. The first experiments to report the transitions to crystalline and glassy states were by Hastings in 1978 [57], Lindsay & Chaikin in 1982 [58] and Murray & Van Winkle in 1987 [59]. Later, in a seminal work, Pusey and van Megen reported an exhaustive phase diagram for hard-sphere colloids [60]. Using PMMA colloids of size $\sigma = 325$nm, they prepared samples spanning a range of Φs that yielded various phases which have close similarity with the predicted phase diagram for hard spheres (Figure 1.4). Interestingly, since the sizes of the colloids were in the visible range of the spectrum, the crystalline phases could be directly inferred from the Bragg reflections of light. The findings of Pusey *et. al.* established colloids as model atoms

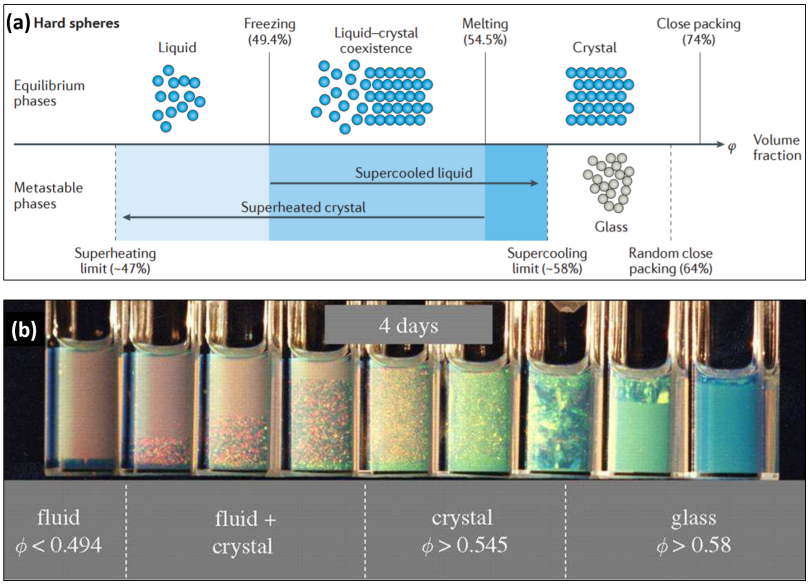

Figure 1.4 (a) Schematic phase diagram of hard spheres. Adopted from [13]. (b) Experimental observation of HS phase diagram in colloidal suspensions of PMMA particles. Adopted from [60].

to investigate diverse phenomena in condensed matter physics. Hence, we will next discuss the inter-particle interactions in colloidal dispersions. Colloids interact via the van der Waals force which arises due to dipole-induced dipole interactions. This force is ubiquitous and most importantly is always attractive in nature. Therefore, colloidal particles, either due to Brownian motion or gravity or both, would have a tendency to form aggregates on collision. Thus, in the following sections, we will focus on ways to stabilize as well as tune the inter-particle interactions in colloidal suspensions.

1.2 Interactions in Colloidal Suspensions

1.2.1 Repulsive Interactions

In order to stabilize the colloidal suspensions, one needs to modify and introduce repulsive interactions between the colloidal particles. This can be achieved either by electrostatic or steric repulsion (Figure 1.5). In the case of electrostatic stabilization, the electric charges on the surface of particles stabilize the colloidal dispersion e.g. polystyrene particles in water. The stability of these colloids are described by DLVO (Derjaguin and Landau, Verwey and Overbeek) theory [61]. According to this theory, the net interaction potential arises due to competition between the van der Waals attraction and the electrostatic repulsion due to formation of the double layer of counter-ions around the colloidal particles (Figure 1.5a and b). Hence, for two spherical

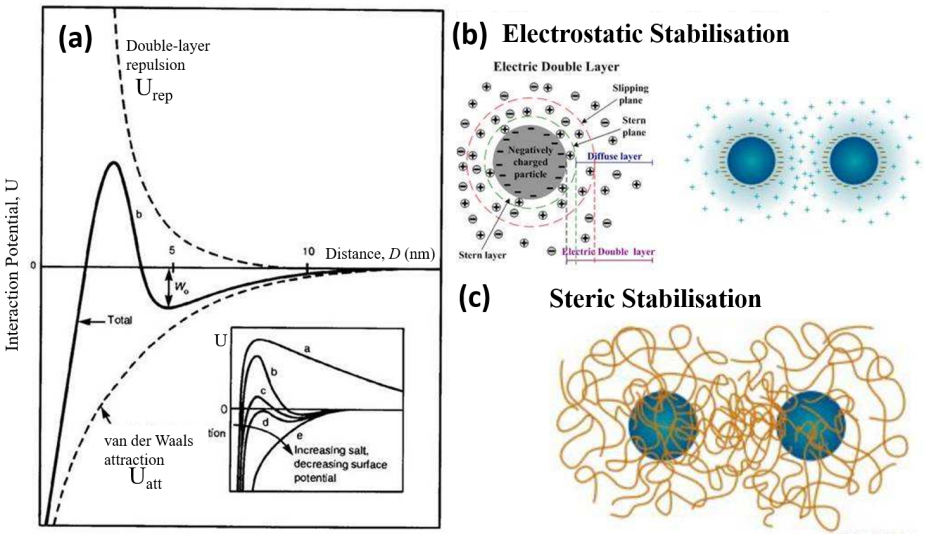

Figure 1.5 (a) Schematic of DLVO potential U. Inset shows the variation of U with the salt concentration. (b) Electrostatic stabilization. The image on left shows the formation of electric double layer around a spherical particle. (c) Steric stabilization. Colloids are represented by solid spheres in (b) and (c). The curves in (c) represent the polymers tethered to the colloids. Adopted from [61].

colloids of size R and separated by a distance D, the net interaction potential U can be expressed as,

$$U = U_{att} + U_{rep} = -\frac{AR}{6\pi D} + \frac{64\pi k_B T R \rho_\infty \gamma^2}{\kappa^2} e^{-\kappa D}. \tag{1.8}$$

Here, A is Hamaker constant, $1/\kappa$ is called Debye screening length and depends on the thickness of electrostatic double layer, k_BT is the thermal energy, ρ_∞ is the ionic concentration in the bulk (at $D = \infty$), and γ is the electrostatic surface potential. κ in Eqn.1.8 is given as,

$$\kappa = \left(\frac{\sum_i \rho_{\infty i} e^2 z_i^2}{\epsilon \epsilon_0 k_B T} \right)^{1/2} \tag{1.9}$$

where e is the electronic charge, ϵ_0 and ϵ are the permittivity of vacuum and the solvent, respectively, i represents the ion index and z is the valency of the ion in the solvent e.g. for H^+, $z = 1$, SO_4^{2-}, $z = 2$. It is evident from Eqn.1.8 and Eqn.1.9 that κ which dictates U, solely depends on the number of ions present in the solvent and hence can be easily tuned by changing the salt concentration in the suspension (inset to Figure 1.5a). Further, it is noteworthy that the presence of surface charges on charge stabilized colloids also allow for their manipulation with application of external fields.

In the case of steric stabilization, polymeric molecules are either chemically attached or physically adsorbed on particle surfaces to stabilize them e.g. polymethyl methaacrylate (PMMA) particles in oil (Figure 1.5c) [61]. Here, the polymer chain dimensions are larger than the van der Waals attraction range. The stability, in this case, is controlled by thickness as well as the density of the polymer layers.

1.2.2 Attractive Interactions

Short-ranged attractive interaction between colloidal particles can be introduced by adding "depletants" to the colloidal suspension. Typically, depletants are much smaller in size than the colloidal particles and are non-adsorbing in nature. In the 1950s, Asakura and Oosawa estimated the depletion interaction potential by taking into account just two factors; osmotic pressure of an ideal solution of depletants and the excluded volume around the colloidal particle [62]. We briefly derive the net interaction potential between two of spherical colloidal particles of diameter $D = 2R_B$ in a bath of depletants with size $d = 2R_S$ and demonstrate the geometric nature of the depletion interactions (Figure 1.6). Assuming that the particles behave as hard spheres, the excluded volume $V_E = \pi(D + d)^3/6$ around every colloid is unavailable to the depletants. Therefore, when the two large spheres come together (center-to-center distance, $x < (D + d)/2$), their excluded volumes overlap and subsequently excluded volume unavailable for the smaller particles is reduced by the overlapping volume

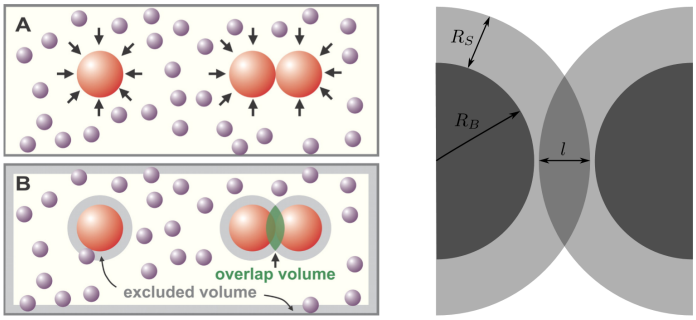

Figure 1.6 (A) Illustration of osmotic pressure exerted by the depletant molecules on colloids (B) Schematic illustration of excluded and overlap volume for hard spheres. The image on right shows the 2D cross-section of the overlap volume. Adopted from [63].

(Figure 1.6B).

$$V'_E = V_E - V_{\text{overlap}} \tag{1.10}$$

$$V'_E = V_E - \frac{2\pi l^2}{3}\left[\frac{3(D+d)}{2} - l\right] \tag{1.11}$$

Here, $l = (D+d)/2 - x/2$, represents the width of the lens formed by the spherical caps (Figure 1.6). Hence, small particles cannot enter this volume V'_E and the osmotic pressure of depletants act on the outer surface of the large colloids and results in a net attraction between the larger spheres.

We can rigorously arrive at the expression for the depletion force between two large particles due to the depletant molecules in the suspension from a statistical mechanics approach also. In the canonical ensemble, the partition function Z is written as,

$$Z = \frac{1}{N!h^{3N}} \int e^{-\beta E} d\Gamma \tag{1.12}$$

where E has contribution from both kinetic and potential energy of the system, $\beta = 1/k_B T$ and h is the Planck's constant. The Helmholtz free energy F can be obtained from Z as

$$F = -k_B T \ln Z. \tag{1.13}$$

Assuming that the small particles also behave as hard-spheres, Z can be approximated as the fraction of total volume $\frac{V_A}{V}$ available to the small particles,

$$Z = \frac{(V_A/V)^N}{N!\Lambda^{3N}} \tag{1.14}$$

where $\Lambda = \frac{h}{\sqrt{2\pi m\beta}}$ is the de-Broglie thermal wavelength and $V_A = V - V_E$ with V being the total volume of the system. Using Eqn.1.14 and Stirling's approximation for $N >> 1$ ($\ln N! \approx N \ln N - N$), Z can be expressed as,

$$F \approx F_{\text{ideal}} - Nk_BT\ln\left(\frac{V_A(x)}{V}\right). \tag{1.15}$$

Here, $F_{\text{ideal}} = -Nk_BT(1 - \ln(N\Lambda^3/V))$ is the ideal contribution to free energy and is independent of x [63]. Now, depending upon whether x is large enough to allow small particles between them or not V_A can be estimated to be,

$$V_A(x) = \begin{cases} V - V_E & \text{if } x \geq d + D, \\ V - V_E + \frac{\pi}{6}(D + d - x)^2(D + d + x/2) & \text{if } x < d + D \end{cases} \tag{1.16}$$

where V_E' have been substituted from Eqn.1.11. Now, using Eqn.1.16 in Eqn.1.15 and subsequent linearisation of the logarithmic expression leads to

$$\ln\left(\frac{V_A(x)}{V}\right) \approx -\frac{V_E}{V} + \frac{\pi}{6V}(D + d - x)^2(D + d + x/2) \qquad \text{for } x < D + d. \tag{1.17}$$

Since depletion force F between two particles suspended in a solution can be evaluated as $F = -\frac{\partial F}{\partial x}\Big|_T$,

$$F = \begin{cases} 0 & \text{if } x \geq d + D \\ -\frac{\pi N k_B T}{4V}(D + d - x)(D + d + x) = -p_0 A & \text{if } x < d + D \end{cases}. \tag{1.18}$$

The negative value of F is the signature of the fact that depletion force is always attractive. Since, the interaction between small spheres was neglected in above derivation, the osmotic pressure p_0 can be expressed in van't Hoff's limit as $p_0 = c_p k_B T$ where c_p is the depletants' concentration in terms of number density. A in Eqn.1.18 is the equivalent circular area of the overlapping volume with radius $r = \sqrt{(D + d)^2 - x^2}/2$. The depletion force between two large spheres is shown in Figure 1.7a. It is worth noting that strength and range of the depletion force can be tuned by varying the concentration c_p and size d of the depletants, respectively. Conventionally, the second term in Eqn.1.15 is termed as the depletion potential U_{depl}.

$$U_{depl} = -Nk_BT\ln\left(\frac{V_A(x)}{V}\right). \tag{1.19}$$

.

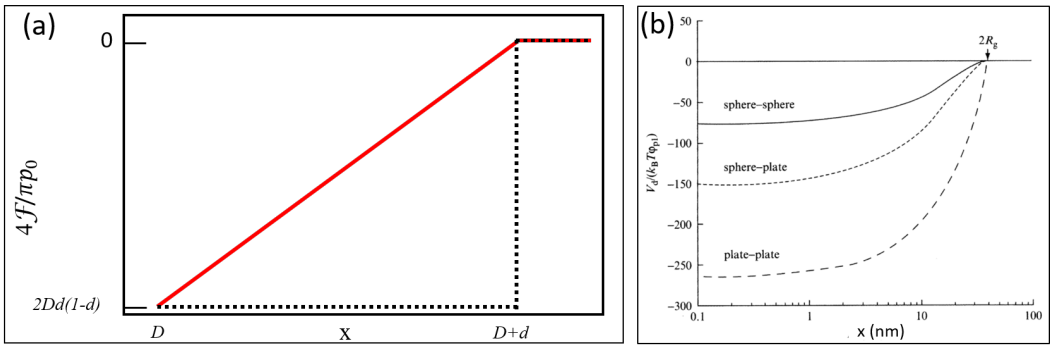

Figure 1.7 (a) Depletion force between two large spheres in a suspension of small spheres with size ratio $R_S/R_B = 0.1$ is drawn in a solid red line. The dashed line shows the profile of depletion force between two plates in a suspension of small spheres. Adopted from [63]. (b) The relative depletion interaction potential versus separation x for two large spheres, a sphere and a plate and two plates, as per Asakura Oosawa model. The radius of gyration of the depletant R_g is 10 nm. The radius of large spheres is 103 nm and the surface of the plate is 150×150 nm. Adopted from [64].

The depletion force is purely entropic in nature and is sensitive only to the local surface topology (Figure 1.7b). Hence, for a given size of the depletant d and fixed density c_p, the overlap volume (Eqn.1.11) solely controls the strength of the attraction between two surfaces. For instance, the strength of attraction between two spheres is almost half the strength between a sphere and a flat wall (Figure 1.7). Although the above derivation is quite simplistic, it works remarkably well for qualitative insights of the interaction potential in complex situations as well.

The colloid-depletant mixture has played a crucial role in probing the microscopic structure and dynamics in equilibrium phenomena like phase transitions as well as in non-equilibrium systems e.g. gelation and glass transition. The phase diagram of colloid-depletant mixtures as function of depletant concentration c_p and colloid volume fraction Φ have been explored and transitions like fluid-gel, fluid-fluid, fluid-crystal etc. have been demonstrated [60, 65, 66]. Interestingly, Dinsmore *et. al.*, in a series of studies, have shown how geometry allows to tune the overlap volume which in-turn have been taken of advantage in micro-fabrication [67–69]. Recently, rich and exotic phase behaviours for complex-colloids−depletant mixtures have been also demonstrated [43, 45–50, 70]. For instance, solid-to-solid phase transitions between square and canted structure have been shown for square shaped colloidal particles [71]; the enhanced attractions between the convex and concave faces in lock-and-key

colloid yield complex colloidal polymers [34]; colloidal dumbbells self-assemble into colloidal micellar aggregates [72]; colloids with valence have been realized by selectively roughening the colloidal spheres on the length scale of size of depletants [73, 74] etc.

Interestingly, exploring the influence of the geometric nature of depletion interactions on site-specific colloidal crystallization as well as on supercooled liquids and glasses of colloidal ellipsoids forms the core theme of the thesis. Thus, while on one hand, it is the geometrical inhomogeneities of the substrates, on the other it is the shape of prolate colloidal ellipsoids which couple with short-ranged depletion interactions and induce anisotropic attractions in the system. While the former created a gradient in the activation energy of the diffusing colloids on the surface that results in a remarkable control over the inter-island separation in colloidal crystal nucleation and growth, the latter allowed us to probe the role of anisotropic interactions in the physics of structural glass transition. In next few sections, we provide background of current approaches to realize colloidal crystals, supercooled liquids and glasses etc. that will enable the readers to better understand and appreciate our motivation behind the problems addressed in the thesis. We begin with colloidal crystals for material applications.

1.3 Colloidal Crystals for Photonics

An ordered array of colloidal particles over large length scales is termed as colloidal crystals (Figure 1.8). The most common example of colloidal crystals is the naturally

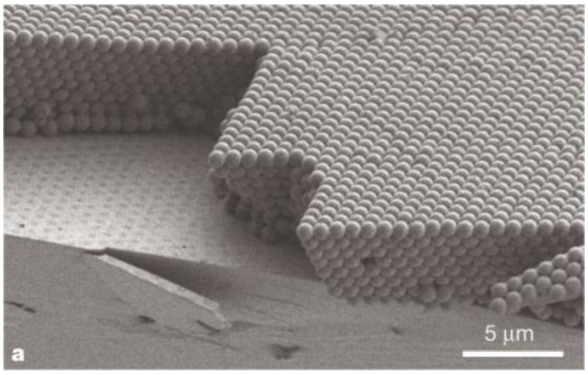

Figure 1.8 SEM image showing thin film of silica colloids grown over a silicon substrate. The size of silica colloids is 895 nm. Adopted from [3].

occurring precious opals which comprise of silica spheres that are 150 to 300 nm in diameter [75]. The precipitation of silica spheres in the siliceous pools and the subsequent compression and sedimentation under gravitational and hydrostatic pressure

over years leads to the formation opals. Interestingly, it is the natural conditions like temperature and pressure which dictate the lattice parameters, orientations and quality of the crystalline structures which results in opals of diverse hues and colors. In fact, based on the parameters of underlying lattices, colloidal crystals interacts strongly with the visible spectrum of the light and show remarkable optical phenomena. In 1887, Rayleigh was first to observe the photonic bandgap in one dimension in periodic multilayered dielectric stacks [76]. However, it was the pioneering work of Eli Yablonovitch [77] and Sajeev John [78] in 1987 that resulted in a surge of research activity in photonic crystals. Photonic crystals comprise of periodic dielectric arrays of micro- and nanostructures that manipulates the propagation of electromagnetic wave in much the same way as the periodic potential in the semiconductors controls the electronic movements by tuning the allowed and forbidden bandgaps. The wavelengths that are allowed by the dielectric structures are called modes and those which are blocked are called photonic bandgaps. Thus far, numerous fabrication strategies have been developed to realize one−, two− and three−dimensional photonic bandgap materials which have potential applications as in optical switch, optical communication and display devices, optical computers [2–8, 79], chemical and biological sensors [4, 9–12], etc.

The colors from the colloidal crystals are dictated by the Bragg's law of diffraction [80].

$$2n_b d\sin\theta_b = m\lambda. \tag{1.20}$$

Here, n_b is the refractive index of material, θ_b is the angle of refraction, λ is the wavelength of scattered light, d is the inter-layer distance and m is an integer. As mentioned earlier, the lattice spacing or the inter-planar spacing of the colloidal crystals can be manipulated by tuning the ionic strength of the dispersing solvents [61, 81], e.g. lattice constant of as large as $\sim 17\mu$m have been realized with 2μm PMMA colloids in cyclohexylbromide (Figure 1.9a). Furthermore, the interstices in the polymer latex colloidal crystals can be infiltrated with inorganic materials and the polymer latex can be subsequently removed to yield inverse opals. In contrast to opals, the much higher refractive index mismatch between the spheres and the medium in the inverse opals result in higher reflectivity and that too over a wider stop-gap (Figure 1.9b). The periodic modulation in the refractive indices can be further enhanced by infilling of the interstices in the colloidal crystals by metals, insulators, semiconductors and polymers. Moreover, the subsequent inversion of the structure by selective removal of

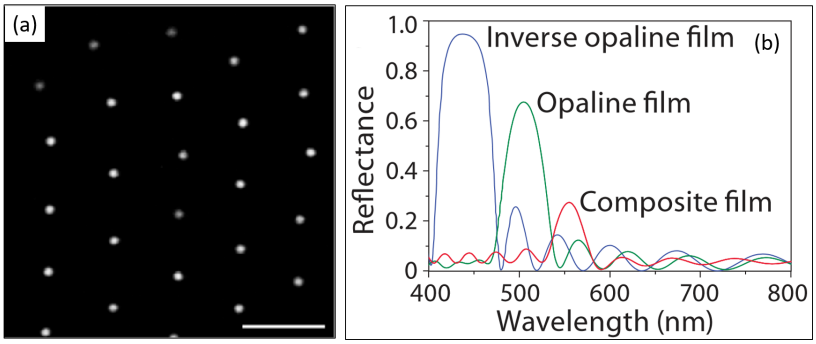

Figure 1.9 (a) PMMA colloidal crystal in cyclohexylbromide solvent. The scale bar represents 20μm. Adopted from [81]. (b) Reflectance profiles of 12 layers thick opaline, composite and inverse opaline film in the (111) direction. Adopted from [4].

the colloidal polymer latex by etchant can allow a still larger degree of control for the modulation of refractive indices.

Colloidal crystals mostly in the form of inverse opals find numerous applications in the photonics industry. Contrary to dyes and pigments, colors from colloidal crystals are entirely due to the underlying structures and hence are also called as structural colors. The pixelated micropatterns in photonic crystals allow for tuning of color and brightness of the reflected lights and can serve as replacements for color filters and backlight units in liquid crystal display (LCD) devices [4]. The display devices based on pixelated photonic crystals are either passive [2] or active [5] mode display. While in the former the lattice constant remains constant and thus the sub-pixelation of red, green, and blue lights are obtained by physical tuning of the colloids' size, the latter allows a dynamic modulation of the lattice constants based on the strength of external fields (Figure 1.10). Unlike the transmission displays, the reflective displays units based on photonic crystals have multiple advantages that include excellent readability even under bright light, higher power efficiency, to name a few. However, fabricating uniform and homogeneous thin films with controlled crystal orientations turns to be the key challenges in realizing a full-fledged digital display from colloidal crystals. Next, we will briefly review the current approaches to realize colloidal crystals for photonics applications.

1.4 Approaches to Realize Colloidal Crystals

The many uses of structural colors have led to an extensive search for viable approaches for realizing colloidal crystals with desired lattice parameters. As mentioned earlier,

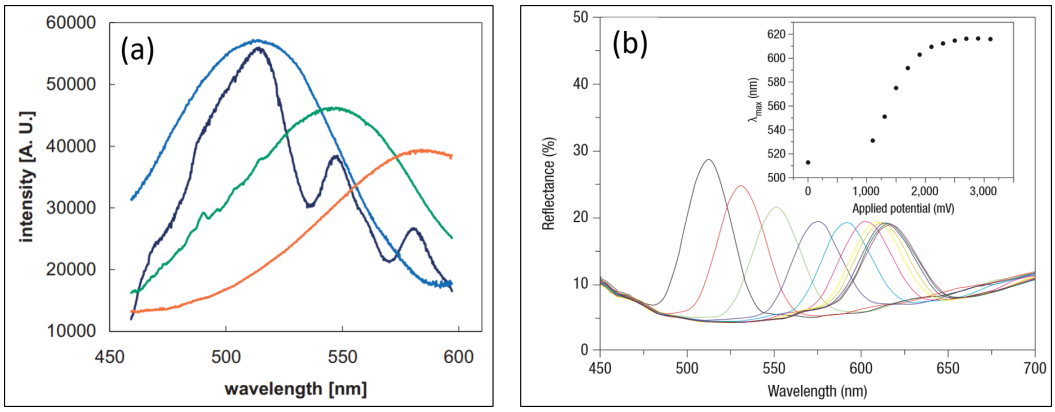

Figure 1.10 Reflectivity from (a) passive and (b) active pixelated multicoloured inverse opal films. While the reflection spectra (a) is due to fixed spatial variation in the lattice constant of the photonic crystal, in (b) the lattice constant can be manipulated with the application of external electric field that results in the variation of reflectance in the entire visible spectrum. The inset in (b) shows the dependence of the peak position on applied potential. (a) and (b) are adopted from [2] and [5], respectively.

since the sizes of these particles are in the sub-micrometer range, their surface mobilities are small. Hence many of the techniques dveloped thus far are a top-down approach to self-assembly and utilize external fields to transport particles to the target sites, prior to the inception of crystal nucleation and growth (Figure 1.11a and b). These include, sedimentation under gravity [60, 82, 83], capillary force driven techniques [3, 6, 84–89], magnetic [7, 90], electrical [91–95], and optical [96, 97] fields driven approaches. More recently, DNA-coated colloids have been used to self-assemble colloidal crystals with diverse sizes and stoichiometries (Figure 1.11c−f) [98, 99]. Further, complex colloids with well-controlled interactions like Janus particles have helped realize crystals with non-trivial packings (Figure 1.11g and h) [41, 45–47]. Although a comprehensive discussion regarding strengths and weaknesses of each of these approaches is beyond the scope of this thesis, it is important to highlight the major challenges of these techniques. Out of all the approaches mentioned above, only external field-based ones have been successful in showing site-specific colloidal crystal nucleation and growth over large length scales, however, they are highly particle-specific. Thus, a mere translation of ideas from one technique (for particles of a specific composition) to another kind of particles becomes a non-trivial chore. Moreover, these techniques are extremely sensitive to the surface charge density on the colloids, number density of the colloids and the free ions in the electrolyte. Interestingly, a bottom-up approach to self-assembly such as epitaxy may allow a larger degree of control over the colloidal crystallization

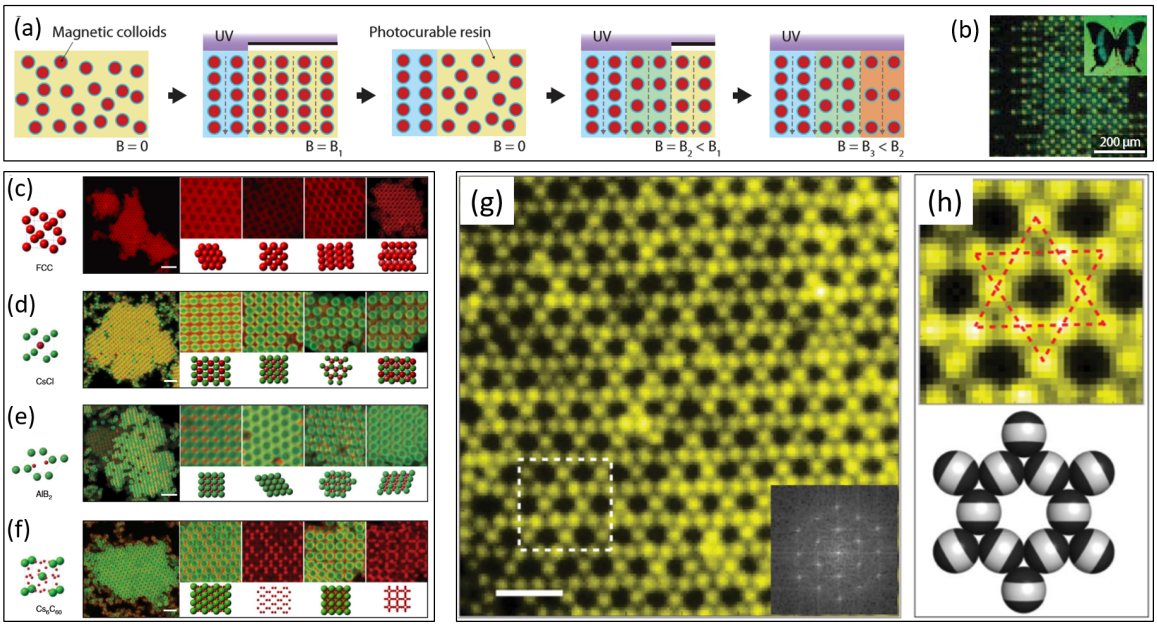

Figure 1.11 (a) Patterning of one-dimensional photonic crystals of colloidal chain-like structures. Superparamagnetic particles are aligned into chains under an external magnetic field. Selective localized UV exposure then fixes the structure. (b) Optical microscopy image of blue and yellow dot patterns forming the butterfly image (in the inset). Adopted from [4]. Confocal fluorescent images and corresponding drawings showing various crystals fabricated from DNA-coated colloids of different sizes and stoichiometries. (c) Face-centered cubic lattice. 111, 100, 110 and 311 planes are displayed. (d) An AB lattice. 110, 100, 111 and 211 planes are shown. (e) An AB_2 crystal. 100, 001, 111 and 101 planes are shown. (f) An AB_6 crystal lattice. 110 and 100 planes are shown, accompanied by the corresponding red channel showing only the structural arrangement of the B particles. Scale bar, 5μm. Adopted from [98]. (g) Fluorescence image of a colloidal kagome lattice (main image) and its fast Fourier transform image (bottom right) from triblock Janus particles. Scale bar is 4 μm. The top panel in (h) shows an enlarged view of the dashed white rectangle in (g). Dotted red lines in (h) highlight two staggered triangles. The bottom panel in (h) shows a schematic illustration of particle orientations. Adopted from [45].

parameters. In fact, atomic heteroepitaxy and pattern-assisted nucleation and growth is routinely used for controlled crystal nucleation and growth for atomic and molecular systems, respectively. In our current endeavour, we have employed epitaxial routes to demonstrate site-specific colloidal crystal nucleation and growth and hence would be delved in detail.

1.4.1 Epitaxial Growth

The growth of a crystalline layer(s) which is facilitated by the underlying crystalline substrate that dictates the symmetry and orientation of the growing crystals is termed as epitaxy. The word epitaxy derives from Greek words 'epi' (above or upon) and 'taxis' (arrangement or order) which roughly translates to arranging upon in an ordered manner. Unlike previous techniques, in epitaxy, the building blocks self-assemble to yield the final nano- or microstructure. Although, epitaxy has been enormously successful for realizing complex and diverse heterostructures for atomic and molecular systems [100–110], lately attempts have been made to extend it to colloids and nanoparticles [17, 111–114]. It is obvious that substrate plays a crucial role is getting desired structure in epitaxial growth. In this context, Blaaderen *et. al.* used an electron beam (e-beam) to etch holes on a soft polymer template to grow colloidal crystals of a specific orientation by faithfully replicating the master template [111]. A slow sedimentation of large volume fraction, $\Phi \sim 50\%$, of the colloidal suspensions allowed a controlled layer-by-layer growth of the colloidal thin film. Around the same time, a simple and facile way to fabricate templates− replica imprinting technique− for soft elastomers was demonstrated by Whitesides' group [115]. The details of this technique will be discussed in Chapter 2. Later, depletion induced short-ranged attraction was ingeniously used by Lin *et. al.* to grow excellent quality colloidal thin films at a much lower Φ [116]. Before we proceed further, it is important to highlight the key thermodynamic/kinetic processes involved in the conventional epitaxial process.

Epitaxy, an inherently out-of-equilibrium growth process is controlled by two parameters− the monomer surface diffusivity D and the deposition flux F (Figure 1.12). D on a periodic potential has Arrhenius form [101],

$$D = D_0 e^{-E_a/k_B T} \tag{1.21}$$

where D_0 depends on the attempt frequency and E_a is the activation energy barrier for hopping from one site to the other. Unlike atomic systems where D is controlled by T,

for colloidal systems, it is the depletion concentration c_p that dictates the bond life time of a colloidal monomer at a given site on the substrate and hence controls D [117]. D decreases with increase in c_p. Like their atomic counterpart, F can be varied by

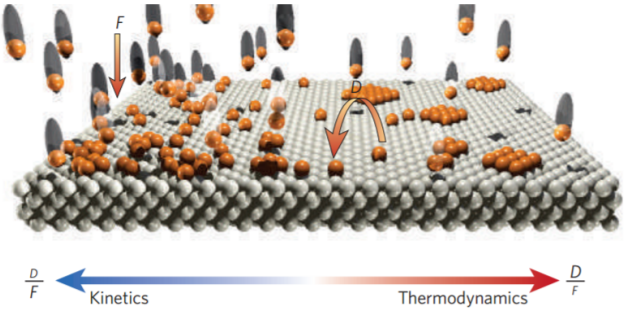

Figure 1.12 Particle-level view of the various processes involved in an epitaxial process. While nucleation and growth and the film morphologies at low D/F are dictated by the kinetics of the systems, at large D/F values, it is governed by the thermodynamic processes. Adopted from [100].

controlling the rate at which particles land on the surface and can be tuned by volume fraction Φ of the colloidal suspension. As the deposition proceeds, the monomers from the bulk land on the surface (at a rate F) and diffuse until they find another particle to form a dimer. In the simplest scenario, these dimers are assumed to be immobile and hence the precursors namely, nuclei for the ensuing growth. In order to follow the nucleation kinetics, we can write the rate equations for both the monomer density n_1 and stable island density n_x [101].

$$\frac{dn_1}{dt} = F - 2\sigma_1 D n_1^2 - \sigma_x D n_1 n_x - \kappa_x F(Ft - n_1) - 2\kappa_1 F n_1 \tag{1.22}$$

$$\frac{dn_x}{dt} = \sigma_1 D n_1^2 + \kappa_1 F n_1 \tag{1.23}$$

Here, σ_1 and σ_x are capture rates for monomers and stable islands, respectively. The first term on right side of Eqn.1.22 represents the increase in monomer density due to flux, second and third term takes into account the decrease in monomer density due to creation of new dimers and capture of monomers by a stable island, respectively. The last two terms represent the direct landing of a monomer on stable islands and the surface. The first term on right side of Eqn.1.23 indicates the increase in stable island density due dimer formation and the second one represents the increase due to direct deposition of a monomer on a stable island. It is observed that with time, the density of monomers in vicinity of a stable island decreases and hence at the edges of

an island, the capture rates should be proportional to the gradient of n_1. However, in mean-field approximations, just outside an island, n_1 takes the average value of the bulk. In principle, with detailed knowledge of σ_1 and σ_x, the coupled Eqn.1.22 and 1.23 can be numerically integrated until saturation of n_x to obtain n_x. For a general case, the expression for n_x looks as [101]

$$n_x = \eta(\Theta, i)\left(\frac{D}{F}\right)^{-\chi} \exp\left(\frac{E_i}{(i+2)k_BT}\right) \qquad \text{with} \qquad \chi = \frac{i}{i+2}. \tag{1.24}$$

Here, i denotes the size of the critical cluster and E_i is the binding energy. An island with $i-$particles is termed critical if the addition of another particle makes it stable against disintegration. For $i = 1$ and surface coverage Θ close to saturation ($\Theta \sim 0.12$), simulations predict $\eta = 0.25$ [118]. Moreover, for $i = 1$, Eqn.1.24 can be simplified as $n_x \propto (D/F)^{-1/3}$. Hence, the ratio D/F solely dictates island density or equivalently mean maximal island separation L on the surface. In a recent experiment, Ganapathy *et. al.* carefully measured the temporal evolution of island density n for a range of D/F values (Figure 1.13a) [17]. With increase in time or the monolayer coverage

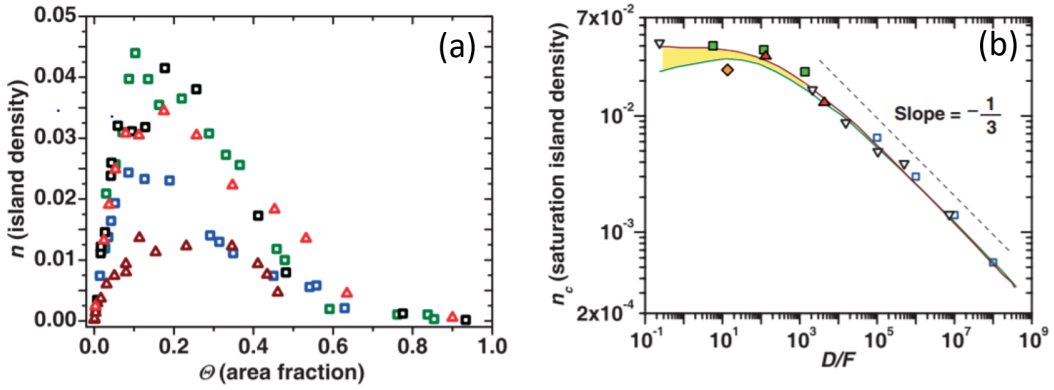

Figure 1.13 (a) Island density n versus monolayer coverage Θ on square and triangular lattice for various D/F values. Square lattice data for $D/F = 1300 \pm 100$ (blue squares), $D/F = 116 \pm 8$ (black squares), $D/F = 5.7 \pm 0.6$ (green squares) and triangular lattice data for $D/F = 4200 \pm 233$ (brown triangles), $D/F = 130 \pm 10$ (red triangles). (b) Saturation island density n_c versus D/F for atomic deposition experiments (inverted black triangles); for Kinetic Monte Carlo simulations (blue open squares); brown line shows the rate equation with post-deposition mobility; rate equation for stable islands is represented by the green line. The experiments with silica colloids on square and triangular lattices are shown in solid green squares and solid red squares, respectively. The orange solid diamond represent the experiments with polystyrene colloid on square lattice. Adopted from [17].

Θ, the density of the monomers landing on the surface increase, and consequently n is observed to increase linearly with time. However, for $\Theta \sim 0.20$, n eventually saturates to n_c signifying that most of the incoming monomers find a stable island within their mean diffusion length L. This implies cessation of further nucleation events and inception of growth. At the later stages, coalescence of the stable island leads to a decrease in n. The variation of n_c with D/F for experiments on colloidal epitaxy as well as for simulations and experiments on atomic thin film growths are shown in Figure 1.13b. Surprisingly, inspite of short-ranged attractive interactions [17], the submonolayer nucleation and growth kinetics in colloidal epitaxy resembles the atomic thin film growth where interactions are longer ranged. These findings were rationalized based on the observations that like the Ehrlich-Schwoebel (ES) barrier in atomic systems [119, 120], colloidal epitaxy also has barriers for movements over step edges and around the corners, but they are purely diffusive in nature [17]. Nonetheless, like the ES barrier in atoms, this effective barriers in colloids play a prominent role in dictating the island morphologies. However, in conventional colloidal/atomic thin film growth, the nucleation sites are not only random but *even* the islands that grow have a broad size distribution which make them unsuitable for many photonics applications. Interestingly, a control over the sites of nucleation as well as island size distribution has been demonstrated in atomic heteropeitaxy [100–110, 121–129] and given the fact that Ganapathy *et. al.* [17] have established that the ideas and concepts from atomic thin film growths can be extended to growth of colloids and nanoparticles, it is tantalizing to speculate if colloidal heteroepitaxy could allow site-specific crystal nucleation and growth. Apart from atomic heteroepitaxy, for molecular systems, templates with periodic and local regions of high nucleation activity (sticky sites) have been fabricated that allow a high degree of control over various crystallization parameters [109, 110]. We will next discuss self-assembly over structured surfaces− atomic heteroepitaxy and template-assisted nucleation and growth− and explore if these techniques could be extended to larger particles like colloids and nanoparticles.

1.4.2 Self-assembly on Structured Surfaces

Atomic Heteroepitaxy

Epitaxy with a relative lattice mismatch between the substrate and the growing layer is termed as heteroepitaxy (Figure 1.14a) [130]. Here, the lattice mismatch is measured

by the misfit parameter ϵ,

$$\epsilon = \frac{a - a_s}{a}, \tag{1.25}$$

where a_s and a are the lattice constant of the substrate and the growing film, respectively. The initial stages of growth in heteroepitaxy proceed via the formation of 2D precursor islands termed as platelets [131, 132]. Since the platelets are small in size, the effects of misfit strain are not relevant to them and thus the nucleation kinetics can be described by equations governing submonolayer nucleation kinetics discussed before [101, 133]. For the subsequent layers, the strain mismatch leads to accumulation of elastic strain energy E_{el} in the growing film that grows linearly with layer thickness h [130, 134].

$$E_{el} = \lambda \epsilon^2 h, \tag{1.26}$$

where λ is a constant that predominantly accounts for the elastic modulus. The layers grow pseudomorphically, layer-by-layer, till a critical thickness h_c, beyond which the strain energy in the growing film is relieved by the formation of dislocations on the surface (Figure 1.14a) [100, 130, 135]. The high mobility of the surface dislocations

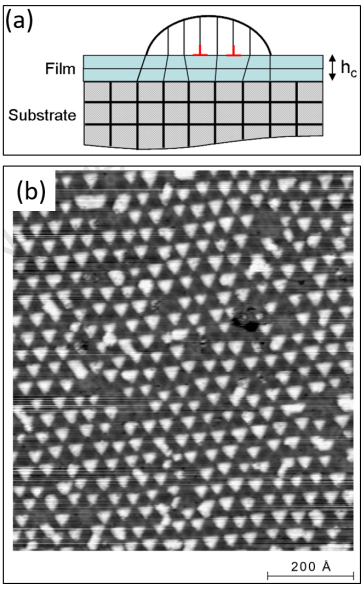

Figure 1.14 (a) Schematic showing the appearance of dislocations after a critical thickness h_c in SK growth mode. Lines represent lattice planes with thicker lines for the substrate lattice and thinner lines for the growing film. The dislocations are highlighted in red at the film/island interface. (b) STM image of periodic array of Fe islands nucleated on the dislocation network of Cu bilayer on Pt(111) at 250 K. Adopted from [108].

along with the fact that they interact via repulsive interactions often leads to highly periodic and symmetric pattern of dislocations on the surface [108]. These dislocations strongly influence the mobility of the incoming adatoms and lead to ordered nucleation and growth of 3D islands on the surface (Figure 1.14b) [106, 107, 136, 103]. Such a growth mode, named after the scientists who noted it first, is also called as Stranski-Krastanowa (SK) mode of growth [137]. It is worth noting that h_c is strongly dependent on lattice mismatch with higher lattice mismatch leading to smaller h_c [130].

Like homoepitaxy, the nucleation and growth kinetics on structured surfaces have been extensively studied with rate equation models [101, 102, 118, 129, 138, 139] which have been often compared with the experiments and kinetic Monte Carlo (KMC) simulations [108, 129, 124, 104]. In heteroepitaxy, the dislocations, by selectively repelling/attracting the incoming adatoms to specific sites, serve as trapping sites on the substrate [108, 133, 140, 141]. Hence, in addition to activation/diffusion energy barrier E_a, trapping energy gain E_t is introduced to take into account the the preferred adsorption of adatoms due to dislocations. Thus, we can write the rate equations for the adatom density n_1, trapped adatom density n_{1t}, stable island density n_x and trapped stable cluster density n_{xt} as [129],

$$\begin{aligned}
\frac{dn_1}{dt} &= F - \sigma_1 D n_1(2n_1 + n_{te} + n_{1t}) - \sigma_x D n_1(n_x + n_{xt} + n_{1t}\nu_0 e^{-(E_t+E_a)/k_BT}, \\
\frac{dn_{1t}}{dt} &= \sigma_1 D n_1(n_{te} - n_{1t}) - n_{1t}\nu_0 e^{-(E_t+E_a)/k_BT}, \\
\frac{dn_x}{dt} &= \sigma_1 D n_1^2, \\
\frac{dn_{xt}}{dt} &= \sigma_1 D n_1 n_{1t}.
\end{aligned} \tag{1.27}$$

Here, n_{te} is the density of empty traps, ν_0 is the attempt frequency, σ_1 is the capture cross section of a trap which is assumed to equal to capture cross section of an adatom, and σ_x is capture cross section of a stable island. At low coverages, the desorption process and the direct impingement of an adatom onto another adatom or a stable island are found to be rare events and hence are neglected in Eqn.1.27 [129]. Numerical integration of Eqn.1.27 with appropriate parameters allows one to follow the evolution of nucleation kinetics with temperature (Black solid line in Figure 1.15a). Figure 1.15a also shows experimentally determined variation of maximal critical nuclei density n_c with temperature for Co on Au(7 8 8) [129]. The excellent agreement between the rate equations predictions and experiments is apparent from Figure 1.15a. Four distinct regime can be clearly observed in the nucleation curve. At low temperatures ($T < 55$K),

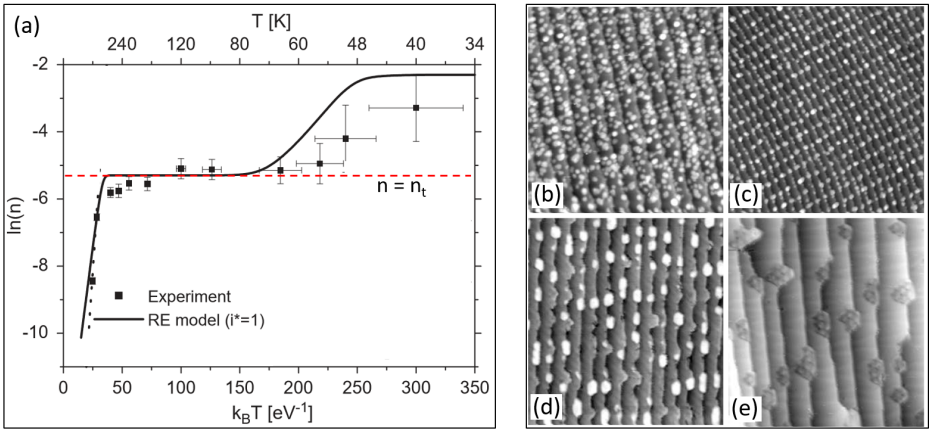

Figure 1.15 (a) Experimental Arrhenius plot of maximal cluster density for Co on Au(7 8 8) (solid squares) with temperature T. The rate equation integration (black solid line) and the trap density/dislocation density (red dashed line) are also shown in the plot. (b) STM images of Co on Au(7 8 8) for various temperatures (b) 50 K (c) 90 K (d) 300 K (e) 450 K (images width 50 nm−except (b) 100 nm). Modified after [129].

atoms are unable to overcome the diffusion energy barrier E_a and the surface acts like a homogeneous substrate [108, 129]. Therefore, the islands nucleate randomly on the surface with no control over the island size distribution (Figure 1.15b). In this regime, for small D, both atoms and colloids follow rate equation predictions and find that n_c depends only on Θ and saturates to a constant value, $n_c \approx 0.03$ for $i = 1$ [17, 101]. For $55\text{K} < T < 80\text{K}$, although adatoms diffuse on the surface, their mean free path remains smaller than the separation between the dislocations and nucleation events continue to occur at random locations. Akin to homoepitaxy, n_c versus $1/T$ exhibits an Arrhenius-like dependence in this regime [108, 129]. A second plateau is observed in n_c for T lying between the $80 - 240\text{K}$. Here, dislocations are able to influence the diffusion of the adatoms on the surface and hence guide them to specific sites on the substrate which subsequently results in site-specific nucleation and growth on the substrate (Figure 1.15c) [108, 129]. It is worth noting that this plateau begins at the temperature T when L that is set by D/F equals the inter-dislocation separation. At high Ts ($T > 240\text{K}$), however, E_a is so large that dislocations are unable to bias the adatoms diffusion on the surface and n_c decrease drastically with T. In this regime, nucleation and growth kinetics once again resembles growth on homogeneous surfaces (Figure 1.15d and e) [108, 129]. In the plateau regime of n_c, since crystalline islands are periodically spaced and have nearly identical monomer capture rates the island

size distribution is expected to be narrower than in the other regime which is indeed observed in experiments and theory (Figure 1.16) [108, 129].

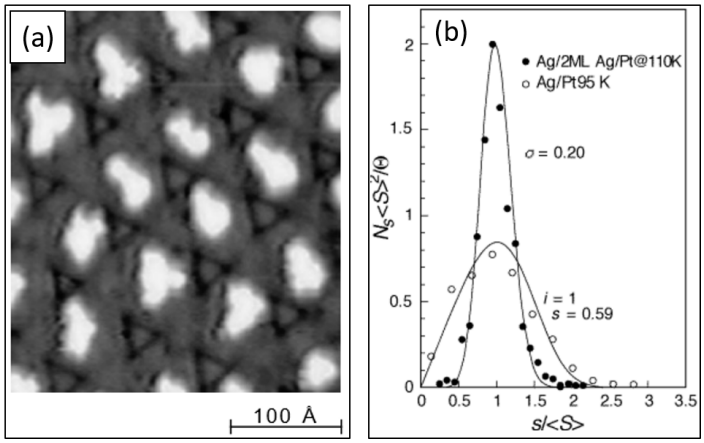

Figure 1.16 (a) A superlattice of islands formed on Ag deposition onto Pt(111) surface at 110 K ($\Theta = 0.10ML$). Island size distribution for random and ordered nucleation in two different regime (curves theory; dots, experiments). The curve for ordered nucleation is a binomial fit. The curve labelled $i = 1$ shows size distribution from scaling theory for random nucleation on an isotropic substrate. Distributions are normalized according to scaling theory (s is the island size in atoms, $\langle S \rangle$ its mean value, and N_s the density of island with size s per substrate atom). Adopted from [108].

In conclusion, it is worth mentioning that though the presence of surface dislocations in atomic heteroepitaxy is the sole reason behind site-selective nucleation and growth of 3D crystalline islands with a narrow size distribution, it is not the only mechanism for strain relaxation in atomic heteroepitaxy. Strain in heteroepitaxy can also be relieved via other means such as surface reconstruction [101, 142]. However, all the strain relaxation mechanisms are mediated via long-ranged interaction potential. On the other hand, the modes of strain relaxation in the colloidal system with short-ranged attraction are yet to be explored in theory, simulations and experiments. In fact, in light of recent experimental observations that vacancies are the only topological defects in rigid colloidal crystals [143, 144], it is unclear whether ideas from atomic heteroepitaxy can be extended easily to colloids.

Pattern-assisted Nucleation and Growth

By selectively patterning the substrate in specific regions, one can create regions of high (low) nucleating activity on the surface which can promote (demote) site-specific

nucleation and growth for molecular systems [109, 110]. For instance, Aizenberg *et. al.* have used the techniques of microcontact printing with elastomeric stamps to pattern metal substrate with self-assembled monolayers (SAM). The schematic protocol followed for fabrication of the template is shown in Figure 1.17a-c. A versatile control over key crystallization processes like location and density of nucleation events, crystallographic orientations, were demonstrated by suitable optimization of various control parameters such as density and sizes of features in master stamps and the concentration of crystallizing solutions [109]. Moreover, for a given density of features on the template,

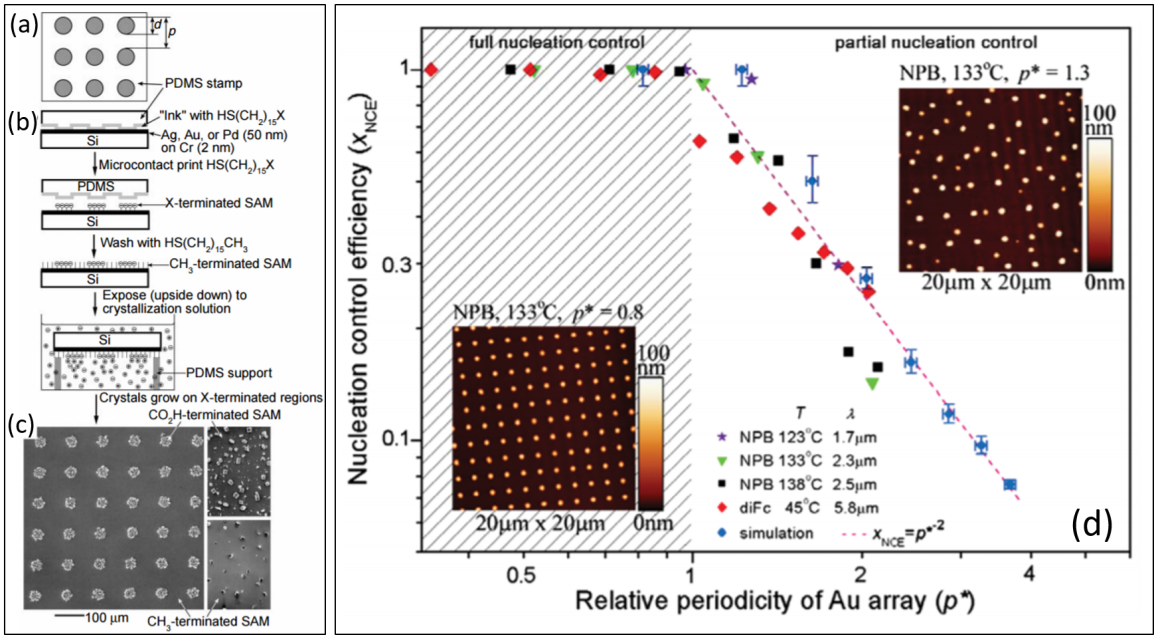

Figure 1.17 (a) Relief structure of the patterned PDMS stamps used for microcontact printing. (b) Schematic representation of the experimental steps. (c) Scanning electron micrograph (SEM) of the sample patterned surface. The insets illustrate crystal grown under identical conditions on a non-patterned SAMs. Adopted from [109]. (d) x_{NCE} versus p^* for experiments with organic molecules under different experimental conditions shown in the legends and Monte Carlo simulations. The dashed pink line shows the relationship $x_{NCE} = p^{*-2}$. Insets show AFM images of growth of organic molecule at 133 ^{o}C, showing full nucleation control at $p^* = 0.8$ (left) and partial nucleation control at $p^* = 1.3$ (right). Adopted from [110].

the diffusion equation was solved to estimate the maximal inter-feature length l_d over which full control over nucleation could be achieved. Strikingly, the value of l_d obtained from solving the diffusion equation under appropriate boundary conditions was in close agreement with one determined experimentally [109]. Furthermore, in concord with deposition-diffusion-aggregation (DDA) model of surface growth [145], l_d was found to

scale with D/F as $l_d \approx (D/F)^{1/4}$. Later, Wang *et. al.* systematically investigated the nucleation control efficiency (NCE) x_{NCE} in epitaxy of organic molecules on selectively patterned surfaces [110]. Mathematically, x_{NCE} is defined as,

$$x_{NCE} = \frac{N_p}{N} \tag{1.28}$$

where N_p and N are the number of patterned sites and total number of experimentally observed islands on the surface, respectively. Further, given that N depends on the experimental control parameters such as T and F, in order to compare x_{NCE} across a range of experimental parameters, a dimensionless periodicity $p^* = p/L$ is defined. Here, p is the pattern periodicity on the substrate and L is the maximal inter-island separation on an unpatterned substrate. L was estimated from island density N/A as $L = (N/A)^{-1/2}$, where A is the area of the unpatterned substrate. Figure 1.17d shows the variation of x_{NCE} with p^*. As expected, while a full control over nucleation is achieved only for $p^* < 1$, beyond which x_{NCE} decreases drastically with p^* [110]. To summarize, L which is controlled by D/F in surface growth experiments sets the upper bound on the pattern periodicity L_p.

A key point to note from the preceding discussion is that the monomer surface mobility is the single most important parameter that dictates nucleation density and morphology of islands during film growth. Low surface mobilities can prevent monomers from reaching the target sites and can result in a partial to complete loss of nucleation control. Further, for a given D/F value, the maximal accessible inter-patterned separation is found to be $L_p^{\max} = L = (D/F)^{\chi}$ where based on different models, the exponent χ lies in the range $\frac{1}{6} < \chi < \frac{1}{4}$ [101, 146]. A closer scrutiny of D/F values accessible in atomic/molecular and colloidal systems reveals that for the former, a broad window of D/F values spanning $10^{-1} - 10^{9}$ can be readily accessed and thus, L can be easily tuned to be larger than L_p allowing complete control over the nucleation over a broad range of island densities. In contrast, for larger particles like colloids and nanoparticles, D turns out to be quite small ($D \sim 0.01\sigma^2/s$) and consequently only a narrower window of D/F values, $10^{-1} < D/F < 10^{4}$, are accessible for them [17]. Unfortunately, over this range, L changes from $5 - 8\sigma$ only. Hence, for $L_p \geq 8\sigma$, full control over the nucleation is not feasible in conventional pattern-assisted nucleation and growth. In such a scenario, we need new design strategies which yield templates that overcome the diffusion-limited length scales and allow a robust control over the

density of nucleation events on the substrate. To better understand this, we will revisit the expression $D = D_0 e^{-E_a/k_B T}$ (Eqn.1.21) for plausible solutions.

The activation energy E_a of a particle on periodic potential is the difference between the saddle-point energy E_s (Figure 1.18a) and the binding energy E_b (Figure 1.18b) [103].

$$E_a = E_s - E_b. \tag{1.29}$$

Given that spatial variation of both $E_s(x)$ and $E_b(x)$ leads to a change in E_a, to know

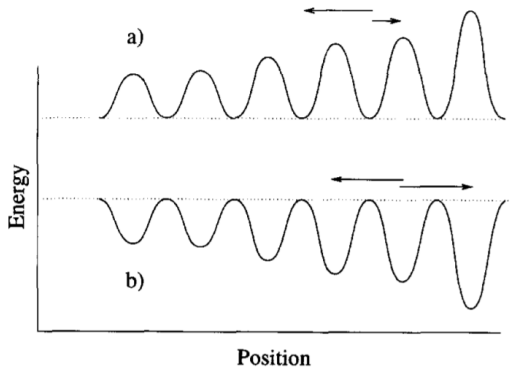

Figure 1.18 The limiting scenario of diffusion barrier. (a) Only the saddle point energy E_s changes. (b) Only the binding energy E_b changes. Adopted from [103].

which one out of two can yield a directed diffusion of the particles on the substrate, let's look at the particle current j_{pq} between to adjacent sites p and q [103].

$$j_{pq} = a(\rho_p w_{p\to q} - \rho_q w_{q\to p}). \tag{1.30}$$

Here, $a^2\rho_p$ represents the probability of finding a particle at site p and $w_{p\to q} = \nu_0 \exp(-\beta(E_s^{pq} - E_B^p))$ represent transition frequency from site p to q. Substituting the value of $w_{p\to q}$ and $w_{q\to p}$ in Eqn.1.30 and expanding only to the linear terms,

$$j_{pq} \approx D_{pq}\frac{\rho_p - \rho_q}{a} + \mu_{pq}\frac{\rho_p + \rho_q}{2}\frac{E_B^p - E_B^q}{a} \tag{1.31}$$

where $D_{pq} = a^2\sqrt{w_{p\to q} w_{q\to p}}$ and $\mu_{pq} = \beta D_{pq}$. Here, D_{pq} and μ_{pq} are local diffusivity and mobility of a monomer. It is evident that while first term in Eqn.1.31 represents the Fick's first law of diffusion [147, 148], the second one is the drift contribution to

the current. Eqn.1.31 can be rewritten in a general form as,

$$J = -D\nabla\rho - \frac{\rho D}{k_B T}\nabla E_B \tag{1.32}$$

It is clear from Eqn.1.31 and Eqn.1.32 that a gradient in the binding energy would add a net drift to the particle current in the direction of increase in binding energy (Figure 1.18b) and hence transport them to the target sites. In Chapter 3, we will demonstrate a new design strategy to fabricate templates that in presence of short-ranged depletion attraction create a gradient in the binding energy and allow a remarkable control over the size and symmetry of the growing colloidal crystallites. Having discussed self-assembly and epitaxy, we will now move on to supercooled liquids and glasses.

1.5 Supercooled Liquids and Glass Transition

The underlying microscopic mechanisms behind glass transition and glasses continue to remain one of the long-standing puzzles in condensed matter physics [14, 22, 149–160]. It is well known that when a liquid is cooled below its freezing temperature T_f, it transforms to crystalline state, with well defined lattice parameters (Figure 1.19a). However, if the same liquid is cooled rapidly, crystallization at T_f is bypassed and

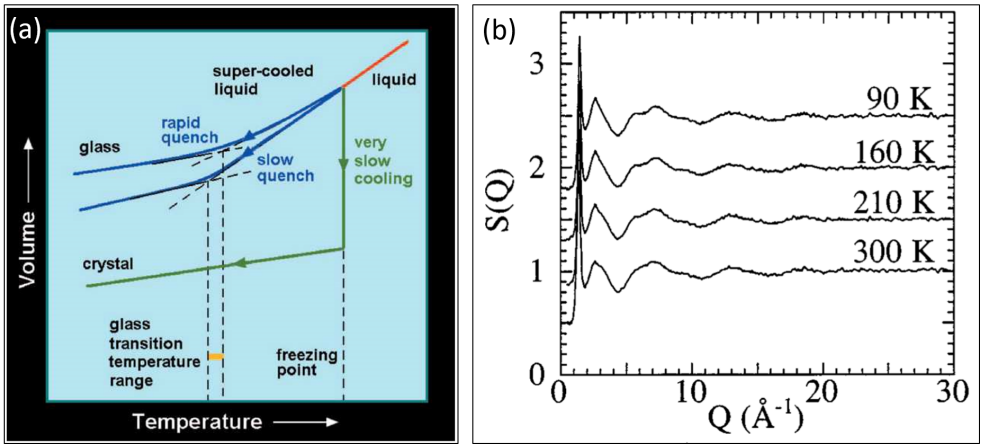

Figure 1.19 (a) Different ways a liquid (red curve) can be transformed to a solid is shown in (V, T) plane at a constant pressure. If the liquid is cooled slowly, it crystallizes below the freezing point (the green curve). If the same liquid is cooled rapidly (blue curve), it bypasses crystallization and passes through a glass transition regime and falls out of equilibrium below T_g. The dependence of T_g on rate of cooling is also shown. Adopted from [156]. (b) The structure factor $S(Q)$ for deuterated propylene glycol ($C_3D_8O_2$) at different temperature. T_g for $C_3D_8O_2$ is 160K. Adopted from [161].

the liquid enters the supercooled regime. On further cooling, at a temperature T_g which depends on the quench rate, the dynamics of the system freeze. Interestingly, accompanying this transition there is an onset of rigidity like in crystals. T_g is called the laboratory glass transition temperature and systems below T_g are termed as glasses. Conventionally, T_g is defined as temperature at which viscosity $\eta = 10^{13}$ poise. Surprisingly, a decrease of temperature to around $2/_3 T_f$ leads to increase in η by almost 14 order of magnitude with no discernible change in the static structure of the liquid (Figure 1.19b). The temperature dependence of the viscosities for various glass forming liquids is best represented in the Angell plot, $\log \eta$ versus T_g/T plot (Figure 1.20) [149, 162, 163] that helps in classifying the glass forming liquids as fragile or strong. Strong glass formers such as silica SiO_2 and gernmania GeO_2 show Arrhenius dependence of viscosity or equivalently the structural relaxation time τ_α with temperature (Figure 1.20),

$$\eta = \eta_0 \exp\left(\frac{E_A}{k_B T}\right) \qquad \text{OR} \qquad \tau_\alpha = \tau_0 \exp\left(\frac{E_A}{k_B T}\right) \tag{1.33}$$

Here, E_A represents the effective activation energy for structural relaxations and can be accounted to the local breaking of chemical bonds such as covalent, ionic, van der Waals bonds etc. On the other hand, the fragile glass formers like *ortho*-terphenyl and toluene have a non-Arrehenius dependence of η with T and hence E_A shows a strong temperature dependent behaviour. This super-Arrehenius increase in E_A with T (Figure 1.20) suggests that the structural relaxation in fragile glass formers can not be accounted for by the energetics of the local bond breaking, rather it must be a collective phenomena involving large number of particles. For fragile glass formers, the variation of τ_α with T can be best fitted by empirical Vogel-Fulcher-Tammann (VFT) law [164–166],

$$\tau_\alpha = \tau_0 \exp\left(\frac{DT_0}{T - T_0}\right) \qquad D, T_0 \text{ are constants,} \tag{1.34}$$

as well as Bässler law [167, 168],

$$\tau_\alpha = \tau_0 \exp\left[K\left(\frac{T_{\text{onset}} - T}{T}\right)^2\right]. \tag{1.35}$$

T_{onset} in Eqn.1.35 is the onset temperature of supercooling. Interestingly, while VFT law suggests some kind of phase transition at a finite temperature T_0 for the fragile

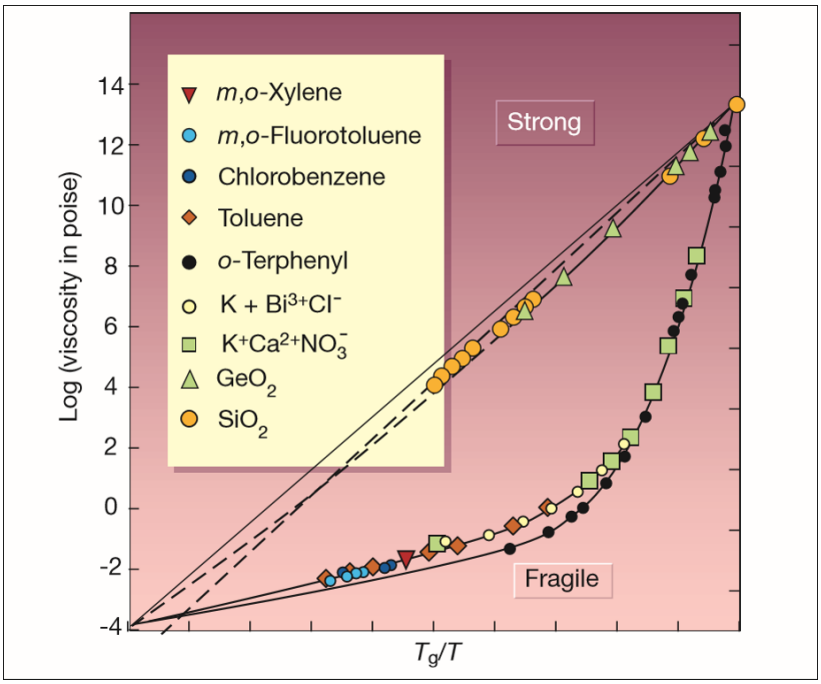

Figure 1.20 Angell plot, viscosity η versus T_g/T for various glass forming liquids. T on $x-$ axis have been scald by respective T_g of the glass forming liquids. Adopted from [153].

glass formers, Bässler law that is purely motivated by kinetic theory predicts glass transition only at absolute zero kelvin.

In the quest to reconcile with the behaviour of η with T, in particular for the fragile glass formers, there have been numerous theoretical attempts to uncover the physics of glass transition. The prominent among them are the free volume theory by Cohen and Turbull (1959) [169, 170], configurational-entropy theory by Adam and Gibbs (1965) [171, 172], energy landscape picture by Stillinger and Weber (1983) [173, 174], mode coupling theory by Bengtzelius, Götze and Sjölander (1984) [175, 176], Random First Order Transition theory by Kirkpatrick, Thirumalai and Wolynes (1987) [177–179], Dynamic Facilitation theory by Garrahan and Chandler (2002) [180, 181]. However, mode coupling theory (MCT) which is a mean field theory is often the first line of attack for the experimentalist. More importantly, this is the only theory that has been extended to systems with shape anisotropy as well as to those with isotropic short-ranged attractions. For the purposes of this thesis, we have used only MCT and thus in the following section we discuss in detail the mode coupling theory of the glass transition. For exhaustive discussions about other theories, readers can see recent review articles by Gokhale *et. al.* [14] and Berthier *et. al.* [22].

1.5.1 Mode Coupling Theory

Mode coupling theory (MCT), one of the earliest mean field theory to explain the slowing down of dynamics of supercooled liquids and glasses, was proposed by Bengtzelius, Götze and Sjölander [175, 176] and independently by Leutheeusser [182]. Here, the coupling of slowly decaying time-correlation functions yields a dynamic crossover temperature T_c with $T_c > T_0$ [158]. MCT predicts a structural arrest based on non-linear feedback mechanisms of microscopic density fluctuations $\rho(\mathbf{q}, t)$.

$$F_s(\mathbf{q}, t) = \frac{\langle \delta\rho^*(\mathbf{q}, t)\delta\rho(\mathbf{q}, 0)\rangle}{N}, \tag{1.36}$$

where $\rho(\mathbf{q}, t)$ for a given wave vector $\mathbf{q}$ is,

$$\rho(q, t) = \sum_{j=1}^{N} \exp[i\mathbf{q} \cdot \mathbf{r}_j(t)]. \tag{1.37}$$

Here, N is the total number of particles, $\mathbf{r}_j(t)$ is the position of j^{th} particle at time t and $\langle\rangle$ denotes the time averaging. $F_s(\mathbf{q}, t)$ is termed as the self-intermediate scattering function and can be easily accessed both in computer simulations and experiments. The static measurement of $F_s(q, t)$ reduces to

$$F_s(q, t = 0) = \frac{\langle \delta\rho^*(\mathbf{q}, 0)\delta\rho(\mathbf{q}, 0)\rangle}{N} \equiv S(q) \tag{1.38}$$

where $S(q)$ is the static structure factor which is nothing but the Fourier transform of particles' position in real space. Further, it can be shown that the pair correlation function $g(r)$ in real space is connected to $S(q)$ via [183]

$$S(q) = 1 + \rho \int \mathrm{d}r e^{-i\mathbf{q}.\mathbf{r}} g(\mathbf{r}) \qquad \text{where } \rho \text{ is density of the system.} \tag{1.39}$$

As per MCT, the starting exact equation of motion for $F_s(q, t)$ is written as [184, 185],

$$\ddot{F}_s(q, t) + \Omega^2(q)F_s(q, t) + \int_0^t M(q, t - t')\dot{F}_s(q, t - t')\mathrm{d}t' = 0 \tag{1.40}$$

Here, $\Omega^2(q) = q^2 k_B T/mS(q)$, and m is the mass. The effects of all the non-trivial interactions except the density fields on density fields itself are contained in the memory

kernel function $M(q,t)$ [22]. The kernel is further split into two terms [184],

$$M(q,t) = M^{\text{reg}}(q,t) + \Omega^2 m(q,t). \tag{1.41}$$

While the first term on right hand side of Eqn.1.41 accounts for the dynamics of the simple liquids at high temperatures, the second term takes care of fluctuating forces due to slowly moving structure. If we assume that $M^{\text{reg}}(q,t)$ is a delta function, $M^{\text{reg}}(q,t) = \nu(q)\delta(t)$, Eqn.1.40 is the equation of motion of a damped harmonic oscillator with an additional term of retarded friction that is proportional to $m(q,t)$ [184]. The key challenge in solving Eqn.1.40 lies in arriving at a suitable approximation for the $m(q,t)$. In the idealised version of MCT, $m(q,t)$ is expressed as a quadratic in $F_s(q,t)$ [184, 185],

$$m(q,t) = \sum_{\mathbf{k}+\mathbf{p}=\mathbf{q}} V(\mathbf{q};\mathbf{k},\mathbf{p}) F_s(k,t) F_s(p,t) \tag{1.42}$$

where the vertices $V(\mathbf{q};\mathbf{k},\mathbf{p})$ are obtained using the structure factors [184]. These assumptions lead to a closed set of coupled equations for $F_s(q,t)$ or the "mode coupling equations" whose solutions yields temporal evolution of the scattering function. The temperature dependence in MCT equations enters via $V(\mathbf{q};\mathbf{k},\mathbf{p})$ and are assumed to be smoothly varying functions of all the control parameters [184]. It is noteworthy that any singularities observed in MCT solutions are not due to the singularity in the input parameters, but due to the non-linearity of the equations of motion itself [185]. Further, given that this non-linearity is associated with the $S(q)$ that is temperature dependent, the observed temperature dependence in the behaviour of $F_s(q,t)$ are entirely due to the structure factor. Unfortunately, the complex nature of MCT equation allows only for the numerical solutions. Hence, Bengtzelius, Götze & Sjölander [175] and Leutheeusser [182] independently, assumed the structure factor to be a $\delta-$function at q_0, the location of first peak in $S(q)$ which transforms Eqn.1.40 into a single equation for correlation function for q_0 [185].

$$\ddot{\Phi}(t) + \Omega^2\Phi(t) + \nu\dot{\Phi}(t) + \Omega^2 \int_0^t m[\Phi(t-t')]\dot{\Phi}(t')\mathrm{d}t' = 0, \tag{1.43}$$

where $m[\Phi]$ is a low order polynomial in Φ and $\Phi(t) = \frac{F_s(q_0,t)}{S(q_0)}$. Eqn.1.43 involves a single correlation function and is termed as schematic model [185]. Notably, in line with MCT, the temperature dependence in Eqn.1.43 enters through the coefficients of

the polynomial $m[\Phi]$. Interestingly, it has been shown that if the non-linearity in the $m[\Phi(t)]$ exceeds beyond a specific threshold, $F_s(q,t)$ does not decay to zero even at infinite time limit and system becomes non-ergodic with the transition being termed as mode coupling crossover. Next, let's look at some of the key predictions of MCT that can be tested in experiments and computer simulations.

Predictions of MCT

In order to investigate the validity of the MCT, it is imperative to study the temporal evolution of correlation functions $\Phi(t)$ over full time as well as over a wide range of temperatures. Figure 1.21 shows, the evolution of $\Phi(t)$ with t for a model with $m(\Phi) = \lambda_1\Phi + \lambda_2\Phi^2$ where coupling parameters $\lambda_i > 0$, as computed by Götze and Sjögren. The change in λ_is in the schematic models is analogous to change in the temperature in real systems [184, 185]. At short times, $\Phi(t)$ shows a quadratic

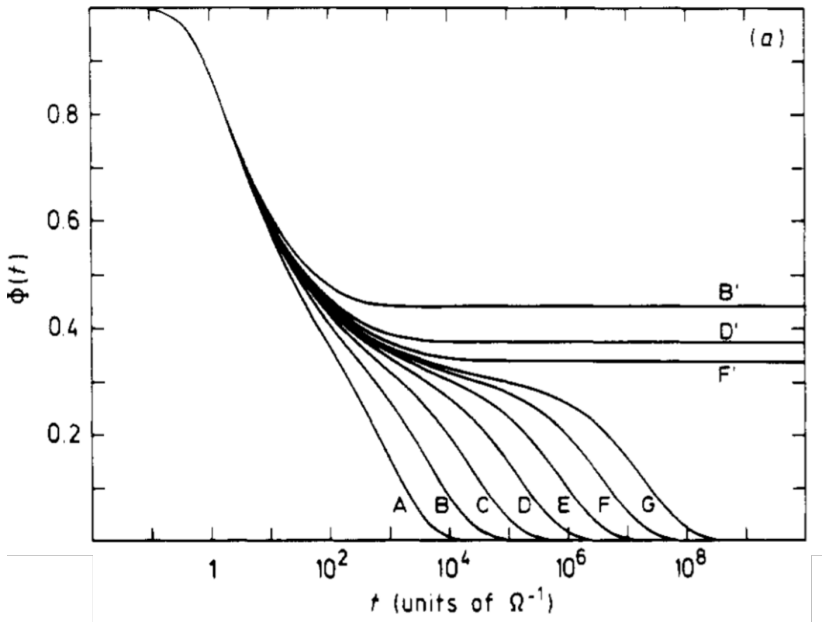

Figure 1.21 $\Phi(t)$ versus t. Different curves corresponds to distinct λ_i value and are chosen in such a way that their distance to their critical values decreases like $0.2/2^n$ for $n = 0, 1, 2, ...$ (liquid, curves A, B, C, ...) and increase like $0.2/2^n$ for $n = 0, 1, 2, ...$ glass, curves F′, D′, B′, ...). Adopted from [186].

dependence on t suggesting ballistic dynamics of particles (Figure 1.21). For high temperatures, curve A, $\Phi(t)$ predominantly show an exponential decay. With decrease in temperature (say curve D), however, a inflection point is observed in $\Phi(t)$ in the vicinity of which correlation functions decay slowly. This regime is termed as $\beta-$relaxation

regime. On further cooling (curve G), a clear plateau is seen at intermediate times, and $\Phi(t)$ enters so called $\alpha-$regime and eventually decay to zero. The physical reason for a two-step relaxation at lower temperature is attributed to the caging of particles by neighbours and is the most outstanding feature of MCT that distinguishes a supercooled liquid from its high temperature counterpart. While the first step corresponds to rattling of particles inside the cages formed by their neighbours (β-relaxation), the second one corresponds to the cage rearrangements and escape of the particles from their respective cages (α-relaxation). Beyond a critical temperature $T < T_c$ (curve F$'$), the height of plateau in $\Phi(t)$ increases and the plateauing begins at a much shorter times. MCT predicts [151, 184] and experiments on polymer glass formers [187] find that the height of the plateau scale as $\sqrt{|T_c - T|}$. Moreover, correlation functions (curves F$'$, D$'$ and B$'$) do not show any decay even at $t = \infty$. The temperature T_c is termed as the mode coupling crossover temperature. Remarkably, MCT predicts the decay behaviours of the relaxations in $\alpha-$ and $\beta-$ relaxation regimes and correlates them to estimate T_c [186, 188, 189].

Decay Behaviour in $\beta-$relaxation regime

The decay behaviour of correlators in $\beta-$relaxation regime is expressed as [185, 189],

$$F_s(q,t) = f_c(q) + h_q\sqrt{\sigma}g_{\pm}(t/t_\sigma) \tag{1.44}$$

where q dependent constants $f_c(q)$ and h_q represents the plateau height (also called the non-ergodicity parameter) and amplitude, respectively. The $\pm$ in $g_\pm$ denote early and late $\beta-$relaxation regime, respectively. σ is the separation parameter,

$$\sigma = C(T - T_c). \tag{1.45}$$

In the early $\beta-$relaxation regime (time intervals close to the plateau but before it) $g_+(t/t_\sigma)$ shows a power law decay (Figure 1.22),

$$g_+(t/t_\sigma) = \left(\frac{t}{t_\sigma}\right)^{-a} \qquad \text{for} \quad \frac{t}{t_\sigma} << 1 \tag{1.46}$$

The above time dependence of $g_+(t)$ is termed as *critical decay law* with exponent $0 < a \leq 1/2$. On the other hand, in the late $\beta-$regime (time intervals close to the plateau but just after it), $g_-(t)$ shows a different power law dependence and is called

von Schweilder law (Figure 1.22),

$$g_{-}(t/t_{\sigma}) = -B\left(\frac{t}{t_{\sigma}}\right)^{b} \qquad \text{for} \quad \frac{t}{t_{\sigma}} >> 1 \tag{1.47}$$

where B is a constant and lies in the range $0 \leq b \leq 1$. Moreover, a and b are also related via the equation,

$$\frac{\Gamma(1-a)^2}{\Gamma(1-2a)} = \frac{\Gamma(1+b)^2}{\Gamma(1+2b)}. \tag{1.48}$$

The time scale of $\beta-$relaxation, t_{σ} is obtained as,

$$t_{\sigma} = \frac{t_0}{|\sigma|^{1/2a}} \tag{1.49}$$

where t_0 is the system universal constant. It is clear from Eqn.1.49 that the intercept on T axis in a plot of ${t_{\sigma}}^{-2a}$ versus T would yield T_c.

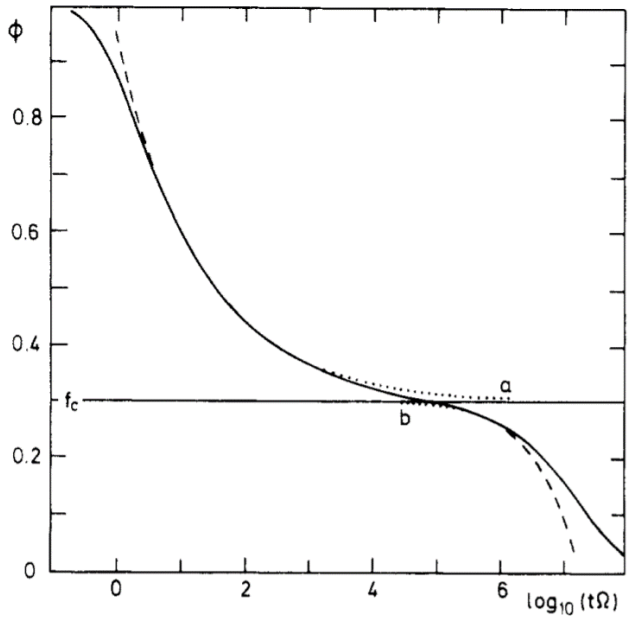

Figure 1.22 $\Phi(t)$ versus t for $\lambda = 0.7$ showing the extraction of power law exponent a (dotted line) and von Schweilder exponent b (dashed line). Adopted from [190].

Further, it is worth noting that the constant h_q in Eqn.1.44 is independent of both time and temperature and thus time dependence in $F_s(q,t)$ is only due to $q-$independent $g_{\pm}(t)$ and hence "universal" in nature for a given system [185, 189]. In other words, Eqn.1.44 implies that the relaxations in $\beta-$relaxation regime can be factorized into space and time dependent components which are completely independent of each

other. The factorization property can be demonstrated by taking the ratio of the spatial-Fourier transform of Eqn.1.44, $F_s(r,t) = f_c(r) + H(r)\sqrt{\sigma}g_{\pm}(t)$ [189, 191],

$$\frac{F_s(r,t) - F_s(r,t')}{F_s(r',t) - F_s(r',t')} = \frac{H(r)}{H(r')} \tag{1.50}$$

and showing that it is independent of t. Here r and r' and are arbitrary and t and t' lie in the $\beta-$relaxation regime (Figure 1.23).

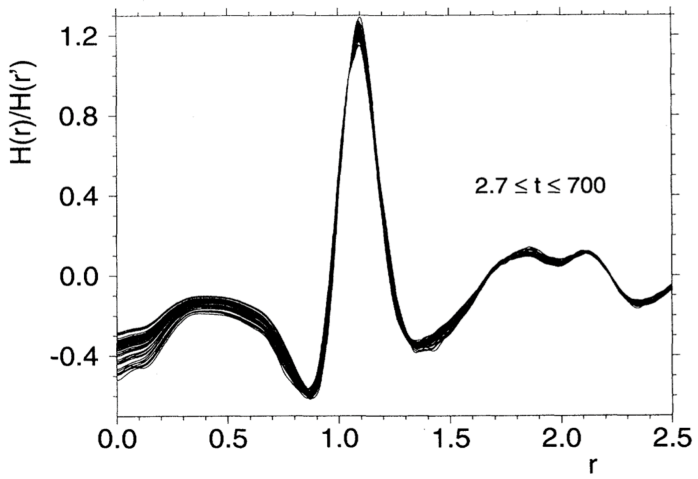

Figure 1.23 Ratio of critical amplitudes for different times in $\beta-$relaxation regime for distinct part of van Hove correlation function in a binary Lennard-Jones system. Adopted from [191].

Decay Behaviour in $\alpha-$regime

The long time decay of $F_s(q,t)$ for supercooled liquids follow a stretched exponential and yields the structural relaxation time τ_α [186, 192],

$$F_s(q,t) = f\exp[-(t/\tau_\alpha)^{\beta}]. \tag{1.51}$$

Here β is the stretching-exponent. MCT predicts τ_α to diverge as power law on approaching T_c,

$$\tau_\alpha(T) \propto (T - T_c)^{-\gamma} \tag{1.52}$$

where the scaling exponent γ is dependent on the exponents a and b as,

$$\gamma = \frac{1}{2a} + \frac{1}{2b}. \tag{1.53}$$

Eqn.1.46 and Eqn.1.47 are often used to calculate a and b, respectively, in experiments and compute simulations. Strikingly, once again intercept on T axis in the plot of ${\tau_\alpha}^{-1/\gamma}$ versus T yields T_c.

The other distinct feature of $\alpha-$relaxation regime is the time-temperature superposition principle (TTSP) [193, 194]. This means that if $F_s(q,t)$ at different temperatures are scaled by their respective τ_α, $F_s(q,t)$ at different T overlaps on a master curve only in the $\alpha-$regime (Figure 1.24).

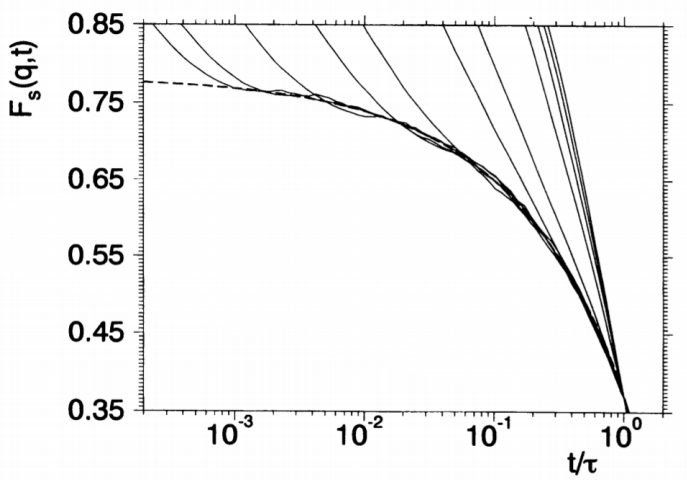

Figure 1.24 The collapse of $F_s(q,t)$ on a master curve (dashed line) in $\alpha-$relaxation regime obtained from von Schweilder law for Lennard-Jones binary system. The time axis rescaled with τ_α. The temperature in kelvin (from left to right): 5.0, 4.0, 3.0, 2.0, 1.0, 0.8, 0.6, 0.55, 0.5, 0.475 and 0.466. Adopted from [194].

In summary, MCT is one of the earliest microscopic theory of glass transition whose predictions have been extensively tested in experiments as well as computer simulations. However, one needs to take note of the fact that MCT best captures the dynamics only in the supercooled regime ($T > T_c$). In the vicinity of T_c, it is believed that hopping processes which are neglected in MCT equations starts playing a dominant role and when included the singularity at T_c vanishes [186]. In the extended version of MCT, it has been indeed shown that the correlation functions decay completely even beyond T_c (Figure 1.25). However, inspite of these limitations, MCT continue to be the most preferred tool to understand the structure and dynamics of supercooled liquids. Quite remarkably, this is the only theory that has been extended to particles with isotropic attractive interactions [195] as well to one with shape anisotropy [196, 197] and will be discussed next.

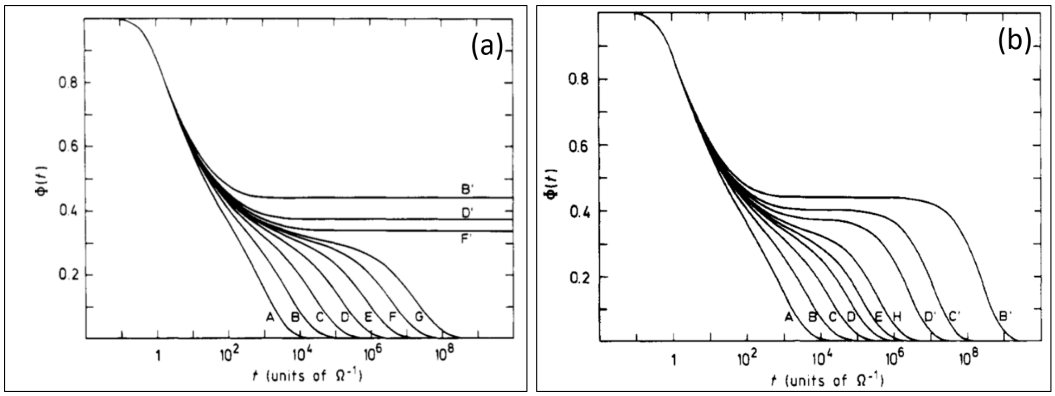

Figure 1.25 The singularity at T_c in (a) ideal MCT equations vanishes in the (b) extended version of MCT that includes the hopping processes. Adopted from [186].

1.5.2 MCT and Attractive Glasses

A systematic tuning of interaction potential in colloidal/molecular systems from hard sphere repulsion to short-ranged attraction leads to the emergence of rich and novel phase diagrams [66, 155, 198, 199]. Using the square-well model of inter-particle attractions, the phase diagram of the colloid-polymer mixture has been extensively probed within the framework of MCT [195, 200]. The key feature of the system with short-ranged attractive interactions is the existence of two competing length scales− the range of hard-core repulsive potential and that of attractive well. However, it is the ratio of the attractive to repulsive range, $\epsilon = \Delta/\sigma$, that dictates the phase behaviour of the system [155]. A large ϵ leads to behaviour that are similar to van der Waals fluids, however, as the range of attraction Δ narrows, the glass transition is observed to be temperature/attraction strength dependent and moves to lower Φs. The typical phase diagram in (T, Φ) plane, as predicted by MCT, is shown in Figure 1.26a. With the addition of square-well short-ranged attraction to the hard sphere potential, MCT predicts two lines of transition from liquid to glass [195, 200]. While one of them extends to high temperature and asymptotically approaches the repulsive glass transition Φ_c, the other line originates at some finite value of attractive potential and is almost parallel to the $\Phi-$axis at lower temperature. The former is called repulsive glass line (RGL) and the latter is termed as attractive glass line (AGL). At a fixed Φ, as we move down the T-axis, the transition line move towards higher Φ (RGL) and comes back to a lower Φ (AGL) with increasing attraction strengths. This phenomena is termed as reentrant in glassy dynamics i.e. at a fixed Φ greater than the repulsive glass transition Φ_c, the repulsive glass melts to an ergodic fluid and forms a novel

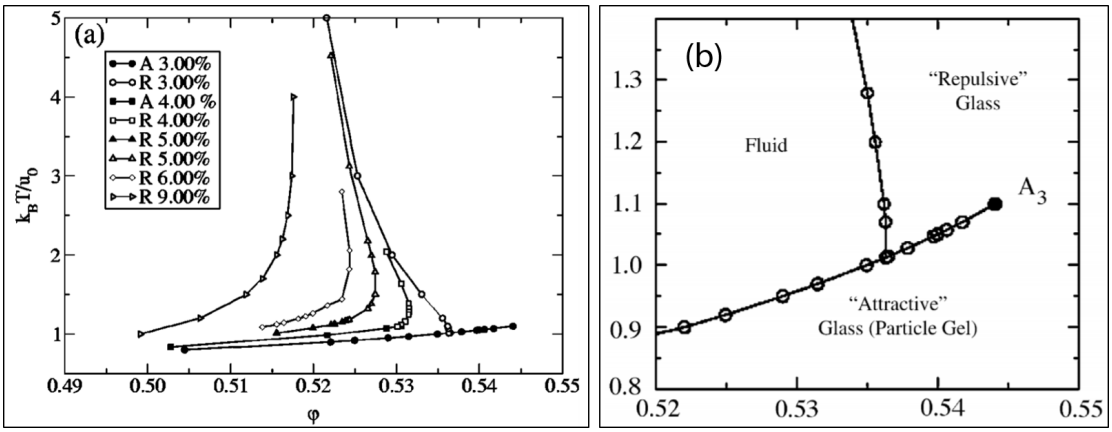

Figure 1.26 (a) Phase diagram for a square-well system at various ϵ. Adopted from [200]. (b) Schematic to show the A_3 singularity. Adopted from [155].

glass - attractive glass - at even higher interaction strengths. As mentioned before, the reasons for emergence of two different glasses are due to two different competing length scales set by attractive and repulsive potentials. The dynamics in repulsive glasses is dominated by cage relaxations whereas in attractive glasses, the bonding between the particles dictate the dynamics. Also, the shift of RGL to higher Φ depends on the relative width of the attractive potential to the repulsive potential ε (Figure 1.26a). MCT further predicts that irrespective of the shape of interaction potential, there exist a window of attraction potential well-widths for which attractive and repulsive glasses coexist (Figure 1.26b) [200, 195]. This coexistence curve terminates in a higher order dynamical singularity, the end point of AGL, called the A_3 singularity, beyond which the distinction between attractive and repulsive glasses vanishes (Figure 1.26b). This implies that the length scale set by the range of the interaction potential is comparable to how much a particle can move within a cage. Furthermore, correlation functions such as $F_s(q,t)$ that exhibit a two-step relaxation for attractive and repulsive glasses are predicted to show a logarithmic decay in the vicinity of the A_3 singularity [195, 200]. Thus far, the experimental evidence of logarithmic decay has only been in a copolymer micellar system (Figure 1.27) [199].

1.5.3 MCT and Phase Diagram of Ellipsoidal Particles

The first tentative phase diagram for ellipsoids, the simplest deviation from spherical particles, as function of aspect ratio $\alpha = l/w$ was proposed by Frenkel *et. al.* in 1984 [201]. Here l and w are major and minor axes of ellipsoid. Later, using molecular mode

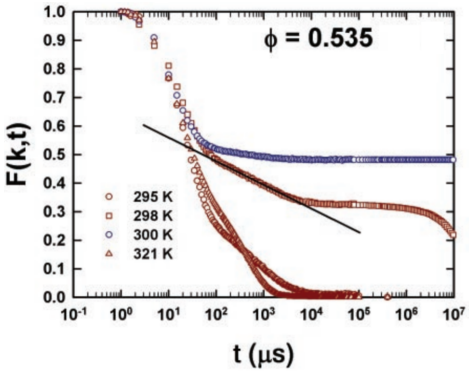

Figure 1.27 The intermediate scattering function $F_s(q,t)$ measured at $\Phi = 0.535$, where liquid-to-attractive glass transition is predicted, as function of T. The logarithmic decay, preceding the plateau region, in the vicinity of A_3 singularity ($T = 298$K) is shown by the solid line in the linear-log plot. Adopted from [199].

coupling theory (MMCT) [202–204], a rich and complex phase diagram for ellipsoids have been proposed (Figure 1.28). MMCT predicts that with increasing α, the glass transition for prolate ellipsoids is primarily driven by the orientational DOF [203]. Additionally, it also predicts a two-step glass transition for $\alpha \geq 2.5$, with formation of nematic domains where interdomain orientational freezing precedes the intradomain translational freezing and a single conventional glass transition for short α ($\alpha \leq 2.5$) [203].

1.6 Colloidal Supercooled Liquids and Glasses

1.6.1 Repulsive Colloidal Glasses

The microscopic insights of structure and dynamics from colloidal supercooled liquids and glasses have helped validate, disprove and guide our basic understanding of glasses and glass transition. However, it is important to highlight at the outset, the fundamental difference between colloids and their atomic counterparts [205–207]. While the short time dynamics are ballistic in atomic systems, they are diffusive in nature for colloids. Further, the role of hydrodynamic couplings in dense colloidal suspensions are not well understood [208]. But, recent simulations have shown that these two effects are unimportant for glass transition physics [209–212]. The third point of difference is in context to polydispersity of the colloidal samples which eventually frustrates the system from crystallization [213, 214] and shifts the glass transition points to a higher Φs [215–217]. In addition, recent observations of spontaneous crystallization of colloidal

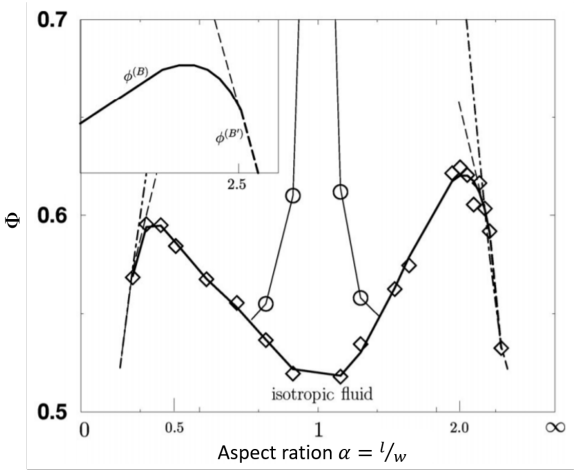

Figure 1.28 Phase diagram for the ideal glass transition of ellipsoids. The solid and dashed lines depict type-B glass transition lines $\phi_c^B(\alpha)$ and $\phi_c^{B'}(\alpha)$, respectively. The thin solid line is the $\phi_c^A(\alpha)$ glass transition line. The nematic instability occurs at $\phi_{nem}(\alpha)$ and is shown as thin dashed-dotted lines. The inset shows the situation around $\phi = 2.5$ where the $\phi_c^B(\alpha)$ glass transition line merges into the $\phi_c^{B'}(\alpha)$ transition line. For $\phi > 2.5$ the $\phi_c^{B'}(\alpha)$ transition is the physical one (thick dashed line) whereas for $\phi < 2.4$ it is an unphysical solution (thin dashed line). Adopted from [203].

glass in microgravity [218] has led to some controversy about the effect of gravity on colloidal glass transition phenomena. However, given the fact that predictions from gravity free simulations are in excellent agreement with colloidal experiments, it is plausible that gravity does not have any role in the observations of colloidal glasses. It is worthwhile to mention that whether or not hard spheres show a glass transition, there is clearly a change in the nucleation mechanism in the vicinity of glass transition [207]. After enlisting the key differences between the atomic/molecular and colloidal glass formers, we turn our attention to colloidal supercooled liquids and glasses.

In 1982, Lindsay and Chaikin were first to observe a glassy phase in a binary colloidal system [58]. Later, a systematic study of phase diagram as function Φ by Pusey and Megen in 1986-87 showed the glass transition in sterically stabilized PMMA colloidal particles [60, 219]. Coincidently, the initial foundations of the key theories on glass transition like MCT had been already laid down by then. Hence, experiments on colloidal supercooled liquids and glasses and simultaneously computer simulations became a hotbed of activity to test the predictions/validity of these theories. Pusey *et. al.* used the techniques of dynamic light scattering (DLS) to probe the dynamics at various Φs [219]. In DLS, the temporal fluctuations of scattered light, at a given wave

vector q, have information about the dynamics of the system. The normalized time correlation of the scattered light for a given q, $g^{(2)}(q,t)$ yields the self-intermediate scattering function $F_s(q,t)$

$$g^{(2)}(q,t) = 1 + \left(\frac{cF_s(q,t)}{S(q)}\right)^2 \tag{1.54}$$

where c is an instrument constant. Figure 1.29 shows the typical decay profile of $F_s(q,t)$. While at low Φs, $F_s(q,t)$ show an exponential decay, for intermediate Φs, it decay

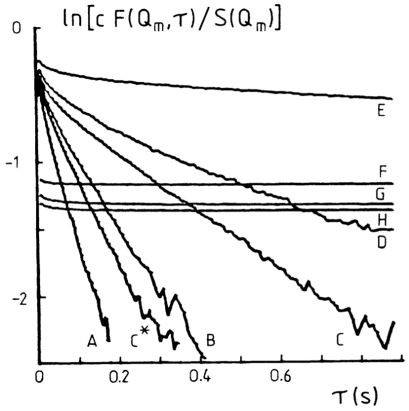

Figure 1.29 Semilogarithmic plots of $F_s(q,t)$, measured at first peak of static structure factor, against delay time τ for different samples. A-fluid; C*- fluid-fluid coexistence; B, C, D- fluid-crystal coexistence; E and F- crystals; G, H, I, J- glass. Adopted from [219].

non-exponentially. For high Φs, $\Phi > 0.565$, only partial decay in $F_s(q,t)$ is observed and the systems were found to be glassy. The lowest Φ at which $F_s(q,t)$ decayed only partially was termed as glass transition volume fraction $\Phi_g = 0.565$. Interestingly, for HS potential, MCT predicts $\Phi_c = 0.52$. The prime reason behind underestimation of Φ_c is thought to be due to the non-inclusion of dynamical heterogeneities and activated hopping in the relaxation process.

In a seminal work, Weeks *et. al.* [19] and Kegel *et. al.* [20] independently used micron sized colloidal particles to investigate the structure and dynamics of supercooled liquid and glasses at single-particle resolution. The particle dynamics was quantified using the mean squared displacements (MSD). In two-dimensions (2D), MSD can be expressed as,

$$\langle \Delta r^2(t) \rangle = \frac{1}{N}\sum_j^N (x_j(t+t_0) - x_j(t))^2 + (y_j(t+t_0) - y_j(t))^2. \tag{1.55}$$

Here N is the total number of particles, $x_j(t)$ and $y_j(t)$ are the coordinates of j^{th} particle, t_0 is the lag time, $\langle\rangle$ indicates average over all particles and for all initial times t for a particular time interval t_0. MSD as a function of Φ is shown in Figure 1.30A. At low Φs, dynamics is diffusive, $\langle \Delta r^2(t) \rangle = 4D\Delta t$ with D being the diffusion

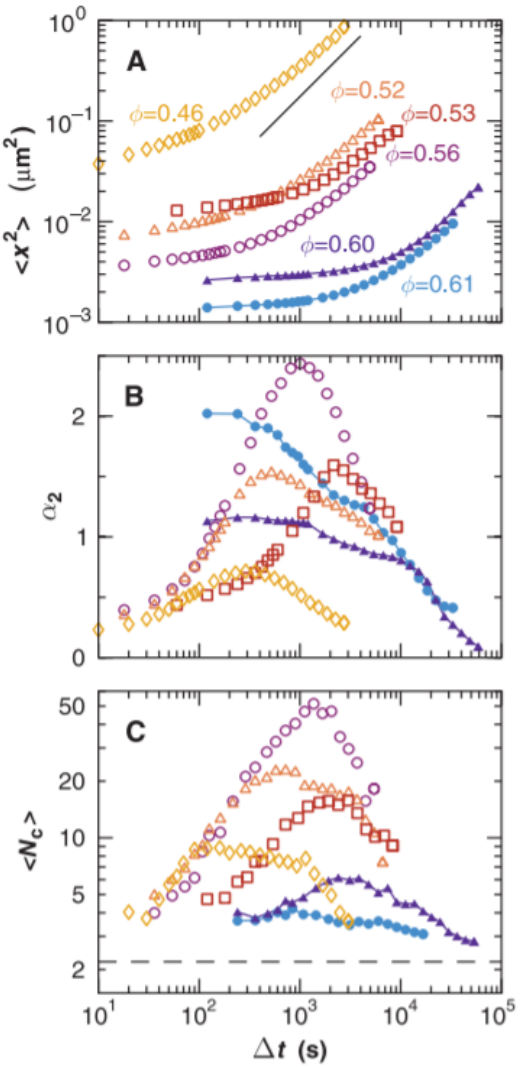

Figure 1.30 (A) $\langle \Delta r^2(t) \rangle$ at various Φs as indicated in the plot. The solid line has a slope 1. (B) The non-Gaussian parameter $\alpha_2(t)$ and (C) the particle averaged cluster size of fast particles $\langle N_c \rangle$ with t. The Φs in (B) and (C) are color coded as in (A). The dashed line in (C) shows the expected result for random distribution of fast particles. Adopted from [19].

coefficient of particles. Interestingly, D can also be estimated independently using the Stokes-Einstein (SE) equation, $D = \frac{k_B T}{6\pi\eta a}$, where a is the size of the particles. We will come back to SE relation while discussing about the transport properties of supercooled

liquids little later. Currently, we focus on the dynamics of supercooled liquids and glasses. With increase in Φ, the MSD develops a plateau at intermediate times and the dynamics become sub-diffusive; $\langle \Delta r^2(t) \rangle = 4D\Delta t^{\nu}$ with $\nu < 1$ [19]. The plateau in MSD indicates caging of particles by their neighbours which become stronger with increasing Φ. These observations are in agreement with MCT [151, 194]. After the plateau, at a characteristic time $t = t^*$, an upturn in MSD indicating cage relaxation is observed. The upturn in MSD signifies inhomogeneities in the particles dynmics and can be quantified using the non-Gaussian parameter, $\alpha_2(t)$ [19].

$$\alpha_2(t) = \frac{\langle \Delta r(t) \rangle^4}{2\langle r(\Delta t) \rangle^2} - 1 \tag{1.56}$$

where $\Delta r(t)$ is the displacements of particles over t. Since for any Gaussian process all higher order (even) moments can be expressed in terms of its second moment $\langle r^2(\Delta t) \rangle$, and hence $\alpha_2(t) = 0$ for diffusive dynamics. However, for supercooled liquids, at a fixed Φ, dynamics become increasingly heterogeneous on approaching t^*, in the vicinity of which dynamics is believed to be most heterogeneous and $\alpha_2(t)$ shows a maximum at $t = t^*$ (Figure 1.30B). Notably, for $\Phi \geq 0.58$, the peaks in $\alpha_2(t)$ are broader with amplitude smaller than what is observed at lower Φs (Figure 1.30B). This sharp change in behaviour of $\alpha_2(t)$ was identified as glass transition with $\Phi_g = 0.58 \pm 0.01$ [19] which was in agreement with the previous works [60, 219, 220]. The non-Gaussian nature of particle dynamics at t^* are best reflected in the probability distribution of displacements, $P(\Delta r(t))$, over t^* (Figure 1.31). The tail of the distribution is non-Gaussian signifying

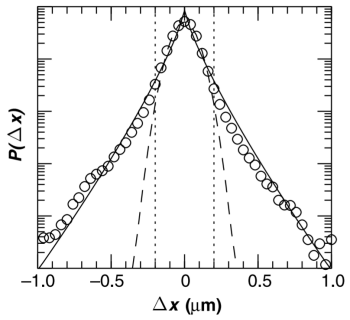

Figure 1.31 The probability distribution of displacements $P(\Delta r(t))$ over t^* for $\Phi = 0.56$. The dashed line is best fit Gaussian, the solid line is a stretched exponential fit to the tail of the distribution. The particles within dotted lines are slowest 95%. Adopted from [19].

that a fraction of total particles have a higher mobilities as compared to their neighbours (Figure 1.31). The dynamics over t^* are thus heterogeneous and more importantly

these dynamical heterogeneities were observed to be spatially clustered (Figure 1.32) [19]. For the first time, dynamical heterogeneities (DH), believed to be pathways of

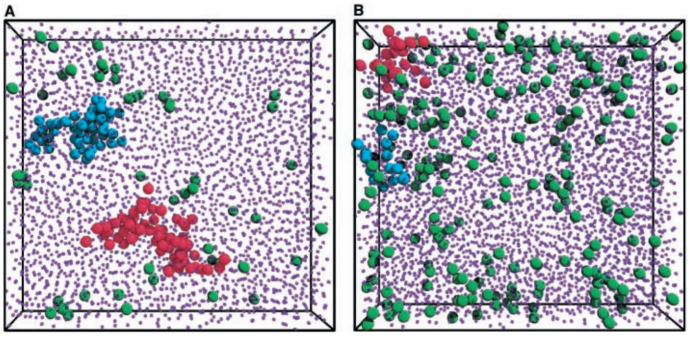

Figure 1.32 Spatial distribution of clusters of fastest particles (large spheres). For clarity, the slowest 95% of the particles are shoen as small spheres in the background. (A) Supercooled liquid at $\Phi = 0.56$ (B) Glass at $\Phi = 0.60$. Particles belonging to same clusters are shown in same colour. Adopted from [19].

structural relaxations in supercooled liquids [172], were observed in an experiment. Further, the particle averaged cluster size of fast particles $\langle N_c \rangle$ defined as [221],

$$\langle N_c \rangle = \frac{\sum_n n^2 P(n)}{\sum_n n P(n)} \tag{1.57}$$

follows the same trend with time as $\alpha_2(t)$ (Figure 1.30C). Here, $P(n)$ is the probability of finding a cluster of size n. $\langle N_c \rangle$ peaks at $t = t^*$ (Figure 1.30C). Moreover, $\langle N_c \rangle$ increases on approaching Φ_g and decreases drastically beyond $\Phi = 0.58 \sim \Phi_g$ [19]. The dramatic change in the behaviour of $\langle N_c \rangle$ reinforces the claim of $\Phi_g = 0.58 \pm 0.01$. The decrease in $\langle N_c \rangle$ beyond Φ_g was attributed to much slower relaxation i.e. t^* in the vicinity of Φ_g corresponds to $\beta-$relaxation and not to cage relaxation [19]. Interestingly, in a recent work, Nagamanasa *et al.* [15] have shown that the shape of DH become progressively compact with increase in supercooling (Figure 1.33) and is in concord with random first order transition (RFOT) theory, a prominent thermodynmic theory of glass transition [222, 223].

1.6.2 Attractive Colloidal Glasses

Verduin and Dhont were first to observe the gel phase in colloid-polymer mixture wherein colloidal particles form interconnected static structure [198]. Interestingly, the dynamical behaviour of the "gel phase" was observed to be similar to the repulsive colloidal glasses [198, 224]. For instance, analogous to increase in Φ for polymer-free

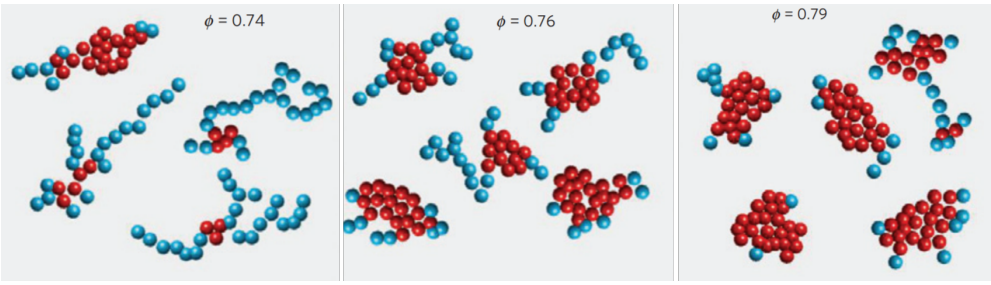

Figure 1.33 Representative cluster morphologies for 25-particles clusters for $\phi = 0.74$, $\phi = 0.76$ and $\phi = 0.79$. Adopted from [15].

repulsive glasses, the dynamics of gels slow down with increase in the attraction strengths (polymer concentration c_p). Remarkably, Pham *et. al.* [66] and Eckert *et. al.* [225] independently, using colloid-polymer mixture, polymer particles induce short-ranged attraction between particle, studied the role of attraction on structure and dynamics of supercooled liquids and glasses. Figure 1.34a shows the colloid-polymer phase diagram in (c_p, Φ) plane with long time decay value of correlation function as the quantifier of the dynamics. For a narrow range of Φs with $\Phi > \text{RG}\Phi_g$, as

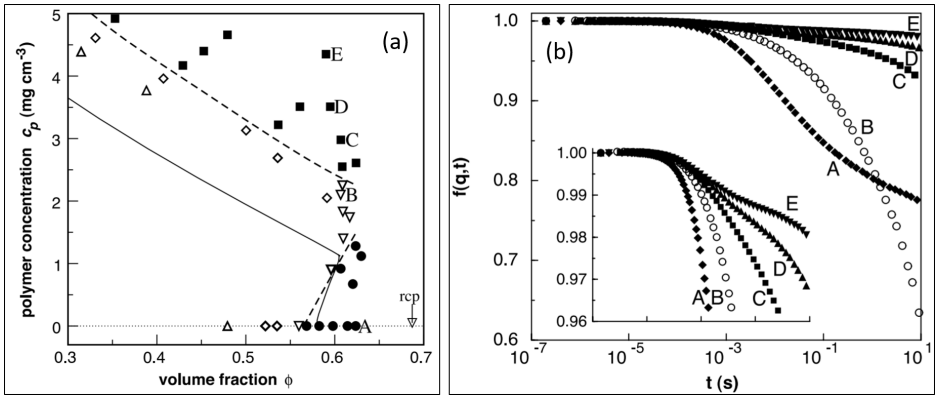

Figure 1.34 (a) Phase diagram of colloid-polymer mixture in (c_p, Φ) plane. Open symbols represent thermally equilibrated samples: fluids (triangles), fluid-crystal coexistence (diamonds), fully crystalline (inverted triangles). Solid symbols represent non-equilibrated samples: repulsion driven glass (circles), attraction driven glass (squares). The dashed curves are guide to the eye for the observed glass transitions. Solid lines are MCT predicted glass transition lines. (b) Self-intermediate scattering function $F_s(q,t)$ as a function of t at various depletion concentrations c_p and at a fixed Φ. Sample A- repulsive glass, sample B- ergodic fluid, sample C, D and E- attractive glass. Adopted from [66].

a function of increasing attraction strengths, a repulsive glass (sample A in Figure 1.34a) melts to an ergodic fluid at intermediate c_ps (sample B in Figure 1.34a) and

enters a novel glassy phase-attractive glass at higher c_p (sample C, D and E in Figure 1.34a). These observation were corroborated with the decay profile of $F_s(q,t)$ (Figure 1.34b). At low and high attraction strengths, as expected in glassy systems, $F_s(q,t)$ showed a two-step relaxation with only a partial decay even at long times. Whereas, at intermediate attraction strengths, analogous to the dynamics in mildly supercooled liquids, $F_s(q,t)$ showed complete decay. Thus Φ_gs at intermediate c_ps shift to higher Φs. Hence, consistent with MCT predictions, at a fixed $\Phi > \mathrm{RG}\Phi_g$, repulsive glass first melts at intermediate c_ps and then reenters yet another glass phase called an attractive glass at higher c_ps. Moreover, the plateau value of $F_s(q,t)$ at long times for attractive glasses (samples C, D and E) are found to be larger than their repulsive counterparts (Figure 1.34b). This is attributed to a relatively stronger freezing in of long-wavelength collective density fluctuation in attractive glasses [66]. Though the short-time dynamics in attractive glasses is dominated by bond breaking, recent simulations have shown that analogous to repulsive glasses, structural relaxations at long times for attractive glasses are governed by cage rearrangements only [226].

It is apparent from the preceding discussions that colloid-polymer mixture exhibit a rich and complex phase diagram that can be rationalized within the framework of MCT [155, 195, 200]. However, given the fact that MCT equations can correctly account for the dynamics only in the mildly supercooled regime, it would be worthwhile to extend other theoretical formalisms such as RFOT to study the phase diagram of the colloid-polymer mixture at high Φs. Further, it is as yet not clear whether the idea of glasses driven by attractions should also encompass the gels, colloid-polymer mixture at relatively low Φs and high c_ps, which unlike attractive glasses, have poor mechanical stability [155]. Moreover, it is believed that insights gleaned from the colloid-polymer mixtures might have implications in biological fields such as crystallization of globular proteins [227–229]. Here, it is thought that the short-range of the attraction potential in globular proteins in comparison to their size leads to suppression of protein crystallization [227, 230].

1.6.3 Shape Anisotropy and Glass Transition

Anisotropy in shape and/or interactions is a feature of many molecular systems [231]. Particle shape strongly influences their packing [156] as Donev *et. al.* [50] have shown that oblate ellipsoids with aspect ratio $\alpha \sim 0.526$ (close to M&M candies) can pack beyond the random closed packing (RCP) of spheres ($\Phi_{\mathrm{RCP}} = 0.64$). They attribute the attainment of the higher packing fraction to the extra degree of freedom (DOF)

available to ellipsoids as compared to spheres. While jamming and glass transition may be linked, it is only recently that the role of shape anisotropy in the physics of glass transitions has been probed. Figure 1.35 shows the complete phase diagram of ellipsoids in (Φ, α) plane [202–204]. In 2003, Cang *et. al.* showed that the 5-CB

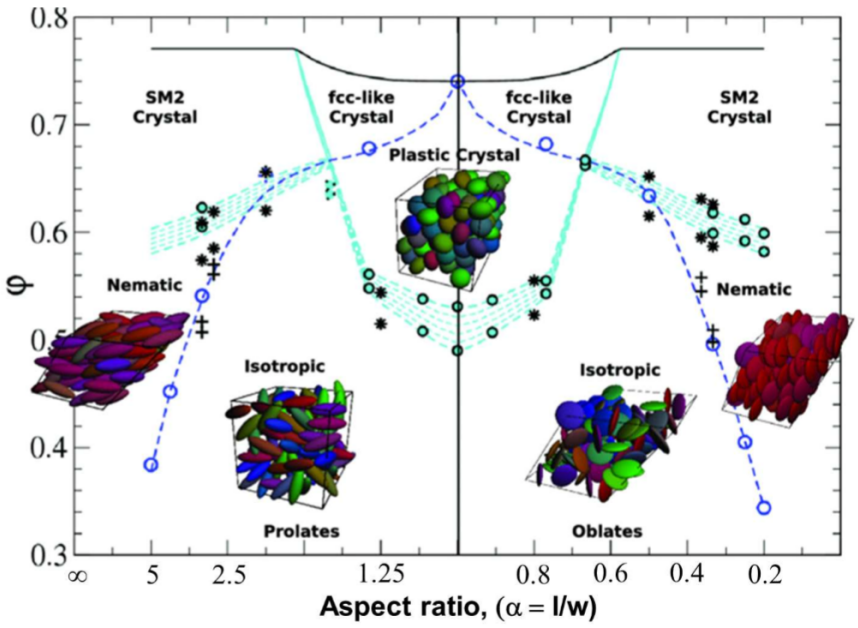

Figure 1.35 Phase diagram of uniaxial hard ellipsoids in (Φ, α) plane. Solid and hollow symbols correspond to fluid-solid transition and isotropic-nematic transition, respectively. The black (dark) line is maximum achievable density [232]. Cyan (light gray) dashed line and blue (dark) dashed lines are guide to the eye which join the fluid-solid transition and isotropic-nematic transition, respectively. The cyan (light gray) solid lines indicate fcc-SM2 transitions [202]. Black (dark) plus symbols (isotropic-nematic) and asterisks (nematic-solid) are taken from the ref. [201]. Adopted from [233].

liquid crystalline molecule has two glass transition temperatures [234]. As predicted by MMCT [203], they alluded the first glass transition temperature T_{CH} to the freezing of the local nematic order associated with the pseudonematic domains and the second T_{CL} to the freezing of intradomain dynamics of pseudonematic domains. Later, using micron sized prolate colloidal ellipsoids of $\alpha = 6$ in quasi-2-dimension (2D), Zheng *et. al.* showed pseudonematic ordering with branch like structures [235]. The translational and orientational dynamics were quantified using $F_s(q,t)$ and orientational correlation

function $L_n(t)$, respectively. Mathematically, $L_n(t)$ in 2D is defined as,

$$L_n(t) = \frac{1}{N}\sum_{j=1}^{N} \cos n(\theta_j(t+t_0) - \theta_j(t)). \tag{1.58}$$

Here, N is the total number of particles, $\theta_j(t)$ is the orientation of the j^{th} ellipsoid at time t, t_0 is the lag time and $\langle\rangle$ denotes the time averaging. The glass transition area fraction ϕ_g for both translational and orientational DOF was estimated using MCT scaling arguments [235]. Consistent with MCT predictions, $\tau_\alpha^{-1/\gamma}$ was found to be linear in ϕ for both translational and orientational DOF and yielded orientational glass transition area fraction $\phi_g^R = 0.72 \pm 0.01$ and translational glass transition area fraction $\phi_g^T = 0.79 \pm 0.01$ (Figure 1.36). This was in qualitative agreement with

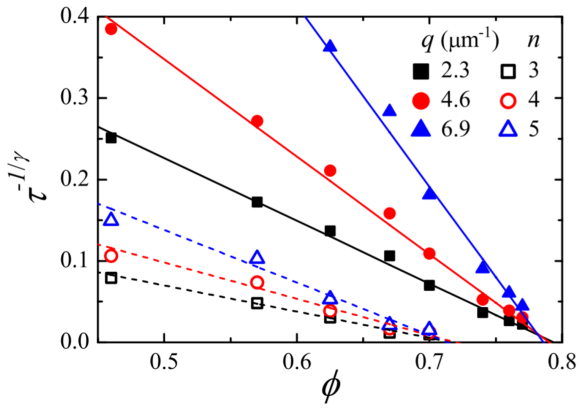

Figure 1.36 $\tau_\alpha^{-1/\gamma}$ versus ϕ. Open and solid symbols correspond to orientational and translation DOF, respectively. Dashed and solid lines are linear fits to the data. Adopted from [235].

experiments on liquid crystals [234], MMCT predictions and computer simulations [196, 197, 203]. Further, in excellent agreement with Cang *et. al.* [234], most of translationally most-mobile particles were confined within the psuedonematic domains and most of rotationally most-mobile particles were observed at the domain boundaries (Figure 1.37) [235]. In addition, the width of the intermediate orientational glass regime which lies between ϕ_g^R and ϕ_g^T increases as the aspect ratio of ellipsoids increase [235].

Interestingly, while colloidal ellipsoids of large aspect ratio yielded a two-step glass transition [235], MMCT predicts a single glass transition in 3D for ellipsoids with $\alpha < 2.5$ [203]. Nevertheless, thus far, even in 2D there is no experimental evidence for the same. Hence, it would be worthwhile to investigate the self-assembly and structural relaxation in supercooled liquid and glasses of short colloidal ellipsoids.

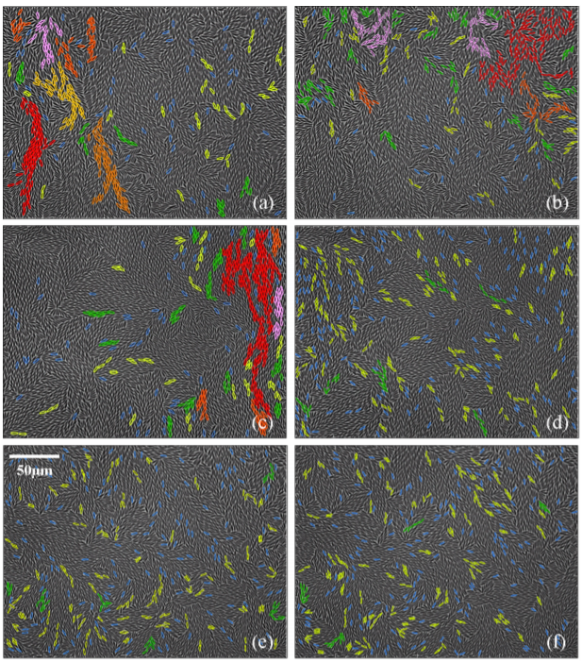

Figure 1.37 The spatial distribution of rotational (b, d, f) and translational (a, c, e) most-mobile particles of the system. (a), (b) at $\phi = 0.70$ (supercooled liquid); (c), (d) at $\phi = 0.77$ (orientational glass); (e), (f) at $\phi = 0.81$ (glass). Ellipsoids in same clusters have same color. Adopted from [235].

More importantly, taking advantage of geometric nature of depletion interactions, the two radii of curvature of ellipsoids in presence of depletants would lead to anisotropic interactions [236] where lateral alignment of ellipsoids would be preferred as compared to their tip-to-tip alignment (Figure 1.38). The role of such interaction anisotropy

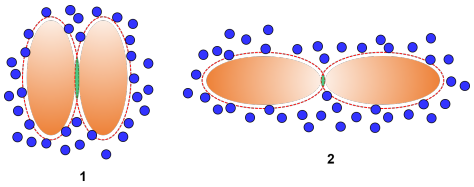

Figure 1.38 Anisotropic depletion attraction in ellipsoids. Due to the larger overlap of the excluded volumes (green shaded regions), configuration 1 is preferred over 2. Depletant molecules are shown in solid blue spheres. Red dashed lines around each ellipsoid represent the excluded volumes.

in the physics of glass transition is yet to be probed in experiments, simulations and theory. Moreover, this can also lead to the exploration of reentrant glass dynamics in systems with anisotropic interactions and in fact has been probed in Chapter 4 of this thesis.

1.7 Transport Properties of Colloidal Suspensions

In contrast to the flow properties of the fluids which are usually Newtonian in nature, the transport properties of the same fluid with dispersed colloidal particles−colloidal dispersions− are often unusual and unique [23, 61, 237–241]. The addition of solid particles increase the effective viscosity of the fluid and at large particle concentrations often lead to pronounced non-Newtonian behaviour like shear thinning [23, 241, 242] and shear thickening [23, 240, 241, 243, 244] that have tremendous application in industries as well as in day-to-day life. We will first look at the transport properties of a single Brownian particle in a fluid. If a particle of size a is dropped in a fluid with viscosity η, the final velocity v of the particle will be the net outcome of gravitational force and the frictional drag force. Further, the mechanism that causes the drag depends on a dimensionless quantity called Reynolds number Re which is defined the ratio of inertial to viscous drag [245, 246],

$$Re = \frac{\rho v a}{\eta} \tag{1.59}$$

where ρ is the density of the particles. Reynolds number quantifies the relative importance of the two forces i.e. inertial and viscous for specific flow conditions. Unlike large particles, for colloids (μm in size), the Re is very low and hence it is the viscous drag that dictates their transport properties. With this in mind, one can find out diffusivity D of the Brownian particle suspended in a fluid. As mentioned earlier, the random bombardment of the liquid molecule on the particle results in a unabated fluctuating motion of the particle. In other words, the motion of the colloid is analogous to the random walk problem i.e. while the averaged mean displacements of particle would be zero, the mean squared displacements would be proportional to the number of steps and hence the time; $\langle(\mathbf{R}(t))^2\rangle = Dt$ [237, 247]. D can be determined by solving the Langevin equation [248–250] and it is found that,

$$\langle(\mathbf{R}(t))^2\rangle = \frac{k_B T}{\varsigma} t. \tag{1.60}$$

Interestingly, before Einstein arrived at the above equation in his doctoral thesis in 1906, Sutherland had already published these findings in 1905 [251]. Thus, the diffusion constant D of the particle is given by the Einstein/Sutherland relation,

$$D = \frac{k_B T}{\varsigma}. \tag{1.61}$$

Although, the form of ς is strongly dependent on the shape of the tracer and in general is unknown [252], for a spherical particle at low Reynolds number, Stokes showed that [253, 254],

$$\varsigma = 6\pi\eta a. \tag{1.62}$$

Hence for a spherical particle, combining Eqn.1.61 and Eqn.1.62, one arrives at

$$D = \frac{k_B T}{6\pi\eta a}. \tag{1.63}$$

Eqn.1.63 is the Sutherland-Stokes-Einstein (SSE) relation, though it is routinely referred as Stokes-Einstein (SE) relation.

1.7.1 Stokes-Einstein Relation for Supercooled Liquid

Although, both supercooled liquids and their high temperature counterpart have similar static structure (Figure 1.19), a key feature unique to the latter is the validity of SE relation. The validity and its limit for supercooled liquids have been extensively investigated in experiments [183, 255–266], theory [183, 267–272] and computational [183, 273–286] studies. A general observation is that for low molecular weight liquids (fragile glass formers), SE relation breakdown, $D \propto (T/\eta)^{\xi}$ with $\xi < 1$, for $1.5T_g < T < T_g$ with T_g being laboratory glass transition temperature. Before the advent colloids as model atoms where diffusion coefficient can be directly measured from the particles trajectories, the translational diffusivity of the tracers D^T used to be obtained from the decay profile of $F_s(q,t)$ that are usually measured using ^{1}H NMR or DLS spectroscopy [257, 260, 261, 265, 287, 288]. The superscript T will be used to denote parameters associated with translational DOF. $F_s(q,t)$ in Eqn.1.36, in the limit of small q and large t can be rewritten as [289],

$$F_s(q,t) = \exp(-D^T q^2 t). \tag{1.64}$$

D^T can also be directly measured from particle trajectories as,

$$D^T \equiv \lim_{\Delta t \to \infty} \frac{1}{6\Delta t} \langle \mathbf{R}^2(\Delta t) \rangle \tag{1.65}$$

where, $\langle \mathbf{R}^2(\Delta t) \rangle$ represents the translational mean squared displacements. Since, τ_α obtained from various correlation function such as overlap function $q(t)$, self-intermediate scattering function $F_s(q,t)$ scales linearly with η/T ($\tau_\alpha \propto \eta/T$) [281, 290,

291], in many of the works that investigate the transport properties of supercooled liquids, D^T is plotted with τ_α for testing the validity of SE relation. Figure 1.39a and b show the variation of D^T with T and τ_α, respectively. Further, it has also been shown

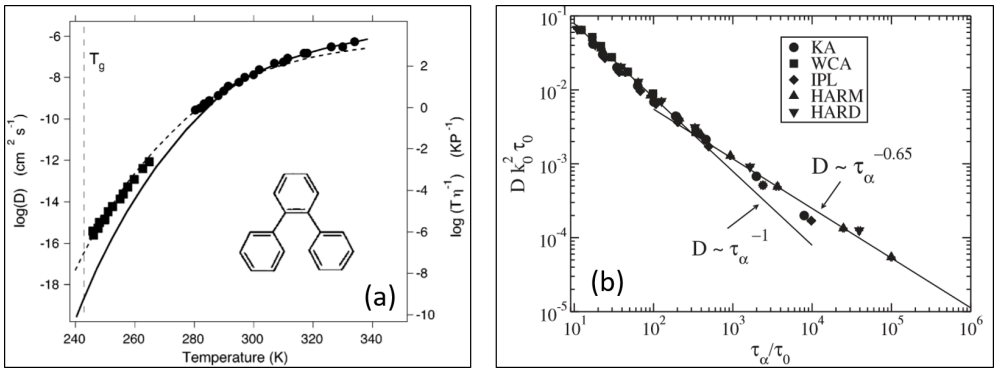

Figure 1.39 (a) Self-diffusion coefficients of OTP compared to viscosity η. The left axis is $\log D$ for diffusion coefficients determined by NMR [288] (solid circle) and isothermal desorption (solid squares). The right axis is T/η (solid line), which has been shifted to overlay the values of high-temperature self-diffusion data. The dotted line is $\eta^{-0.80}$, vertically shifted. The inset shows the structure of OTP. Adopted from [257]. (b) Scaled diffusion coefficients D versus scaled structural relaxation time τ_α for various interaction potenials. Adopted from [283].

that the extent of SE breakdown depends on the spatial dimensionality also− with weak or no breakdown $\xi \sim 1$ until T_g in four dimensions, and breakdown becoming progressively stronger ($\xi < 1$) with decreasing dimensionality [281, 292]. Surprisingly, simulations find that in 2D, SE relation is not valid even at high temperature [282, 281]. However, SE exponent still shows a crossover from $\xi > 1$ to $\xi < 1$ in the vicinity of $T \sim 1.2T_g$ [281, 282].

Thus far, the prime reason for the breakdown of SE relation in supercooled liquids have been attributed to the presence of dynamical heterogeneities i.e. the regions of predominantly fast particles that contribute primarily of D are spatially decoupled from the slow regions that governs the bulk viscosity (η) or equivalently structural relaxation time (τ_α) [183, 267, 268]. Interestingly, this breakdown is appropriately reflected in numerous parameters such as stretching exponent β, non-Gaussian parameter $\alpha_2(t)$, dynamical susceptibility χ_4 that quantify the dynamical heterogeneities (DH) in supercooled liquids and glasses [19, 183, 235, 293–297]. We recall that for supercooled liquids, the long-time decay of density correlation functions like $F_s(q,t)$ do not show an exponential decay, rather it decay as a stretched exponential; $F_s(q,t) \propto e^{-(t/\tau_\alpha)^\beta}$. A value of $\beta < 1$ signifies the presence of DH [19, 183]. Moreover, β decreases with

increase in supercooling (Figure 1.40). Similarly, as discussed before, $\alpha_2(t)$ measures the

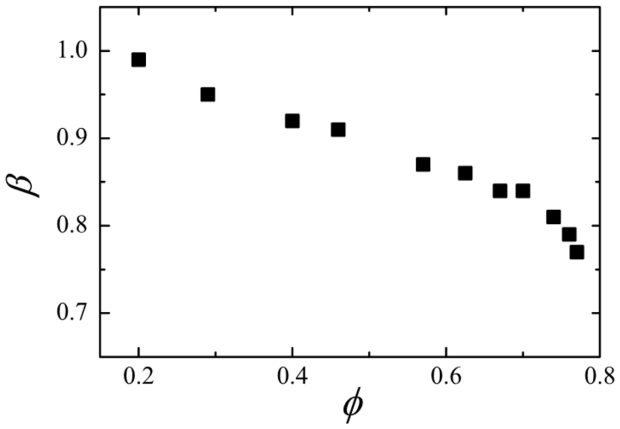

Figure 1.40 The stretching exponent β obtained from fitting of long-time decay of $F_s(q_m, t)$, q_m is the position of first peak position in structure factor $S(q)$. Modified from [235].

contribution of non-Gaussian displacements to dynamics and hence $\alpha_2(t) > 0$ indicates the presence of DH in the system and the magnitude of $\alpha_2(t^*)$ increases with increase in supercooling (Figure 1.30B) [19, 183]. Thus, it is clear from above that both β and $\alpha_2(t)$ are two-point correlation functions and unambiguously reflect the presence of dynamical heterogeneities in supercooled and glasses. However, two-point correlators fail to reveal whether these dynamical heterogeneities arise due to *purely local* fluctuations or rather associated with *spatially correlated* fluctuations whose length scale grows with increase in supercooling. As a matter of fact, this length scale quantified using four-point dynamic correlation function $\chi_4(t)$ has been shown to increase on approaching the glass transition [183, 293–298]. In simple word, while two-point correlators measure the dynamics of the systems, four-point ones quantify the fluctuations in two-point correlators i.e. fluctuations in the dynamics of the system. It is important to note that there is a fundamental difference in the way $\alpha_2(t)$ and $\chi_4(t)$ measure DH. While, in former the dynamics of most-mobile particles of supercooled liquids are monitored, in the latter it is the correlation of slow particles that is investigated. The number of slow particles $N_s(t)$ in a time duration t is defined as [283, 299],

$$N_s(t) = \sum_{k=1}^{N} w_k(t) \tag{1.66}$$

where $w_k(t)$ is the microscopic overlap function,

$$w_k(t) = \vartheta\Big[a - |r_k(t) - r_k(0)|\Big] \tag{1.67}$$

where ϑ is the Heaviside's step function and $r_k(t)$ is the position of k^{th} particle at time t. Physically, $w_k(t)$ takes a value of 1 only if particles have displacements that are less than a over t. Usually a is chosen to be less than the particle size. The fluctuations in the number of slow particle $N_s(t)$ yields $\chi_4(t)$ [299].

$$\chi_4(t) = \frac{1}{N}\Big(\langle N_s^2(t) - \langle N_s(t)\rangle^2\Big). \tag{1.68}$$

$\chi_4(t)$ directly measures the number of particles involved in a correlated rearrangements or the size of DH. As mentioned earlier, unlike $\alpha_2(t)$ which shows a maximum in the vicinity of characteristics cage rearrangement time $t^* < \tau_\alpha$, $\chi_4(t)$ peaks in the vicinity of τ_α [19, 183, 235, 293–297]. As expected, both τ_α and the peak-amplitude of χ_4 increase with increasing supercooling (Figure 1.41a). Interestingly, the scaling

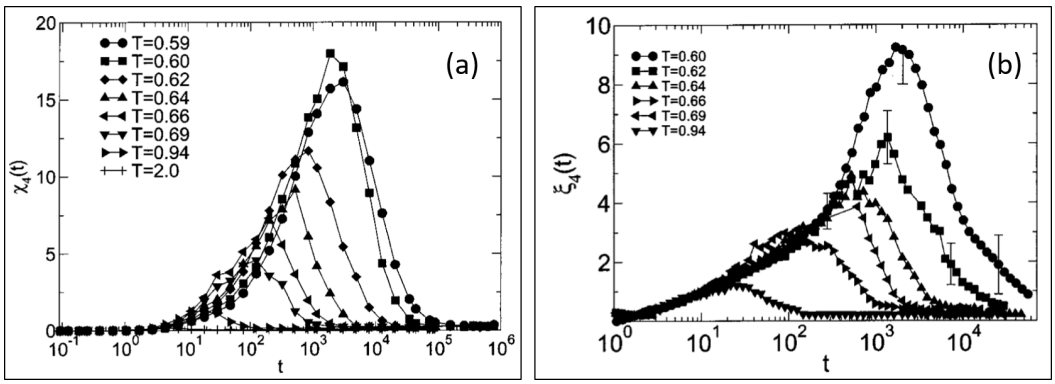

Figure 1.41 Time and temperature dependence of (a) $\chi_4(t)$ and (b) $\xi_4(t)$. As T decreases, the peak in $\chi_4(t)$ and $\xi_4(t)$ monotinically increases and shifts to longer time. Adopted from [295].

arguments between χ_4 and the four-point correlation length ξ_4 can be used to predict the change in morphology of DH on approaching the glass transition. To this end, inspired from Ornstein Zernicke theory, ξ_4 is defined as [183, 299],

$$\xi_4^2(t) = \lim_{q\to 0}\left(\frac{1}{q^2}\frac{\xi_4(t)}{S_4(q;t)} - 1\right) \tag{1.69}$$

where four-point dynamic structure factor $S_4(q;t)$ is

$$S_4(q;t) = \frac{1}{N}\Big(W(\mathbf{q},t)W(-\mathbf{q},t) - |W(\mathbf{q};t)|^2\Big). \tag{1.70}$$

Here, $W(\mathbf{q};t)$ is the Fourier transform of overlap function,

$$W(\mathbf{q};t) = \sum_k w_k(t)\exp[-iq.r_k(0)]. \tag{1.71}$$

At a fixed T or Φ, $\xi_4(t)$ shows a behavior similar to $\chi_4(t)$ (Figure 1.41b), but measures the spatial extent of DH. Consequently, a scaling between $\xi_4(\tau_\alpha)$ and $\chi_4(\tau_\alpha)$ can reveal vital information regarding the morphology of DH. Infact, using computer simulations, Flenner *et. al.* [283], showed that the scaling between $\xi_4(\tau_\alpha)$ and $\chi_4(\tau_\alpha)$, for a variety of interaction potentials, changes at a temperature T_s or volume fraction Φ_s (Figure 1.42). Below T_s, since $\chi_4 \propto (\xi_4)^3$, the clusters are expected to be compact in shape.

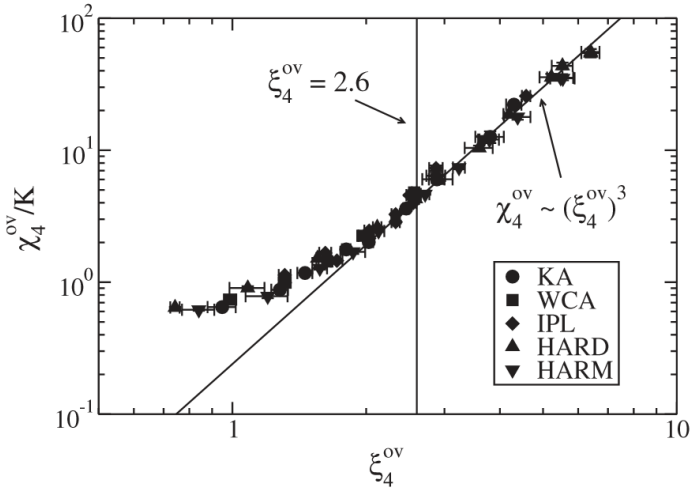

Figure 1.42 Rescaled susceptibility χ_4 versus dynamic correlation length ξ_4. The vertical line corresponds to the $\xi_4 = 2.6$, the temperature at which the SE relation shows a crossover from $\xi = 1$ to $\xi < 1$. Adopted from [283].

More importantly, T_s was found to be $T_c < T_s < T_{\text{onset}}$ where we recall that T_c is the mode-coupling dynamics crossover temperature and T_{onset} is the onset temperature for slowing down of the dynamics. Interestingly, all the quantifiers of DH would indicate its presence with $\beta < 1$, $\alpha_2(t^*) > 0$ and $\chi_4(\tau_\alpha) > 0$ right below T_{onset}. However, contrary to this notion, the breakdown temperature for the SE relation coincides with the change in scaling between ξ_4 and χ_4 at T_s and not with T_{onset} [283, 299]. Notably, these observations are in concord with RFOT theory of glass transition. In conclusion,

the simulation works of Szamel and co-workers [283, 299], clearly suggest that the breakdown of SE relation should be associated with the change in the morphology of DH from string-like to compact and not with their presence, however, there are no experimental evidence, thus far, for the same.

1.7.2 Stokes-Einstein-Debye (SED) Relation

The rotational diffusion of an anisotropic particle in a simple fluid have been traditionally measured using time-correlated single photon counting or the photobleaching method [260, 300, 301]. In both the techniques, first, an orientationally anisotropic subset of the probe molecules, is photoselected using the polarized light. The time dependence fluorescence of the polarized light is used to obtain the rotational correlation time τ_c [260, 300, 301]. Quantitatively, the observed orientational correlation function in experiments is found to be [260],

$$\psi_n(t) = 2/_5\langle P_2[\hat{e}_a(0).\hat{e}_e(t)]\rangle. \tag{1.72}$$

Here, P_2 is second order Legendre polynomial and $\hat{e}_a(0)$ and $\hat{e}_e(t)$ are the unit vector corresponding to the absorption and emission dipoles, respectively. Interestingly, assuming that a Brownian particle reorient in a simple fluid in small steps, Debye model predicts an exponential decay of the orientational correlation function $C_\ell(t)$ [302].

$$C_\ell(t) = \exp\left(\frac{t}{\tau_\ell}\right), \tag{1.73}$$

where the τ_ℓ for various ℓ is related to particle's rotational diffusivity D^R as,

$$\tau_\ell = \frac{1}{\ell(\ell+1)D^R} \tag{1.74}$$

Usually τ_2 is accessible in molecular experiments. Motivated by functional form for $\psi_n(t)$ in experiments, the general expression for $C_\ell(t)$ can be written as [285, 303],

$$C_\ell(t) = \frac{\sum_i P_\ell(\hat{e}_i(0).\hat{e}_i(t))}{\sum_i P_\ell(\hat{e}_i(0).\hat{e}_i(0))} \tag{1.75}$$

where $\hat{e}_i(0)$ is the unit vector along the major axis or the symmetry axis of i^{th} the tracers and P_ℓ is the ℓ^{th} order Legendre polynomial. It is apparent that for $\ell = 2$, Eqn.1.75 would reduce to Eqn.1.72.

Debye derived the orientational frictional drag ς on a sphere with radius a to be [302],

$$\varsigma = 8\pi\eta a^3. \tag{1.76}$$

Now, substituting Eqn.1.76 in Einstein relation (Eqn.1.61), one arrives at the Stokes-Einstein-Debye (SED) relation for the rotational DOF.

$$D^R = \frac{k_B T}{8\pi\eta a^3}. \tag{1.77}$$

Interestingly, the orientational dynamics can be either quantified using τ_c in experiments with molecular tracers (τ_ℓ in computer simulations) or directly from the particle trajectories in computer simulations and experiments with colloids as,

$$D^R \equiv \lim_{\Delta t \to \infty} \frac{1}{4\Delta t} \langle \varphi^2(\Delta t) \rangle \tag{1.78}$$

where $\langle \varphi^2(\Delta t) \rangle$ is the rotational mean squared displacements. Hence, the validity of SED relation can be tested either by plotting D^R with η/T or $1/\tau_\ell$ with η/T. In literature, at times, while the former formalism is termed as Einstein model, the latter is called the Debye formalism of SED relation. It is worth recalling that, like SE relation, here too, τ_α can be plotted in place η/T for ascertaining the validity of SED relation.

1.7.3 SED relation for Supercooled Liquids

There is no consensus regarding the validity of SED relation for supercooled liquids and the prime reason for it has been the contradicting results from the two formalisms for testing the validity of the SED relation. While, SED relation via Debye formalism holds good even for deep supercooling [260, 261, 265, 266], via Einstein method, it breakdown to the same extent as the SE relation and show a fractional SED relation for supercooled liquids, $D^R \propto (\tau_\alpha)^{-\chi}$ with $\chi < 1$ [258, 277, 285, 287, 304] (Figure 1.43). It is worth noting that Debye model fails for supercooled liquids i.e. $C_\ell(t)$ or $\psi_n(t)$ do not show an exponential decay and hence τ_ℓ or τ_c are extracted by fitting a stretched-exponential ($c_\ell \propto e^{-(t/\tau_\ell)^\beta}$) to the long-time decay of orientational correlators. Further, recent colloid experiment that probed the dynamics of anisotropic traces in the bath of smaller hard spheres, however, find that SED relation remains valid even close to the glass transition, irrespective of the method used [264]. However, in light of

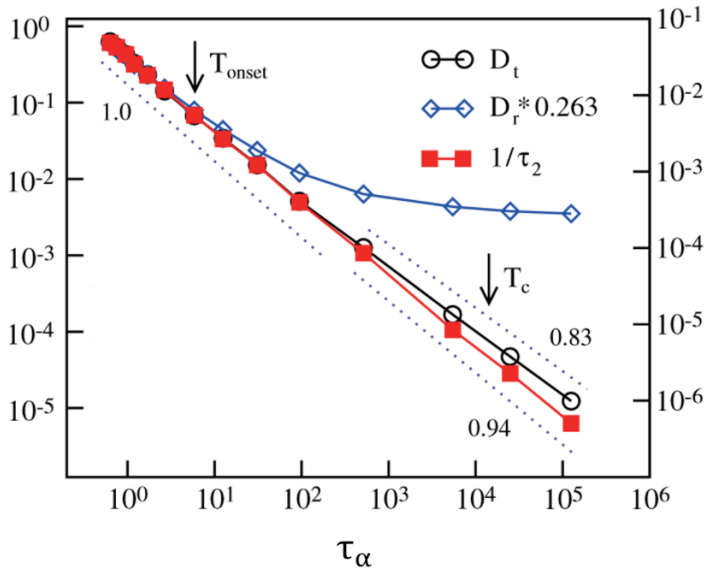

Figure 1.43 Log-log plot of translational D^T (circles, right axis) and rotational D^R (diamonds, right axis, shifted so that D^T and D^R agree at high T) diffusion coefficient and the inverse of rotational relaxation time $1/\tau_2$ (filled squares, right axis) versus structural relaxation time τ_α. The dotted straight lines refer to τ_α^x with exponents x mentioned in the figure. T_{onset} and T_c have been shown by arrows. Adopted from [284].

experimental observations that the validity of SE/SED relation is strongly dependent on the size, shape and roughness of the tracer particles with the host [260, 305–307], a consensus on the validity of SED relation for supercooled liquids continues to elude us.

Recent computer simulations [283, 299] as well as experiments [15] have well-established that the shape of DH, in agreement with key predictions of RFOT, changes from string-like to compact in the vicinity of mode-coupling crossover temperatures/area-fractions. However, it is yet to be investigated in experiments whether the change in morphology of DH has any bearings on the breakdown of SE/SED relation for supercooled liquids. Further, in light of the fact that validity of SE/SED relation is strongly dependent on the physical parameters of the tracers with respect to the host [260, 264, 305–307], it would be therefore worthwhile to investigate the SE/SED relation in an experimental model systems where particles' self-diffusivities, as opposed to tracers' diffusivities, can be directly measured. Hence, in Chapter 5, we have investigated the limits of validity of SE and SED relations for supercooled liquids of colloidal ellipsoids and explored if the breakdown of these relations have any connections with the morphology of DH.

Chapter 2

Experimental

2.1 Introduction

The significant advances in the synthesis of colloidal particles with tailored shape and interaction anisotropies have led to remarkable microscopic insights into complex and diverse condensed matter phenomena (Chapter 1). The central goal of this thesis as discussed in Chapter 1 is to demonstrate the importance and ubiquity of interactions that are driven completely by the geometry, either due to the substrate or particle shape itself. To this end, we have designed templates with complex surface features which in presence of short-ranged attractive interactions presented activation energy gradients for the diffusing colloids. As a result, these templates allowed a facile control over not only the sites of nucleation but also the size and symmetry of the growing crystallites (Chapter 3). In the other set of problems addressed in this thesis (Chapter 4 and Chapter 5), we have probed the role of anisotropic interactions in the physics of structural glass transition in suspensions of colloidal ellipsoids. Quite notably, the shape-sensitive nature of depletion attraction leads to anisotropic attraction between ellipsoids, thereby enabling us to test the validity of some key predictions of mode coupling theory (MCT) for systems with particle shape and/or interaction anisotropy. This chapter provides a detailed description of various experimental techniques such as soft lithography, synthesis of colloids with simple and complex symmetries, etc that were used for addressing the above questions.

2.2 Soft Lithography

Miniaturization has played the most prominent role in the advancements of electronic and optical gadgets and the success of miniaturization hinges on lithography, especially electron-beam and photolithography [308]. However, outside the fields of microelectronics, these techniques turn out to be extremely expensive, and in most cases inapplicable to the emerging fields that use soft materials. These limitations led to the development of soft lithography, a technique that essentially uses molding and embossing with elastomeric stamps [308–313]. These techniques invariably use soft elastomers like poly(dimethylsiloxane) (PDMS), polyurethanes, etc and hence the term soft lithography. Remarkably, over the last couple of decades, there has been significant advances in the field of soft lithography that includes development of techniques like microcontact printing [314], microtransfer molding [315], micromolding in capillaries [316], solvent-assisted micromolding [317], replica molding [115], phase-shift photolithography [318], embossing [319], cast molding [320], and injection molding [321]. Each of these techniques, based on the target relief structures, have their definitive advantages over the other. However, in our current endeavour, we have used the salient features of replica molding techniques to realize templates with simple and complex surface topographies.

To put in plain words, replica molding is a duplication technique [115]. Here, the features from the hard masters (say optical gratings) are first transferred to soft-elastomers like PDMS. PDMS has a low glass transition temperature and hence is liquid at room temperature. Chemically, it has an inorganic siloxane backbone with methyl groups attached to the silicone that can be crosslinked in the presence of crosslinkers which provide elasticity to PDMS [310, 312]. The high thermal stability of PDMS (up to 186°C in air) along with its inert chemical nature in ambient environmental conditions makes it an excellent candidate for soft-lithography. The structural features in PDMS molds can then be transferred to hard UV- or thermally-curable prepolymers which upon curing retain features of the PDMS molds thereby serving as the hard master template for the further lithographic processes. Interestingly, while the relief structures in PDMS are complementary to that of the master optical grating, those in cured UV-curable prepolymer are exactly identical to the master grating. The major advantages of transferring the features to soft elastomers like PDMS are:

- The high elasticity of PDMS allows mechanical manipulation in the features' parameters. For instance, unlike the rigid optical grating, the linear spacing and

curvatures in PDMS molds can be easily tuned, though most of the times with decreased groove depths [310].

- The high durability of PDMS stamps allow multiple transfers (> 10 times) to UV-curable prepolymer. Moreover, the rigid optical grating itself can be used for numerous transfers (> 50 times) to the PDMS [310].

However, PDMS has a few limitations too, firstly, it shrinks by almost 1% on curing and swells on exposure to nonpolar organic solvents like toluene, hexane, etc that leads to uncontrolled modifications in the features' parameters [322]. Second, the thermal expansion and elasticity of PDMS make the reproduction of features over large scale a major challenge in soft lithography [322].

We will next discuss how using the techniques of replica-imprinting, we have realized templates with well-controlled lattice constants as well as one with non-trivial surface geometries.

2.2.1 Fabrication of Square and Hexagonal Templates

Templates with hexagonal and square symmetry were fabricated using the replica imprinting technique with a blazed diffraction grating (Thorlabs, 1200 lines/mm, blazed angle 36.8°) as the master template (Figure 2.1a). In order to grow the colloidal crystal with desired symmetry and for repeated use of the master template, the grating pattern was first transferred to PDMS (SYLGARD 184, Dow Corning). More importantly, the linear spacing in the grating can be easily tuned by a uniaxial stretch. It is obvious that it is the periodicity of the linear array of trenches, λ, at this stage (in PDMS) that dictates the symmetry of the growing crystals. For instance, while $\lambda = \sigma$ where σ is the colloid diameter promotes crystal growth with square symmetry, $\lambda = \sqrt{3}/2\sigma$ leads to crystal growth with hexagonal symmetry. Next, using glass coverslips (#$1\frac{1}{2}$, Electron Microscopy Sciences) as the support, the linear grating pattern in PDMS was transferred to a UV light-curable optical adhesive (Norland, #68). These substrates were subsequently used as the hard master template for further imprinting process (Figure 2.1b). Simultaneously, a $\sim$ 500 nm thick layer of PMMA (Sigma, Mol. Wt. 120,000), dissolved in anisole (SDFCL, 9% w/w) is spin-coated (at $\sim$1,000 rpm) on a cleaned glass coverslip [116, 323]. To evaporate the residual anisole from the film and increase the bonding of PMMA film with the glass substrate, the coverslip is then baked at $T = 165$°C. The in-house modified hot-plate used for the replica imprinting is shown in the Figure 2.2. To transfer the linear grating patterns from UV adhesives to

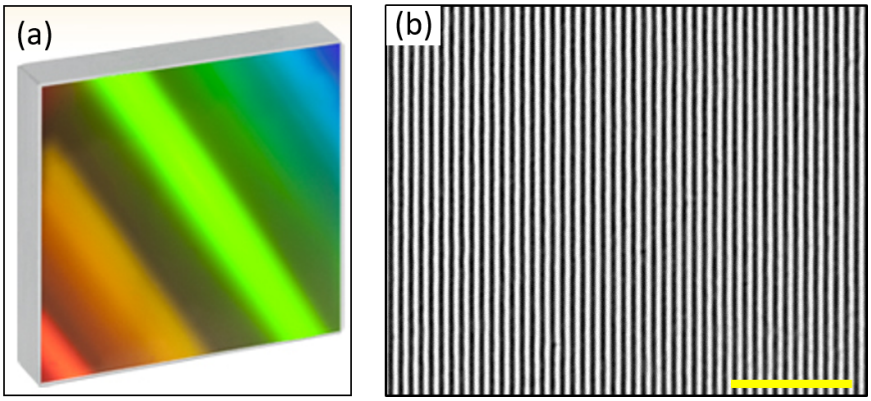

Figure 2.1 (a) Snapshot of a reflective blazed angle linear grating (1200 lines/mm) procured from Thorlabs. (b) Optical micrograph of the grating pattern in UV adhesive, transferred from PDMS. The scale bar represents 10 μm.

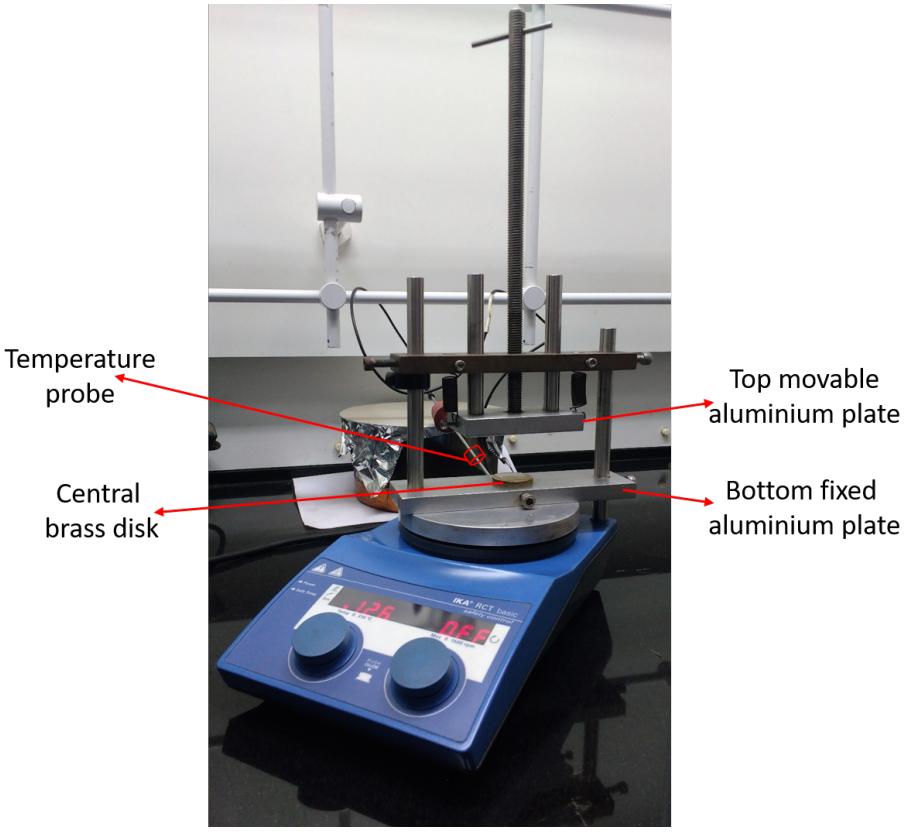

Figure 2.2 The IKA hot-plate modified for replica imprinting. The master imprints in UV adhesive is fixed to the central brass disk attached with the bottom aluminium plate. The temperature probe is housed in a thin cylindrical socket at the back of the bottom aluminium plate. The movable top plate allows us to manually press the PMMA coated coverslip against the imprints on UV adhesive.

PMMA, the PMMA-coated coverslip was manually pressed against the linear grating pattern on UV adhesive that was premaintained at temperature T_1. $T_1 \sim 126°\text{C} > T_g$ where T_g is the glass transition temperature of PMMA. Interestingly, we were able to make multiple imprints on the same PMMA coated coverslip, however, successive imprints could be transferred *only* at a slightly lower temperature than the preceding ones. Thus, the second imprint at a temperature $T_2 \sim 122° < T_1$ and at an angle θ relative to the first one results in a pattern with either square or hexagonal symmetry. While $\theta = 90°$ yields a template with square symmetry, one with $\theta = 60°$ leads to a pattern with hexagonal symmetry (Figure 2.3).

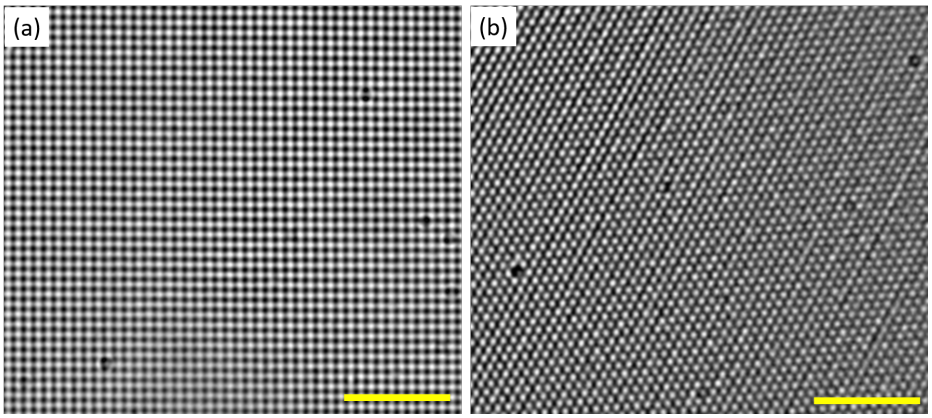

Figure 2.3 Optical micrographs of substrates with (a) Square and (b) Hexagonal symmetry in PMMA. While lattice constant of the crystalline substrate in (a) and (b) are same (950 nm), the linear spacing, λ, in UV adhesive for (a) and (b) were 950 nm and 833 nm, respectively. The scale bars in (a) and (b) represent 10 μm.

2.2.2 Fabrication of Moiré Templates

The overlaying of patterns, not necessarily the same one but at a slightly different angle or displaced with respect to each other results in the moiré patterns. As far as our experiments are concerned, we realized the linear moiré template by making the second imprint (at $T = 122°\text{C}$) in PMMA in aforementioned protocols at an angle $\theta \leq 45°$ relative to the first. Apart from preserving the linear periodicity of the parent template, this resulted in a long wavelength modulation of the trench (hole) depths (Figure 2.4a and b). While λ decides the symmetry of the growing crystals, the wavelength of the moiré pattern sets the super-periodicity of the colloidal crystals, L_p, and can be independently controlled by varying θ as shown in Figure 2.4a and b. Typically, θ was varied between $0° < \theta < 20°$. To fabricate square moiré patterns,

the square imprints in PMMA, realized above, was once again transferred to PDMS molds. The square pattern in PDMS was then transferred to UV adhesive which was then used as hard master to fabricate the square moiré patterns in PMMA (Figure 2.4c). The long wavelength modulations in the feature sizes are clearly evident in

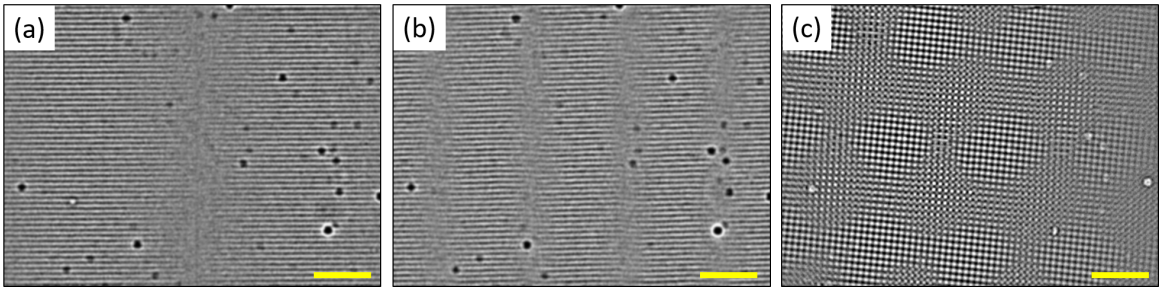

Figure 2.4 Optical micrographs of linear moiré patterns for (a) $\theta \sim 2^\circ$ (b) $\theta \sim 8^\circ$, and (c) Square moiré pattern for $\theta \sim 8^\circ$. While, $\lambda = 950$ nm in all the snapshots, (a) $L_p = 42\sigma$, (b) and (c) $L_p = 16\sigma$. The scale bars in (a), (b) and (c) represent 10 μm.

both computer-generated patterns (Figure 2.5a) as well as the AFM measurements (Figure 2.5b). The AFM measurements were performed using Veeco AFM apparatus in non-contact mode. Before the measurements, a thin layer of gold, $\sim$ 20 nm, was coated on the moiré template to prevent the AFM tip from sticking to the template. Consistent with earlier studies [310], we found that multiple transfers for making the

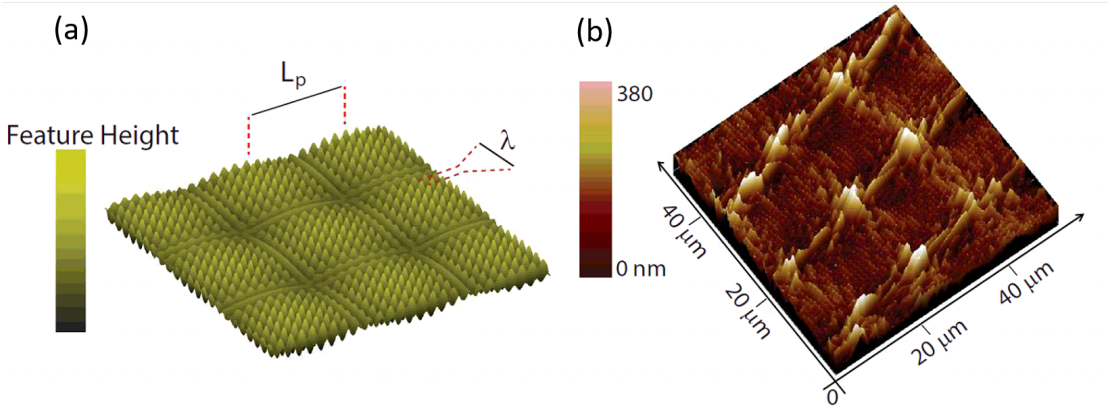

Figure 2.5 (a) Computer-generated (in Matlab) and (b) AFM topography maps for square moiré patterns at $\theta \sim 8^\circ$.

square moiré patterns, PDMS (line) to UV glue (line) to PMMA (squares) to PDMS (square) to UV glue (square) to PMMA (square moiré template), result in a significant loss in the groove depths. Hence, the yield of square moiré template was much less than the linear moiré templates. However, improvements in the imprinting technique

such as starting with square patterns with larger groove depth can enormously improve the yield of square moiré templates.

Having discussed the replica imprinting technique to fabricate templates with simple (square and hexagonal substrates) and complex topographies (moiré templates), we move on to describe the synthesis protocols for spherical and complex colloidal particles for the use in epitaxy experiments. The motivations behind synthesis of complex colloidal clusters like dimers and trimers were to probe the role of translational & orientational degrees of freedom (DOF) and *if possible* the coupling of two DOF on nucleation and growth kinetics of rigid colloidal clusters on square and hexagonal templates. Also, since the surface mobilities of colloidal clusters with different sizes would be distinct, moiré templates might allow self-segregation of these clusters at specific locations on the surface. Thus, in order to address these questions, we have synthesized, following well-established synthesis protocols, spherical colloids of silica, polystyrene as well as their complex colloidal clusters. The next section briefly covers the synthesis details for these particles. Before proceeding further, I must acknowledge that silica spheres were synthesized by a previous lab member Mamata Jotkar, however, for the sake of continuity we will mention its synthesis protocol also.

2.3 Synthesis Protocols

2.3.1 Synthesis of Silica Colloids

The charge stabilized spherical silica particles were synthesized using the Stöber process [324] and we followed the protocols established by Zhang *et. al.* [325]. Briefly, 67 mL of ethanol (HPLC grade) and 5 mL of ammonia (25% w/w, SDFCL) were taken in a 500 mL round-bottom flask to which 0.01 g of (3-amino-propyl)triethoxysilane (APS, Sigma) and 3mL of tetraethoxysilane (TEOS, Sigma) were added drop-wise. The mixture was stirred overnight at 28°C. Then, 25 mL of TEOS and 20 mL of water (Milli-Q, TKA, 18.2 MΩ) were added simultaneously after 24 hours. The size of particles at this stage was $\sim$ 400 nm. Further increments in the particle size were achieved by using a seeded growth reaction. This was carried out as follows: to the reaction mixture containing the silica particles, 25 mL of TEOS, 0.01 g of APS, 20 mL of water and 1.55 mL of ammonia were added and the mixture was left stirring for 24 hours. This resulted in an increase in particle radius and the above process was iterated until the desired particle size was obtained. The particles were cleaned

with repeated centrifugation (at 1500 rpm) and redispersal first in ethanol and then in deionized water. The particles size was estimated by allowing them to crystallize in the presence of short-ranged depletion interactions and lattice constant estimated from optical microscopy was found to be 950 nm (Figure 2.6).

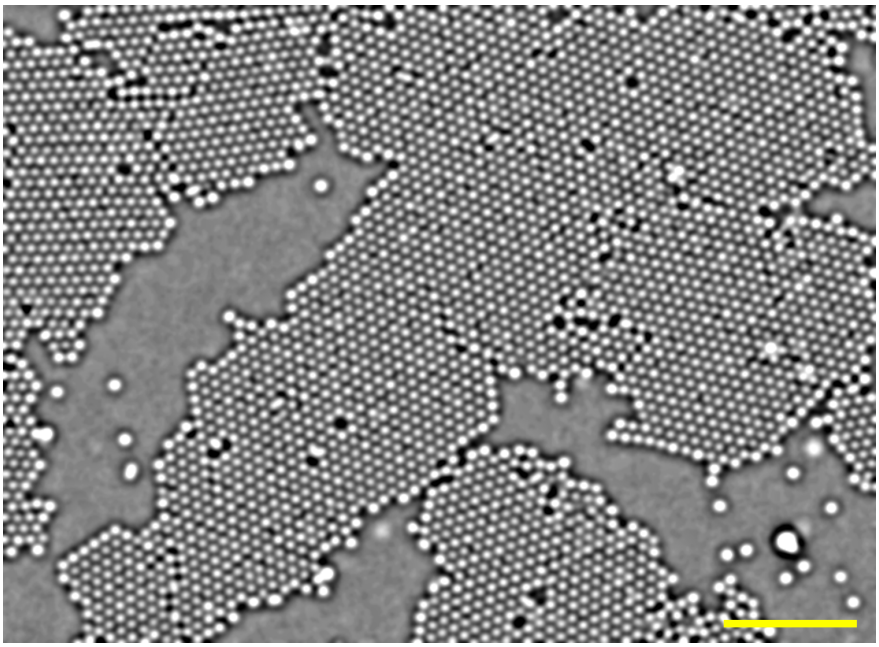

Figure 2.6 Crystal of colloidal silica particles. The scale bar represents 10 μm.

2.3.2 Synthesis of Crosslinked Polystyrene Spheres

Following the protocols established by Shim *et. al.* [326, 327], micron-sized crosslinked polystyrene (PS) particles were synthesized via multi-stage emulsion polymerization techniques. Since the presence of oxygen inhibits polymerization, the entire reaction was carried under the nitrogen atmosphere. In the first stage of the reaction, 50 mL of deionized water was taken in a 3-necked round bottom flask which was placed in an oil bath maintained at 60°C. Next, 9.2 g of distilled styrene (Sigma) and 0.8 g of divinylbenzene (DVB, Sigma) as crosslinker were added to the reaction flask. The reaction mixture was stirred at 350 rpm for 20 minutes. After equilibration, 0.05 g of initiator (here potassium persulfate, KPS, Sigma) dissolved in 50 mL of water was added to the reaction pot. The change in color of the reaction mixture from colorless to milky white indicates the start of the polymerisation process. The reaction was continued for 12 hours. The size of the particles at the end of the first stage was $\sim$ 700 nm. In the second stage of the seeded-growth reaction, 187.6 g of preheated

deionized water at the reaction temperature (60°C), 30 g of styrene and 3 g of DVB were added under nitrogen atmosphere to the reaction flask containing the products of the first stage. Once the system had equilibrated for 30 minutes, 0.66 g of initiator (DVB) was added to the reaction pot. The reaction mixture was stirred at 350 rpm and the temperature was held constant at 60°C. The reaction continued for 16 hours. The reaction mixture was then cooled and filtered using glass wool to remove large aggregates. The particles were cleaned by repeated centrifugation at 2000-2500 rpm and redispersal in water. To get rid of irregular clusters, the colloidal suspension was further cleaned under gravity sedimentation. Here, a relatively low volume fraction, Φ, of the colloidal suspension was loaded into a long and thin glass tubes (inner diameter was approximately 5 mm) and was allowed to settle under gravity. The cleaned and monodisperse particles at the top of the tube were collected at regular intervals of 2 days. The particles were allowed to crystallize in presence of short-ranged depletion interactions and their size, as observed in optical microscopy, was found to be 1.10 μm (Figure 2.7).

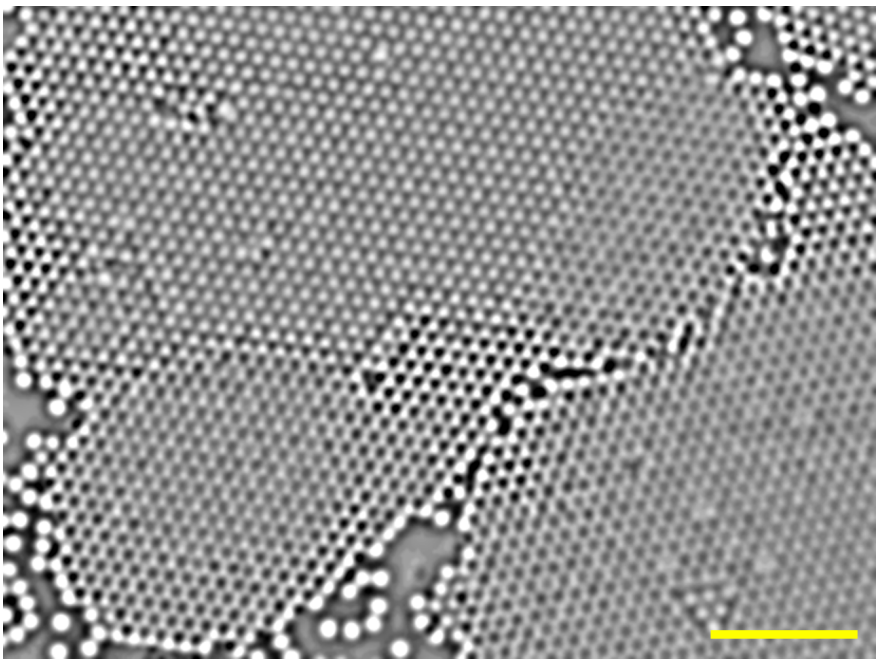

Figure 2.7 Crystal of crosslinked colloidal PS particles. The scale bar represents 10 μm.

2.3.3 Synthesis of Complex Colloids

We have synthesized complex colloidal clusters, predominantly dimers, trimers, and tetramers, of both crosslinked PS and silica particles. The key idea in this process is to emulsify the colloidal suspension in small droplets of varying sizes [32, 328]. The colloidal particles in the oil medium are contained within each of the emulsion droplets. The subsequent selective evaporation of the solvent contained within each of the droplets forces colloidal particles to stick irreversibly via van der Waals attractions resulting in clusters of well-defined symmetries.

PS Colloidal Clusters

To synthesize PS colloidal clusters [32], the aqueous dispersion of cleaned and monodisperse 1.1 μm crosslinked PS colloidal particles ($\Phi \sim 0.05$) was first transferred to toluene by repeated centrifugation at 2500 rpm and redispersal in ethanol (four times) and toluene (four times). It is worth noting that PS particles swell in toluene and hence the amount of crosslinking agent (DVB) should be high enough so that their irregular deformation from spherical shape is avoided on transfer to toluene. Subsequently, 3 mL of the colloidal suspension was added to 17 mL of aqueous solution of Pluronic F108 (1% w/w, Sigma). Since toluene is immiscible in water, the mixture phase separated with the colloidal suspension floating on top of water-surfactant mixture. Next, the mixture was emulsified using a homogeniser (Remi, RQT-127A/D) for 60 seconds at 6000 rpm. The oil-in-water emulsion of toluene droplets varied in size from a few microns to tens of microns. The presence of non-ionic surfactant (Pluronic F108) stabilizes the droplets from agglomeration. After homogenization, the system was further diluted with 100 mL of water and subsequently boiled at 100°C to preferentially remove most of the toluene from the droplets. This in principle should lead to a closed packing of the PS particles within each of the droplets. Further evaporation of toluene leads to the generation of strong capillary forces that results in rapid rearrangement of particles within each of the spherical droplets. As the last drop of toluene evaporated, the PS particles deswell and bind to each other due to the van der Waals attractions and results in the formation of small colloidal clusters. The large polydispersity in the initial sizes of emulsion droplets was also reflected in the sizes of colloidal clusters. However, an appropriate combination of various control parameters such as Φ of the colloidal suspension, the homogenization speed and time can yield colloidal clusters of a specific size (predominantly). The clusters were separated using the density gradient

centrifugation [32]. To achieve this, we prepared a 3 to 9% w/w linear gradient of Ficoll 400 in 1% w/w Pluronic F108/water mixture. 500 μL of above obtained colloidal clusters were gently loaded from above on the linear density gradient. Next, the system was centrifuged at 2000g in a swing-bucket centrifuge. Clusters with distinct sizes settled in distinct bands in the linear density gradient; with monomers at the top, followed by dimers, trimers and so on. We carefully and gently pipetted the suspension in the batch of 0.5 mL from the top. Each batch was observed under an optical microscope for determining the predominant composition of the size of the colloidal clusters. The clusters of specific sizes were then cleaned and transferred to water with repeated centrifugation at 2500 rpm and redispersal in water.

Silica Colloidal Clusters

Unlike PS particles, the first step in the synthesis of colloidal clusters of silica particles was to modify their surface chemistry to make them hydrophobic [328]. To achieve this, we first dispersed hydrophilic silica particles ($\Phi \sim 0.05$) in 99.0 mL of ethanol and 1.0 mL of ammonium hydroxide ($NH_3.H_2O$, 29.5%) by repeated centrifugation, redispersal, and ultrasonication (for 15 minutes) in ethanol (4 times). To the above dispersion, 10 mL of octadecyltrimethoxysilane (OTMOS, Sigma) in chloroform (10% v/v) was added dropwise with vigorous stirring. After 24 hours, the organically modified hydrophobic silica particles were cleaned by repeated centrifugation-redispersal in ethanol (4 times) to remove the unreacted precursors and the chloroform. The organosilica spheres in ethanol were then transferred to hexane which was used for making silica clusters on the similar lines described above for PS particles. Briefly, 2 mL of hydrophobic silica ($\Phi \sim 0.1$) in hexane was added to 16 mL of aqueous solution of Pluronic P123 (0.3% w/w, Sigma). To make the emulsion droplets, the resultant mixture was homogenized at 8000 rpm for 60 seconds. The above homogenized mixture was subsequently diluted with 15 mL of water and boiled to selectively evaporate hexane from the emulsion droplets. This yielded hydrophobic silica colloidal clusters with varying sizes. Finally, to the resulting dispersion of colloidal clusters, 0.25 mL of TEOS and 0.5 mL of NH_4OH were added and the mixture was stirred overnight that rendered hydrophilicity to the silica clusters. Analogous to PS clusters, the silica clusters of various sizes were also separated by density gradient centrifugation. SEM images of silica clusters of various size are shown in Figure 2.8. We found that the yield of colloidal cluster synthesis either with crosslinked PS particles or with the silica particle was very low and hence posed a severe limitation for any study of their self-assembly on the templates.

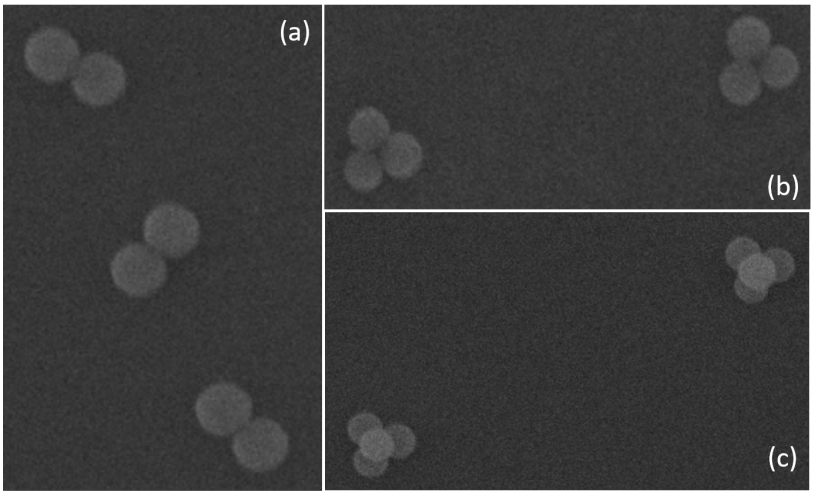

Figure 2.8 Representative SEM images of colloidal clusters synthesized from 950 nm silica colloidal particles. (a) Dimers (b) Trimers and (c) Tetramers.

Next, with an aim to probe the role of anisotropic interactions in the relaxation and transport properties of supercooled liquids and glasses, we will describe the synthesis details for colloidal ellipsoids, the simplest possible deviation from spheres.

2.3.4 Synthesis of Polystyrene Ellipsoids

Polystyrene (PS) Ellipsoidal particles were synthesized using the protocols established by Ho *et. al.* in 1993 [29]. Here, the easily accessible glass transition temperature of *uncrosslinked* PS spheres is utilized to uniaxially deform their shape to obtain colloidal ellipsoids.

Synthesis of Uncrosslinked Polystyrene Spheres

Uncrosslinked PS particles were synthesized via a free-radical polymerisation technique in presence of nitrogen atmosphere [29, 329]. 167.5 ml of 25 mM of aqueous sodium chloride (NaCl) was taken in a 3-necked round bottom flask which was placed in an oil bath and stirred at 350 rpm. The system was left to stabilize at 80°C for 15 minutes. Then, 20 ml of distilled styrene (Sigma) was added to the reaction pot. After equilibration, 38 mg of KPS (as initiator) dissolved in 7.5 ml of water was added to the reaction pot. The solution slowly turned turbid signifying the onset of polymerisation. The reaction continued for 24 hours. The system was then cooled and filtered using glass wool to remove large aggregates. The particles were cleaned by repeated centrifugation at 3000 rpm and redispersal in water. To estimate the particle

size, the particles were allowed to crystallize using depletion interactions and the lattice constant estimated from optical microscopy was found to be 1.4 μm.

Synthesis of Polystyrene Ellipsoids

Since uncrosslinked PS particles are thermoplastic, they can be deformed to a desired shape when heated beyond their glass transition temperature T_g (for PS $T_g = 100°C$). To stretch the PS spheres, we need a film forming material like polyvinyl alcohol (PVA) that acts as a matrix in which the spherical particles can be embedded. For the synthesis of PVA, we followed the protocol by Ho *et. al.* [29]. 15 g of polyvinylacetate, PVAc, (Sigma Aldrich, Mol. Wt. 5,00,000) was dissolved in 250 ml of methanol and water solution (1:4 v/v). The solution was stirred for 2-3 days which allowed most of the PVAc to dissolve. To the solution, 2.25 g of sodium hydroxide (NaOH) was added and refluxed for 4 hours at 105°C. The solution was neutralized using concentrated hydrochloric acid (HCl) and subsequently, $\sim$ 200 ml of isopropanol was added till a saturated white gel was obtained. We carefully discarded the supernatant and soaked the gel in water and washed it every 2-3 hour over a 24 hours period. Then, 165 ml of isopropanol:methanol:water solution (6:1:4 v/v) was added to the gel and was gradually heated from 35°C to 80°C with continuous stirring at 200 rpm. The gel dissolved completely in this solution within 2-3 hours. The viscous solution of PVA was dialyzed using a dialysis membrane in a water environment and the water was changed every 2-3 hours over a day.

For forming the film, we used a perspex tray of size 13×9 cm^2. 500 μl of uncrosslinked PS spheres ($\Phi = 20 - 30\%$) was dissolved in 50 ml of PVA. The above solution was poured slowly into the perspex tray and then placed inside the vacuum oven. The solution was allowed to stabilize at 28°C and 0.1 atm. After 2 days, the temperature was ramped to 45°C in steps of 2.5°C every 12 hours to avoid the formation of bubbles during the drying process. The film took 4-5 days to dry. For uniform stretching, the smooth film was cut into strips of dimension 4×6 cm^2. To achieve a better control on the uniformity of stretched PS particles, square grids of dimension 0.5×0.5 cm^2 were marked on the strips (Figure 2.9). The film was then clamped to a home made film-stretching apparatus as shown in Figure 2.10. The entire apparatus was dipped into an oil-bath maintained at 180°C. We manually stretched the film uniaxially to a draw ratio of 3. The apparatus was taken out and allowed to cool down to room temperature. Only rectangular grids of same aspect ratio were taken for recovery of the ellipsoidal particles (Figure 2.11). To extract the ellipsoidal particles, the film was

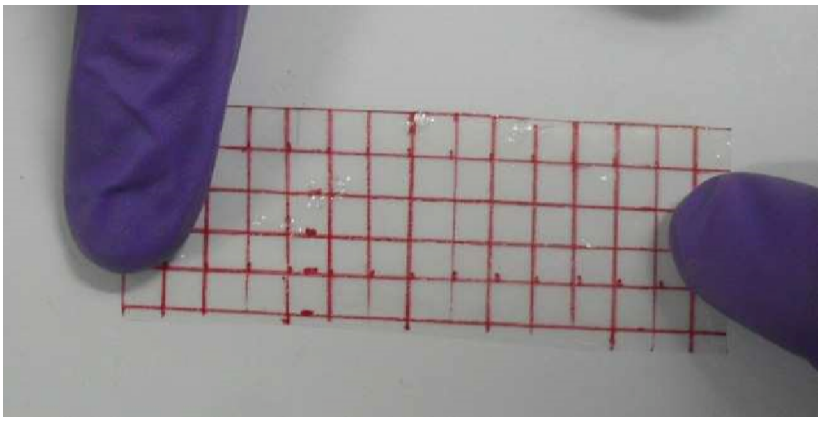

Figure 2.9 Unstretched PVA film with PS spherical particles embedded in it. The red lines marks the square grids of size 0.5×0.5 cm^2.

soaked in a solution of isopropanol:water (3:7 v/v) overnight and then refluxed at 80°C for $4-5$ hours. The film dissolved completely and the resulting turbid suspension was centrifuged at ~ 3000 rpm to recover the colloids. The supernatant was discarded and the particles were redispersed in isopropanol-water solution and again refluxed at 80°C for 5 hours to remove any residual traces of PVA. The suspension was cleaned repeatedly using water. We obtained the aspect ratio of our ellipsoids from FESEM measurements (Figure 2.12). From the analysis of over 100 ellipsoids, we found that the aspect ratio α of the ellipsoids was 2.1 with the major and minor axes of $2l = 2.1$ μm and $2w = 1.0$ μm, respectively. The polydispersity in l and w was observed to be 11% and 8%, respectively.

In order to probe the reentrant glass dynamics for colloidal ellipsoids with various αs, as the phase diagram of ellipsoids is strongly dependent upon α (Figure 1.35, Chapter 1), following the protocols described above, we have also synthesized colloidal ellipsoids with $\alpha \sim 1.6$ and $\alpha \sim 3.2$ (Figure 2.13). However, the yield in these synthesis were not sufficient to perform multiple experiments at different depletion concentrations and hence we were unable to probe their reentrant glass dynamics.

2.3.5 Depletant

In all our experiments, we have used sodium carboxyl methyl cellulose (NaCMC, Fischer-Scientific, Mol. Wt. 700000) as the depletant. Using Kramer's equation [330] the overlap concentration c^* of the depletant, from rheological measurements, was found to be $c^* = 0.11$ mg/ml. The highest depletant concentration c_p used in our work was $c_p = 0.05$ mg/ml which is less than c^*. Using well established scaling arguments[330],

Figure 2.10 The film stretching apparatus, developed in-house. The film is clamped in between two aluminium blocks as shown and stretching is done manually.

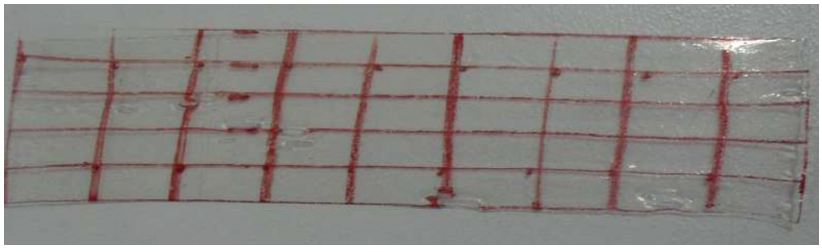

Figure 2.11 Stretched film. The square grids prior to stretching have elongated uniaxially.

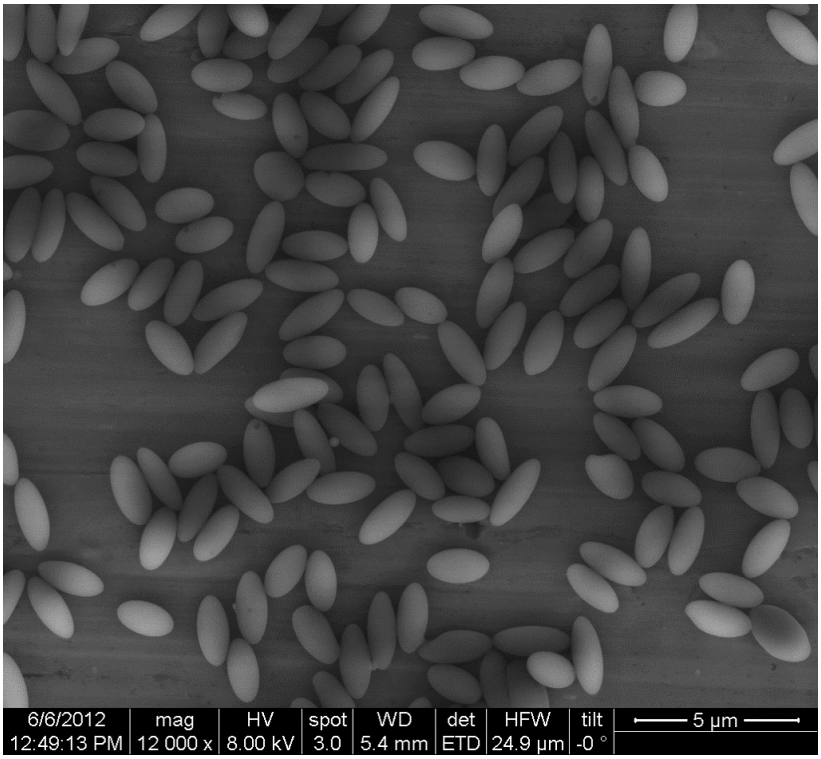

Figure 2.12 FESEM images of the colloidal ellipsoids of aspect ratio $\alpha = 2.1$.

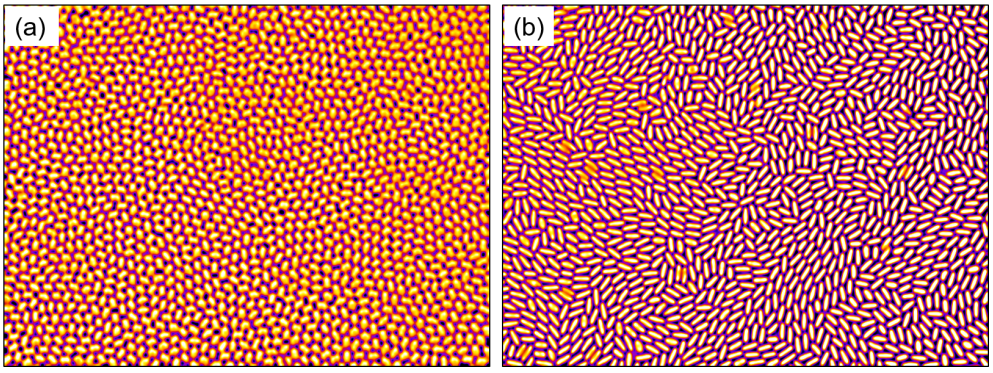

Figure 2.13 Optical micrograph of colloidal ellipsoids of (a) $\alpha \sim 1.6$ and (b) $\alpha \sim 3.2$. These ellipsoids were synthesized from 1.4μm uncrosslinked PS spheres.

we estimated the radius of gyration of the depletant to be 60 nm. Now, in the last two section of this chapter, we will focus on experimental cell designs and imaging used for addressing the problems on colloidal epitaxy and structural glass transition.

2.4 Cell Design for Experiments on Colloidal Epitaxy and Imaging

To enable comparison of the nucleation kinetics for various depletion concentrations c_p and deposition fluxes F, experiments were carried out on the same template. To this end, we fabricated glass flow cells, like in the work of Ganapathy *et. al.* [17], where the bottom of the flow cell is a PMMA-coated glass coverslip having the required template (Figure 2.14). The flow cell was filled with a 1:1 mixture of dimethyl sulfoxide

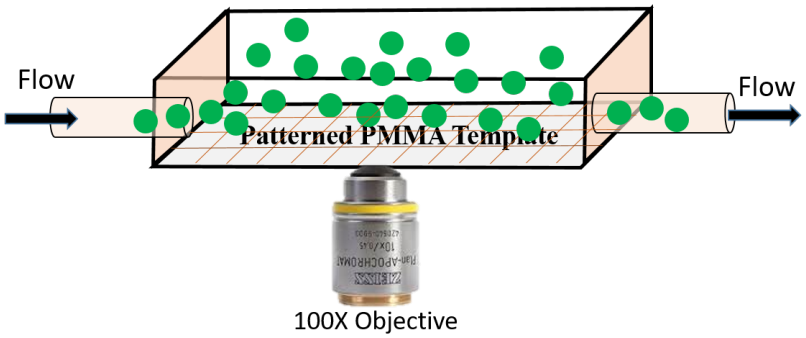

Figure 2.14 Schematic of the flow cell designed for the epitaxy experiments. The solid green spheres represent 950 nm silica colloids. The height of the flow cell was 1.3 mm. For the experiments on a given template with varying depletion concentrations, the relative position of the objective and the flow cell is fixed. After loading the flow cell with colloidal suspension, along with suitable depletion concentration, the flexible tubes on the sides are sealed with binder clips.

(Merck) and water containing the requisite amounts of NaCMC (depletant) and 950 nm silica colloids. Particles were then allowed to sediment onto the substrate and the nucleation and growth kinetics were followed by optical microscopy (Leica DMI 6000B with a 100X oil immersion objective Leica, Plan-Apochromat, N.A. 1.4). Images were captured using a digital camera (Foculus 234SB) with a frame rate between 2 and 5 frames per second. To improve statistics, nucleation and growth were investigated over a substantially larger field of view using a Photron FastCam SA4 to capture individual images at suitably spaced time intervals. The images were processed using ImageJ

and Matlab, and center-of-mass coordinates of colloids were obtained using standard Matlab algorithms [331].

The geometric height modulations of the underlying moiré templates in the above cells create an activation energy gradient for the diffusing colloids and hence D on moiré templates should be a spatially varying quantity. Thus, estimating D/F for the experiments on moiré templates turned out to be tricky. However, since the spatially averaged D on linear moiré templates was found to be equal to the D on a linear array of trenches at the same c_p (Figure 2.15), D on the linear grating patterns were used for determining D/F on moiré templates also. Also, since D of the particles on the linear grating and linear moiré template is anisotropic (Figure 2.15), only D along the channel was used to estimate D/F. The deposition rates F were controlled by the

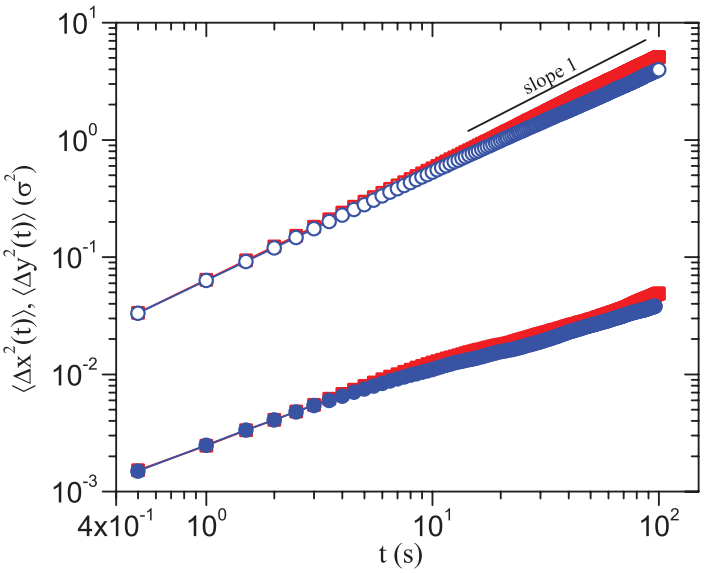

Figure 2.15 MSD along ($x-$axis, open symbols) and orthogonal direction ($y-$axis, solid symbols) to the channel for the linear grating patterns (red squares) and the linear moiré templates (blue circles), $\theta \sim 8°, L_p \sim 16\sigma$ at $c_p = 0.14$ mg/mL. The solid line represents slope 1. D was found to be $D = 0.023 \pm 0.001\sigma^2 s^{-1}$.

Φ of the colloidal suspension and was independently measured in each experiments (Figure 2.16). F is quoted in units of monolayer per second (ML/s).

In order to study the similarity, *if any*, between the nucleation and growth kinetics on square moiré templates and atomic heteroepitaxy, the experiments on square moiré patterns were performed over a wide range of c_ps with fixed deposition flux F. Interestingly, c_p mimicked the behaviour of the inverse in temperature in atomic experiments (Figure 2.16).

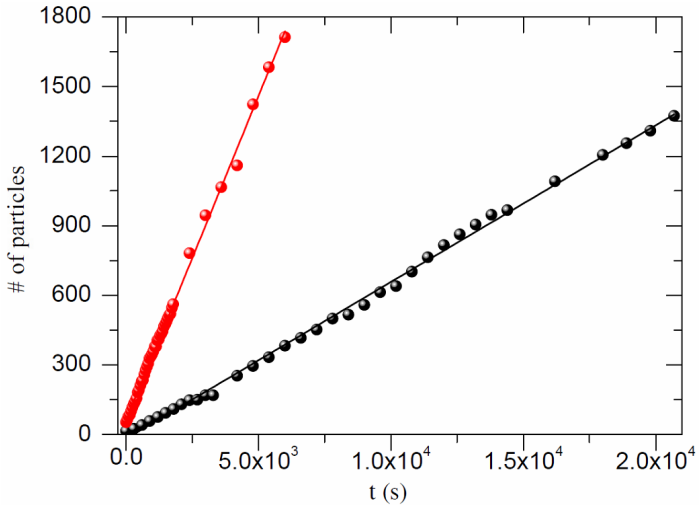

Figure 2.16 The number of particles landing on linear grating pattern, for two different Φs, versus time. The slope of the curve in each experiment were used to determine F on the templates. $F = 2 \times 10^{-5}$ MLs^{-1} (black spheres, $\Phi = \Phi_1$), and $F = 8.5 \times 10^{-5}$ MLs^{-1} (red spheres, $\Phi \sim 4\Phi_1$). The solid lines are linear fits to the data.

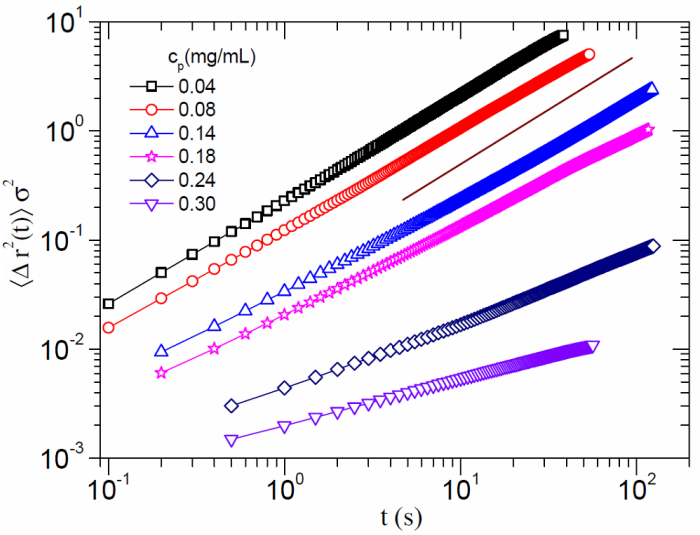

Figure 2.17 Spatial averaged MSD of the monomers on the square moiré templates for varying depletion concentrations c_ps. The solid line represents slope 1. Analogous to decrease in temperature T for experiments on atomic heteroepitaxy, diffusivity (long-time slope of MSD) decrease with increase in c_p.

2.5 Cell Design for Experiments on Supercooled Liquids of Colloidal Ellipsoids and Imaging

The ellipsoidal particles obtained after the aforementioned cleaning protocols along with a suitable depletant concentration were loaded in wedge shape cells (glass coverslips, Electron Microscopy Sciences) (Figure 2.18). Prior to loading the cell with the sample,

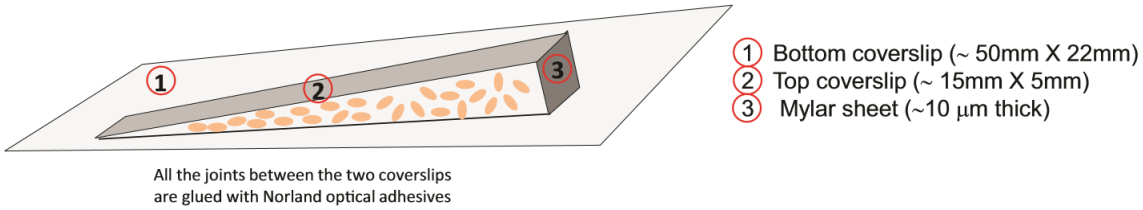

Figure 2.18 Schematic sketch of quasi-two-dimensional sample cell.

we ensured that coverslips were hydrophilic, by thoroughly cleaning them with the base solution (5g of NaOH dissolved in a solution of 20 ml water and 30 ml ethanol). The small wedge angle of the sample cell leads to strong capillary forces which result in particles rushing to the thin regions of the cell and sticking permanently. To circumvent this issue, prior to loading the sample, we injected a known amount of water into the cell. The cell was left vertically standing to allow the particles to sediment to the thin 2D regions of the cell. As and when a required area fraction, ϕ, was attained, video microscopy was done using a 100X oil immersion objective (Leica, Plan-Apochromat, N.A. 1.4) at a frame rate of 5 fps for a typical duration of 20 minutes. It took roughly 2 to 15 days to vary the ϕ in the range of $0.23 \leq \phi \leq 0.79$. The data for $\phi = 0.84$, for the purely repulsive case, was taken at a frame rate of 1 fps for 2 hours. The sample was allowed to equilibrate horizontally on the microscope for $4-6$ hours before capturing the data. The particle number fluctuations at any ϕ were not more than 0.1%. To ensure that the viewing region was quasi 2-dimensional (2D), we analysed the change in major, Δl, and minor, Δw, axes of each ellipsoid in successive frames. A thick cell can support out of plane fluctuations of an ellipsoid which can result in an effective change in its aspect ratio, α, in the imaging plane as shown in Figure 2.19a. We find that the distributions of Δl and Δw are Gaussian with standard deviation of 0.03μm and 0.06μm, respectively, as shown in Figure 2.19 b and c. The small standard deviations along with the small depth of field of the microscope objective (~ 200 nm) show that the cells were indeed quasi 2D. The experiment was done in a typical viewing region of size $65 \times 47\mu\text{m}^2$.

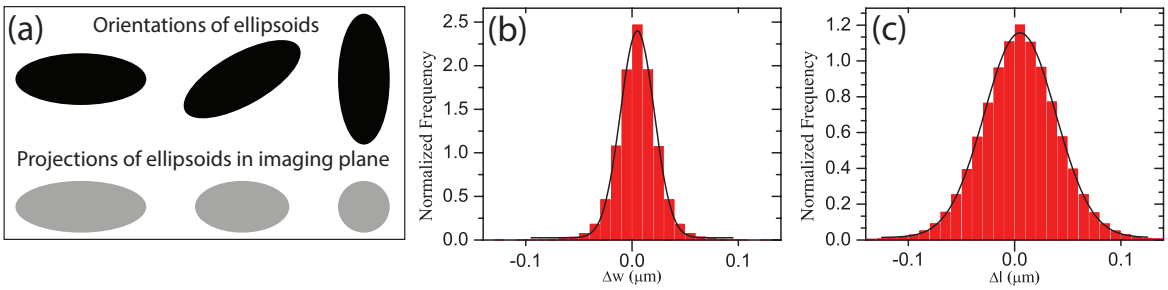

Figure 2.19 (a) Out-of-plane orientations of the ellipsoids in a thick cell and their projections in the imaging plane. Distribution of the change in (b) major axis Δl and (c) minor axis Δw of the ellipsoids between successive frames. The solid lines represents Gaussian fits to the distribution.

The images were pre-processed using ImageJ which yielded the coordinates of centre-of-mass and the orientations of each ellipsoid as shown in the Figure 2.20. The

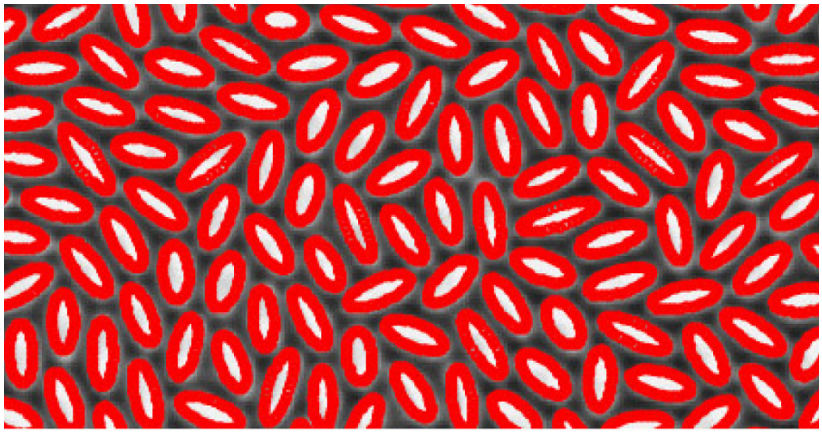

Figure 2.20 The image shows the tracking of the ellipsoid at $\phi = 0.79$. The red lines are the boundaries of the ellipsoids which have been drawn in Matlab with the information obtained from ImageJ.

data was analysed using standard [331] as well as custom developed Matlab codes. To obtain the spatial and orientational tracking resolution in our experiments, we analysed the mean squared displacements $\langle \Delta r^2 \rangle$ and mean squared orientational displacements $\langle \Delta \theta^2 \rangle$ of the ellipsoids in very dilute regime ($\phi = 0.04$). The dynamics were observed to be diffusive for both translational and orientational DOF (Figure 2.21). The intercepts of $\langle \Delta r^2 \rangle$ and $\langle \Delta \theta^2 \rangle$ on the y-axes yielded the spatial and angular resolutions to be 60 nm and 1°, respectively. To monitor ageing, we divided the experimental window at $\phi = 0.76$ into 3 equal time interval (t_{w1} to t_{w3}) and showed that mean-squared-

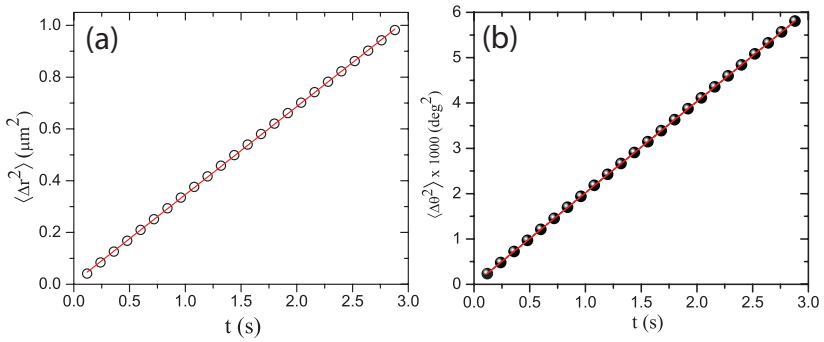

Figure 2.21 (a) $\langle \Delta r^2 \rangle$ and (b) $\langle \Delta \theta^2 \rangle$ versus t at $\phi = 0.04$ for estimating the spatial and orientational resolution in our experiments. The red lines are linear fit to the data.

displacements (MSD) during successive interval do not show any change from that obtained from the total experimental time (t_{total}) (Figure 2.22).

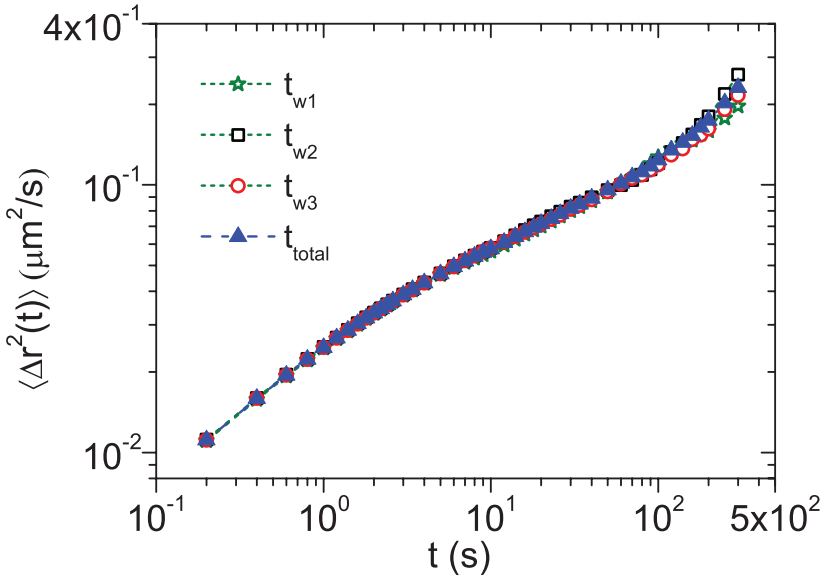

Figure 2.22 Mean squared displacements, $\langle \Delta r^2 \rangle$ for different time window t_w at $\phi = 0.76$.

2.6 Conclusions

Having elaborated on experimental details for performing experiments on colloidal epitaxy and supercooled liquids and glasses of colloidal ellipsoids, we move on to discuss in the following chapters our results from these studies.

Chapter 3

Site-specific Colloidal Crystal Nucleation by Template-enhanced Particle Transport

3.1 Introduction

Realizing ordered surface nano- and microstructures of well-defined size and shape from the autonomous assembly of their constituent building blocks continues to remain one of the key challenges in materials science [100, 101, 123, 332]. With regard to atomic/molecular surface assembly, using templates that preferentially enhance crystal nucleation events at specific sites is a proven approach towards realizing mesoscopically ordered structures like quantum dot arrays and supramolecular nanoassemblies [108, 109] (Section 1.4.2, Chapter 1). Extending this technique to tailor surface structures composed of nanoparticles and colloids is highly desirable for applications that include sensors, structural color-based filters, and optoelectronic devices [4, 111, 116]. Although recent experiments find that colloidal and atomic thin film growth on homogeneous surfaces obeys identical scaling laws [17, 112], translating concepts gleaned from site-specific nucleation studies on atoms/molecules to colloids is anything but easy. To achieve site-specific nucleation with high fidelity, the particles' surface mean free path, L, should be larger than the distance between the preferential nucleating sites L_p. In conventional surface growth studies, L is set by the ratio of the monomer surface diffusion constant to its deposition flux D/F with $L \sim (\frac{D}{F})^{1/6}$ for $D/F > 10^4$ [101, 146]. For atoms, a broad window of D/F values spanning $10^{-1} - 10^9$ can be readily accessed

and thus, L can be easily tuned to be larger than L_p. However for colloids, owing to their large size, D is small and the D/F window is limited to $10^{-1} - 10^4$. To further complicate matters, over this window, simulations, atomic and colloid experiments find deviations from mean-field scalings and L, or equivalently the island density is found to saturate with decreasing D/F [17, 101]. In fact for micrometer-sized colloids, the maximum L is $\sim 5-7$ particle diameters only. Consequently, it is as yet unclear whether site-specific nucleation is even a viable strategy to fabricate mesoscopically-organized structures made of nano- and microscale particles. This has resulted in numerous alternate approaches that include selective evaporation [87, 333–335] and external field driven assembly [4, 7, 336–338] to help realize the target structures. Many of these techniques, however, are often particle specific and do not allow exquisite control over the nucleation and growth process. Here, in this chapter, we will demonstrate how utilizing the geometrical nature of short-ranged depletion attraction on templates with complex surface features, in this case moiré templates, results in a remarkable control over not only the sites of nucleation but also over the size and symmetry of the growing colloidal crystals can be achieved.

3.2 Results and Discussions

3.2.1 Enhancing Particles' Mean Free Path

A plausible route to help alleviate the restrictions on L, imposed by D/F, is to utilize surfaces with energy gradients to transport particles to desired locations. Using the facile replica imprinting technique [115] (Section 2.2, Chapter 2), we present a new design principle based on templates with spatially varying feature sizes which in the presence of short-range depletion attraction induced activation energy gradients for the diffusing colloids. Our substrates comprised of linear and square moiré patterns on polymethylmethacrylate (PMMA) layers spin-coated on glass coverslips. We fabricated these patterns, by first transferring a linear (square) array of trenches (holes), with periodicity λ, from a master grating to the PMMA substrate [116]. This was followed by a second imprint at an angle, θ, relative to the first, which resulted in a long wavelength modulation of the trench (hole) depths (Section 2.1.2, Chapter 2). While λ decides the symmetry of the growing crystallites, the wavelength of the moiré pattern sets L_p, and can be independently controlled by varying θ as seen in Figure 3.1a and b. Next, we sedimented colloidal particles (silica, diameter $\sigma = 940$ nm) in the presence of a

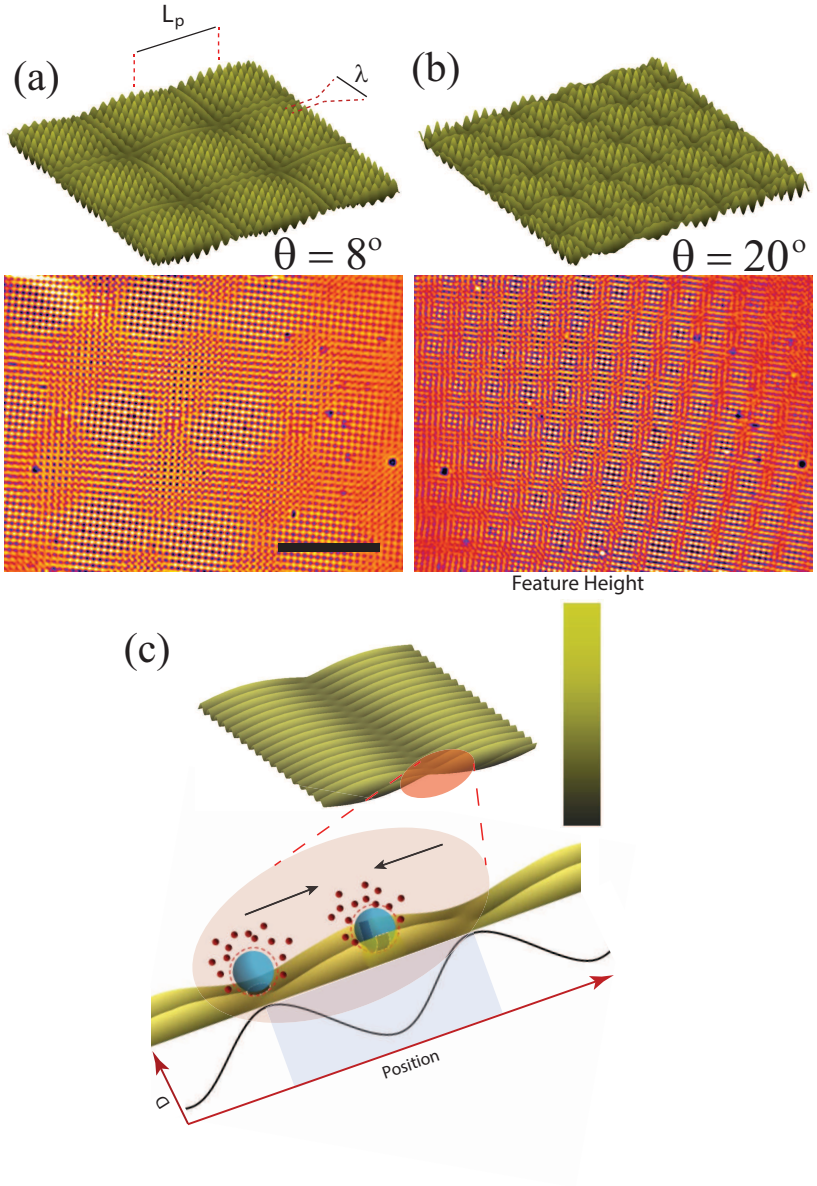

Figure 3.1 Particle locomotion to traps induced by surface energy gradients. (a) and (b) show representative optical micrographs of square moiré patterns (bottom panel) and the corresponding computer-generated topography maps (top panel) for two different θs. The scale bar in (a) represents 15 μm. (c) Schematic representing particle-substrate interactions on a linear moiré pattern. The overlap volume increases in the direction of the arrows and results in a net migration of particles to regions of high overlap (high E_a).

depletant polymer (Sodium carboxylmethyl cellulose, $R_g = 60$ nm) on these substrates (Section 2.3.5, Chapter 2). Particle diffusion on templated surfaces has an activated form [101],

$$D = D_0 \exp\left(\frac{-E_a}{k_B T}\right) \tag{3.1}$$

where E_a is the barrier height, D_0 is the attempt frequency and $k_B T$ is the thermal energy. Apart from the polymer concentration c_p, the strength of the depletion attraction between the colloids and the substrate is also proportional to the excluded overlap volume that is freed up when they come in contact [62]. Thus, on moiré patterns, gradients in trench (hole) depths induced gradients in E_a for the diffusing colloids and results in particle migration to the nearest energy minima (Figure 3.1c). We confirmed the enhancement in particle mean free paths by analysing the motion of individual particles on a linear moiré substrate, with $L_p = 16\sigma$ (Figure 3.2a) and $L_p = 42\sigma$ (Figure 3.2c). The grey shaded region in Figure 3.2a and c represents regions of the template with a high E_a. While the particles that land within this region stay localised, those that land outside (regions of low E_a), migrate nearly $L_p/2$ to the high E_a regions and are subsequently trapped. Figure 3.2b and d show snapshots of particles localized in trap sites on moiré templates. Furthermore, in order to quantified the change in activation energy on the linear moiré template ($\theta \sim 8°$), $\Delta E_a = E_a^{max} - E_a^{min}$, across a super-period L_p, we have measured D in high (red shaded regions in Figure 3.2d) and low (unshaded regions in Figure 3.2d) E_a regions, respectively. The substitution of D in Eqn.3.1 yielded $\Delta E_a \approx 0.5 k_B T$.

3.2.2 Nucleation Control on Linear Moiré Templates

It is apparent from the preceding discussions that in comparison to conventional templates, the enhanced mean path of colloids on the moiré template would allow a better control over the site-specific crystal nucleation and growth. Thus, in order to quantify and demonstrate this efficacy, we will take a small detour and first find out the limits of control over nucleation on conventional templates with no surface energy gradients. To this end, we have performed epitaxy experiments on a linear array of trenches (no surface energy gradients) for the same c_p and λ as the linear moiré templates. We found that during the early stages of the film growth, the increase in particle density on the surface led to the nucleation of new islands and hence the critical island density n increased with surface coverage Θ. An island with i-particles is termed a critical cluster if the addition of another particle makes it stable against

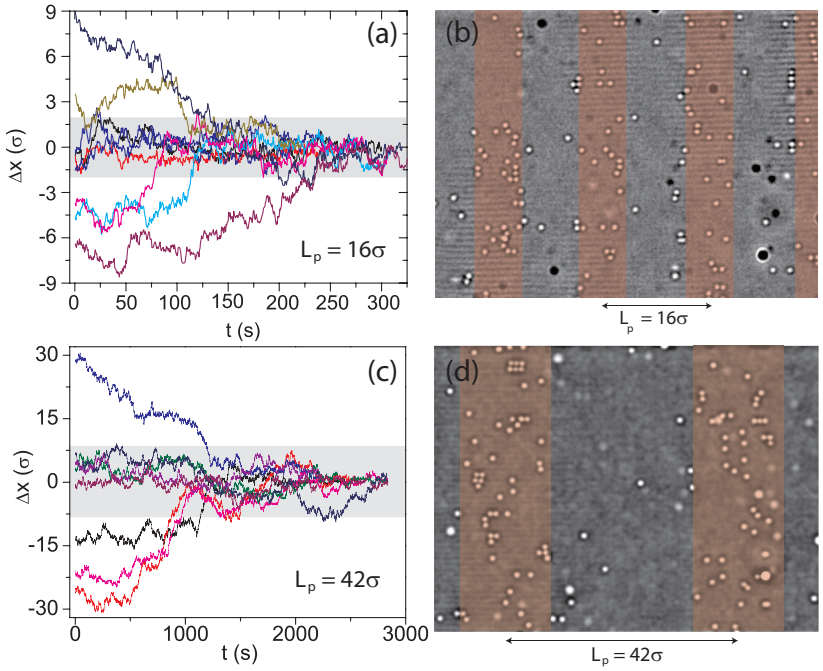

Figure 3.2 Particle trajectories and representative images of particle localisation on linear moiré templates with (a) & (b) $L_p \sim 16\sigma$ and (c) & (d) $L_p \sim 42\sigma$, respectively. The grey and red region corresponds to regions of the pattern with high E_a.

disintegration. For each D/F studied, we determined the stability of the nuclei for various i, starting from $i = 1$. First, we counted the number of islands, N_1, containing i-particles that became islands of $(i + 1)$-particles over a time interval Δt (Figure 3.3). Next, we counted the subset of these islands, N_2, that were stable against disintegration over a subsequent time interval of the same duration. If $\frac{N_2}{N_1} \geq 0.65$, i is termed as the critical nuclei, or else, the process was iterated for increasing values of i till the above criterion was satisfied (Figure 3.3). The critical island size for various D/F values on linear grating pattern and linear moiré template are summarized in Table 3.1.

c_p(mg/ml)	D/F	i (linear grid)	i (linear moiré)
0.14	265	2	2
0.14	405	2	2
0.14	1400	2	2
0.14	4035	3	2

Table 3.1 Critical nuclei for linear grid and linear moiré templates. For moiré template, at largest D/F studied, owing to the lateral flux of the particles to the regions with high activation energy, dimers ($i = 2$) continue to be the critical nuclei.

As expected, beyond a critical Θ, arriving monomers diffuse to nearby stable islands

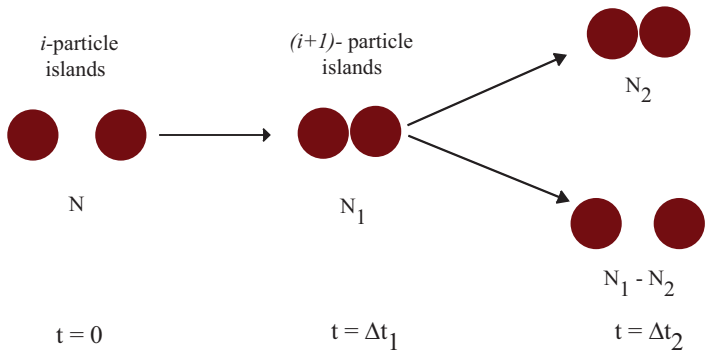

Figure 3.3 Schematic of the algorithm for finding critical nuclei. An island of i-particles was termed termed as a critical nuclei when the condition $\frac{N_2}{N_1} \geq 0.65$ was satisfied.

without nucleating new ones and n reached a maximum n_c (Figure 3.4a). At the later stages of the film growth n decreases as island coalesce. The average island separation at $n = n_c$ yielded L. As mentioned earlier, these experiments were performed at a constant c_p and varying F. Over the accessible range of D/F values in colloidal epitaxy, n_c does not show any marked change (Figure 3.4a). Consequently, L changed from $5-8\sigma$ only and was consistent with the direct measurements of L from the snapshots at $\Theta \sim \Theta_c$ (Figure 3.4b and c). In fact, even at the highest D/F studied, $L \sim 8.2\sigma \pm 2\sigma$ and was consistent with deposition-diffusion-aggregation (DDA) model which predicts $L \sim (D/F)^{1/4} \sim 8\sigma$ [146]. Thus, for the pattern periodicity $L_p > 8\sigma$, conventional templates would fail to yield a full control over sites of nucleation. In contrast to linear grating pattern, L_p of the moiré templates solely dictates the maximal separation between two sites of nucleation. Now, having discussed the limits of colloidal epitaxy on conventional templates, we return back to our initial dissussions on quantifying the efficacy of linear moiré templates over the linear grid patterns. As expected, the accumulation of particles in regions of high activation energy also increased the likelihood of crystal nucleation events at these sites. For site-specific nucleation to occur with a high fidelity, however, an optimal balance between F and the particle surface mean free path, albeit enhanced here, is needed [101, 146]. Figure 3.5a and b shows representative snapshots of crystals grown on linear moiré templates with $L_p = 42\sigma$ at identical c_p and surface coverage, Θ, and for two different Fs, respectively. At the smaller F, particles were able to migrate to traps prior to encountering arriving monomer(s) and the crystals formed are compact and confined to trap sites (Figure 3.5a). For the higher F, however, this is not the case and the crystals within the traps are more ramified and colloidal islands with six-fold symmetry (highlighted by circles

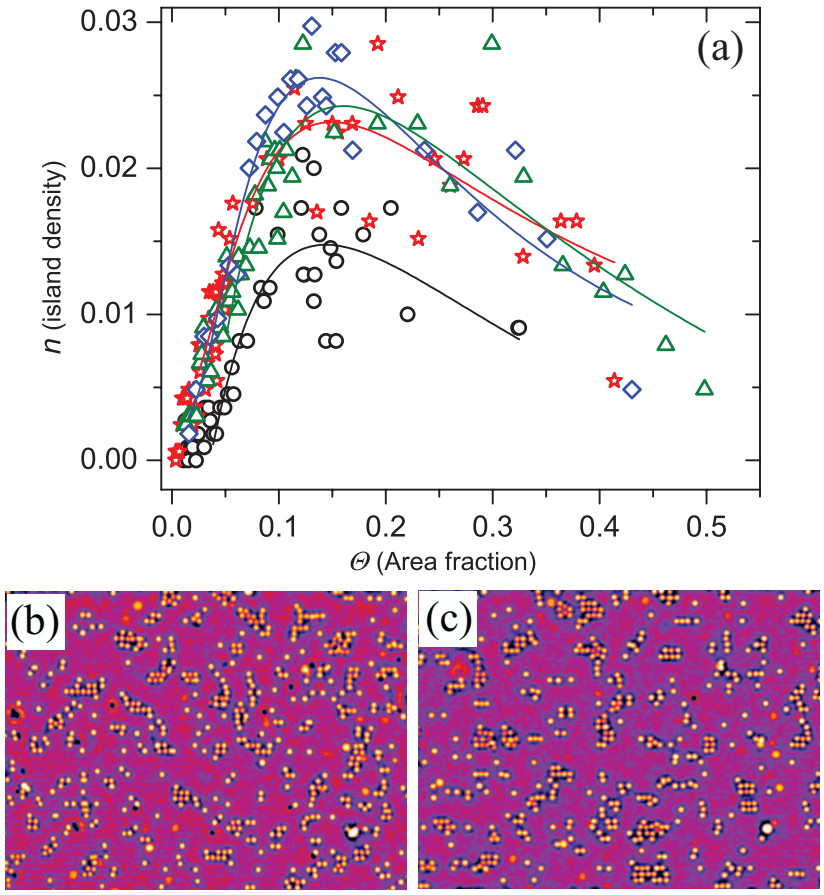

Figure 3.4 L for linear grating patterns. (a) Island density n versus Θ for linear grating patterns at a fixed $c_p = 0.14$mg/ml and varying F, $F = 4035$ (black circles), $F = 1400$ (green triangles), $F = 405$ (blue diamonds), and $F = 265$ (red stars). The solid lines are log-normal fits to the data. Optical microscope snapshots at $\Theta \sim \Theta_c$ for (b) $F = 265$, and (c) $F = 4035$.

in Figure 3.5b) nucleated outside the traps as well. We parametrized the fidelity of nucleation events at trap sites by the nucleation control efficiency, x_{NCE}

$$x_{NCE} = \frac{N_m}{N_{Tot}}. \tag{3.2}$$

Here, N_m is the subset of particles that migrated to traps in a time interval Δt and then crystallised and N_{Tot} is the total number of particles that landed outside traps over the same time interval [110, 339]. We note that x_{NCE} in [110] is defined as the

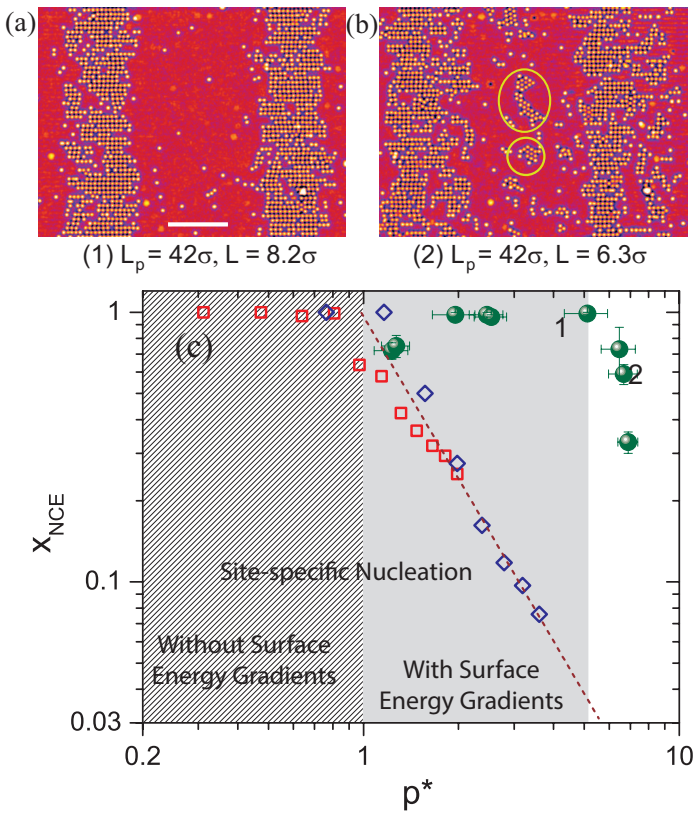

Figure 3.5 Nucleation control on moiré patterns.(a) and (b) Representative images of crystals growth on linear moiré patterns at constant c_p and for two different Fs. Since, $\lambda = \sigma$, the templates promoted the growth of crystals with square symmetry. (b) Loss of nucleation control results in the nucleation of hexagonally ordered crystallites outside of the traps and is highlighted by circles (c) Comparison of x_{NCE} versus p^* for conventional site-specific nucleation studies and on moiré patterns. The red and blue squares correspond to experiments and simulation results for vapor deposition of organic molecules (adapted from [110]). Here, nucleation control is lost ($x_{NCE} < 1$) beyond the striped region. The green circles correspond to colloid experiments on linear moiré patterns for various L_p, c_p and F values. Owing to the enhancement in particle mean free path on these substrates, $x_{NCE} < 1$ only for $p^* > 6$.

ratio of number of traps to the number of islands. This definition, however, poses difficulties in estimating x_{NCE} for spatially extended traps that can support multiple stable nuclei in the early stages of film growth, as is the case here. x_{NCE}, defined here, not only circumvents this limitation but also allows for direct comparison with previous experiments.

Next, we carried out thin film growth experiments on linear moiré templates for different c_p, F and L_p values. To succinctly capture the dependence of x_{NCE} on these parameters and to isolate the contribution arising from the enhancement in mean free paths, we plotted x_{NCE} versus $p^* = \frac{L_p}{L}$. Here, L is the mean free path of particles under identical experimental conditions but in the absence of energy gradients. L was obtained by measuring the density of critical clusters, n_c, at the onset of coalescence (Figure 3.4). In Figure 3.5c, we compare x_{NCE} versus p^* from our experiments with simulation and experimental results for site-specific nucleation and growth of organic molecules (Section 1.4.2, Chapter 1) [110]. The data points denoted by 1 and 2 correspond to Figure 3.5a and b, respectively. Strikingly, as opposed to previous studies where complete nucleation control ($x_{NCE} = 1$) [110] was possible only for $p^* \leq 1$, on moiré patterns $x_{NCE} \approx 1$ until $p^* = 6$ and beyond which it decreases. Further, the lateral drift of the colloids to the regions of high activation energy on the moiré templates resulted in a faster crystal growth. While it took $t \sim 10^4$ s to reach n_c on the linear grating patterns (solid black circles in Figure 3.6), nucleation was almost three times faster on Moiré templates with $L_p \sim 16\sigma$ that too with $x_{NCE} = 0.98 \pm 0.02$ (open blue circles in Figure 3.6) and twice as fast for $L_p \sim 42\sigma$ with $x_{NCE} = 0.99 \pm 0.01$ (open red triangles in Figure 3.6).

3.2.3 Nucleation Kinetics and Island Growth on Square Moiré Templates

The above findings clearly exemplify the efficacy of our approach in achieving site-specific nucleation for colloidal particles over a range of L_p values. In order to shed light on the nucleation kinetics, we mimicked atomic heteroepitaxy experiments [129, 124, 340] and measured n_c as a function of c_p, at constant F, on square moiré patterns with $L_p = 16\sigma$. Here, c_p plays the role of an inverse temperature. At the largest c_ps studied ($c_p \geq 0.27$ mg/ml), particles were unable to overcome the energy barriers for surface diffusion *even* in the low E_a regions and the moiré template thus acts like a homogeneous surface. On such surfaces, for small D, atomic and colloid experiments

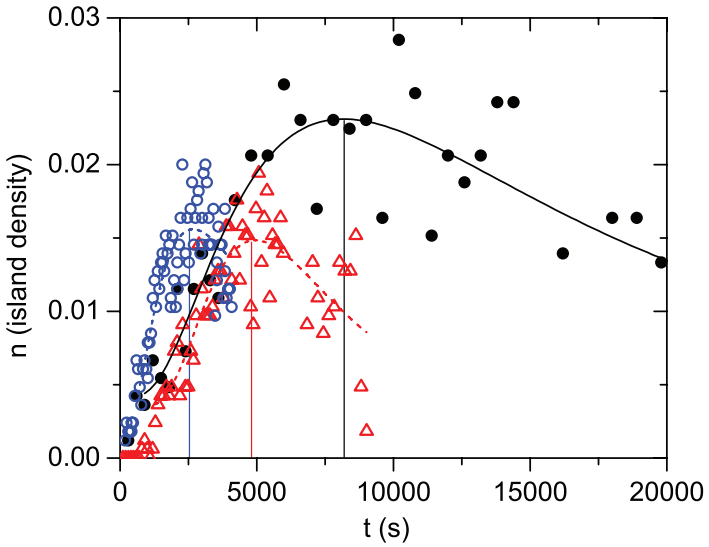

Figure 3.6 Faster nucleation and growth on moiré templates. Temporal evolution of n for linear moiré templates; $\theta \sim 8°, L_p \sim 16\sigma$ (hollow blue circles), $\theta \sim 2°, L_p \sim 42\sigma$ (hollow red triangles) and linear grid template (solid black circles) for similar D/F values. The lines are log-normal fits to the data. The vertical lines shows the time at which $n = n_c$.

follow rate equation predictions and find that n_c depends only on Θ and saturates to a constant, $n_c \approx 0.03$ for $i = 1$ [101, 129]. This was indeed found to hold in our experiments as well (triangles in Figure 3.7a). For $0.2 < c_p < 0.27$ mg/ml, although particles diffuse, their mean free path remains smaller than L_p and nucleation events continue to occur at random locations (panel labeled 3 in Figure 3.7a). Akin to the behaviour on a homogeneous surface n_c versus c_p exhibits an Arrhenius-like dependence. We found a second plateau in n_c for c_p lying between $0.1 - 0.2$ mg/ml (green squares and red circle in Figure 3.7a). In this regime, particles perceive the heterogeneous nature of the surface energy landscape and thus their diffusivities are preferentially smaller at trap sites, which subsequently resulted in site-specific nucleation (panel 2 in Figure 3.7a). Finally, for the lowest c_ps studied ($c_p \leq 0.1$ mg/ml), particles are oblivious to the underlying surface topography and n_c decreases owing to an increase in the critical cluster size ($i \geq 4$) (panel marked 1 in Figure 3.7a).

Although the overall shape of the nucleation curve (red line in Figure 3.7a) for colloids is strikingly similar to that seen for atoms [129, 124], there are fundamental differences. The black line in the schematic in Figure 3.7b shows n_c versus D/F, or the scaled $1/T$, for homogeneous surface growth. When dimers are stable and also immobile, rate equation predicts and experiments find that $L \propto (\frac{D}{F})^{1/6}$ for $D/F > 10^4$ [101].

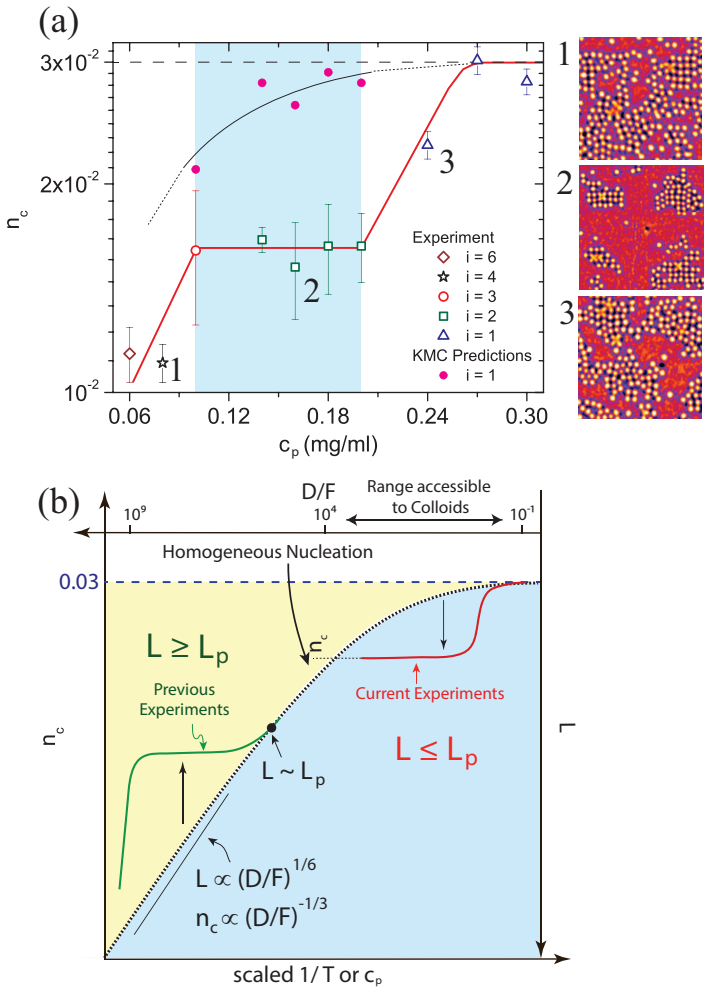

Figure 3.7 Nucleation and island growth on square moiré patterns. (a) n_c versus c_p at fixed F. The legends in (a) represent the size of the critical cluster. The red line is a guide to the eye. The blue shaded region corresponds to the regime of organized growth. The magenta circles within the blue shaded region represent the expected n_c from homogeneous nucleation, for D/Fs in the plateau region (Adopted from [101]). (b) Schematic of nucleation curves for homogeneous nucleation (black curve) and heterogeneous nucleation with and without energy gradients shown by red and green curves, respectively. Mean-field scaling predictions for L and n_c for $D/F > 10^4$ is also shown.

However, for $D/F \leq 10^4$, the regime accessible in colloid experiments, L saturates with decreasing D/F [17, 101]. For site-specific nucleation studies, which are typically performed at a fixed F, a plateau in n_c begins when $L \sim L_p$ (black solid circle in Figure 3.7b) and continues until particles fail to feel the underlying substrate. More importantly, the plateau is restricted only to the yellow shaded region, corresponding to $L \geq L_p$, of Figure 3.7b. On moiré templates, however, the enhancement in particle mean free path due to surface energy gradients, corresponds to a larger effective D/F and the plateau in n_c should therefore lie below the homogeneous nucleation curve (blue shaded region of Figure 3.7b). Figure 3.7a also shows the n_c expected for homogeneous nucleation (magenta circles in Figure 3.7a) for D/F values corresponding to the plateau region in the nucleation curve (blue shaded region in Figure 3.7a) [101]. The spatially averaged D on square moiré templates has been used while estimating D/F (Section 2.4, Chapter 2). In line with expectations, n_c on moiré template lies below the homogeneous nucleation curve (Figure 3.7a).

In the plateau regime of n_c, since crystalline islands are periodically spaced and have nearly identical monomer capture rates the island size distribution is expected to be narrower than on a homogeneous surface [101, 129]. We measured the island

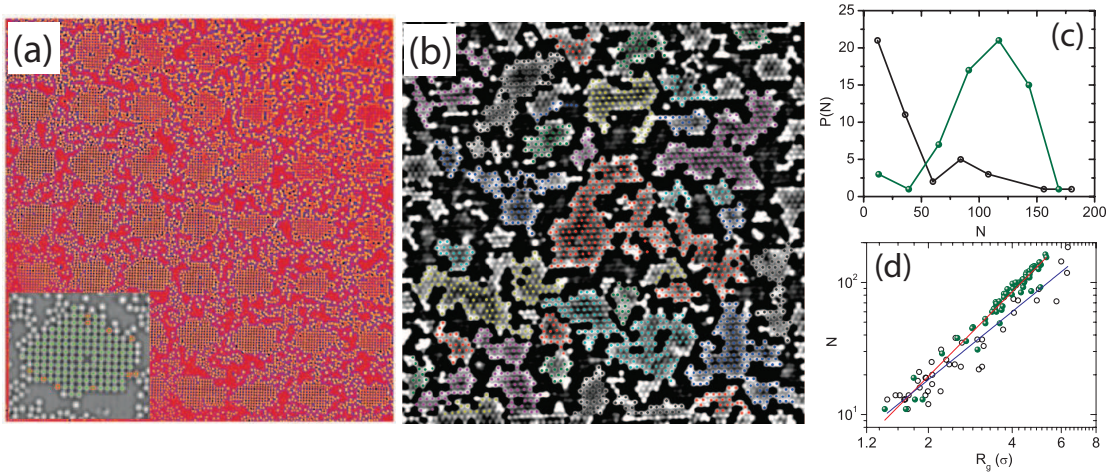

Figure 3.8 Representative snapshot of island growth on (a) square moiré patterns with $L_p = 32\sigma$ and (b) colloidal homoepitaxy. For both the snapshots $\Theta \sim 0.50$. (The snapshot in (b) is adopted from Ganapathy *et. al.* [17]). The underlying template in (b) has a hexagonal crystalline symmetry. The crystalline particles are clustered based on nearest-neighbor algorithm. Particles in distinct clusters have different colors. The inset in (a) shows particles clustered based on their bond-order parameter. Green represents particles with $\Psi_4 > 0.7$ and red represents particles with $\Psi_6 > 0.7$. (c) and (d) Island size distributions and fractal dimensions corresponding to (a)−green circles and (b)−black circles, respectively.

size distribution on square moiré patterns with $L_p = 32\sigma$ by clustering particles based on their local bond-order parameter (Figure 3.8a and inset) and compared it with homogeneous surface growth experiments for the same Θ (Figure 3.8b) [17]. To achieve this, we first identified the crystalline particles based on the hexagonal and square bond-order parameters - ψ_6 and ψ_4, respectively

$$\psi_6(j) = \frac{1}{N}\sum_k e^{6i\theta_{jk}} \tag{3.3}$$

$$\psi_4(j) = \frac{1}{N}\sum_k e^{4i\theta_{jk}}. \tag{3.4}$$

Here, j is the particle index, N is the number of nearest-neighbors, and θ_{jk} represents the bond angle between j^{th} and k^{th} particles with respect to a reference axis. Two particles were termed as nearest-neighbour, if the distance between their centres is less than 1.4σ. Subsequently, the crystalline particles ($\psi_6 \geq 0.7$ and/or $\psi_4 \geq 0.7$) were clustered based on the above cut-off. For the analysis of the size distribution and morphology of the crystallites, clusters sizes $s \geq 10$ have only been used. While we found a broad range of island sizes on homogeneous surfaces (black circles in Figure 3.8c) [17], on moiré templates the distribution was peaked with a maximum that roughly coincided with the trap size (green circles in Figure 3.8c). Further, at the same $\Theta \sim 50\%$, we found islands on moiré templates to be more compact with a fractal dimension $d_f \sim 2$ while on the homogeneous surface we found $d_f \sim 1.7$ in agreement with theoretical predicitions (green and black circles in Figure 3.8d, respectively) [146].

With continued particle deposition, crystals with hexagonal order nucleated and grew outside the traps and subsequent layers were found to be in registry with the underlying symmetry. We found this to be true even on templates with complex moiré periodicities. Figure 3.9a shows a representative image of the third layer of crystals grown on a template that was fabricated by making multiple imprints at different θs. The symmetry and the width of the crystals reflect the underlying substrate periodicity with a motif: $8\sigma\square \rightarrow 8\sigma\hexagon \rightarrow 8\sigma\square \rightarrow 4\sigma\hexagon$. Moreover, by tuning F, c_p and groove depth, a desired crystal growth can be achieved. For instance, at relatively higher D and F, the crystallites predominantly grew as pyramidal structures (Figure 3.9b). This is consistent with recent work of Ganapathy *et. al.* that showed the existence of step-edge barrier even for system interacting via short-range attractive interactions [17].

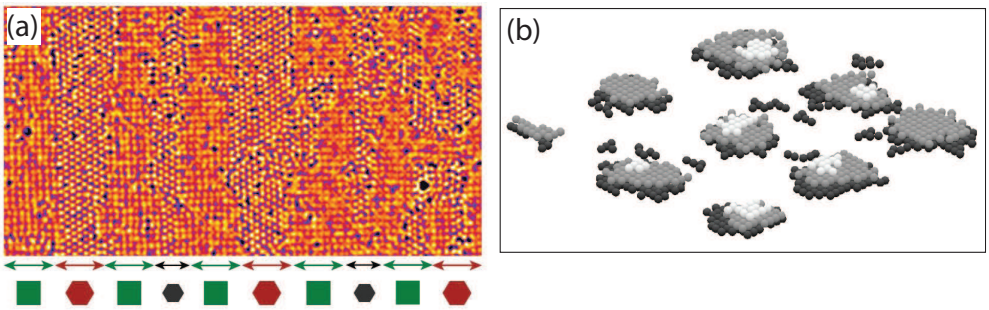

Figure 3.9 Snapshots of crystal growth at large coverages. (a) $D = 0.03\sigma^2/\text{s}$, $F = 10^{-4}\text{ML/s}$, and $\Theta \sim 0.97$. (b) $D = 0.14\sigma^2/\text{s}$, $F \sim 5\text{X}10^{-5}\text{ML/s}$. The particle coordinates in (b) with $\psi_{4,6} > 0.7$ and island size $s > 3$ have been rendered in Matlab. Three layers of controlled colloidal crystallite growth have been shown with gray shade decreasing with increasing number of layers. Particles in a layer have same gray shade.

3.2.4 Diffusion of Complex Colloids on Hexagonal Templates

As a marked improvement over the external field-based techniques that are particle specific, the approach established in this chapter pave way for fabricating non-trivial architectures composed of complex colloids such as colloidal dimers, trimers as well. More importantly, analogous to atomic systems, complex colloids may provide an addition handle to tune the morphologies of colloidal thin films [123], a crucial prerequisite in the device fabrication. Motivated by these, we have synthesized complex colloidal clusters (Figure 3.10a and b; Section 2.3.3, Chapter 2) and studied their diffusion kinetics on hexagonal templates (Figure 3.10c). Owing to the orientational degrees of freedom, complex colloids were observed to undergo interesting in- and out-of-plane rotation. Based on our preliminary observations, we believe that probing the nucleation and growth kinetics of complex colloidal clusters on templates with and without surface energy gradients would a worthwhile endeavour. However, in order to investigate and explore the self-assembly of complex colloids on patterned surfaces, we first need to figure out new synthesis protocols with better yields.

3.3 Conclusions

Collectively, non-trivial substrate topographies, realized via a relatively simple approach, in the presence of short-range depletion interactions transported particles to desired locations and helped achieve site-specific nucleation with high fidelity *even* for micron-sized colloidal particles. Depletion interactions being sensitive only to the local geometry

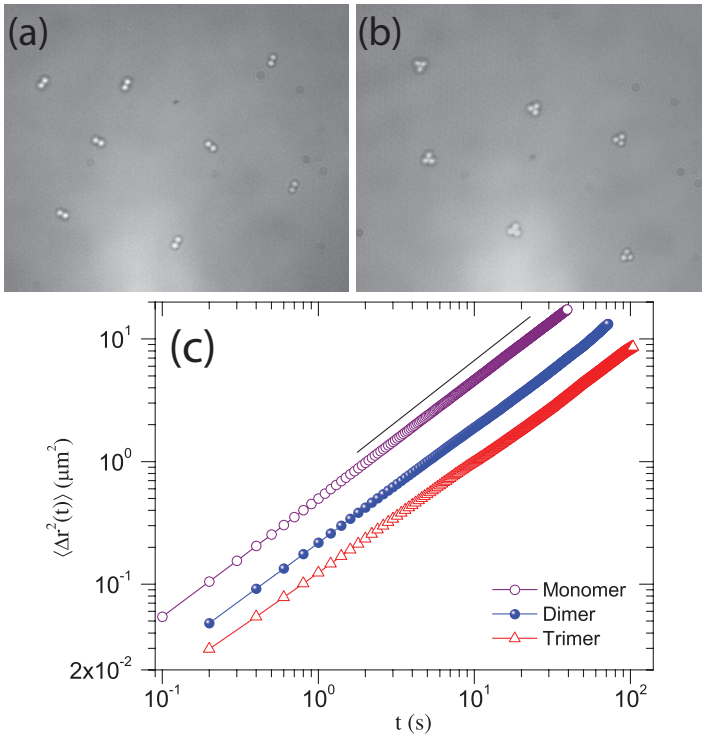

Figure 3.10 Snapshots of colloidal (a) dimer and (b) trimer diffusion on a hexagonal substrate. (c) Mean squared displacements $\langle \Delta r^2(t) \rangle$ for monomers, dimers and trimers.

[34, 43, 45], a feature already exploited here, we believe our approach offers unparalleled opportunities in directing the self-assembly of complex colloids regardless of their surface chemistry and composition [32, 144, 341]. The idea outlined here, however, is far more generic. By suitable manipulation of energy barriers for surface diffusion, control over nucleation density can be exercised over a substantially broader range of D and F values. It is, well-known that in atomic heteroepitaxy strain fields around misfit dislocations lead to directional adatom currents [103, 106]. It is tempting to speculate if this can be exploited to guide growth for small D/F values. In the context of nanoparticles, techniques for creating binding energy gradients by controlling the density of ligands on the surface already exists [342]. In light of our findings, we believe this approach should now be exploited in guiding the self-assembly of nanoparticles as well.

Chapter 4

Reentrant Glass Transition in Suspensions of Colloidal Ellipsoids

4.1 Introduction

The microscopic underpinnings of glasses and the glass transition continue to remain one of the grand challenges in condensed matter physics [149, 150]. There have been significant advances in our understanding of the glassy state and the approach to this state using model systems of colloids with isotropic shape and/or interactions [19, 20, 60, 66, 200, 225]. Although particle shape strongly influences their packing [156], it is only recently that experiments have probed its role in glass transition phenomena [235, 343]. In particular, quasi-2-dimensional (2D) experiments on prolate colloidal ellipsoids of intermediate aspect ratio $\alpha = 6$ and with purely repulsive interactions show two glass transitions [235]. The first corresponds to the orientational freezing of particle dynamics and the second to their translational freezing and are in qualitative agreement with experiments on liquid crystals [234], molecular mode coupling theory (MMCT) predictions and computer simulations [196, 197]. Nevertheless, even in 2D, experiments are yet to confirm that ellipsoids with $\alpha < 2.5$ show a single glass transition as predicted by MMCT [203]. Apart from the rich phase behavior resulting from particle shape anisotropy, recent colloid experiments have shown that interaction anisotropy can result in novel phases [45, 72]. Interaction anisotropy is likely to have wider relevance in the dynamics of gels and glasses also [155, 343]. It is well-established that even with isotropic short-range attraction, hard spheres show rich reentrant glass phenomena [66, 195, 200, 225, 226, 344–347]. At a fixed volume fraction greater than the repulsive glass transition volume fraction, a repulsive glass (RG) melts to an

ergodic fluid and forms a novel glass - attractive glass (AG) - at even higher interaction strengths [66, 195, 200, 225, 226, 344–347]. However, the consequences of interaction anisotropy for reentrant glass behaviour are yet to be explored by theory, simulations and experiments. Thus, this chapter presents a study on colloidal ellipsoids of $\alpha = 2.1$ in quasi-two-dimensions (2D) with an aim to explore the reentrant glass transition phenomena.

4.2 Experimental Details

Colloidal ellipsoids of aspect ratio $\alpha = 2.1$ were synthesized using well-established protocols (Section 2.3.4, Chapter 2). The major and minor axes were $2l = 2.1\mu$m and $2w = 1.0\mu$m with polydispersities of 11% and 8%, respectively. We used sodium carboxyl methyl cellulose (NaCMC) as the depletant. Suspensions of ellipsoids in water, at suitable depletant concentration c_p, below the overlap concentration $c^* = 0.11$ mg/ml, were loaded into wedge-shaped cells and left standing under gravity to allow sedimentation to the 2D regions of the cell (Section 2.5, Chapter 2). For each c_p, experiments were done for at least six area fractions ϕs ranging from $0.23 \leq \phi \leq 0.84$. Video microscopy was done using a 100X oil immersion objective (Leica, Plan-Apochromat, numerical aperture 1.4) at a frame rate of 5 frames per second for a typical duration of 20 minutes. The center-of-mass coordinates and the orientations of the ellipsoids were obtained using ImageJ and the data were analyzed using standard Matlab algorithms [331]. The spatial resolution was found to be 60 nm and the angular resolution was 1°. We begin our discussions with colloidal ellipsoids with purely repulsive interactions.

4.3 Results and Discussions

4.3.1 Ellipsoids with Purely Repulsive Interactions

Unlike observations on ellipsoids with $\alpha = 6$ [235], in our experiments, even after months, we did not observe the formation of pseudonematic domains even at the highest area fraction $\phi = 0.84$ studied (Figure 4.1). The dynamics at various ϕs were quantified using translational and n^{th} order orientational correlation functions $F_s(\mathbf{q}, t)$

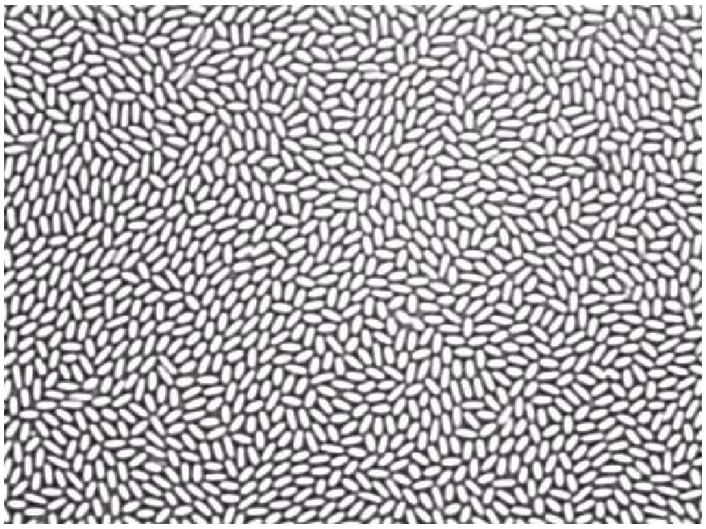

Figure 4.1 Representative image of colloidal ellipsoids at $\phi = 0.84$.

and $L_n(t)$, respectively.

$$F_s(\mathbf{q},t) = \frac{1}{N}\Big\langle \sum_{j=1}^{N} \exp\Big(i\mathbf{q}\cdot(\mathbf{r}_j(t+t_0) - \mathbf{r}_j(t))\Big)\Big\rangle. \tag{4.1}$$

$$L_n(t) = \frac{1}{N}\Big\langle \sum_{j=1}^{N} \cos\Big(n(\theta_j(t+t_0) - \theta_j(t))\Big)\Big\rangle. \tag{4.2}$$

Here, N is the total number of particles, $r_j(t)$ and $\theta_j(t)$ are the position and orientation of the j^{th} ellipsoid at time t, t_0 is the lag time, $\mathbf{q}$ is the wave vector, $n = 1, 2, 3, ...$, and $\langle\rangle$ denotes the time averaging. The magnitude of q is chosen to be the first maximum in radial pair correlation function $g(r)$. The variation of $F_s(q,t)$ and $L_5(t)$ as a function of ϕ are shown in Figure 4.2 and Figure 4.3, respectively. Although at low ϕ, $F_s(\mathbf{q},t)$ and $L_n(t)$ decay exponentially, at high ϕ, both show a two-step relaxation that is typical of glass-forming liquids [151, 190]. While the first decay corresponds to rattling of particles inside the cages formed by the neighbouring particles, the second corresponds to its subsequent escape from the cage. The first relaxation is termed as $\beta-$relaxation and the second one as $\alpha-$relaxation. The onset of caging was evidenced by non-exponential relaxation in $F_s(q,t)$ and $L_n(t)$ for $\phi = 0.73$ (Figure 4.2 and Figure 4.3). While at $\phi = 0.79$, $F_s(q,t)$ decayed completely and $L_n(t)$ by $\approx 25\%$ over 700 s, for $\phi = 0.84$, $F_s(q,t)$ decayed by only about 20% and $L_n(t)$ by 7% over 4000 s (Figure 4.2 and Figure 4.3). This suggests an ergodic-nonergodic transition with

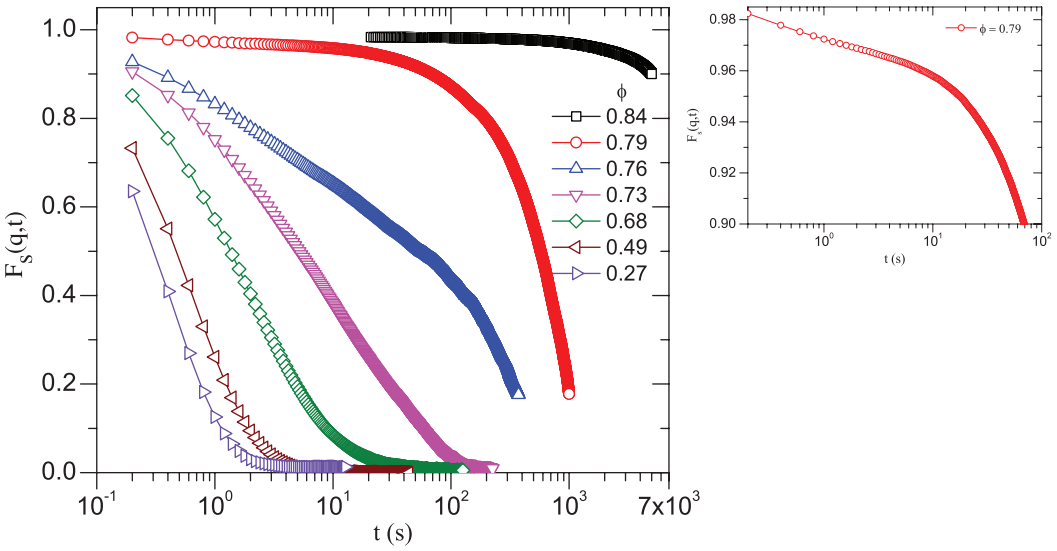

Figure 4.2 Self intermediate scattering function $F_s(q = 5.6\mu\text{m}^{-1}, t)$ with time t for various ϕs. Inset on right is shown with expanded y-axis to show two-step relaxation at $\phi = 0.79$.

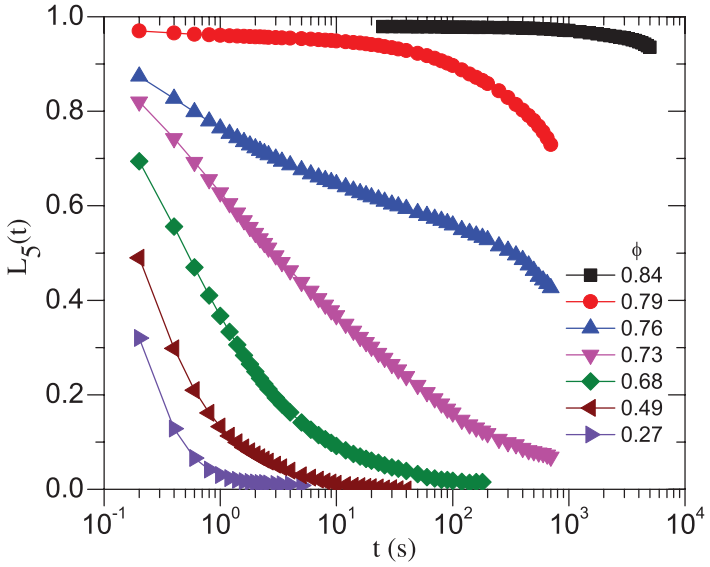

Figure 4.3 Dynamic orientational correlation function $L_5(t)$ with time t for various ϕs.

$0.79 < {\phi_g}^{R,T} < 0.84$ [66, 225]. Here, ${\phi_g}^{R}$ and ${\phi_g}^{T}$ are orientational and translational glass transition area fraction, respectively.

We estimated the glass transitions for both the DOFs using MCT scaling analysis [151, 190, 194, 235] described in Section 1.5.1 of Chapter 1. As per MCT, as ϕ_g is approached, structural relaxation time τ_α diverges as

$$\tau_\alpha(\phi) \propto (\phi_g - \phi)^{-\gamma} \tag{4.3}$$

where $\gamma = \frac{1}{2a} + \frac{1}{2b}$. Here, a and b are exponents in the critical decay law and the von-Schweilder law, respectively [151, 190, 194, 197, 235]. In cases where $F_s(q,t)$ and $L_n(t)$ showed complete decay, τ_α was taken to be time where correlation decayed to $1/e$ [194, 197]. While for correlation functions that showed only a partial decay ($\sim 70\%$), τ_α was estimated by fitting a stretched exponential to the long time decay of $F_s(q,t)$ and $L_n(t)$ [235]. Further, it is worth mentioning that the two procedures to estimate τ_α yielded the same value. In our experiments, we obtained b from power-law fits to the crossover regime from late β to early $\alpha-$relaxation in $F_s(q,t)$ and $L_n(t)$. Owing to a poor temporal resolution in the early $\beta-$relaxation regime, we obtained a using the relation [151], $\frac{\Gamma(1-a)^2}{\Gamma(1-2a)} = \frac{\Gamma(1+b)^2}{\Gamma(1+2b)}$. Consistent with MCT predictions, we found that ${\tau_\alpha}^{-1/\gamma}$ was linear in ϕ (Figure 4.4) for all qs and ns studied. Strikingly, this scaling yielded the same $\phi_g = 0.80 \pm 0.01$ for both translational and orientational DOF (Figure 4.4).

To show that ϕ_g was indeed at 0.80 ± 0.01, we have quantified the size distribution and scaling of the most-mobile particle clusters. These clusters, believed to be pathways for structural relaxation in supercooled liquids and glasses [172], show qualitative trends with ϕ across ϕ_g [19, 235]. To quantify dynamical heterogeneities, we first obtained the translational and rotational mean squared displacements (MSD) of the particles.

$$\langle \Delta r^2 \rangle = \frac{1}{N} \Big\langle \sum_{j=1}^{N} \Big((x_j(t+t_0) - x_j(t))^2 + (y_j(t+t_0) - y_j(t))^2 \Big) \Big\rangle. \tag{4.4}$$

$$\langle \Delta \theta^2(t) \rangle = \frac{1}{N} \Big\langle \sum_{j=1}^{N} \Big((\theta_j(t+t_0) - \theta_j(t))^2 \Big) \Big\rangle. \tag{4.5}$$

Here N is total number of particles, $x_j(t)$ and $y_j(t)$ are the coordinates and θ_j is the orientation of j^{th} ellipsoid, t_0 is the lag time and Δr is the displacement of the particles over time t. The particle dynamics were diffusive at lower ϕs (Figure 4.5 and Figure 4.6). For $\phi \geq 0.73$ and at short times, the dynamics was sub-diffusive which signifies

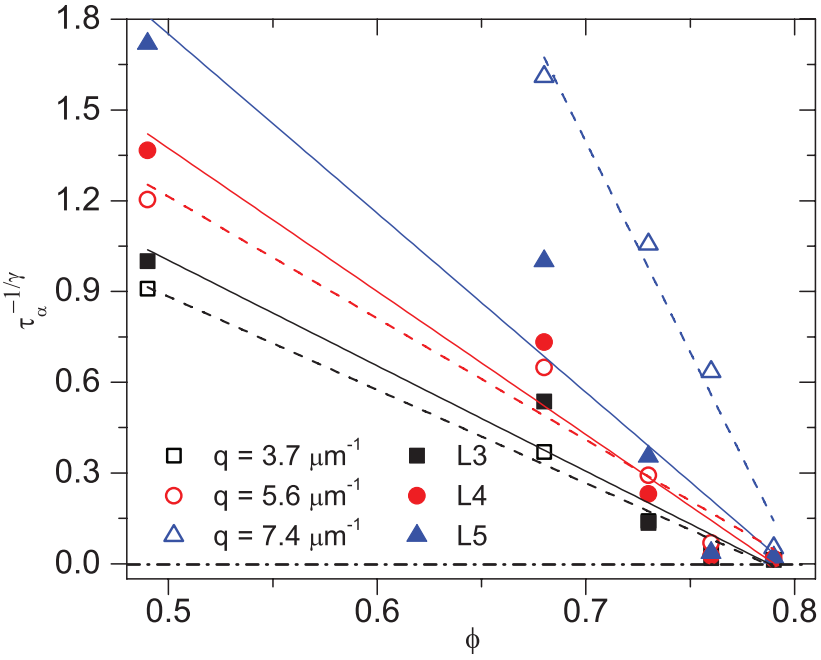

Figure 4.4 $\tau_\alpha{}^{-1/\gamma}$ versus ϕ. Here, $\gamma^T = 1.93$ and $\gamma^R = 2.24$. Dashed and solid lines are power law fits to the translational and orientational data, respectively.

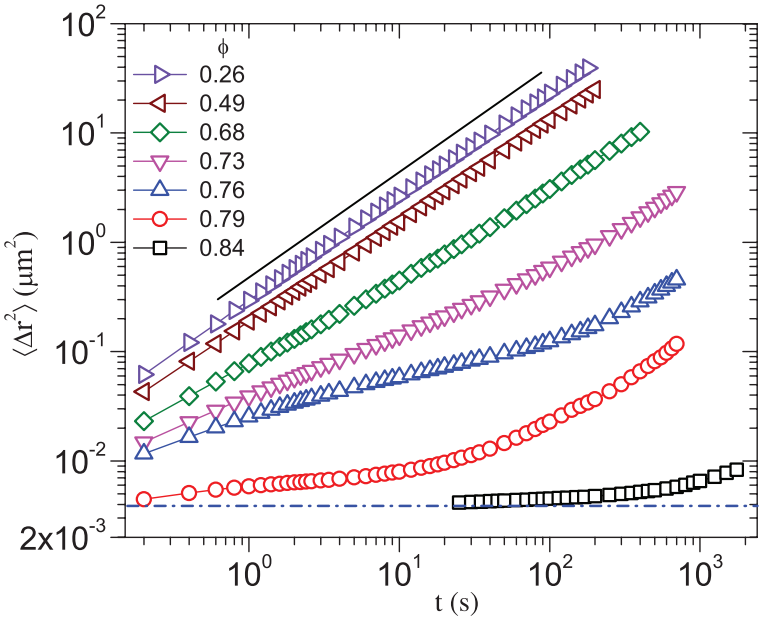

Figure 4.5 $\langle \Delta r^2(t) \rangle$ at various ϕ. The solid and dashed lines represent slope 1 and the minimum tracking resolution in our experiments, respectively.

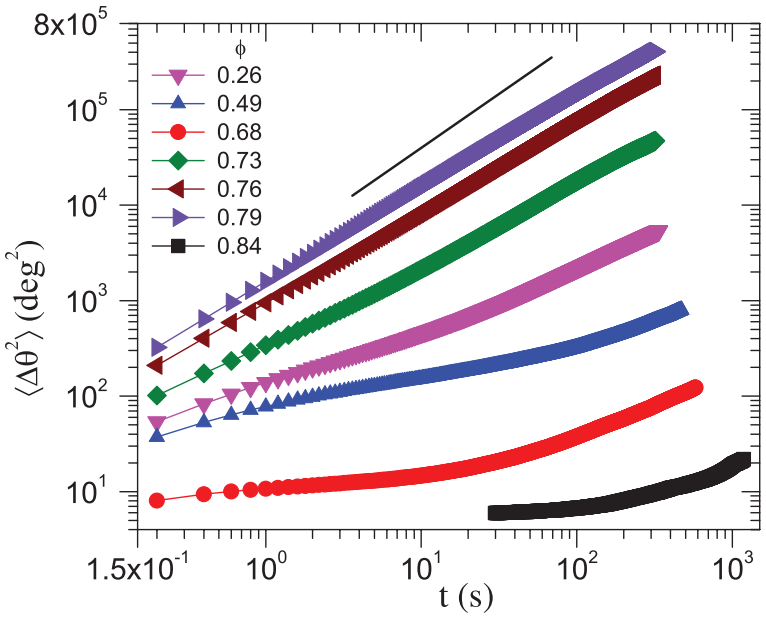

Figure 4.6 $\langle \Delta\theta^2(t) \rangle$ versus t for various ϕs. The solid line represents slope 1.

particle caging. At a characteristic relaxation time t^*, $\langle \Delta r^2(t) \rangle$ showed an upturn which reflects the escape of particles from their respective cages (Figure 4.5 and Figure 4.6) and the long time dynamics after t^* approaches the diffusive limit.

For both $\langle \Delta r^2(t) \rangle$ and $\langle \Delta\theta^2(t) \rangle$, at t^*, the dynamics is highly non-Gaussian and this was quantified using the non-Gaussian parameter, $\alpha_2(t)$ [19], which is defined as,

$$\alpha_2^T(t) = \frac{\langle \Delta r(t)^4 \rangle}{2\langle \Delta r(t)^2 \rangle} - 1 \tag{4.6}$$

$$\alpha_2^R(t) = \frac{\langle \Delta\theta(t)^4 \rangle}{3\langle \Delta\theta(t)^2 \rangle} - 1 \tag{4.7}$$

where $\Delta r(t)$ and $\Delta\theta(t)$ are the particle displacements and change in orientations over time t, respectively. Since for any Gaussian process all the higher order (even) moments can be expressed in terms of second moment [348] i.e. $\Delta r^2(t)$ or $\Delta\theta^2(t)$, $\alpha_2^{T,R}(t) = 0$ for diffusive dynamics. However, for supercooled liquids, $\alpha_2^{T,R}(t)$ shows a maximum in the vicinity of t^* due to cage rearrangements (Figure 4.7) [19]. Both t^* and the peak amplitude $\alpha_2(t^*)$ increases as the glass transition is approached (Figure 4.7). In the vicinity of ϕ_g and beyond, the particle dynamics slow down as evident from the plot of probability distribution of displacements of particles, $P(\Delta(r))$ over t^* (Figure 4.8). Thus, for ϕs close to but less than ϕ_g, the absence of large cooperative cage rearrangements led to a decrease in t^* [19, 235] and was consistent

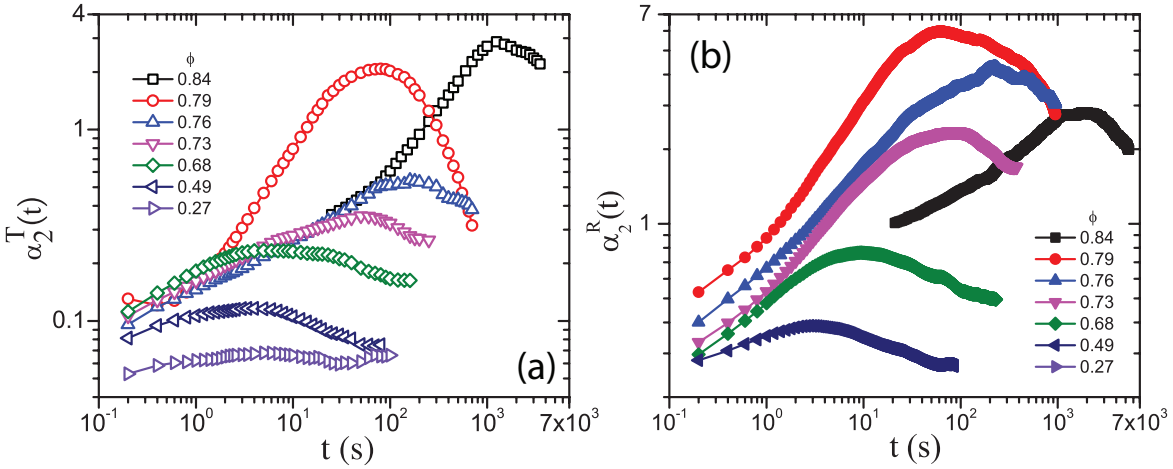

Figure 4.7 Non-Gaussian parameter (a) $\alpha_2^T(t)$ and (b) $\alpha_2^R(t)$ versus t for various ϕs.

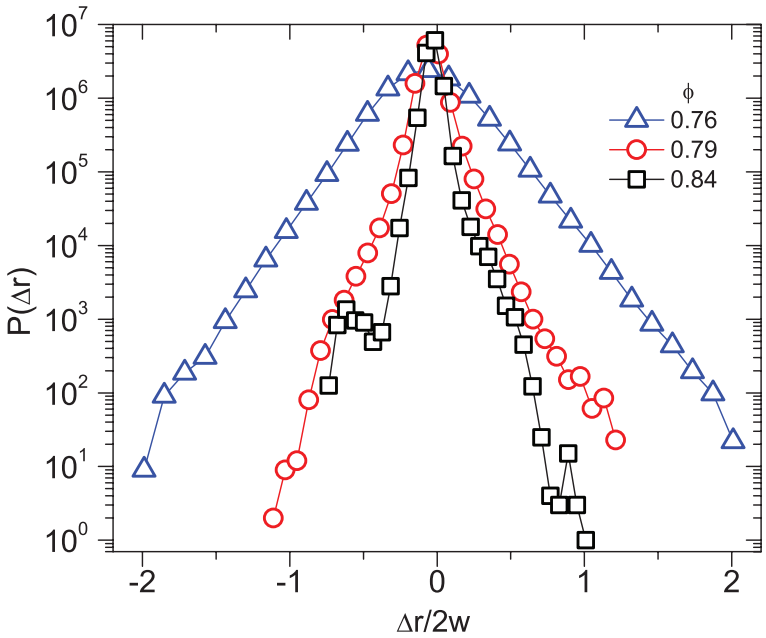

Figure 4.8 $P(\Delta r(t^*))$ versus Δr at three ϕs in the vicinity of ϕ_g. Here t^* corresponds to the cage breaking time.

with our observations of ${t^*}_{\phi=0.79} < {t^*}_{\phi=0.76}$. However, beyond ϕ_g, the absence of large cooperative cage rearrangements should result in decrease in both t^* and $\alpha_2(t^*)$ [19]. Unlike at low ϕs, t^* in the vicinity of ϕ_g and beyond is thought to represent the β-relaxation time [19]. Since $\alpha_2(t)$ is fairly sensitive to noise, the increase in t^* at $\phi = 0.84$, in our case, was probably due to particle tracking errors from negligible particle displacement that were comparable to the spatial resolution in our experiments [349]. It is important to note that the coupling between rotational and translational DOF can lead to non-gaussian effects in the lab frame for ellipsoids even in the dilute limit [350]. We have verified that all trends reported here were preserved in the body frame of ellipsoids also, where this coupling is absent. The particle dynamics were heterogeneous over t^* as shown in Figure 4.9. The top 10% most-mobile particles over t^* were found to be spatially clustered (Figure 4.9). Two most-mobile particles

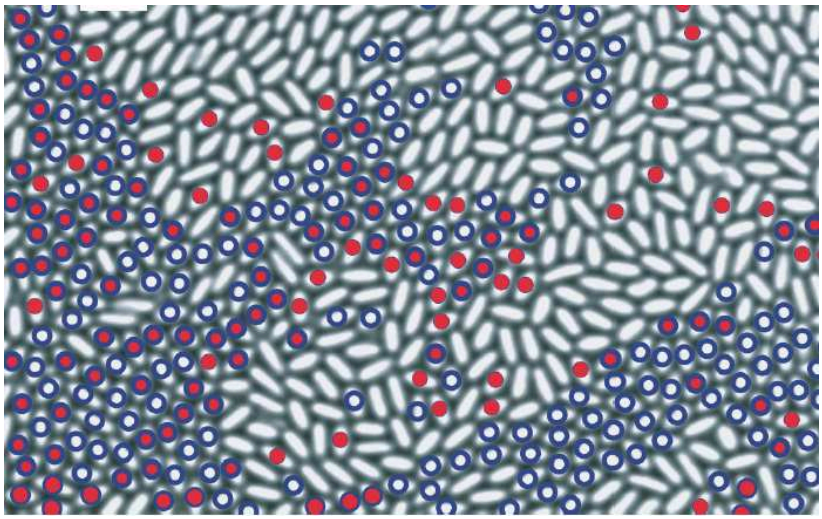

Figure 4.9 Top 10% translationally most-mobile (open blue circles) and orientationally most-mobile (solid red circles) particles at $\phi = 0.79$.

belong to the same cluster if one ellipsoid when expanded 1.4 times, maintaining its orientation, encompasses the other's centre, subject to the condition that there is no immobile ellipsoid between them. We found that a significant fraction of orientationally most-mobile particles were also translationally most-mobile and was consistent with the absence of pseudo-nematic domains (Figure 4.9).

To quantify these clusters at a given ϕ, we have used average cluster size $\langle N_c \rangle$, $\langle {N_c}^{T,R} \rangle = \frac{\sum_n n^2 P(n)}{\sum_n nP(n)}$ [221], where $P(n)$ is the cluster size distribution. Analogous to observations in supercooled liquids of colloidal spheres [19], $\langle {N_c}^{T,R} \rangle$ increased as ϕ_g is approached and shows a sudden decrease beyond ϕ_g for both translational and

orientational DOF (Figure 4.10a). These observations confirmed that $0.79 < {\phi_g}^T, {\phi_g}^R <$

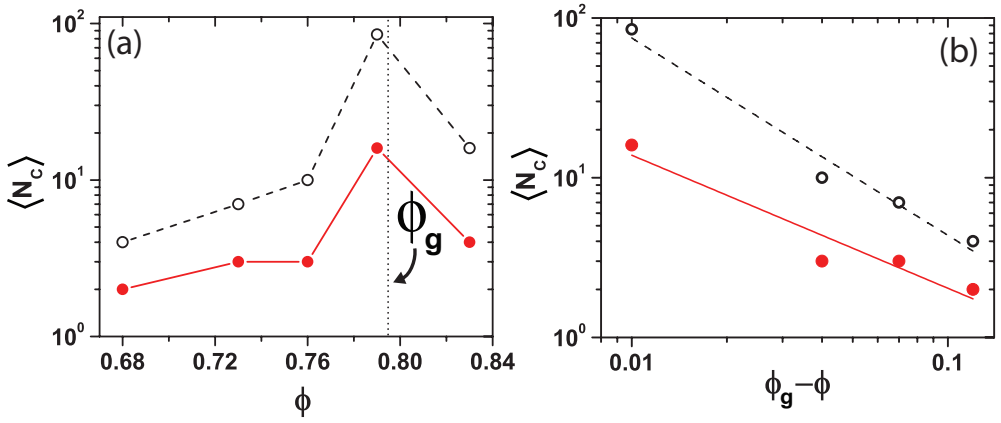

Figure 4.10 (a) The variation of average cluster size, $\langle N_c \rangle$ with ϕ. The vertical dashed line represents the glass transition area fraction ϕ_g. (b) Divergence of average cluster size: $\langle N_c \rangle$ versus $(\phi_g - \phi)$.

0.84 and was consistent with $\phi_g = 0.80 \pm 0.01$ estimated from MCT scaling analysis. Further, $\langle {N_c}^{T,R} \rangle$ diverged as a power law as ϕ_g is approached (Figure 4.10b).

$$\langle {N_c}^{T,R} \rangle \propto (\phi_g - \phi)^{-\eta}, \tag{4.8}$$

where η is scaling exponent. Though the physical origin of such a scaling is not clear, similar behaviour has also been observed for supercooled liquids of colloidal ellipsoids of $\alpha = 6$ [235] and binary Lennard-Jones glass forming liquids [351]. This further validates our observation of single ϕ_g for both translational and orientational DOF at $\phi = 0.80 \pm 0.01$.

Moreover, using Vogel-Fulcher-Tammann (VFT) equation [349, 352, 353], we have estimated the ideal glass transition area fraction ϕ_0 at which diffusive motion ceases.

$$\tau_\alpha(\phi) = \tau_\infty \exp\left(\frac{A}{(1 - \phi/\phi_0)}.\right) \tag{4.9}$$

Here, A and ϕ_0 are adjustable parameters. To determine ϕ_0, we have plotted the variation of residuals of linear fits as a function of ϕ_0 (inset to Figure 4.11). The minimum in the residuals for a given wave vector q corresponds to the best fit to the VFT equation. The average value of ϕ_0 obtained from two different values of q yields $\phi_0 = 0.89 \pm 0.02$ (Figure 4.11). As seen in previous studies [349, 352], the dynamic cross over area fraction ϕ_g determined from MCT scaling lies between the area fraction that

corresponds to the onset of caging $\phi = 0.73$ and ϕ_0. Though there are no theoretical or computational predictions of ϕ_0 for ellipsoids of $\alpha = 2.1$, the value of ϕ_0 is in the vicinity of the predicted value ($\phi_0 \approx 0.88$) for bi-disperse ellipsoids, $\alpha \sim 2.2$, in 2D [354].

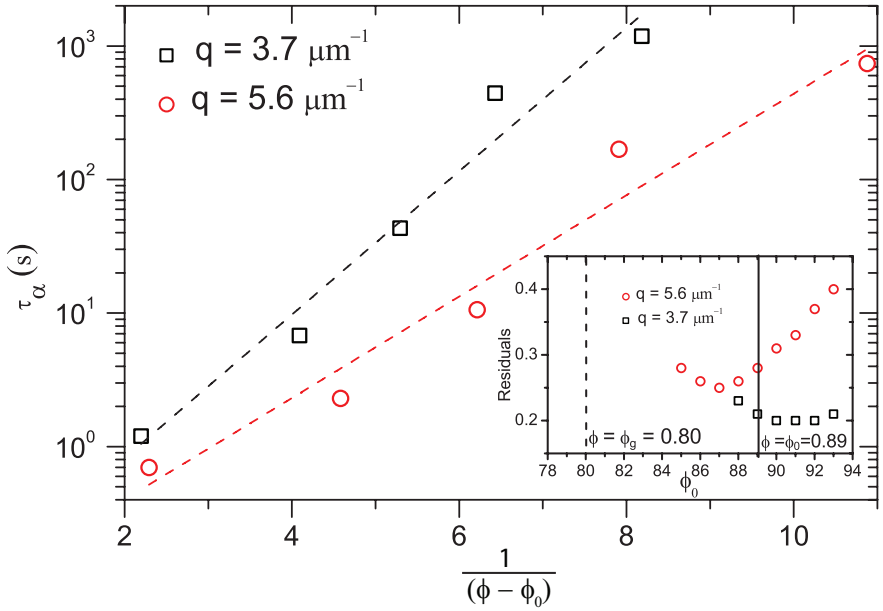

Figure 4.11 The scaling of structural relaxation time, τ_α with $(1 - (\phi/\phi_0))$. The inset shows the residuals of the linear fits as a function of fitting parameter ϕ_0. The dashed vertical line corresponds to ϕ_g for purely repulsive ellipsoids. The solid vertical line represents the average value of ϕ_0.

In summary, in concord with MCT predictions (Section 1.5.3, Chapter 1), liquids of colloidal ellipsoids of $\alpha = 2.1$ showed a single glass transition for both translational and orientational DOF at $\phi_g = 0.80 \pm 0.01$. We now move on to discuss the dynamics in suspensions of colloidal ellipsoids with short-ranged depletion attractions.

4.3.2 Hard Ellipsoids with Depletion Attraction

While depletion induced attractions for spherical particles are isotropic [62], it leads to an anisotropic interaction for ellipsoidal particles (Section 1.2.2, Chapter 1) [236]. Figure 4.12 clearly shows that ellipsoids prefer lateral alignment as compared to tip-to-tip alignment in presence of depletion induced attraction.

First, we focus on change in the dynamics of colloidal ellipsoids as the strength inter-particle pair potential U was varied. In 2D, the relationship between depletion concentration, c_p, and attraction strength U is not well-understood [355]. Therefore,

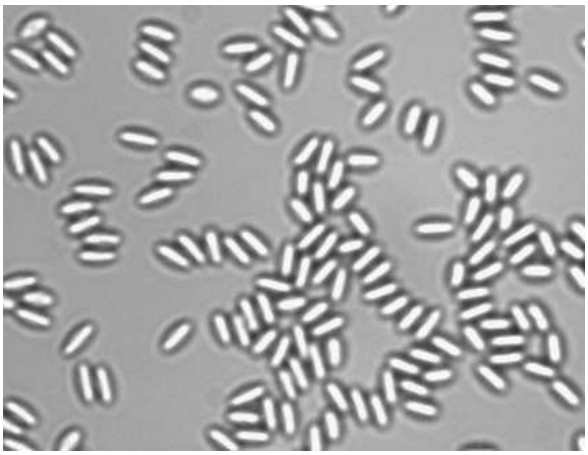

Figure 4.12 Snapshot showing lateral alignment being promoted with introduction of short-ranged depletion attraction.

for all c_ps investigated here, we directly measured the change in depth of the scaled depletion potential $\Delta u = -\frac{\Delta U}{k_B T}$, averaged over all orientations, with respect to $c_p = 0$, from dimer life time measurements [117]. Here, k_B is the Boltzmann constant and T is the temperature. To evaluate the change in the depth of attractive potential, Δu, we measured the monomer diffusion constant, D, and the dimer lifetime, τ, averaged over all orientations, at $\phi \approx 0.25$ for the various c_ps studied. The distributions of τ were observed to be exponential (Figure 4.13b and c) and the decay constant yielded τ_0. However, for $c_p = 10\ \mu\text{gml}^{-1}$, as the values of τ are small (Figure 4.13a), τ_0 was taken to be the peak of the distribution. Following Savage *et. al.* [117], we evaluated Δu using the τ_0 calculated above.

$$\tau_0 \propto D^{-1} \exp\left(\frac{U}{k_B T}\right) \tag{4.10}$$

$$-\frac{\Delta(U_1 - U_2)}{k_B T} = \Delta u = \ln\left(\frac{\tau_0^{(2)} D_2}{\tau_0^{(1)} D_1}\right) \tag{4.11}$$

where 1 and 2 in Eqn.4.11 denote the two systems at different interaction strength. $\tau_0 D$ with c_p showed an exponential dependence (Figure 4.13), although the origin of this is unclear. Since, we could not collect data at $\phi \sim 0.25$ for $c_p = 30\mu\text{g/ml}$, the value of $\tau_0 D$ was obtained from fits to the data shown in Figure 4.13d.

$\langle \Delta r^2(t) \rangle$ and $\langle \Delta\theta^2(t) \rangle$ at different Δu are shown in Figure 4.14 and Figure 4.15, respectively. With the introduction of depletion attractions, the overlap of excluded volume between ellipsoids frees up volume and hence dynamics was observed to

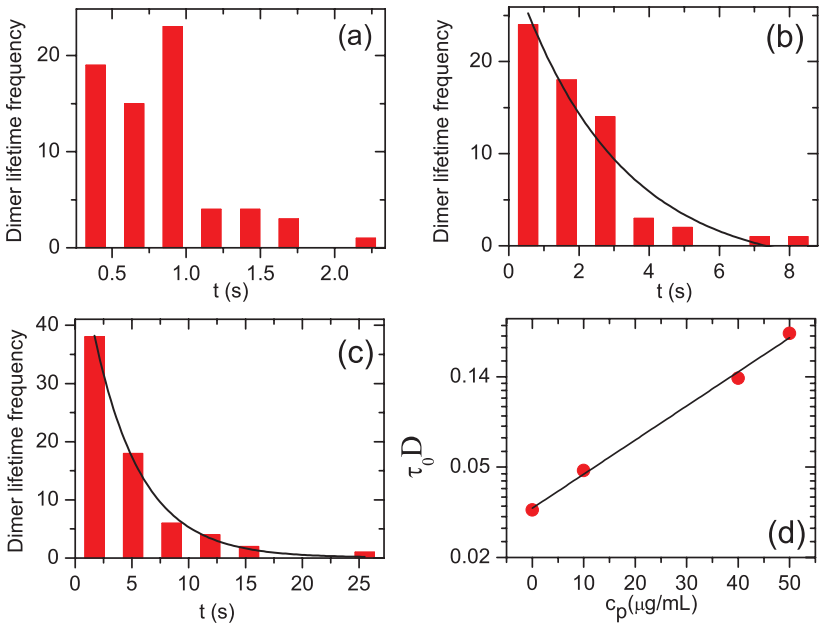

Figure 4.13 Distribution of dimer lifetimes for (a) $c_p = 10\mu$g/ml (b) 40μg/ml (c) 50μg/ml. The solid line in (b) and (c) shows exponential fits to the data. (d) Log-Linear plot of $\tau_0 D$ versus c_p. The solid line is linear fit to the data from which $\tau_0 D$ at $c_p = 30\mu$g ml^{-1} was obtained.

become faster till the intermediate attraction strengths. However, for higher attraction strengths, owing to stronger bonding between ellipsoids, the dynamics of the system slowed down (Figure 4.14 and Figure 4.15).

4.3.3 Reentrant Glass Dynamics in Hard Ellipsoids

In this section, we will discuss the change in translational and orientational dynamics of colloidal ellipsoids as a function of particle interaction potential Δu at a $\phi \sim$ RG $\phi_g = 0.80$. We begin with correlation functions $F_s(q,t)$ and $L_n(t)$. Figure 4.16a and b, show $F_s(q = 5.6\mu\text{m}^{-1}, t)$ and $L_3(t)$ for $\phi \approx 0.79 \approx \phi_g$ for different Δus, respectively. In contrast to low and high attraction strengths ($\Delta u = 0$ and $\Delta u = 1.47$) where $F_s(q,t)$ shows a two-step decay (inset to Figure 4.16a), a logarithmic decay is observed for $\Delta u = 1.16$ (Figure 4.16a). Here, it worth mentioning that MCT predicts such a trend in decay behaviour of correlation functions in the vicinity of A_3 singularity (Section 1.5.2, Chapter 1) [195, 347]. While experiments on copolymer micellar system have shown the logarithmic decay of $F_s(q,t)$ [199], our experiments are the first to probe the dynamics at single particle resolution in the vicinity of A_3 singularity. Moreover, while akin to $F_s(q,t)$, a two-step decay of $L_3(t)$ was observed at low and high attraction

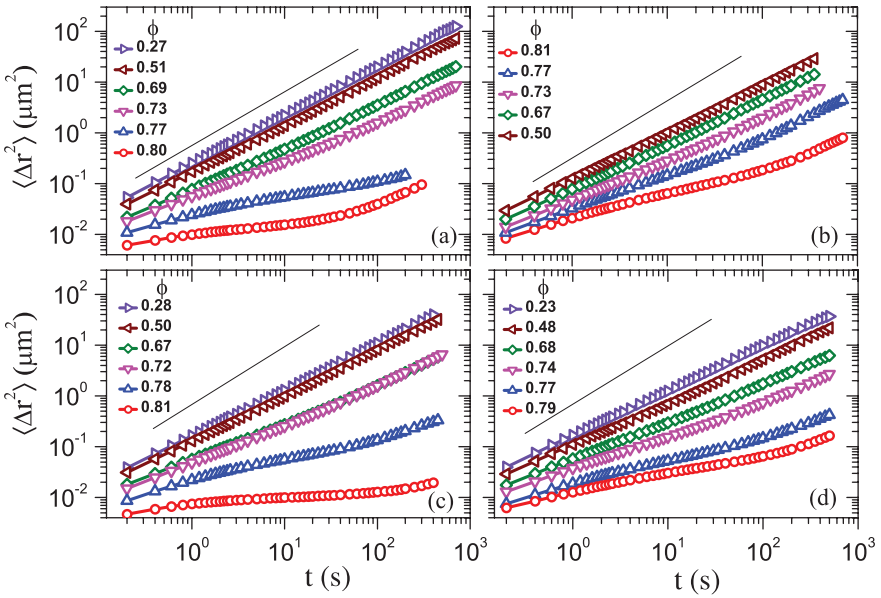

Figure 4.14 $\langle \Delta r^2(t) \rangle$ at different ϕs and for (a) $\Delta u = 0.44$ (b) $\Delta u = 1.16$ (c) $\Delta u = 1.47$ and (d) $\Delta u = 1.95$. $\langle \Delta r^2(t) \rangle$ at $\phi = 0.67$ and $\phi = 0.72$ in (c) were observed to be same. The faster dynamics at $\phi = 0.72$ could be due to thicker cell area in the viewing region.The solid lines in all sub-plots represent slope 1.

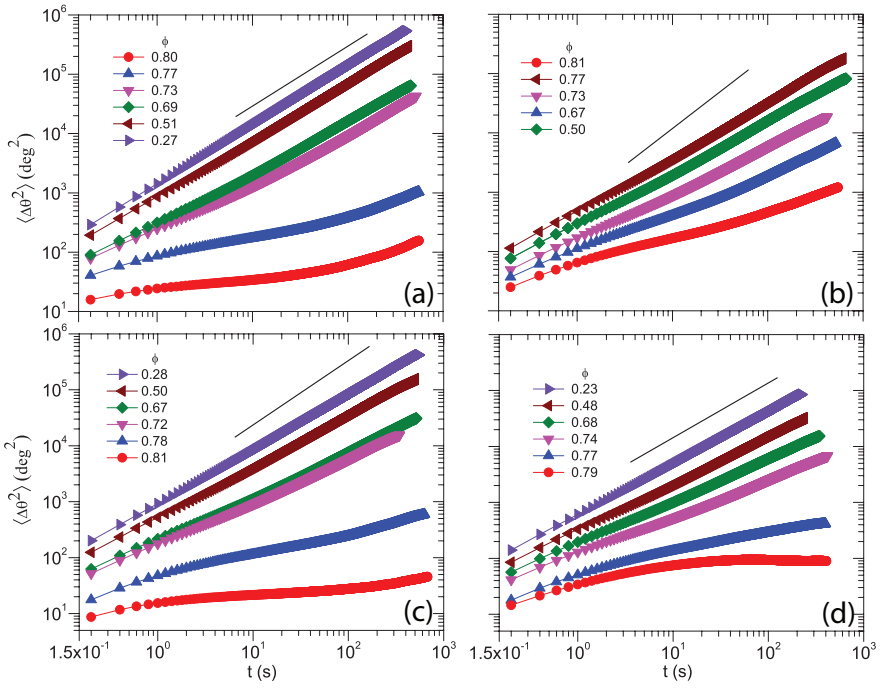

Figure 4.15 $\langle \Delta \theta^2(t) \rangle$ at different ϕs and for (a) $\Delta u = 0.44$ (b) $\Delta u = 1.16$ (c) $\Delta u = 1.47$ and (d) $\Delta u = 1.95$. The $\langle \Delta \theta^2(t) \rangle$ at $\phi = 0.67$ and $\phi = 0.72$ in (c) were observed to be same. Here also, the faster dynamics at $\phi = 0.72$ could be due to thicker cell area in the viewing region.The solid lines in all sub-plots represent slope 1.

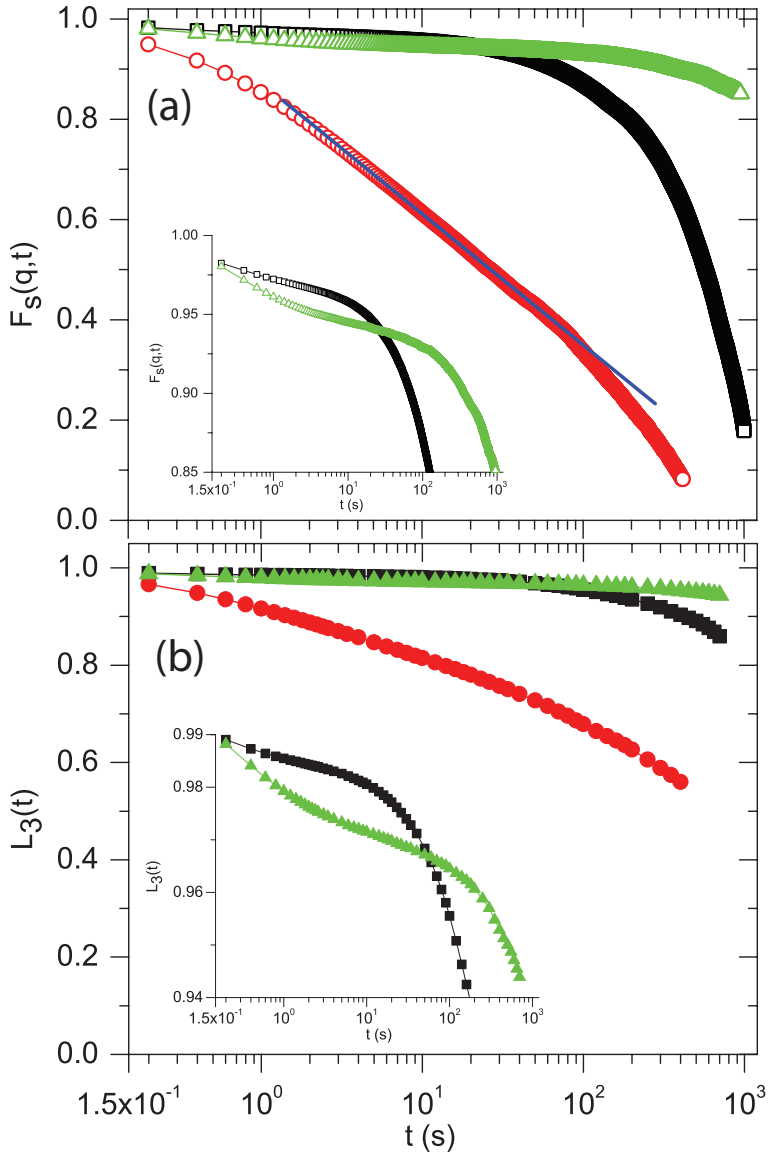

Figure 4.16 $F_s(q = 5.6\mu m^{-1}, t)$ and (b) $L_3(t)$ for $\Delta u = 0$ at $\phi = 0.79$ (black squares), $\Delta u = 1.16$ at $\phi = 0.81$ (red circles), $\Delta u = 1.47$ at $\phi = 0.81$ (green triangles). Inset to (a) and (b) – with expanded y-axis to show two-step relaxation. Solid and open symbols correspond to orientational and translational scaling of τ_α, respectively. The logarithmic decay of $F_s(q,t)$ for $\Delta u = 1.16$ is shown by solid blue line in the linear-log plot of (a).

strengths (inset to Figure 4.16b), a significant decay of $L_3(t)$ was not observed for $\Delta u = 1.16$ (Figure 4.16b). Thus, we were unable to comment about its closeness to A_3 singularity associated with orientational DOF. Furthermore, while for $\Delta u = 1.16$, $F_s(q,t)$ decayed completely (Figure 4.16a), only a partial decay was observed in $L_n(t)$ (Figure 4.16b). These observations suggest that the dynamics in translational and orientational DOF might be different. Hence, in order to ascertain if ϕ_g at intermediate attractions strengths had indeed shifted to a $\phi >$ RG ϕ_g, we have performed the aforementioned MCT scaling for all Δus studied. In line with theoretical predictions [195, 347], ${\tau_\alpha}^{-1/\gamma}$ was linear in ϕ for attractive glasses too and allowed us to extract ${\phi_g}^R$ and ${\phi_g}^T$ (Figure 4.17). Strikingly, for $\Delta u = 1.16$ we observed a two-step glass

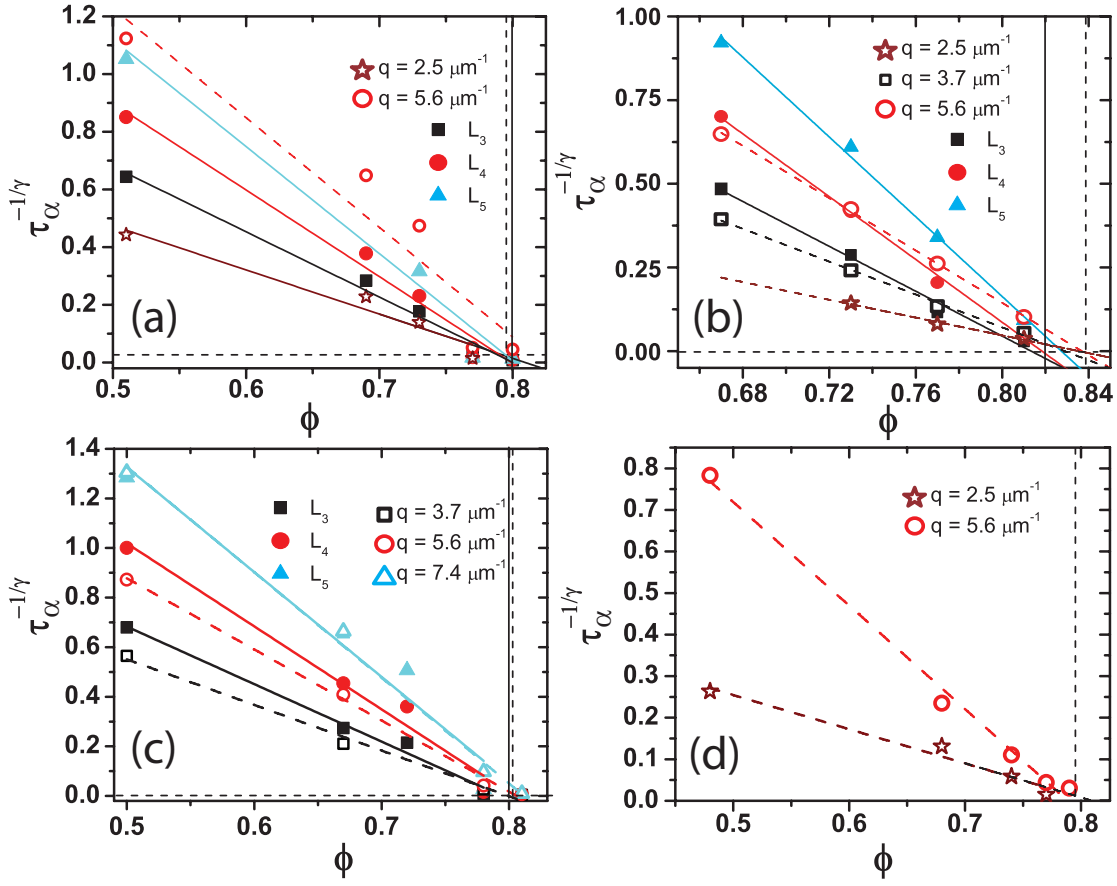

Figure 4.17 MCT scaling of τ_α for $\Delta u = 0.44$ (a), $\Delta u = 1.16$ (b), $\Delta u = 1.47$ (c) and $\Delta u = 1.95$ (d). Solid and open symbols correspond to orientational and translational scaling of τ_α, respectively. The lines are linear fits to the data. The solid and dashed vertical lines in (c) and (d) denote ${\phi_g}^R$ and ${\phi_g}^T$ respectively.

transition with ${\phi_g}^R = 0.81 \pm 0.01$ and ${\phi_g}^T = 0.84 \pm 0.01$ (Figure 4.17b). For $\Delta u = 1.47$, ${\phi_g}^T$ reverted to a lower ϕ with ${\phi_g}^T = 0.81 \pm 0.01$ and ${\phi_g}^R = 0.80 \pm 0.02$ (Figure 4.17c).

Due to strong hindrance in rotation of the particles for $\Delta u = 1.95$, $L_n(t)$ did not decay over the experimental time duration. Hence, we could not estimate the ϕ_g^R for $\Delta u = 1.95$.

To further validate the above observations, we explored the complete phase diagram in the $(\phi, \Delta u)$ plane with $\alpha_2^{T,R}(t = t^*)$, $F_s(q, t_\infty)$ and $L_3(t_\infty)$ as the quantifier of particle dynamics. Here t_∞ denotes experimental time duration. Figure 4.18 shows the translational and orientational phase diagram, along with MCT predicted glass transitions. Since, sedimentation to the 2D regions of the cell was extremely slow for

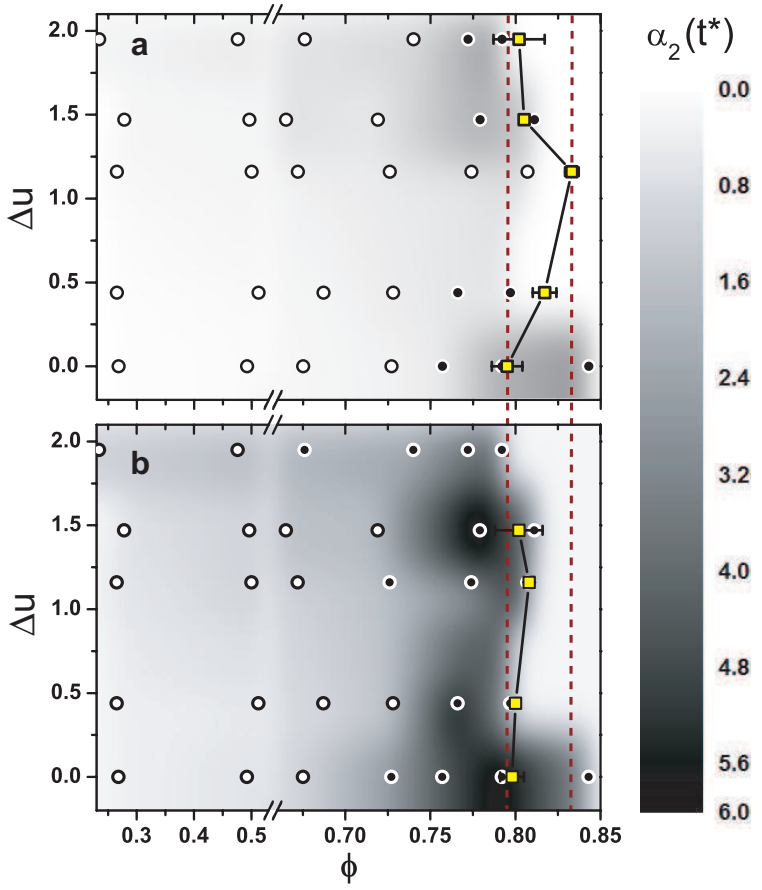

Figure 4.18 Phase diagram in $(\Delta u, \phi)$ plane. The circles represent the Δu and ϕ at which experiments were performed. (a) Translational DOF. (b) Orientational DOF. The black circles denote $F_s(q, t_\infty)$ and $L_3(t_\infty)$ that decayed completely. The white circles denote $F_s(q, t_\infty)$ and $L_3(t_\infty)$ that decayed partially. The color bar indicates the value of $\alpha_2(t = t^*)$. $\alpha_2^{T,R}(t^*)$ for ϕ's in between experimental data points were obtained from linear interpolation. Note the break in ϕ-axis at $\phi \approx 0.53$. ${\phi_g}^T$ and ${\phi_g}^R$, obtained from MCT scaling analysis, are shown by squares in (a) and (b) respectively.

ellipsoids with attractive interactions, we were unable to collect data beyond $\phi \approx 0.81$. Overall, $\alpha_2^T(t^*) < \alpha_2^R(t^*)$ indicating that orientational relaxations were relatively more hindered as compared to translational ones. While at low ϕ and at small Δus, an ergodic phase was observed, for large Δus, we found percolating networks of ellipsoids which we identified as a gel phase (Figure 4.19) [66, 225]. Most remarkably, at a fixed

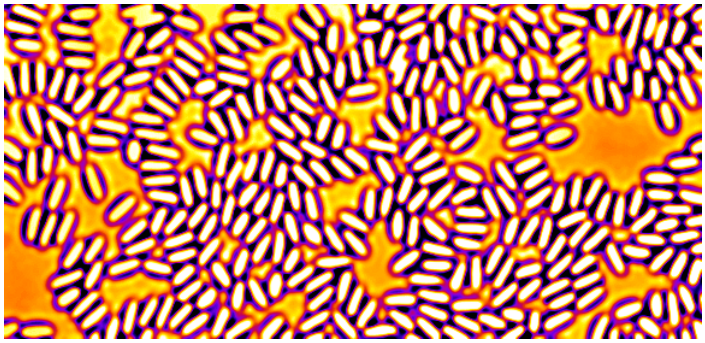

Figure 4.19 Representative image of the gel phase at $\phi = 0.47$ and $\Delta u = 1.95$.

$\phi \geq$ RG ϕ_g and with Δu, while we observed a minimum in $\alpha_2^T(t^*)$ (Figure 4.18a) at intermediate attraction strengths, we did not see this for $\alpha_2^R(t^*)$ (Figure 4.18b). This clearly implies a melting of the glass only in the translational DOF and is consistent with our observations that in contrast to $F_s(q, t_\infty)$ (Figure 4.16a), $L_n(t_\infty)$ (Figure 4.16b) shows only a partial decay. Lending further credit to these observations, while the MCT predicted ${\phi_g}^T$ shows systematic reentrant behaviour (Figure 4.18a), within experimental certainty, ${\phi_g}^R$ (Figure 4.18b) does not. Thus, inspite of having a single glass transition in the purely repulsive limit, reentrant behaviour in translational and orientational DOF were clearly different.

4.3.4 Rationalizing Our Observations

Why do we see a two-step glass transition for intermediate Δu*?* To address this question, we quantified the structure and dynamics in body frame of ellipsoids for $\phi \approx$ RG ϕ_g with Δu. The structure was isotropic for $\Delta u = 0$ (Figure 4.20a). While for $\Delta u = 1.16$, depletion enhanced lateral alignment of ellipsoids resulting in quasi-long range ordering (Figure 4.20b); for $\Delta u = 1.47$, the longer bond life time precluded the ellipsoids from sampling various configurations and led to smaller domain sizes as is shown in Figure 4.20c. These variations in structure with increasing attraction strengths have been quantified using pair correlation function $g(r)$ and static orientational correlation function $g_2(r)$. While $g(r)$ quantifies the change in number density of the particles as

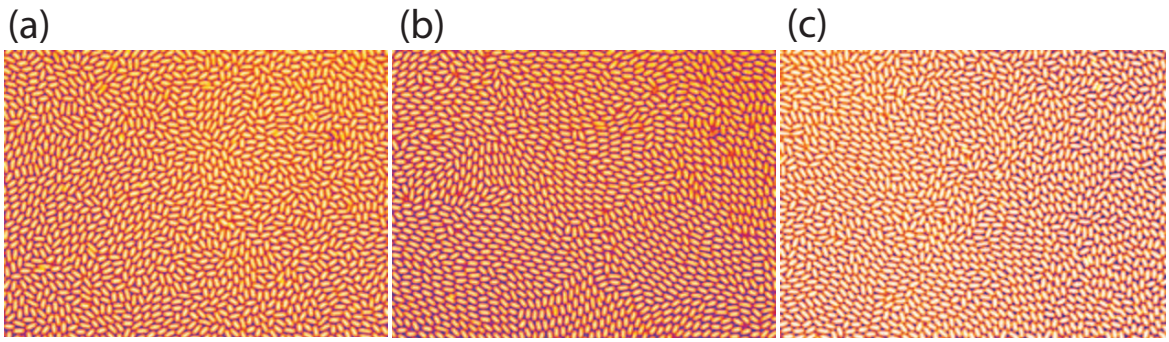

Figure 4.20 Representative images showing structure at (a) $\Delta u = 0$ at $\phi = 0.79$; (b) $\Delta u = 1.16$ at $\phi = 0.81$ and (c) $\Delta u = 1.47$ at $\phi = 0.81$.

a function of distance r with respect to a reference particle, $g_2(r)$ reveals information regarding the orientational order and hence the domain size. Mathematically, $g_2(r)$ is defined as [356],

$$g_2(r) = \langle cos(2[\theta(0) - \theta(r)]) \rangle \tag{4.12}$$

where θ is the orientation of the ellipsoid and r is centre-to-centre distance between two ellipsoids and $\langle\rangle$ denotes the ensemble averaged over all pairs of ellipsoids located at distance r. While the absence of peak at $\frac{r}{2w} = 1.7$ in $g(r)$ (Figure 4.21a), confirms that perpendicular alignment of the ellipsoids are absent for $\Delta u = 1.16$, a higher value of $g_2(r)$ at the same position (Figure 4.21b) was a clear indication of quasi-long range ordering (QLRO) at $\Delta u = 1.16$. Apart from the analysis of $g(r)$ and $g_2(r)$, our arguments of QLRO at intermediate Δu were also supported by the analysis of dynamics in the bodyframe of ellipsoids. We have followed Han *et. al.* [350] to construct the trajectories in the bodyframe. Briefly, displacements of particles between two successive frame in the labframe were resolved along major and minor axis of the ellipsoids. These displacements along major and minor axes were summed to obtain the complete trajectory for a given ellipsoid. From these constructed trajectories, we have evaluated the MSD along major ($\langle \Delta r^2 \rangle_l$) and minor ($\langle \Delta r^2 \rangle_w$) axes of ellipsoids. As shown in Figure 4.22, the anisotropy in diffusion ($\frac{\langle \Delta r^2 \rangle_l}{\langle \Delta r^2 \rangle_w}$) is enhanced at $\Delta u = 1.16$ due to the relatively unhindered motion of the ellipsoids along their major axes within the domains. The time at which $\frac{\langle \Delta r^2 \rangle_l}{\langle \Delta r^2 \rangle_w}$ peaks in Figure 4.22 is the cage relaxation time t^*, as discussed before. Since the diffusion was anisotropic, especially at intermediate attraction strengths, the cage relaxations were predominantly due to realaxation along the major axes of ellipsoids. Thus, while inter-particle attractions free up volume and shift ${\phi_g}^T$ to a higher $\phi = 0.84 \pm 0.01$, QLRO hinders rotational relaxation and

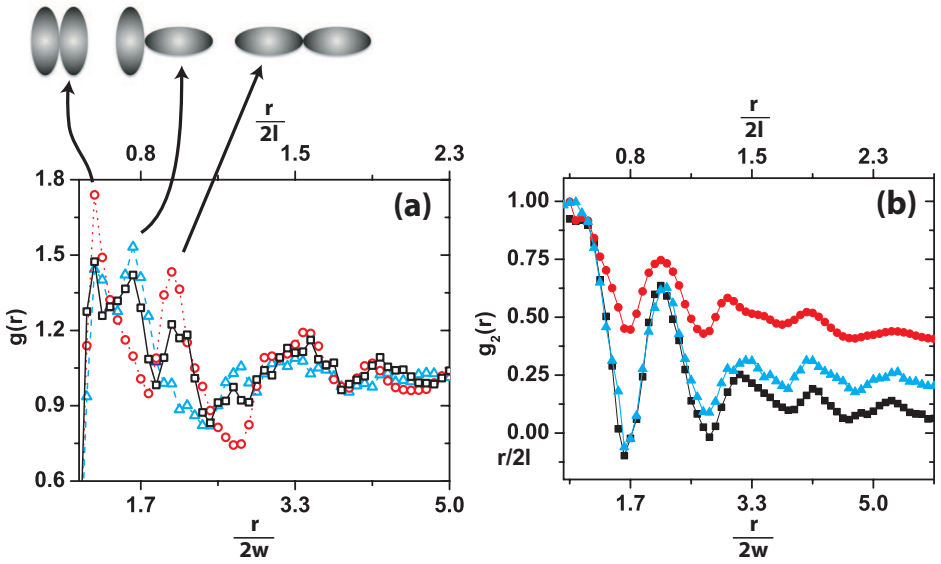

Figure 4.21 (a) Pair correlation function $g(r)$ and (b) Static orientational correlation function $g_2(r)$ for $\Delta u = 0$ at $\phi = 0.79$ (black squares); $\Delta u = 1.16$ at $\phi = 0.81$ (red circles); and $\Delta u = 1.47$ at $\phi = 0.81$ (cyan triangles).

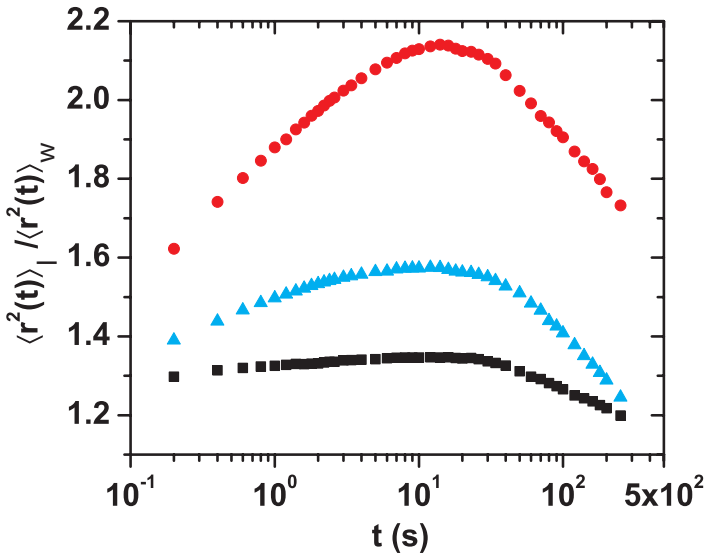

Figure 4.22 Ratio of mean-squared displacements along major and minor axis of ellipsoids for $\Delta u = 0$ at $\phi = 0.79$ (black squares); $\Delta u = 1.16$ at $\phi = 0.81$ (red circles); and $\Delta u = 1.47$ at $\phi = 0.81$ (cyan triangles).

results only in a marginal shift in ${\phi_g}^R = 0.81 \pm 0.01$. Further, we find that the orientationally most-mobile particles are predominantly at inter-domain boundaries and the translationally most-mobile particles are in the ordered regions as observed for ellipsoidal system of $\alpha = 6$ (Figure 4.23) [235].

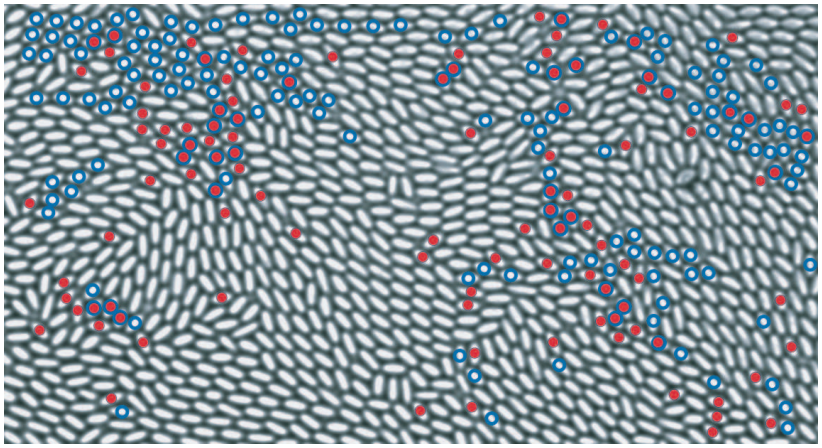

Figure 4.23 Top 10 % orientationally (solid) and translationally (hollow) most-mobile particles at $\Delta u = 1.16$ and $\phi = 0.81$.

4.4 Conclusions

In conclusion, our experiments highlight for the first time, the crucial role of particle shape and interaction anisotropy in reentrant glass phenomena. We have shown that 2D suspensions of colloidal ellipsoids ($\alpha = 2.1$) with purely repulsive interactions show a single glass transition. This is in qualitative agreement with MMCT predictions in 3D [203]. Owing to the lack of pseudonematic ordering, we find that an appreciable fraction of orientationally most-mobile particles are also translationally most-mobile. Confirming theoretical predictions [195, 347], we found that MCT scaling laws can be readily extended to systems with short-range attraction as well. Interestingly, quasi-long ranged ordering is promoted at intermediate Δus and results in a two-step glass transition with an intervening orientational glass regime. Although our experiments showed clear reentrant behavior only in the translational DOF, it would be worthwhile to investigate the role of α on reentrant glass dynamics. Further, in concord with MCT predictions [195, 200, 347], our experiments are first to probe the dynamics at single particle resolution for anisotropic particles in the vicinity of the A_3 singularity. Moreover, in light of recent experiments which have shown that shape

of dynamical heterogeneities plays a key role in relaxation mechanism of supercooled liquids and glasses [14, 15], it would be worthwhile to probe the transport properties of the supercooled liquids and its correlation, *if any*, with the morphology of dynamical heterogeneities. Answers to these questions form the content of the subsequent chapter.

Chapter 5

Transport Properties of Supercooled Liquids of Colloidal Ellipsoids

5.1 Introduction

While it is not possible to distinguish conventional liquids from supercooled ones using conventional static structural measures, a dynamical signature unique to the latter is the presence of spatial and temporal heterogeneities [19, 20, 172, 183, 265, 267, 268]. Regions of predominantly fast particles that contribute primarily to diffusivity, D, are spatially decoupled from the slow regions that govern the bulk viscosity η or equivalently the structural relaxation time τ_α [183, 267, 268]. A consequence of dynamical heterogeneities (DH) is the Stokes-Einstein (SE) relation [249],

$$D^T = \frac{k_B T}{6\pi\eta a} \tag{5.1}$$

and/or the Stokes-Einstein-Debye (SED) relation [302],

$$D^\theta = \frac{k_B T}{8\pi\eta a^3} \tag{5.2}$$

that are hallmarks of simple liquids, breakdown [183, 258, 267, 268, 271, 273, 280]. Here, the superscripts T, θ denote translational and rotational degrees of freedom (DOF), respectively, a is the particle radius and $k_B T$ is the thermal energy. The breakdown occurs at $T \sim 1.2T_g$ where T_g is the glass transition temperature. Below

T_g, the SE relation has a fractional form,

$$D^T \propto {\tau_\alpha}^{-\xi} \quad \text{with } \xi < 1. \tag{5.3}$$

It has been shown recently that the extent of SE breakdown depends on spatial dimensionality - with weak or no breakdown ($\xi \sim 1$) till T_g in four dimensions and the breakdown becoming progressively stronger ($\xi < 1$) with decreasing dimensionality [281, 292]. Moreover, simulations predict that in two-dimensions (2D), the SE relation is not valid ($\xi > 1$) even at high T [281, 282]. However, with increasing supercooling a crossover in the exponent from $\xi > 1$ to $\xi < 1$ is observed [281, 282] . Thus far, numerous studies have explored the connections between the extent of SE/SED breakdown and the standard quantifiers of DH, namely, the stretching exponent β, the non-Gaussian parameter, $\alpha_2(t)$ and the four-point dynamic susceptibility χ_4 [183, 281, 357, 358]. A key question, however, has remained unanswered. *Do morphological changes in DH influence the breakdown of SE and/or SED relations?*. This question becomes all the more relevant in the context of random first-order transition (RFOT) theory, a prominent thermodynamic approach, which predicts a change in the morphology of DH from string-like to compact on approaching the glass transition [222]. These predictions have been verified in recent experiments [15]. In fact, recent simulations have suggested that in three dimensions although DH emerges at the onset temperature of slow dynamics T_o, the violation of SE relation starts at the dynamical crossover temperature $T_s < T_o$ [283, 299]. Interestingly, for $T < T_s$, $\chi_4 \propto {\xi_4}^3$ which indicates that DH are compact [283, 299]. Here, ξ_4 is dynamic correlation length. Furthermore, recent colloid experiments have shown that the shape of DH change from string-like to compact on introducing attractive interactions [359], albeit its influence on the breakdown of SE relation has not been explored. In fact, at present it is *even* unclear whether DH in the rotational DOF also shows morphological changes on approaching the glass transition, let alone its influence on the validity of the SED relation.

Before moving further, it is necessary to briefly highlight the lack of consensus between the two complementary approaches used to investigate the validity of SED relation in supercooled liquids. Numerical studies, where D^θ is directly extracted from particle trajectories - 'Einstein Method', find that the SED relation breakdown to the same extent as SE [277, 285],

$$D^\theta \propto {\tau_\alpha}^{-\chi} \quad \text{with } \chi < 1. \tag{5.4}$$

On the contrary, studies that have access to the n^{th}-order orientational relaxation time τ_n, only $n = 2$ can be accessed in molecular experiments, invoke the 'Debye Model', $D^\theta \propto \frac{1}{\tau_n}$, and find the SED relation to be valid even for deep supercooling [260, 265, 287],

$$\frac{1}{\tau_n} \propto {\tau_\alpha}^{-\chi} \quad \text{with } \chi = 1. \tag{5.5}$$

In supercooled liquids, the orientational correlators decay as stretched-exponentials leading to the failure of the Debye Model. Simulations on hard dumbbells find that $\frac{1}{\tau_2}$, nevertheless, continues to scale linearly with τ_α, albeit D^θ extracted from the Einstein method shows a breakdown [284]. Recent colloid experiments that probed the dynamics of anisotropic tracers in a bath of smaller hard spheres, however find that the SED relation remains valid even close to glass transition irrespective of the method used [264]. It is well-known that the breakdown of the SED/SE relation depends on the size, shape and roughness of the tracers with respect to the host [305–307, 357]. It would be therefore be worthwhile to investigate the SED and SE relation in an experimental model system where particle self-diffusivities, as opposed to tracer diffusivities, can be directly accessed. Interestingly, suspensions of micrometer-sized colloidal ellipsoids are an ideal test bed to probe translational and rotational dynamics in real-space and with single-particle resolution.

Here, we have used the microscopy data from Chapter 4 to investigate the SE and SED relations in quasi-two-dimensional (2D) suspensions of colloidal ellipsoids, aspect ratio $\alpha = 2.1$, with repulsive as well as attractive interactions.

5.2 Results and Discussions

5.2.1 Stokes-Einstein-Debye (SED) Relation

We have examined the validity of the SED relation, using the aforementioned approaches, for ellipsoids with purely repulsive interactions. To ascertain if the 'Debye Model' can be used to estimate D^θ, we computed the n^{th}-order orientational correlation function (Section 4.3.1, Chapter 4),

$$L_n(t) \equiv \frac{1}{N}\left\langle \sum_{k=1}^{N} \cos n(\Delta\theta_k(t)) \right\rangle \tag{5.6}$$

for $n = 2..5$, and for all area fractions, ϕ, investigated. Here, $\Delta\theta$ is the angular displacement of the k^{th} ellipsoid, t is the lag time and $\langle ... \rangle$ represents the time averaging. As seen in earlier experiments on colloidal ellipsoids ($\alpha = 6, 9$) [235], even for $\phi = 0.28$, the long-time decay of $L_n(t) = \exp[-(t/\tau_n)^\beta]$ was found to be a stretched-exponential ($\beta < 1$) (Figure 5.1a). On approaching the glass transition area fraction $\phi_g^\theta = 0.80$, and in concord with findings from experiments and simulations [235, 284, 303, 357, 358], β was found to decrease (Figure 5.1a). This clearly signals a growing departure from the simple Debye type relaxation dynamics and is consistent with earlier observations of the increase in the size of DH in the rotational DOF on approaching ϕ_g (Figure 4.10a, Section 4.3.1, Chapter 4). The presence of DH is also reflected in the non-Gaussian nature of particle displacements evaluated over the cage rearrangement time t^* (Figure 5.1b). Next, following the Einstein Method, we directly evaluated D^θ from the long-

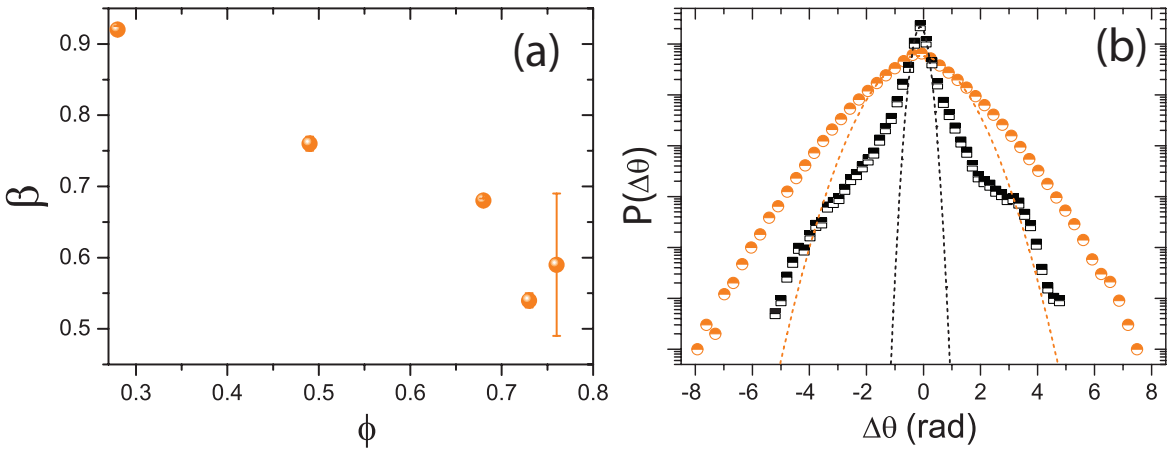

Figure 5.1 (a) Variation of the stretching exponent, β, obtained from fits to $L_2(t)$, with ϕ. (b) Distribution of $\Delta\theta$, over t^* for $\phi = 0.49$ (hall-filled circles) and $\phi = 0.76$ (half-filled squares). The dotted lines in (b) are Gaussian fits to $P(\Delta\theta)$.

time diffusive region of the mean-squared angular displacements, $\langle \Delta\theta^2(t) \rangle = 2D^\theta t$ (Figure 5.2a). We were unable to calculate D^θ for $\phi > 0.76$, since $\langle \Delta\theta^2(t) \rangle$ does not reach the diffusive limit. Figure 5.3 shows $\frac{1}{\tau_n}$, for $n = 2..5$, and D^θ plotted against τ_α. τ_α at various ϕs were obtained from the decay of the self-intermediate scattering function,

$$F_s(q,t) \equiv \frac{1}{N} \left\langle \sum_{k=1}^{N} \exp[i\mathbf{q} \cdot \Delta\mathbf{r}_k(t)] \right\rangle \tag{5.7}$$

to $\frac{1}{e}$. Here, the wavevector q is chosen to correspond to the first peak of the pair-correlation function since for this particular choice, τ_α mimics the behaviour of η [290].

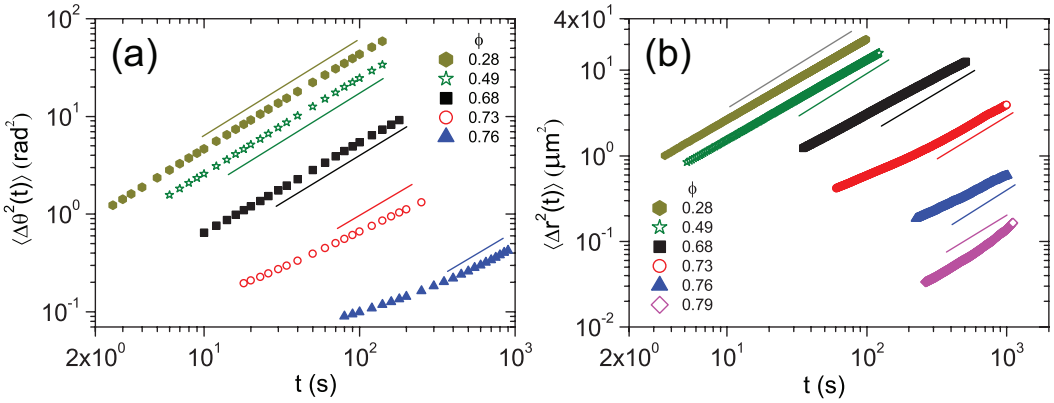

Figure 5.2 (a) Mean squared angular displacements, $\langle \Delta\theta^2(t) \rangle$, and (b) mean squared displacements, $\langle \Delta r^2(t) \rangle$ at different ϕs for purely repulsive interaction potential. Only the long time diffusive regime has been shown in (a) and (b). The solid lines in (a) and (b) represent lines of slope 1.

Owing to the failure of the Debye Model even at low ϕs, $\frac{1}{n^2\tau_n}$ and D^θ do not collapse although they scale similarly with τ_α for $\phi \leq 0.68$. At low ϕs, D^θ and $\frac{1}{n^2\tau_n}$ are found to scale as ${\tau_\alpha}^{-\chi}$, with $\chi > 1$ (Figure 5.3). Although, the physical origins for these observations are lacking, our findings are consistent with previous studies [281, 282]. Moreover, while a weak crossover in the fractional SED relation is observed via the Einstein formalism for $\phi > 0.68$, $\frac{1}{n^2\tau_n}$ for all n show complete collapse and stay coupled to τ_α (Figure 5.3). These results are in agreement with recent simulations on hard dumbbells [284]. Further, analogous to τ_α, τ_n is also dominated by the dynamics of slow particles and since for $\alpha = 2.1$ investigated here, rotational and translational DH are not spatially decoupled (Figure 4.9, Section 4.3.1, Chapter 4) [360], we expect $\frac{1}{\tau_n}$ to stay coupled to τ_α.

5.2.2 SED Relation and Morphology of Orientational DH

We next set out to determine if there were any morphological changes in the DH and to explore its connection to the crossover in the fractional SED relation by Einstein method. To identify DH, we picked the top 10% orientationally most-mobile particles over t^* and clustered them using the protocol discussed in Section 4.3.1 of Chapter 4 (Figure 5.4). We quantified the shapes of these clusters by finding the most probable number of orientationally fast nearest-neighbours for an orientationally fast particle, $P(NN^\theta)$ [15, 359]. A narrow $P(NN^\theta)$ that is peaked at $NN^\theta = 2$ implies string-like DH, while a broader distribution with $NN^\theta > 2$ signals the presence of more compact

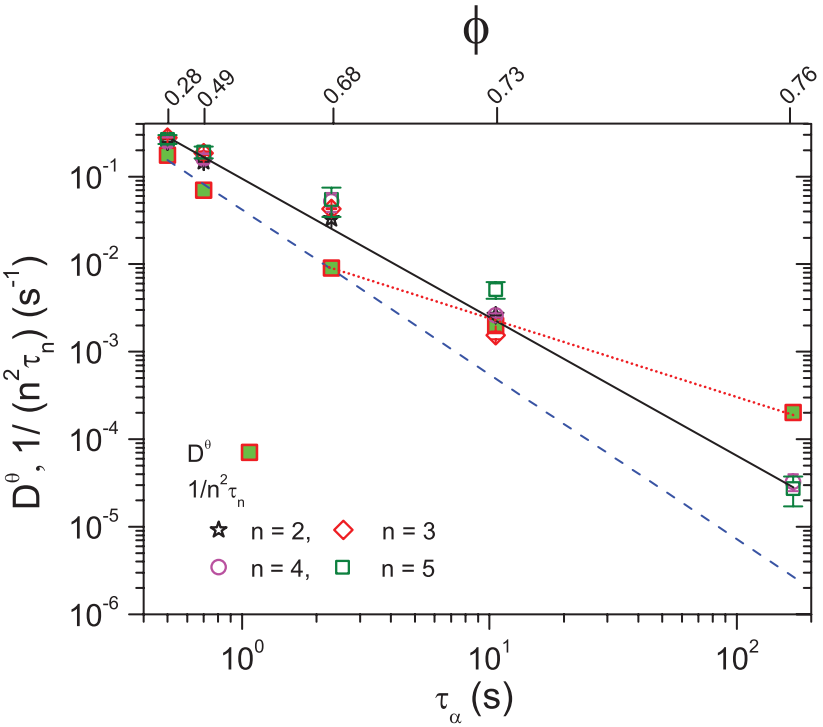

Figure 5.3 Orientational diffusion coefficient, D^θ, and inverse of the n^{th}-order orientational relaxation time, $1/n^2\tau_n$, versus the structural relaxation time τ_α. The lines show $\tau_\alpha^{-1.2}$ (solid and dashed lines) and $\tau_\alpha^{-0.9}$ (dotted line) dependencies.

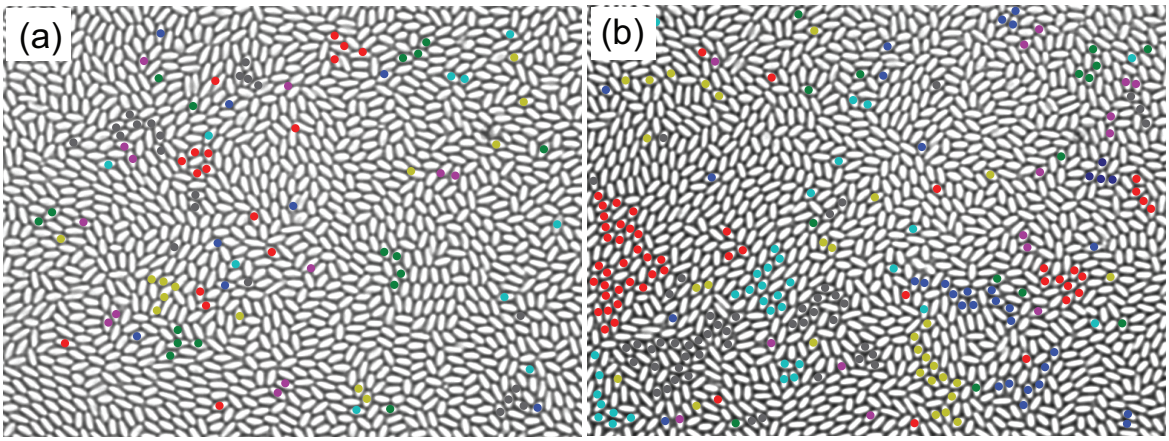

Figure 5.4 Clusters of top 10% orientationally most-mobile particles for (a) $\phi = 0.76$ and (b) $\phi = 0.79$ for ellipsoids with purely repulsive interactions. The colors correspond to distinct clusters.

DH. Since small clusters will bias $P(NN^{\theta})$, we only consider cluster sizes $N^{\theta} \geq 4$ to quantify their morphology. We find that DH for the orientational DOF become more compact with supercooling (Figure 5.5) [15, 222]. Interestingly, the morphological

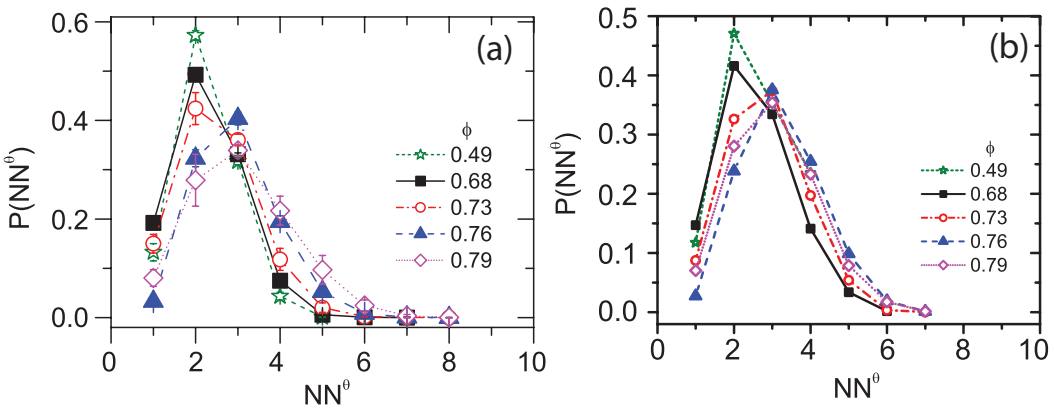

Figure 5.5 Distribution of orientationally fast nearest-neighbours for a orientationally fast particle $P(NN^{\theta})$ for different ϕs. The experimental window at each ϕ was divided into four equal time intervals and the $P(NN^{\theta})$ for various intervals were averaged to obtain the error bars. (b) $P(NN^{\theta})$ for 10 particles clusters at various ϕs.

changes in DH from string-like to compact also coincides with the ϕ beyond which a crossover in the fractional SED relation is observed (Figure 5.5a). To show that the progressive broadening of $P(NN^{T})$ is not a trivial outcome of growing averaged cluster size $\langle N_c \rangle$ on approaching ϕ_g, we focused on clusters with a fixed size, $N = 10$ particles (Figure 5.5b) and found that clusters of fixed sizes also become more compact on approaching ϕ_g. To further strengthen our observations, we define I^{θ} as,

$$I^{\theta} = \int_{3}^{\infty} P(NN^{\theta}) dNN^{\theta} \tag{5.8}$$

where the limits of the integration ensure that the dominant contribution to I^{θ} is from compact clusters. Unlike $\langle N_c \rangle$ which diverges as a power law on approaching ϕ_g (Figure 4.10b, Section 4.3.1, Chapter 4), I^{θ} versus $(\phi_g - \phi)$ shows a change in the slope that coincides with the change in the cluster morphology from string-like to compact (Figure 5.4–5.6).

5.2.3 SE Relation and Morphology of Translational DH

Motivated by the above observations, the obvious next step was to examine the connections between the shape of DH in the translational DOF and the SE relation.

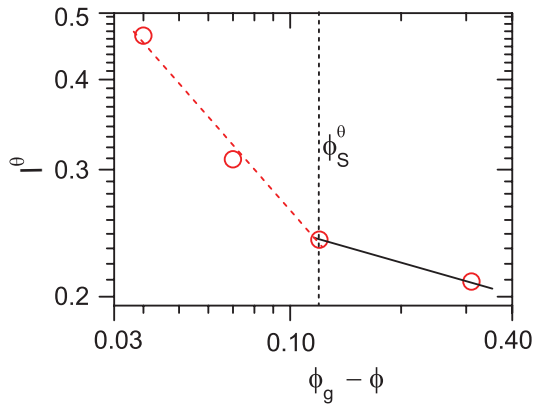

Figure 5.6 I^θ versus $(\phi_g - \phi)$. Here, $\phi_g = 0.80 \pm 0.01$ (Chapter 4).The black solid and red dashed lines are guide to the eye. The vertical dashed line represents ϕ_s^θ beyond which $\chi < 1$, by Einstein formalism.

Albeit the SE relation has been a subject of a large number of investigations [183, 258, 267, 268, 271, 273, 280], it is only recently that simulations have associated the breakdown of the SE relation with the morphological changes of DH [283, 299]. Figure 5.7 shows the variation of D^T with τ_α for ellipsoids with purely repulsive interactions. Analogous to D^θ, D^T was extracted from long-time slope of the mean squared displacements, $\langle \Delta r^2(t) \rangle = 4D^T t$ (Figure 5.2b). For $\phi \leq 0.68$, $D^T \propto {\tau_\alpha}^{-\xi}$ and again $\xi > 1$ (Figure 5.7). However, for $\phi > 0.68$, a crossover in the fractional SE relation is observed; $D^T \propto {\tau_\alpha}^{-\xi}$ with $\xi \approx 0.7$ (Figure 5.7) [281, 282]. Following our earlier line of analysis, we identified the most-probable number of translationally fast nearest-neighbours $P(NN^T)$ for a translationally fast particle (Figure 5.8). Across $\phi = 0.68$, the DH become more compact and $P(NN^T)$ becomes progressively broader with ϕ (Figure 5.9a). Akin to $P(NN^\theta)$, we found that the progressive broadening of $P(NN^T)$ is not a trivial outcome of growing $\langle N_c \rangle$ on approaching ϕ_g (Figure 5.9). Figure 5.9b–e show that the clusters of fixed sizes indeed become more compact on approaching ϕ_g. This allowed us to identify $\phi = 0.68$ with the dynamical crossover area fraction ϕ_s^T. Interestingly, consistent with observations in the orientational DOF,

$$I^T = \int_3^\infty P(NN^T) dNN^T \tag{5.9}$$

versus $(\phi_g - \phi)$ shows two slopes with an apparent change in the trend occurring in the vicinity of ϕ_s^T (Figure 5.9f). These observations are in line with recent numerical predictions [283, 299] and suggest that the crossover in the fractional SE and SED relation is accompanied by a change in shape of DH from string-like to compact.

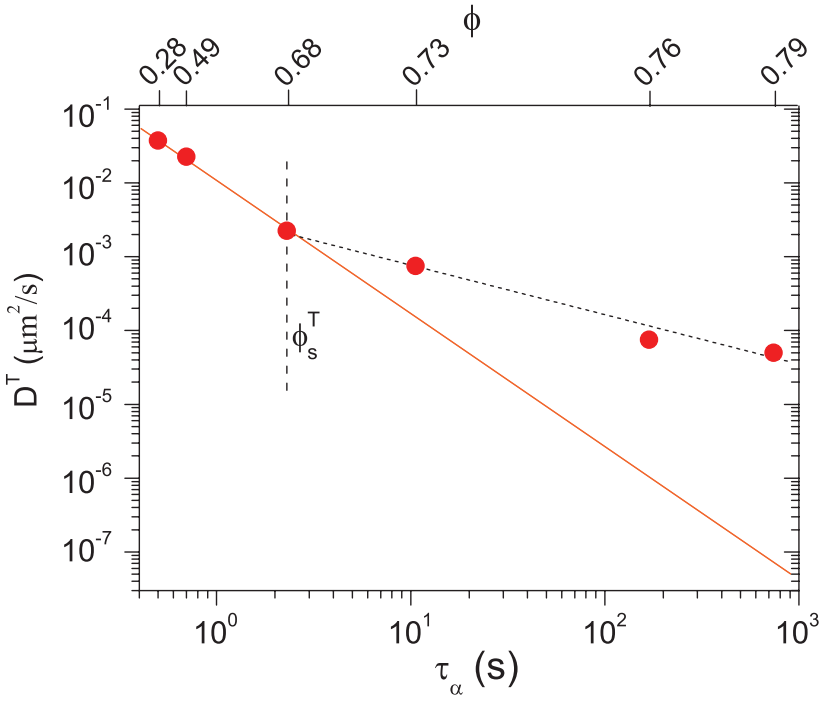

Figure 5.7 Translational diffusivity D^T versus the structural relaxation time τ_α. The lines show $\tau_\alpha^{-1.8}$ (solid) and $\tau_\alpha^{-0.7}$ (dotted line) dependencies. The vertical dashed line represents the dynamic crossover area fraction $\phi_s^T = 0.68$.

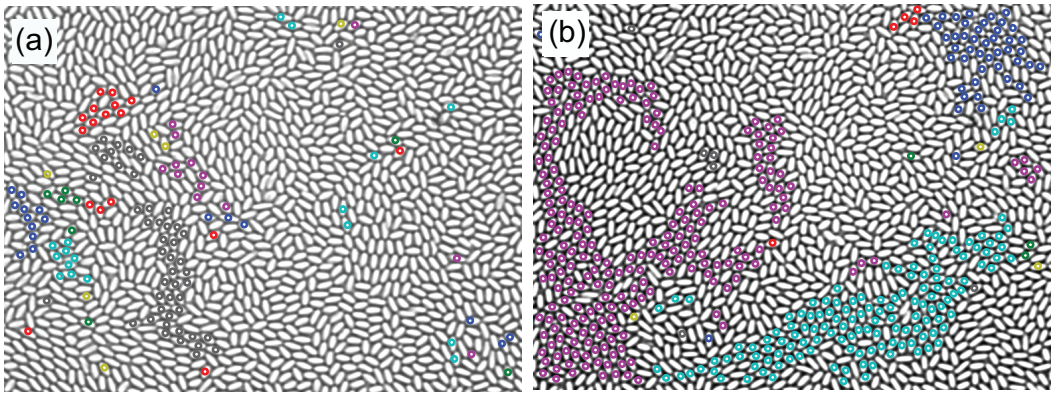

Figure 5.8 Clusters of top 10% translationally most-mobile particles for (a) $\phi = 0.76$ and (b) $\phi = 0.79$ for ellipsoids with purely repulsive interactions. The colors correspond to distinct clusters.

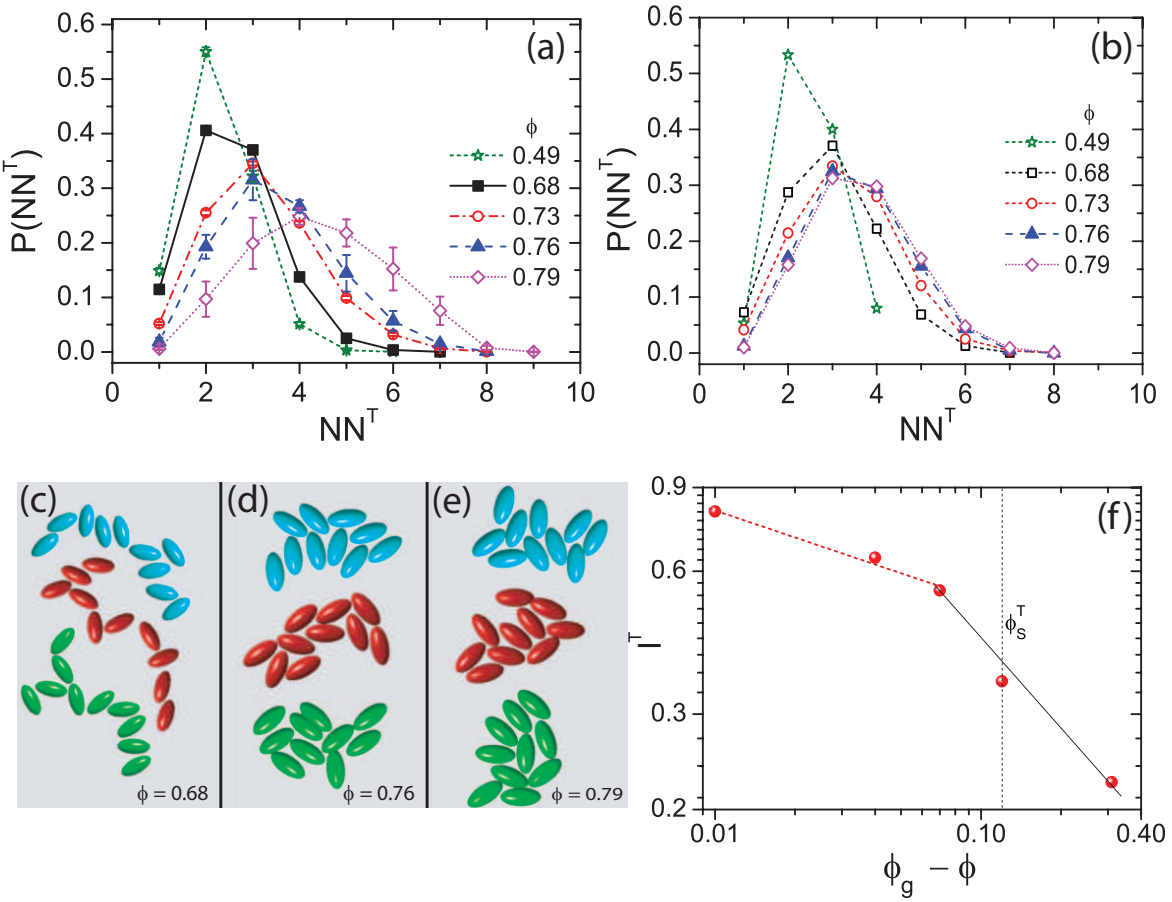

Figure 5.9 (b) Most probable number of translationally fast nearest-neighbours for a translationally fast particle $P(NN^T)$ for different ϕs. Error bars in were obtained as mentioned earlier (Figure 5.5a). (b) $P(NN^T)$ for 10 particles clusters at various ϕs and corresponding representative cluster morphologies for (c) $\phi = 0.68$ (d) $\phi = 0.76$ (e) $\phi = 0.79$. In (c) - (e), the colors correspond to distinct clusters. (f) I^T versus $(\phi_g - \phi)$. Here, $\phi_g = 0.80 \pm 0.01$ (Chapter 4). The black solid and red dashed line in (e) are guide to the eye. The vertical dashed line represents ϕ_s^T beyond which $\xi < 1$.

5.2.4 SE and SED Relations for Attractive Ellipsoids

To bolster our claims, it would suffice to show that in the *absence* of changes in the shape of DH, χ and ξ do not show a change on approaching ϕ_g. To this end, we take recourse to the findings from molecular dynamics simulation on attractive hard sphere glasses where a reentrant behaviour in the validity of the SE relation was observed [361]. While the SE relation breakdown for the repulsive as well as the strong attraction case, the dynamics was found to be faster at intermediate attraction strengths with the SE relation remaining valid even for the deep supercooling [361]. This study, however, did not probe the connection between the validity of the SE relation and the nature of DH. In the context of ellipsoids, as discussed in the previous chapters, the introduction of small depletant molecules results in an anisotropic attraction that favors the lateral alignment of ellipsoids over to tip-to-tip ones. Although MCT for hard ellipsoids predicts a single glass transition for both the rotational and translational DOF for $\alpha < 2.5$ [203], we observed that depletion attraction enhances pseudonematic ordering at intermediate attraction strengths. Consequently, the orientational glass transition was found to precede the translational one and reentrant glass dynamics was observed only in the translational DOF. The dynamics was observed to be fastest for an intermediate attraction strength of $\frac{\Delta U}{K_B T} = -1.16$, and allowed access to D^T, D^θ and τ_n close to the glass transition. Moreover, the decay of $F_s(q,t)$ was found to be logarithmic close to ϕ_g^T and is indicative of its vicinity to the A_3 singularity (Figure 4.16a, Section 4.3.3, Chapter 4). β was once again found to decrease on approaching ϕ_g. In contrast to the repulsive case, the growth of pseudonematic domains with ϕ hinders the relaxation of lower order orientational correlators to a greater degree than the higher order ones. Thus, while $\frac{1}{n^2\tau_n}$ collapses at low ϕ for all n, they show marked deviations on approaching ϕ_g^θ (Figure 5.10a). Also, a recent study on the same system has observed that orientational and translational DH are spatially decoupled at this interaction strength [360] and we expect $\frac{1}{\tau_n}$ to progressively decouple from τ_α as well. This is indeed the case here with the decoupling of lower order orientational correlators being more pronounced (Figure 5.10a). By Einstein method, $D^\theta \propto {\tau_\alpha}^{-\chi}$ with $\chi > 1$ (Figure 5.10a), even close to ϕ_g^θ. Most remarkably, consistent with the absence of crossover in the fractional SED relation, while $P(NN^\theta)$ does not evolve with ϕ (Figure 5.10b), I^θ versus $(\phi_g^\theta - \phi)$ shows no change in slope (Figure 5.10e). Further, for the SE relation, $D^T \propto {\tau_\alpha}^{-\xi}$ with $\xi = 1$, even for deep supercooling (Figure 5.10c). Lending further strength to our findings and in stark contrast to our earlier observations (Fig.

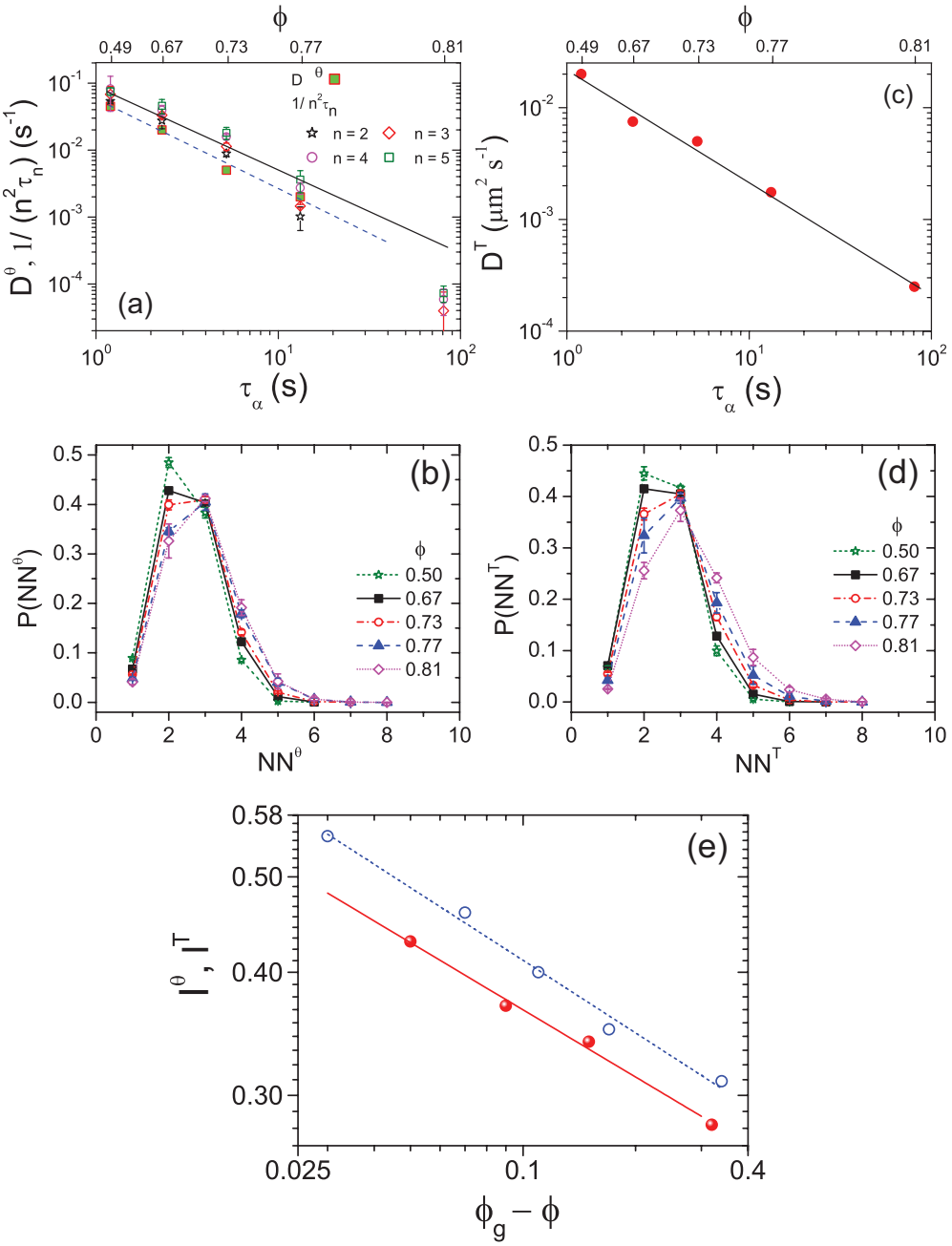

Figure 5.10 SE and SED relation and morphology of DH at $\frac{\Delta U}{k_B T} = -1.16$. (a) D^θ and $1/n^2\tau_n$ versus τ_α. The lines in (a) show $\tau_\alpha^{-1.3}$ dependencies. (b) $P(NN^\theta)$ for different ϕs. (c) D^T versus τ_α. The solid line in (c) shows ${\tau_\alpha}^{-1}$ dependency. (d) $P(NN^T)$ for different ϕs. Error bars in were obtained as mentioned earlier (Figure 5.5a) (e) I^θ (solid circle) and I^T (hollow circle) versus $(\phi_g - \phi)$. Here, $\phi_g^\theta = 0.82 \pm 0.01$ and $\phi_g^T = 0.84 \pm 0.01$ (Chapter 4). The solid and dashed line in (e) are guide to the eye.

5.10b), $P(NN^T)$ does not show any appreciable change with increasing ϕ (Fig. 5.10d). Moreover, I^T mimics the behavior of I^θ on approaching ϕ_g^T (Fig. 5.10e).

Our observations that the change in the shape of DH coincides with the crossover in fractional SE and SED relation is further substantiated by results for $\frac{\Delta U}{k_B T} = -0.44$ (Figure 5.11). Here, we observe that a crossover in the fractional SE relation at $\phi_s^T \sim 0.73$ is accompanied by the change in the shape of translational DH from string-like to compact (Figure 5.11). However, for orientational DOF the shape of DH continues to remain string-like and no crossover is observed in the fractional SED relation within the range of ϕs studied. At higher attraction strengths ($\frac{\Delta U}{k_B T} < -1.16$), owing to slow dynamics for $\phi > 0.72$, $\langle \Delta\theta^2(t) \rangle$ and $\langle \Delta r^2(t) \rangle$ did not approach the diffusive limit with in the experimental duration and consequently we were unable to extract $D^{T,\theta}$. We find that for $\phi \leq 0.72$, no crossover in the fractional SE and SED relations for $\frac{\Delta U}{k_B T} = -1.47$ (Figure 5.12) was observed and as expected $P(NN^{T,\theta})$ do not evolve with ϕ.

5.3 Conclusions

Taken together, our study has helped establish a causal link between the morphological evolution of DH and crossover in the fractional SE and SED relations. Our findings show that, albeit DH are present at $\phi < \phi_s^{\theta,T} \sim 0.68$ in both the translational and orientational DOF, it is the change in the shape from string-like to compact that coincides with the observed crossover. These results are in agreement with recent simulations in 3D [283, 299]. Consistent with predictions of RFOT theory [15, 222], DH indeed become more compact on approaching the glass transition. While for ellipsoids with purely repulsive interactions, a crossover in the fractional SE and SED relation (Einstein method) is observed beyond ϕ_s, $\frac{1}{\tau_n}$ stays coupled to τ_α. For suitable strengths of short-ranged attractive interaction, the glass melted and allowed us to access the translational and orientational dynamics even for deep supercooling. Although earlier studies, on the same system, have provided clear evidence for the presence of DH (Chapter 4), these heterogeneities continue to remain string-like and consequently, there is no change in exponent in the SE and SED relation. These observations further provide the first experimental confirmation of the validity of the SE relation along the A_3 singularity, a scenario that has remained untested even in supercooled liquids of attractive hard spheres.

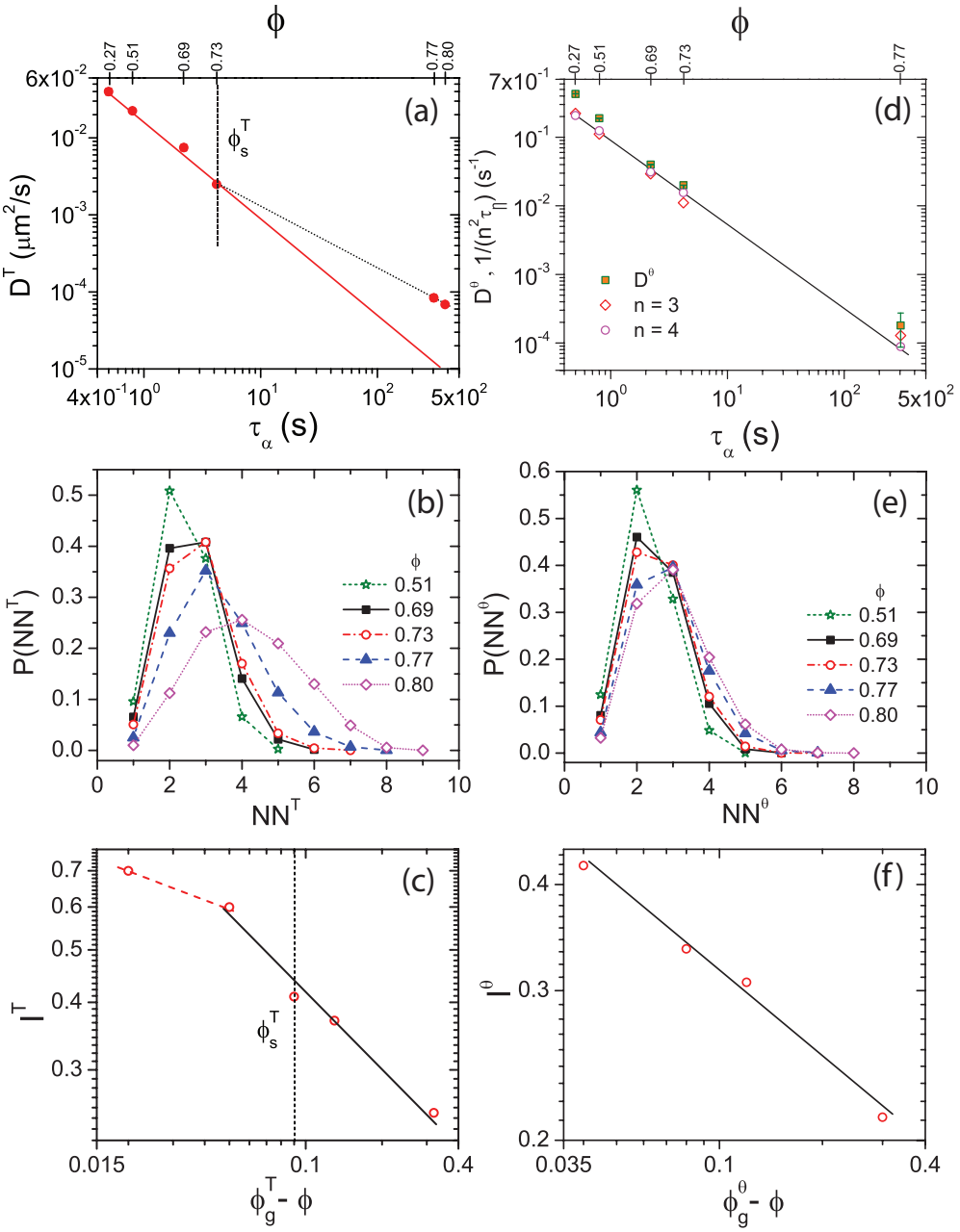

Figure 5.11 SE and SED relation and morphology of DH at $\frac{\Delta U}{k_B T} = -0.44$. (a) D^T versus τ_α. The lines in (a) show $\tau_\alpha^{-1.3}$ (solid) and $\tau_\alpha^{-0.8}$ (dotted) dependencies. (b) $P(NN^T)$ for different ϕs. (c) I^T versus $(\phi_g^T - \phi)$. Here, $\phi_g^T = 0.82 \pm 0.02$ (Chapter 4).The black solid and red dashed line in (e) are guide to the eye. The vertical dashed line represents ϕ_s^T beyond which $\xi < 1$. (d) D^θ, and $1/n^2\tau_n$, versus τ_α. The line in (d) show $\tau_\alpha^{-1.2}$ dependency. (e) $P(NN^\theta)$ for different ϕs. (f) I^θ versus $(\phi_g^\theta - \phi)$. Here, $\phi_g^\theta = 0.81 \pm 0.01$ (Chapter 4). The black solid in (f) is guide to the eye.

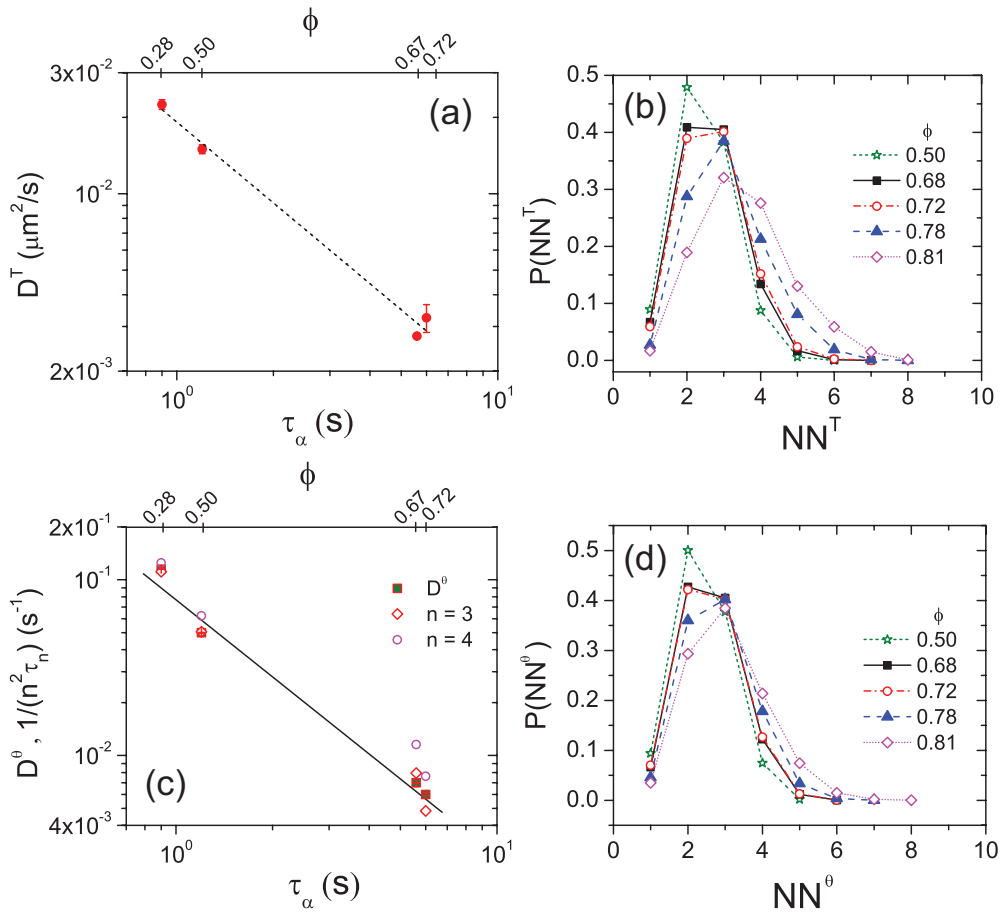

Figure 5.12 SE and SED relation and morphology of DH at $\frac{\Delta U}{k_B T} = -1.47$. (a) D^T versus τ_α. The dotted line in (a) show $\tau_\alpha^{-1.1}$ dependency. (b) $P(NN^T)$ for different ϕs. (c) D^θ, and $1/n^2\tau_n$, versus τ_α. The solid lines in (c) show $\tau_\alpha^{-1.5}$ dependency. (d) $P(NN^\theta)$ for different ϕs.

Chapter 6

Summary and Outlook

Colloids are indispensable both from the perspective of academics as well as applications. In the works presented in this thesis, the shape sensitive interactions in colloidal suspensions were utilized to address some fundamental questions in colloid research. From the point of view of their applications in photonics and optoelectronics, we have established a new design strategy that allowed a facile control over site-specific nucleation and growth of colloidal crystals [362]. We have also studied fundamental condensed matter phenomena such as the glass transition dynamics in two-dimensional (2D) suspensions of colloidal ellipsoids. Using repulsive as well as attractive interactions between the particles, we tested some key predictions of mode coupling theory (MCT), one of the earliest microscopic theory of the glass transition [363]. Further, we probed the limits of validity of Stokes-Einstein (SE) and Stokes-Einstein-Debye (SED) relations for dense suspensions of colloidal ellipsoids. Interestingly, the optimal combination of the aspect ratio and anisotropic attractions between the ellipsoids, due to geometrical nature of depletion interactions, allowed us to unravel the underlying microscopic mechanisms for the breakdown of SE and SED relations for supercooled liquids [364].

Our techniques of fabricating moiré templates pave the way to realize, sans application of external fields, site-specific colloidal crystal nucleation and growth. In Chapter 2, we elaborated on replica imprinting techniques to realize moiré template, a template with geometric height modulations on the surface. The height modulations of the substrate coupled with short-ranged depletion attractions created a gradient in the activation energy for the diffusing colloids. This aided in transporting the particles to the target sites, prior to the onset of nucleation. The activated transport of the particles led to a faster nucleation and growth of the colloidal crystal. More importantly, the enhancement in particles' surface mean free path allowed control over

nucleation density in a regime that cannot be accessed in conventional template-assisted growth (Chapter 3). Interestingly, the island density as well as the size of the colloidal crystallites can be tuned by a single control parameter i.e. superposition angle θ. In a nutshell, by appropriately tuning of the surface mobilities of the colloids, moiré templates yield control over colloidal crystal growth. Therefore a natural extension will be to investigate if moire substrates can serve as a *shape/size spectrometer* i.e. it allows self-segregation of mixtures of colloidal particles with distinct surface mobilities to specific regions on the surface. Further, analogous to atomic heteroepitaxy, microscopic insights into strain relaxation mechanisms in colloidal heteroepitaxy may provide an alternate route to realize site-specific colloidal crystal nucleation and growth with well-controlled size and symmetry.

By utilizing the geometrical nature of the depletion attractions, in Chapter 4, we explored the role of interaction anisotropy in reentrant glass dynamics in dense suspensions of the colloidal ellipsoids (aspect ratio, $\alpha = 2.1$). For the purely repulsive case, consistent with the mode coupling theory (MCT) predictions, we found that the orientational and translational glass transitions occur at the same area fraction. By introducing depletion attraction between ellipsoids, we showed, for the first time, that MCT scaling arguments continue to hold good for attractive colloids as well. Interestingly, for intermediate depletion attraction strengths, the orientational glass transition preceded the translational one. By quantifying the structure and dynamics at intermediate attraction strengths, we found that the anisotropic attraction in ellipsoids leads to quasi-long-range ordering, a feature of large aspect ratio ellipsoids [235], and hence results in two-step glass transition. Most interestingly, within experimental certainty, we observe reentrant glass dynamics only in the translational degrees of freedom (DOF). These observations lead us to speculate *if there is any reentrant in glass dynamics for orientational DOF*. A plausible way to address the above question, based on our findings, would be to probe the reentrant glass dynamics in suspensions of colloidal ellipsoids with $\alpha < 2.1$. However, given the fact that coupling between the translational and orientational degrees of freedom become stronger with decreasing α and depletion promoting lateral alignments of the ellipsoids, making any guess regarding the phase behaviour of short aspect ratio ellipsoids is anything but easy. Interestingly, these experiments (with ellipsoids of small α) would also enable one to probe type-A glass transition, yet another key prediction of MCT for ellipsoidal particles [203]. Notably, ellipsoids with $\alpha > 2.5$ undergo type-B glass transition. It is worth noting that MCT, apart from being extended to complex colloids, is also the

sole theory hitherto that predicts, as a function of attraction strength, a reentrant glass dynamics for spherical particles. However, it is well-established that in the deeply supercooled regime where activated hopping become important, MCT fails to capture the dynamics of the system. This entails the extension of other theories such as random first order transition (RFOT), dynamic facilitation (DF) theory to the particle with shape and/or interaction anisotropies.

In Chapter 5, we established a causal link between the morphological evolution cooperatively rearranging regions (CRRs) and the breakdown/crossover of Stokes-Einstein (SE) and Stokes-Einstein-Debye (SED) relations. We have shown that in quasi-two-dimensional (2D) suspensions of colloidal ellipsoids of $\alpha = 2.1$, both SE and SED relations are violated at all area fractions ϕ. However, with the increase in supercooling, a crossover in SE and SED relation was observed at ϕ_s. Interestingly, $\phi_s < \phi_g$, ϕ_g is the glass transition area fraction obtained using the MCT scaling analysis. In concord with RFOT, a prominent thermodynamic theory of the glass transition, the shape of CRRs become increasingly compact with the increase in supercooling. Quite remarkably, ϕ_s coincided with the change in the shape of CRRs from string-like to compact and not with their onset. Moreover, by introducing suitable depletion attraction between the ellipsoids, the shape of CRRs continued to remain string-like even for deep supercooling and accompanying this there was no crossover observed in SE and SED relation. Thus it is not the mere presence of CRRs, rather it is their change in the shape from string-like to compact that coincides with the crossover/breakdown of the SE and SED relations. While our findings are consistent with recent simulations [283], a clear understanding of why only compact CRRs lead to the breakdown of SE/SED relation is still lacking. Further, in the light of recent simulations that show that the glass transition dynamics is fundamentally different in two- and three-dimensions [365], it would be interesting to see if our findings continue to hold in three-dimensions.

Bibliography

[1] Huang, W. *Fundamental Studies of the Interaction Between Femtosecond Laser and Patterned Monolayer Plasmonic Nanostructures* (ProQuest, 2008).

[2] Lee, S.-K., Yi, G.-R., Moon, J. H., Yang, S.-M. & Pine, D. J. Pixellated photonic crystal films by selective photopolymerization. *Advanced Materials* **18**, 2111 (2006).

[3] Vlasov, Y. A., Bo, X.-Z., Sturm, J. C. & Norris, D. J. On-chip natural assembly of silicon photonic bandgap crystals. *Nature* **414**, 289 (2001).

[4] Kim, S.-H., Lee, S. Y., Yang, S.-M. & Yi, G.-R. Self-assembled colloidal structures for photonics. *NPG Asia Materials* **3**, 25 (2011).

[5] Arsenault, A. C., Puzzo, D. P., Manners, I. & Ozin, G. A. Photonic-crystal full-colour displays. *Nature Photonics* **1**, 468 (2007).

[6] Kim, S.-H., Park, H. S., Choi, J. H., Shim, J. W. & Yang, S.-M. Integration of colloidal photonic crystals toward miniaturized spectrometers. *Advanced Materials* **22**, 946 (2010).

[7] Kim, H. *et al.* Structural colour printing using a magnetically tunable and lithographically fixable photonic crystal. *Nature Photonics* **3**, 534 (2009).

[8] Krauss, T. F., Richard, M. & Brand, S. Two-dimensional photonic-bandgap structures operating at near-infrared wavelengths. *Nature* **383**, 699 (1996).

[9] Holtz, J. H. & Asher, S. A. Polymerized colloidal crystal hydrogel films as intelligent chemical sensing materials. *Nature* **389**, 829 (1997).

[10] Asher, S. A. *et al.* Photonic crystal carbohydrate sensors: low ionic strength sugar sensing. *Journal of the American Chemical Society* **125**, 3322 (2003).

[11] Sharma, A. C. *et al.* A general photonic crystal sensing motif: creatinine in bodily fluids. *Journal of the American Chemical Society* **126**, 2971 (2004).

[12] Zhao, Y.-J. *et al.* Multiplex label-free detection of biomolecules with an imprinted suspension array. *Angewandte Chemie International Edition* **48**, 7350 (2009).

[13] Li, B., Zhou, D. & Han, Y. Assembly and phase transitions of colloidal crystals. *Nature Reviews Materials* **1**, 15011 (2016).

[14] Gokhale, S., Sood, A. & Ganapathy, R. Deconstructing the glass transition through critical experiments on colloids. *Advances in Physics* **65**, 363 (2016).

[15] Nagamanasa, K. H., Gokhale, S., Sood, A. & Ganapathy, R. Direct measurements of growing amorphous order and non-monotonic dynamic correlations in a colloidal glass-former. *Nature Physics* **11**, 403 (2015).

[16] Gokhale, S., Nagamanasa, K. H., Ganapathy, R. & Sood, A. Growing dynamical facilitation on approaching the random pinning colloidal glass transition. *Nature Communications* **5** (2014).

[17] Ganapathy, R., Buckley, M. R., Gerbode, S. J. & Cohen, I. Direct measurements of island growth and step-edge barriers in colloidal epitaxy. *Science* **327**, 445 (2010).

[18] Alsayed, A. M., Islam, M. F., Zhang, J., Collings, P. J. & Yodh, A. G. Premelting at defects within bulk colloidal crystals. *Science* **309**, 1207 (2005).

[19] Weeks, E. R., Crocker, J. C., Levitt, A. C., Schofield, A. & Weitz, D. A. Three-dimensional direct imaging of structural relaxation near the colloidal glass transition. *Science* **287**, 627 (2000).

[20] Kegel, W. K. & van Blaaderen, A. Direct observation of dynamical heterogeneities in colloidal hard-sphere suspensions. *Science* **287**, 290 (2000).

[21] Wang, Z., Wang, F., Peng, Y., Zheng, Z. & Han, Y. Imaging the homogeneous nucleation during the melting of superheated colloidal crystals. *Science* **338**, 87 (2012).

[22] Berthier, L. & Biroli, G. Theoretical perspective on the glass transition and amorphous materials. *Reviews of Modern Physics* **83**, 587 (2011).

[23] Cheng, X., McCoy, J. H., Israelachvili, J. N. & Cohen, I. Imaging the microscopic structure of shear thinning and thickening colloidal suspensions. *Science* **333**, 1276 (2011).

[24] Glotzer, S. C. & Solomon, M. J. Anisotropy of building blocks and their assembly into complex structures. *Nature Materials* **6**, 557 (2007).

[25] Kuijk, A., van Blaaderen, A. & Imhof, A. Synthesis of monodisperse, rodlike silica colloids with tunable aspect ratio. *Journal of the American Chemical Society* **133**, 2346 (2011).

[26] Manna, L., Scher, E. C. & Alivisatos, A. P. Synthesis of soluble and processable rod-, arrow-, teardrop-, and tetrapod-shaped cdse nanocrystals. *Journal of the American Chemical Society* **122**, 12700 (2000).

[27] Snoeks, E. *et al.* Colloidal ellipsoids with continuously variable shape. *Advanced Materials* **12**, 1511 (2000).

[28] Sacanna, S. & Pine, D. J. Shape-anisotropic colloids: Building blocks for complex assemblies. *Current Opinion in Colloid & Interface Science* **16**, 96 (2011).

[29] Ho, C., Keller, A., Odell, J. & Ottewill, R. Preparation of monodisperse ellipsoidal polystyrene particles. *Colloid and Polymer Science* **271**, 469 (1993).

[30] Johnson, P. M., van Kats, C. M. & van Blaaderen, A. Synthesis of colloidal silica dumbbells. *Langmuir* **21**, 11510 (2005).

[31] Jackson, A. M., Myerson, J. W. & Stellacci, F. Spontaneous assembly of subnanometre-ordered domains in the ligand shell of monolayer-protected nanoparticles. *Nature Materials* **3**, 330 (2004).

[32] Manoharan, V. N., Elsesser, M. T. & Pine, D. J. Dense packing and symmetry in small clusters of microspheres. *Science* **301**, 483 (2003).

[33] van Blaaderen, A. Chemistry: colloidal molecules and beyond. *Science* **301**, 470 (2003).

[34] Sacanna, S., Irvine, W., Chaikin, P. M. & Pine, D. J. Lock and key colloids. *Nature* **464**, 575 (2010).

[35] DeVries, G. A. *et al.* Divalent metal nanoparticles. *Science* **315**, 358 (2007).

[36] Yi, G.-R., Pine, D. J. & Sacanna, S. Recent progress on patchy colloids and their self-assembly. *Journal of Physics: Condensed Matter* **25**, 193101 (2013).

[37] Du, J. & O'Reilly, R. K. Anisotropic particles with patchy, multicompartment and janus architectures: preparation and application. *Chemical Society Reviews* **40**, 2402 (2011).

[38] Zhang, G., Wang, D. & Möhwald, H. Decoration of microspheres with gold nanodots− giving colloidal spheres valences. *Angewandte Chemie International Edition* **44**, 7767 (2005).

[39] Hong, L., Cacciuto, A., Luijten, E. & Granick, S. Clusters of charged janus spheres. *Nano Letters* **6**, 2510 (2006).

[40] Hong, L., Jiang, S. & Granick, S. Simple method to produce janus colloidal particles in large quantity. *Langmuir* **22**, 9495 (2006).

[41] Yan, J., Bloom, M., Bae, S. C., Luijten, E. & Granick, S. Linking synchronization to self-assembly using magnetic janus colloids. *Nature* **491**, 578 (2012).

[42] Ahmadi, T. S., Wang, Z. L., Green, T. C., Henglein, A. & El-Sayed, M. A. Shape-controlled synthesis of colloidal platinum nanoparticles. *Science* **272**, 1924 (1996).

[43] Rossi, L. *et al.* Cubic crystals from cubic colloids. *Soft Matter* **7**, 4139 (2011).

[44] Jin, R. *et al.* Photoinduced conversion of silver nanospheres to nanoprisms. *Science* **294**, 1901 (2001).

[45] Chen, Q., Bae, S. C. & Granick, S. Directed self-assembly of a colloidal kagome lattice. *Nature* **469**, 381 (2011).

[46] Romano, F. & Sciortino, F. Colloidal self-assembly: patchy from the bottom up. *Nature Materials* **10**, 171 (2011).

[47] Mao, X., Chen, Q. & Granick, S. Entropy favours open colloidal lattices. *Nature Materials* **12**, 217 (2013).

[48] Yang, S.-M., Kim, S.-H., Lim, J.-M. & Yi, G.-R. Synthesis and assembly of structured colloidal particles. *Journal of Materials Chemistry* **18**, 2177 (2008).

[49] Bianchi, E., Blaak, R. & Likos, C. N. Patchy colloids: state of the art and perspectives. *Physical Chemistry Chemical Physics* **13**, 6397 (2011).

[50] Donev, A. *et al.* Improving the density of jammed disordered packings using ellipsoids. *Science* **303**, 990 (2004).

[51] Wood, W. W. & Jacobson, J. Preliminary results from a recalculation of the monte carlo equation of state of hard spheres. *Journal of Chemical Physics* **27**, 1207 (1957).

[52] Alder, B. & Wainwright, T. Phase transition for a hard sphere system. *Journal of Chemical Physics* **27**, 1208 (1957).

[53] Hoover, W. G. & Ree, F. H. Melting transition and communal entropy for hard spheres. *Journal of Chemical Physics* **49**, 3609 (1968).

[54] Rintoul, M. & Torquato, S. Hard-sphere statistics along the metastable amorphous branch. *Physical Review E* **58**, 532 (1998).

[55] Sciortino, F. & Tartaglia, P. Glassy colloidal systems. *Advances in Physics* **54**, 471 (2005).

[56] Rintoul, M. & Torquato, S. Computer simulations of dense hard-sphere systems. *Journal of Chemical Physics* **105**, 9258 (1996).

[57] Hastings, R. On the crystallization of macroionic solutions. *Journal of Chemical Physics* **68**, 675 (1978).

[58] Lindsay, H. & Chaikin, P. Elastic properties of colloidal crystals and glasses. *Journal of Chemical Physics* **76**, 3774 (1982).

[59] Murray, C. & Van Winkle, D. Experimental observation of two-stage melting in a classical two-dimensional screened coulomb system. *Physical Review Letters* **58**, 1200 (1987).

[60] Pusey, P. & Van Megen, W. Phase behaviour of concentrated suspensions of nearly hard colloidal spheres. *Nature* **320**, 340 (1986).

[61] Israelachvili, J. N. *Intermolecular and Surface forces* (Academic press, 2011).

[62] Asakura, S. & Oosawa, F. On interaction between two bodies immersed in a solution of macromolecules. *Journal of Chemical Physics* **22**, 1255 (1954).

[63] Mravlak, M. Depletion force. *University of Ljubljana* 3 (2008).

[64] Goodwin, J. *Colloids and Interfaces with Surfactants and Polymers* (John Wiley & Sons, 2009).

[65] Ramakrishnan, S., Fuchs, M., Schweizer, K. S. & Zukoski, C. F. Entropy driven phase transitions in colloid–polymer suspensions: Tests of depletion theories. *Journal of Chemical Physics* **116**, 2201 (2002).

[66] Pham, K. N. *et al.* Multiple glassy states in a simple model system. *Science* **296**, 104 (2002).

[67] Dinsmore, A., Yodh, A., Pine, D. *et al.* Entropic control of particle motion using passive surface microstructures. *Nature* **383**, 239 (1996).

[68] Dinsmore, A., Wong, D., Nelson, P. & Yodh, A. Hard spheres in vesicles: curvature-induced forces and particle-induced curvature. *Physical Review Letters* **80**, 409 (1998).

[69] Dinsmore, A. & Yodh, A. Entropic confinement of colloidal spheres in corners on silicon substrates. *Langmuir* **15**, 314 (1999).

[70] Yethiraj, A. Tunable colloids: control of colloidal phase transitions with tunable interactions. *Soft Matter* **3**, 1099 (2007).

[71] Rossi, L. *et al.* Shape-sensitive crystallization in colloidal superball fluids. *Proceedings of the National Academy of Sciences* **112**, 5286 (2015).

[72] Kraft, D. J. *et al.* Surface roughness directed self-assembly of patchy particles into colloidal micelles. *Proceedings of the National Academy of Sciences* **109**, 10787 (2012).

[73] Kamp, M. *et al.* Selective depletion interactions in mixtures of rough and smooth silica spheres. *Langmuir* **32**, 1233 (2016).

[74] Zhao, K. & Mason, T. G. Directing colloidal self-assembly through roughness-controlled depletion attractions. *Physical Review Letters* **99**, 268301 (2007).

[75] Sanders, J. Colour of precious opal. *Nature* **204**, 1151 (1964).

[76] Rayleigh, L. On the remarkable phenomenon of crystalline reflexion described by prof. stokes. *Philosophical Magazine and Journal of Science* **26**, 256 (1888).

[77] Yablonovitch, E. Inhibited spontaneous emission in solid-state physics and electronics. *Physical Review Letters* **58**, 2059 (1987).

[78] John, S. Strong localization of photons in certain disordered dielectric superlattices. *Physical Review Letters* **58**, 2486 (1987).

[79] Painter, O. *et al.* Two-dimensional photonic band-gap defect mode laser. *Science* **284**, 1819 (1999).

[80] Bragg, W. H. & Bragg, W. L. The reflection of x-rays by crystals. *Proceedings of the Royal Society of London* **88**, 428 (1913).

[81] Royall, C., Leunissen, M. & Van Blaaderen, A. A new colloidal model system to study long-range interactions quantitatively in real space. *Journal of Physics: Condensed Matter* **15**, S3581 (2003).

[82] Míguez, H. *et al.* Control of the photonic crystal properties of fcc-packed submicrometer sio2 spheres by sintering. *Advanced Materials* **10**, 480 (1998).

[83] Davis, K., Russel, W. & Glantschnig, W. Disorder-to-order transition in settling suspensions of colloidal silica: X-ray measurements. *Science* **245**, 507 (1989).

[84] Denkov, N. D. Two-dimensional crystallization. *Nature* **361**, 26 (1993).

[85] Jiang, P., Bertone, J., Hwang, K. & Colvin, V. Single-crystal colloidal multilayers of controlled thickness. *Chemistry of Materials* **11**, 2132 (1999).

[86] Mıguez, H., Yang, S. & Ozin, G. Colloidal photonic crystal microchannel array with periodically modulated thickness. *Applied Physics Letters* **81**, 2493 (2002).

[87] Kim, E., Xia, Y. & Whitesides, G. M. Micromolding in capillaries: applications in materials science. *Journal of the American Chemical Society* **118**, 5722 (1996).

[88] Kim, E., Xia, Y. & Whitesides, G. M. Two-and three-dimensional crystallization of polymeric microspheres by micromolding in capillaries. *Advanced Materials* **8**, 245 (1996).

[89] Wong, S., Kitaev, V. & Ozin, G. A. Colloidal crystal films: advances in universality and perfection. *Journal of the American Chemical Society* **125**, 15589 (2003).

[90] Helseth, L. Self-assembly of colloidal pyramids in magnetic fields. *Langmuir* **21**, 7276 (2005).

[91] Trau, M., Saville, D. & Aksay, I. Field-induced layering of colloidal crystals. *Science* **272**, 706 (1996).

[92] Juárez, J. J., Feicht, S. E. & Bevan, M. A. Electric field mediated assembly of three dimensional equilibrium colloidal crystals. *Soft Matter* **8**, 94 (2012).

[93] Edwards, T. D. & Bevan, M. A. Controlling colloidal particles with electric fields. *Langmuir* **30**, 10793 (2014).

[94] Zhang, K.-Q. & Liu, X. Y. In situ observation of colloidal monolayer nucleation driven by an alternating electric field. *Nature* **429**, 739 (2004).

[95] Yethiraj, A. & van Blaaderen, A. A colloidal model system with an interaction tunable from hard sphere to soft and dipolar. *Nature* **421**, 513 (2003).

[96] Korda, P. T. & Grier, D. G. Annealing thin colloidal crystals with optical gradient forces. *Journal of Chemical Physics* **114**, 7570 (2001).

[97] Gu, Z.-Z., Fujishima, A. & Sato, O. Patterning of a colloidal crystal film on a modified hydrophilic and hydrophobic surface. *Angewandte Chemie* **114**, 2171 (2002).

[98] Wang, Y. *et al.* Crystallization of dna-coated colloids. *Nature Communications* **6** (2015).

[99] Jones, M. R. *et al.* Dna-nanoparticle superlattices formed from anisotropic building blocks. *Nature Materials* **9**, 913 (2010).

[100] Barth, J. V., Costantini, G. & Kern, K. Engineering atomic and molecular nanostructures at surfaces. *Nature* **437**, 671 (2005).

[101] Brune, H. Microscopic view of epitaxial metal growth: nucleation and aggregation. *Surface Science Reports* **31**, 125 (1998).

[102] Venables, J. A. Atomic processes in crystal growth. *Surface Science* **299**, 798 (1994).

[103] Schroeder, M. & Wolf, D. Diffusion on strained surfaces. *Surface Science* **375**, 129 (1997).

[104] Lin, H. *et al.* Self-organized growth of nanopucks on pb quantum islands. *Physical Review Letters* **94**, 136101 (2005).

[105] Roder, H., Hahn, E., Brune, H., Bucher, J.-P. & Kern, K. Building one-dimensional and 2-dimensional nanostructures by diffusion-controlled aggregation at surfaces. *Nature* **366**, 141 (1993).

[106] Larsson, M., Cho, K. & Clemens, B. Surface diffusion mechanisms for strain-induced self-assembly. *Physical Review B* **69**, 155426 (2004).

[107] Brune, H. *et al.* Effect of strain on surface diffusion and nucleation. *Physical Review B* **52**, R14380 (1995).

[108] Brune, H., Giovannini, M., Bromann, K. & Kern, K. Self-organized growth of nanostructure arrays on strain-relief patterns. *Nature* **394**, 451 (1998).

[109] Aizenberg, J., Black, A. J. & Whitesides, G. M. Control of crystal nucleation by patterned self-assembled monolayers. *Nature* **398**, 495 (1999).

[110] Wang, W. *et al.* Patterned nucleation control in vacuum deposition of organic molecules. *Physical Review Letters* **98**, 225504 (2007).

[111] van Blaaderen, A., Ruel, R., Wiltzius, P. *et al.* Template-directed colloidal crystallization. *Nature* **385**, 321 (1997).

[112] Savage, J. R. *et al.* Entropy-driven crystal formation on highly strained substrates. *Proceedings of the National Academy of Sciences* **110**, 9301 (2013).

[113] van Blaaderen, A. & Wiltzius, P. Growing large, well-oriented colloidal crystals. *Advanced Materials* **9**, 833 (1997).

[114] Hoogenboom, J. P., van Langen-Suurling, A., Romijn, J. & van Blaaderen, A. Hard-sphere crystals with hcp and non-close-packed structure grown by colloidal epitaxy. *Physical Review Letters* **90**, 138301 (2003).

[115] Xia, Y., Kim, E., Zhao, X.-M., Rogers, J. A. *et al.* Complex optical surfaces formed by replica molding against elastomeric masters. *Science* **273**, 347 (1996).

[116] Lin, K.-h. *et al.* Entropically driven colloidal crystallization on patterned surfaces. *Physical Review Letters* **85**, 1770 (2000).

[117] Savage, J., Blair, D., Levine, A., Guyer, R. & Dinsmore, A. Imaging the sublimation dynamics of colloidal crystallites. *Science* **314**, 795 (2006).

[118] Venables, J., Spiller, G. & Hanbucken, M. Nucleation and growth of thin films. *Reports on Progress in Physics* **47**, 399 (1984).

[119] Ehrlich, G. & Hudda, F. Atomic view of surface self-diffusion: Tungsten on tungsten. *Journal of Chemical Physics* **44**, 1039 (1966).

[120] Schwoebel, R. L. & Shipsey, E. J. Step motion on crystal surfaces. *Journal of Applied Physics* **37**, 3682 (1966).

[121] Schindler, A. *Theoretical Aspects of Growth on One- and Two-dimensional Strained Crystal Surfaces.* Ph.D. thesis, Universität Duisburg-Essen, Fakultät für Physik (1999).

[122] Lee, H., Johnson, J., He, M., Speck, J. & Petroff, P. Strain-engineered self-assembled semiconductor quantum dot lattices. *Applied Physics Letters* **78**, 105 (2001).

[123] Shchukin, V. A. & Bimberg, D. Spontaneous ordering of nanostructures on crystal surfaces. *Reviews of Modern Physics* **71**, 1125 (1999).

[124] Rousset, S. *et al.* Self-organized epitaxial growth on spontaneously nano-patterned templates. *Comptes Rendus Physique* **6**, 33 (2005).

[125] Gerardot, B. *et al.* Self-assembling quantum dot lattices through nucleation site engineering. *Journal of Crystal Growth* **236**, 647 (2002).

[126] Yokoyama, T., Yokoyama, S., Kamikado, T., Okuno, Y. & Mashiko, S. Selective assembly on a surface of supramolecular aggregates with controlled size and shape. *Nature* **413**, 619 (2001).

[127] Fischer, B., Brune, H., Barth, J. V., Fricke, A. & Kern, K. Nucleation kinetics on inhomogeneous substrates: Al/au (111). *Physical Review Letters* **82**, 1732 (1999).

[128] Brune, H. & Kern, K. Heteroepitaxial metal growth: the effects of strain. *Chemical Physics of Solid Surfaces* **8**, 149 (1997).

[129] Rohart, S., Baudot, G., Repain, V., Girard, Y. & Rousset, S. Site selective nucleation on surfaces: the rate equation model compared with vt-stm experiment of co on au (788). *Journal of Crystal Growth* **275**, e203 (2005).

[130] Matthews, J. *Epitaxial Growth* (Elsevier, 2012).

[131] Priester, C. & Lannoo, M. Origin of self-assembled quantum dots in highly mismatched heteroepitaxy. *Physical Review Letters* **75**, 93 (1995).

[132] Daruka, I. & Barabási, A.-L. Island formation and critical thickness in heteroepitaxy. *Physical Review Letters* **78**, 3027 (1997).

[133] Lee, C. & Barabási, A.-L. Spatial ordering of islands grown on patterned surfaces. *Applied Physics Letters* **73**, 2651 (1998).

[134] Seifert, W. *et al.* In-situ growth of quantum dot structures by the stranski-krastanow growth mode. *Progress in Crystal Growth and Characterization of Materials* **33**, 423 (1996).

[135] Heidemeyer, H., Denker, U., Müller, C. & Schmidt, O. Morphology response to strain field interferences in stacks of highly ordered quantum dot arrays. *Physical Review Letters* **91**, 196103 (2003).

[136] Aminpour, M., Trushin, O. & Rahman, T. S. Effect of misfit dislocation on surface diffusion. *Physical Review B* **84**, 035455 (2011).

[137] Stranski, I. N. & Krastanow, L. v. Zur theorie der orientierten ausscheidung von ionenkristallen aufeinander. *Monatshefte für Chemie* **71**, 351 (1937).

[138] Venables, J. A. Nucleation growth and pattern formation in heteroepitaxy. *Physica A* **239**, 35 (1997).

[139] Repain, V., Baudot, G., Ellmer, H. & Rousset, S. Two-dimensional long-range–ordered growth of uniform cobalt nanostructures on a au (111) vicinal template. *Europhysics Letters* **58**, 730 (2002).

[140] Nayfeh, A., Chui, C. O., Saraswat, K. C. & Yonehara, T. Effects of hydrogen annealing on heteroepitaxial-ge layers on si: Surface roughness and electrical quality. *Applied Physics Letters* **85**, 2815 (2004).

[141] Tersoff, J., Teichert, C. & Lagally, M. Self-organization in growth of quantum dot superlattices. *Physical Review Letters* **76**, 1675 (1996).

[142] Hanbücken, M. & Deville, J.-P. *Stress and Strain in Epitaxy* (Elsevier Science, 2001).

[143] Meng, G., Paulose, J., Nelson, D. R. & Manoharan, V. N. Elastic instability of a crystal growing on a curved surface. *Science* **343**, 634 (2014).

[144] Manoharan, V. N. Colloidal matter: Packing, geometry, and entropy. *Science* **349**, 1253751 (2015).

[145] Barabási, A.-L. & Stanley, H. E. *Fractal Concepts in Surface Growth* (Cambridge university press, 1995).

[146] Jensen, P., Barabási, A.-L., Larralde, H., Havlin, S. & Stanley, H. Deposition, diffusion, and aggregation of atoms on surfaces: A model for nanostructure growth. *Physical Review B* **50**, 15316 (1994).

[147] Fick, A. On liquid diffusion. *Philosophical Magazine and Journal of Science* **10**, 30 (1855).

[148] Fick, A. Über diffusion. *Poggendorff's Annalen der Physik* **94**, 59 (1855).

[149] Angell, C. A. Formation of glasses from liquids and biopolymers. *Science* **267**, 1924 (1995).

[150] Stillinger, F. H. A topographic view of supercooled liquids and glass formation. *Science* **267**, 1935 (1995).

[151] Götze, W. & Sjögren, L. Relaxation processes in supercooled liquids. *Reports on Progress in Physics* **55**, 241 (1992).

[152] Ediger, M. D., Angell, C. & Nagel, S. R. Supercooled liquids and glasses. *Journal of Physical Chemistry* **100**, 13200 (1996).

[153] Debenedetti, P. G. & Stillinger, F. H. Supercooled liquids and the glass transition. *Nature* **410**, 259 (2001).

[154] Andersen, H. C. Molecular dynamics studies of heterogeneous dynamics and dynamic crossover in supercooled atomic liquids. *Proceedings of the National Academy of Sciences* **102**, 6686 (2005).

[155] Dawson, K. A. The glass paradigm for colloidal glasses, gels, and other arrested states driven by attractive interactions. *Current opinion in Colloid & Interface Science* **7**, 218 (2002).

[156] Torquato, S. & Stillinger, F. H. Jammed hard-particle packings: From kepler to bernal and beyond. *Reviews of Modern Physics* **82**, 2633 (2010).

[157] Debenedetti, P. G. *Metastable Liquids: Concepts and Principles* (Princeton University Press, 1996).

[158] Das, S. P. Mode-coupling theory and the glass transition in supercooled liquids. *Reviews of Modern Physics* **76**, 785 (2004).

[159] Dyre, J. C. Colloquium: The glass transition and elastic models of glass-forming liquids. *Reviews of Modern Physics* **78**, 953 (2006).

[160] Kauzmann, W. The nature of the glassy state and the behavior of liquids at low temperatures. *Chemical Reviews* **43**, 219 (1948).

[161] Leheny, R. L. *et al.* Structural studies of an organic liquid through the glass transition. *Journal of Chemical Physics* **105**, 7783 (1996).

[162] Angell, C. Perspective on the glass transition. *Journal of Physics and Chemistry of Solids* **49**, 863 (1988).

[163] Angell, C. Relaxation in liquids, polymers and plastic crystals—strong/fragile patterns and problems. *Journal of Non-Crystalline Solids* **131**, 13 (1991).

[164] Vogel, H. The law of the relation between the viscosity of liquids and the temperature. *Phys. Z* **22**, 645 (1921).

[165] Fulcher, G. S. Analysis of recent measurements of the viscosity of glasses. *Journal of the American Ceramic Society* **8**, 339 (1925).

[166] Tammann, G. & Hesse, W. Die abhängigkeit der viscosität von der temperatur bie unterkühlten flüssigkeiten. *Zeitschrift für anorganische und allgemeine Chemie* **156**, 245 (1926).

[167] Bässler, H. Viscous flow in supercooled liquids analyzed in terms of transport theory for random media with energetic disorder. *Physical Review Letters* **58**, 767 (1987).

[168] Elmatad, Y. S., Chandler, D. & Garrahan, J. P. Corresponding states of structural glass formers. *Journal of Physical Chemistry B* **113**, 5563 (2009).

[169] Cohen, M. H. & Turnbull, D. Molecular transport in liquids and glasses. *Journal of Chemical Physics* **31**, 1164 (1959).

[170] Turnbull, D. & Cohen, M. H. Free-volume model of the amorphous phase: glass transition. *Journal of Chemical Physics* **34**, 120 (1961).

[171] Gibbs, J. H. & DiMarzio, E. A. Nature of the glass transition and the glassy state. *Journal of Chemical Physics* **28**, 373 (1958).

[172] Adam, G. & Gibbs, J. H. On the temperature dependence of cooperative relaxation properties in glass-forming liquids. *Journal of Chemical Physics* **43**, 139 (1965).

[173] Stillinger, F. H. & Weber, T. A. Hidden structure in liquids. *Physical Review A* **25**, 978 (1982).

[174] Stillinger, F. H. & Weber, T. A. Dynamics of structural transitions in liquids. *Physical Review A* **28**, 2408 (1983).

[175] Bengtzelius, U., Gotze, W. & Sjolander, A. Dynamics of supercooled liquids and the glass transition. *Journal of Physics C* **17**, 5915 (1984).

[176] Bosse, J., Götze, W. & Lücke, M. Mode-coupling theory of simple classical liquids. *Physical Review A* **17**, 434 (1978).

[177] Kirkpatrick, T. & Thirumalai, D. Dynamics of the structural glass transition and the p-spin—interaction spin-glass model. *Physical Review Letters* **58**, 2091 (1987).

[178] Kirkpatrick, T. & Thirumalai, D. p-spin-interaction spin-glass models: Connections with the structural glass problem. *Physical Review B* **36**, 5388 (1987).

[179] Kirkpatrick, T., Thirumalai, D. & Wolynes, P. G. Scaling concepts for the dynamics of viscous liquids near an ideal glassy state. *Physical Review A* **40**, 1045 (1989).

[180] Garrahan, J. P. & Chandler, D. Geometrical explanation and scaling of dynamical heterogeneities in glass forming systems. *Physical Review Letters* **89**, 035704 (2002).

[181] Garrahan, J. P. & Chandler, D. Coarse-grained microscopic model of glass formers. *Proceedings of the National Academy of Sciences* **100**, 9710 (2003).

[182] Leutheusser, E. Dynamical model of the liquid-glass transition. *Physical Review A* **29**, 2765 (1984).

[183] Berthier, L., Biroli, G., Bouchaud, J.-P., Cipelletti, L. & van Saarloos, W. *Dynamical Heterogeneities in Glasses, Colloids, and Granular Media*, vol. 150 (OUP Oxford, 2011).

[184] Götze, W. The essentials of the mode-coupling theory for glassy dynamics. *Condensed Matter Physics* **4**, 873 (1998).

[185] Kob, W. The mode-coupling theory of the glass transition. *arXiv preprint cond-mat/9702073* (1997).

[186] Götze, W. & Sjögren, L. Scaling properties in supercooled liquids near the glass transition. *Journal of Physics C* **21**, 3407 (1988).

[187] Frick, B., Farago, B. & Richter, D. Temperature dependence of the nonergodicity parameter in polybutadiene in the neighborhood of the glass transition. *Physical Review Letters* **64**, 2921 (1990).

[188] Fuchs, M., Gotze, W., Hildebrand, S. & Latz, A. A theory for the $\beta-$relaxation process near the liquid-to-glass crossover. *Journal of Physics: Condensed Matter* **4**, 7709 (1992).

[189] Gleim, T. & Kob, W. The $\beta-$relaxation dynamics of a simple liquid. *European Physical Journal B* **13**, 83 (2000).

[190] Götze, W. The scaling functions for the $\beta-$relaxation process of supercooled liquids and glasses. *Journal of Physics: Condensed Matter* **2**, 8485 (1990).

[191] Kob, W. & Andersen, H. C. Testing mode-coupling theory for a supercooled binary lennard-jones mixture i: The van hove correlation function. *Physical Review E* **51**, 4626 (1995).

[192] Götze, W. & Sjögren, L. α-relaxation near the liquid-glass transition. *Journal of Physics C* **20**, 879 (1987).

[193] Kob, W. & Andersen, H. C. Testing mode-coupling theory for a supercooled binary lennard-jones mixture. ii. intermediate scattering function and dynamic susceptibility. *Physical Review E* **52**, 4134 (1995).

[194] Kob, W. & Andersen, H. C. Scaling behavior in the β-relaxation regime of a supercooled lennard-jones mixture. *Physical Review Letters* **73**, 1376 (1994).

[195] Dawson, K., Foffi, G., Sciortino, F., Tartaglia, P. & Zaccarelli, E. Mode-coupling theory of colloids with short-range attractions. *Journal of Physics: Condensed Matter* **13**, 9113 (2001).

[196] De Michele, C., Schilling, R. & Sciortino, F. Dynamics of uniaxial hard ellipsoids. *Physical Review Letters* **98**, 265702 (2007).

[197] Pfleiderer, P., Milinkovic, K. & Schilling, T. Glassy dynamics in monodisperse hard ellipsoids. *Europhysics Letters* **84**, 16003 (2008).

[198] Verduin, H. & Dhont, J. K. Phase diagram of a model adhesive hard-sphere dispersion. *Journal of Colloid & Interface Science* **172**, 425 (1995).

[199] Chen, S.-H., Chen, W.-R. & Mallamace, F. The glass-to-glass transition and its end point in a copolymer micellar system. *Science* **300**, 619 (2003).

[200] Dawson, K. *et al.* Higher-order glass-transition singularities in colloidal systems with attractive interactions. *Physical Review E* **63**, 011401 (2000).

[201] Frenkel, D. & Mulder, B. The hard ellipsoid-of-revolution fluid: Monte carlo simulations. *Molecular Physics* **55**, 1171 (1985).

[202] Radu, M., Pfleiderer, P. & Schilling, T. Solid-solid phase transition in hard ellipsoids. *Journal of Chemical Physics* **131**, 164513 (2009).

[203] Letz, M., Schilling, R. & Latz, A. Ideal glass transitions for hard ellipsoids. *Physical Review E* **62**, 5173 (2000).

[204] Pfleiderer, P. & Schilling, T. Simple monoclinic crystal phase in suspensions of hard ellipsoids. *Physical Review E* **75**, 020402 (2007).

[205] Bartsch, E. Diffusion in concentrated colloidal suspensions and glasses. *Current Opinion in Colloid & Interface Science* **3**, 577 (1998).

[206] Schweizer, K. S. Dynamical fluctuation effects in glassy colloidal suspensions. *Current Opinion in Colloid & Interface Science* **12**, 297 (2007).

[207] Hunter, G. L. & Weeks, E. R. The physics of the colloidal glass transition. *Reports on Progress in Physics* **75**, 066501 (2012).

[208] Di Cola, E., Moussaïd, A., Sztucki, M., Narayanan, T. & Zaccarelli, E. Correlation between structure and rheology of a model colloidal glass. *Journal of Chemical Physics* **131**, 144903 (2009).

[209] Gleim, T., Kob, W. & Binder, K. How does the relaxation of a supercooled liquid depend on its microscopic dynamics? *Physical Review Letters* **81**, 4404 (1998).

[210] Szamel, G. & Flenner, E. Independence of the relaxation of a supercooled fluid from its microscopic dynamics: Need for yet another extension of the mode-coupling theory. *Europhysics Letters* **67**, 779 (2004).

[211] Tokuyama, M., Yamazaki, H. & Terada, Y. Test of mean-field equations for two types of hard-sphere systems by a brownian-dynamics simulation and a molecular-dynamics simulation. *Physical Review E* **67**, 062403 (2003).

[212] Berthier, L. *et al.* Spontaneous and induced dynamic fluctuations in glass formers. i. general results and dependence on ensemble and dynamics. *Journal of Chemical Physics* **126**, 184503 (2007).

[213] Auer, S. & Frenkel, D. Suppression of crystal nucleation in polydisperse colloids due to increase of the surface free energy. *Nature* **413**, 711 (2001).

[214] Henderson, S. & Van Megen, W. Metastability and crystallization in suspensions of mixtures of hard spheres. *Physical Review Letters* **80**, 877 (1998).

[215] Bolhuis, P. G. & Kofke, D. A. Monte carlo study of freezing of polydisperse hard spheres. *Physical Review E* **54**, 634 (1996).

[216] Fasolo, M. & Sollich, P. Equilibrium phase behavior of polydisperse hard spheres. *Physical Review Letters* **91**, 068301 (2003).

[217] Sollich, P. & Wilding, N. B. Crystalline phases of polydisperse spheres. *Physical Review Letters* **104**, 118302 (2010).

[218] Zhu, J. *et al.* Crystallization of hard-sphere colloids in microgravity. *Nature* **387**, 883 (1997).

[219] Pusey, P. N. & van Megen, W. Observation of a glass transition in suspensions of spherical colloidal particles. *Physical Review Letters* **59**, 2083 (1987).

[220] Kasper, A., Bartsch, E. & Sillescu, H. Self-diffusion in concentrated colloid suspensions studied by digital video microscopy of core-shell tracer particles. *Langmuir* **14**, 5004 (1998).

[221] Glotzer, S. C. Spatially heterogeneous dynamics in liquids: insights from simulation. *Journal of Non-Crystalline Solids* **274**, 342 (2000).

[222] Stevenson, J. D., Schmalian, J. & Wolynes, P. G. The shapes of cooperatively rearranging regions in glass-forming liquids. *Nature Physics* **2**, 268 (2006).

[223] Kob, W., Roldán-Vargas, S. & Berthier, L. Non-monotonic temperature evolution of dynamic correlations in glass-forming liquids. *Nature Physics* **8**, 164 (2012).

[224] Pusey, P., Pirie, A. & Poon, W. Dynamics of colloid-polymer mixtures. *Physica A* **201**, 322 (1993).

[225] Eckert, T. & Bartsch, E. Re-entrant glass transition in a colloid-polymer mixture with depletion attractions. *Physical Review Letters* **89**, 125701 (2002).

[226] Zaccarelli, E. & Poon, W. C. Colloidal glasses and gels: The interplay of bonding and caging. *Proceedings of the National Academy of Sciences* **106**, 15203 (2009).

[227] Foffi, G. *et al.* Phase equilibria and glass transition in colloidal systems with short-ranged attractive interactions: application to protein crystallization. *Physical Review E* **65**, 031407 (2002).

[228] Poon, W. Crystallization of globular proteins. *Physical Review E* **55**, 3762 (1997).

[229] Piazza, R. Interactions and phase transitions in protein solutions. *Current Opinion in Colloid & Interface Science* **5**, 38 (2000).

[230] Malfois, M., Bonneté, F., Belloni, L. & Tardieu, A. A model of attractive interactions to account for fluid–fluid phase separation of protein solutions. *Journal of Chemical Physics* **105**, 3290 (1996).

[231] Weeks, E. R. Viewpoint: Two for one in a colloidal glass. *Physics* **4**, 61 (2011).

[232] Donev, A., Stillinger, F. H., Chaikin, P. & Torquato, S. Unusually dense crystal packings of ellipsoids. *Physical Review Letters* **92**, 255506 (2004).

[233] Odriozola, G. Revisiting the phase diagram of hard ellipsoids. *Journal of Chemical Physics* **136**, 134505 (2012).

[234] Cang, H., Li, J., Novikov, V. & Fayer, M. Dynamical signature of two "ideal glass transitions" in nematic liquid crystals. *Journal of Chemical Physics* **119**, 10421 (2003).

[235] Zheng, Z., Wang, F., Han, Y. *et al.* Glass transitions in quasi-two-dimensional suspensions of colloidal ellipsoids. *Physical Review Letters* **107**, 065702 (2011).

[236] Kruger, S., Mögel, H.-J., Wahab, M. & Schiller, P. Depletion force between anisometric colloidal particles. *Langmuir* **27**, 646 (2010).

[237] Jones, R. A. *Soft Condensed Matter*, vol. 6 (Oxford University Press, 2002).

[238] de Kruif, C. d., Van Iersel, E., Vrij, A. & Russel, W. Hard sphere colloidal dispersions: Viscosity as a function of shear rate and volume fraction. *Journal of Chemical Physics* **83**, 4717 (1985).

[239] Van der Werff, J. & De Kruif, C. Hard-sphere colloidal dispersions: The scaling of rheological properties with particle size, volume fraction, and shear rate. *Journal of Rheology* **33**, 421 (1989).

[240] Bender, J. & Wagner, N. J. Reversible shear thickening in monodisperse and bidisperse colloidal dispersions. *Journal of Rheology* **40**, 899 (1996).

[241] Russel, W. B., Saville, D. A. & Schowalter, W. R. *Colloidal Dispersions* (Cambridge university press, 1989).

[242] Lionberger, R. Shear thinning of colloidal dispersions. *Journal of Rheology* **42**, 843 (1998).

[243] Wagner, N. J. & Brady, J. F. Shear thickening in colloidal dispersions. *Physics Today* **62**, 27 (2009).

[244] Hoffman, R. L. Explanations for the cause of shear thickening in concentrated colloidal suspensions. *Journal of Rheology* **42**, 111 (1998).

[245] Reynolds, O. An experimental investigation of the circumstances which determine whether the motion of water shall be direct or sinuous, and of the law of resistance in parallel channels. *Proceedings of the Royal Society of London* **35**, 84 (1883).

[246] Rott, N. Note on the history of the reynolds number. *Annual Review of Fluid Mechanics* **22**, 1 (1990).

[247] Feynman, R. P., Leighton, R. B. & Sands, M. *The Feynman Lectures on Physics, Volume I*, vol. 1 (Basic books, 2013).

[248] Einstein, A. The theory of the brownian movement. *Ann. der Physik* **17**, 549 (1905).

[249] Einstein, A. *Investigations on the Theory of the Brownian Movement* (Courier Corporation, 1956).

[250] Von Smoluchowski, M. Zur kinetischen theorie der brownschen molekularbewegung und der suspensionen. *Annalen der Physik* **326**, 756 (1906).

[251] Sutherland, W. A dynamical theory of diffusion for non-electrolytes and the molecular mass of albumin. *Philosophical Magazine and Journal of Science* **9**, 781 (1905).

[252] Edward, J. T. Molecular volumes and the stokes-einstein equation. *J. Chem. Educ* **47**, 261 (1970).

[253] Lamb, H. *Hydrodynamics* (Cambridge university press, 1932).

[254] Batchelor, G. K. *An Introduction to Fluid Dynamics* (Cambridge university press, 2000).

[255] Swallen, S. F., Bonvallet, P. A., McMahon, R. J. & Ediger, M. Self-diffusion of tris-naphthylbenzene near the glass transition temperature. *Physical Review Letters* **90**, 015901 (2003).

[256] Swallen, S. F., Traynor, K., McMahon, R. J., Ediger, M. & Mates, T. E. Self-diffusion of supercooled tris-naphthylbenzene. *Journal of Physical Chemistry B* **113**, 4600 (2009).

[257] Mapes, M. K., Swallen, S. F. & Ediger, M. Self-diffusion of supercooled o-terphenyl near the glass transition temperature. *Journal of Physical Chemistry B* **110**, 507 (2006).

[258] Rössler, E. Indications for a change of diffusion mechanism in supercooled liquids. *Physical Review Letters* **65**, 1595 (1990).

[259] Andreozzi, L., Bagnoli, M., Faetti, M. & Giordano, M. Rotational probe relaxation and scaling in fragile glass formers. *Journal of Non-crystalline Solids* **303**, 262 (2002).

[260] Cicerone, M. T., Blackburn, F. & Ediger, M. How do molecules move near tg? molecular rotation of six probes in o-terphenyl across 14 decades in time. *Journal of Chemical Physics* **102**, 471 (1995).

[261] Blackburn, F., Wang, C.-Y. & Ediger, M. Translational and rotational motion of probes in supercooled 1, 3, 5-tris (naphthyl) benzene. *Journal of Physical Chemistry* **100**, 18249 (1996).

[262] Chen, S.-H. *et al.* The violation of the stokes-einstein relation in supercooled water. *Proceedings of the National Academy of Sciences* **103**, 12974 (2006).

[263] Chen, B., Sigmund, E. E. & Halperin, W. Stokes-einstein relation in supercooled aqueous solutions of glycerol. *Physical Review Letters* **96**, 145502 (2006).

[264] Edmond, K. V., Elsesser, M. T., Hunter, G. L., Pine, D. J. & Weeks, E. R. Decoupling of rotational and translational diffusion in supercooled colloidal fluids. *Proceedings of the National Academy of Sciences* **109**, 17891 (2012).

[265] Ediger, M. D. Spatially heterogeneous dynamics in supercooled liquids. *Annual Review of Physical Chemistry* **51**, 99 (2000).

[266] Sillescu, H. Heterogeneity at the glass transition: a review. *Journal of Non-Crystalline Solids* **243**, 81 (1999).

[267] Hodgdon, J. A. & Stillinger, F. H. Stokes-einstein violation in glass-forming liquids. *Physical Review E* **48**, 207 (1993).

[268] Stillinger, F. H. & Hodgdon, J. A. Translation-rotation paradox for diffusion in fragile glass-forming liquids. *Physical Review E* **50**, 2064 (1994).

[269] Douglas, J. & Leporini, D. Obstruction model of the fractional stokes–einstein relation in glass-forming liquids. *Journal of Non-crystalline Solids* **235**, 137 (1998).

[270] Kim, J. & Keyes, T. On the breakdown of the stokes-einstein law in supercooled liquids. *Journal of Physical Chemistry B* **109**, 21445 (2005).

[271] Tarjus, G. & Kivelson, D. Breakdown of the stokes–einstein relation in supercooled liquids. *Journal of Chemical Physics* **103**, 3071 (1995).

[272] Schweizer, K. S. & Saltzman, E. J. Activated hopping, barrier fluctuations, and heterogeneity in glassy suspensions and liquids. *Journal of Physical Chemistry B* **108**, 19729 (2004).

[273] Kumar, P. *et al.* Relation between the widom line and the breakdown of the stokes–einstein relation in supercooled water. *Proceedings of the National Academy of Sciences* **104**, 9575 (2007).

[274] De Michele, C. & Leporini, D. Viscous flow and jump dynamics in molecular supercooled liquids. ii. rotations. *Physical Review E* **63**, 036702 (2001).

[275] Netz, P. A., Starr, F. W., Stanley, H. E. & Barbosa, M. C. Static and dynamic properties of stretched water. *Journal of Chemical Physics* **115**, 344 (2001).

[276] Netz, P. A., Starr, F. W., Barbosa, M. C. & Stanley, H. E. Relation between structural and dynamical anomalies in supercooled water. *Physica A* **314**, 470 (2002).

[277] Becker, S. R., Poole, P. H. & Starr, F. W. Fractional stokes-einstein and debye-stokes-einstein relations in a network-forming liquid. *Physical Review Letters* **97**, 055901 (2006).

[278] Berthier, L., Chandler, D. & Garrahan, J. P. Length scale for the onset of fickian diffusion in supercooled liquids. *Europhysics Letters* **69**, 320 (2004).

[279] Dzugutov, M., Simdyankin, S. I. & Zetterling, F. H. Decoupling of diffusion from structural relaxation and spatial heterogeneity in a supercooled simple liquid. *Physical Review Letters* **89**, 195701 (2002).

[280] Xu, L. *et al.* Appearance of a fractional stokes–einstein relation in water and a structural interpretation of its onset. *Nature Physics* **5**, 565 (2009).

[281] Sengupta, S., Karmakar, S., Dasgupta, C. & Sastry, S. Breakdown of the stokes-einstein relation in two, three, and four dimensions. *Journal of Chemical Physics* **138**, 12A548 (2013).

[282] Perera, D. N. & Harrowell, P. Origin of the difference in the temperature dependences of diffusion and structural relaxation in a supercooled liquid. *Physical Review Letters* **81**, 120 (1998).

[283] Flenner, E., Staley, H. & Szamel, G. Universal features of dynamic heterogeneity in supercooled liquids. *Physical Review Letters* **112**, 097801 (2014).

[284] Chong, S.-H. & Kob, W. Coupling and decoupling between translational and rotational dynamics in a supercooled molecular liquid. *Physical Review Letters* **102**, 025702 (2009).

[285] Mazza, M. G., Giovambattista, N., Stanley, H. E. & Starr, F. W. Connection of translational and rotational dynamical heterogeneities with the breakdown of the stokes-einstein and stokes-einstein-debye relations in water. *Physical Review E* **76**, 031203 (2007).

[286] Jung, Y., Garrahan, J. P. & Chandler, D. Excitation lines and the breakdown of stokes-einstein relations in supercooled liquids. *Physical Review E* **69**, 061205 (2004).

[287] Chang, I. *et al.* Translational and rotational molecular motion in supercooled liquids studied by nmr and forced rayleigh scattering. *Journal of Non-crystalline Solids* **172**, 248 (1994).

[288] Fujara, F., Geil, B., Sillescu, H. & Fleischer, G. Translational and rotational diffusion in supercooled orthoterphenyl close to the glass transition. *Zeitschrift für Physik B Condensed Matter* **88**, 195 (1992).

[289] Berne, B. J. & Pecora, R. *Dynamic Light Lcattering: with Applications to Chemistry, Biology, and Physics* (Courier Corporation, 1976).

[290] Yamamoto, R. & Onuki, A. Heterogeneous diffusion in highly supercooled liquids. *Physical Review Letters* **81**, 4915 (1998).

[291] Mezei, F., Knaak, W. & Farago, B. Neutron spin-echo study of dynamic correlations near the liquid-glass transition. *Physical Review Letters* **58**, 571 (1987).

[292] Eaves, J. D. & Reichman, D. R. Spatial dimension and the dynamics of supercooled liquids. *Proceedings of the National Academy of Sciences* **106**, 15171 (2009).

[293] Dasgupta, C., Indrani, A., Ramaswamy, S. & Phani, M. Is there a growing correlation length near the glass transition? *Europhysics Letters* **15**, 307 (1991).

[294] Donati, C., Franz, S., Glotzer, S. C. & Parisi, G. Theory of non-linear susceptibility and correlation length in glasses and liquids. *Journal of Non-crystalline Solids* **307**, 215 (2002).

[295] Lačević, N., Starr, F. W., Schrøder, T. & Glotzer, S. Spatially heterogeneous dynamics investigated via a time-dependent four-point density correlation function. *Journal of Chemical Physics* **119**, 7372 (2003).

[296] Bennemann, C., Donati, C., Baschnagel, J. & Glotzer, S. C. Growing range of correlated motion in a polymer melt on cooling towards the glass transition. *Nature* **399**, 246 (1999).

[297] Donati, C., Glotzer, S. C. & Poole, P. H. Growing spatial correlations of particle displacements in a simulated liquid on cooling toward the glass transition. *Physical Review Letters* **82**, 5064 (1999).

[298] Berthier, L. *et al.* Direct experimental evidence of a growing length scale accompanying the glass transition. *Science* **310**, 1797 (2005).

[299] Flenner, E., Zhang, M. & Szamel, G. Analysis of a growing dynamic length scale in a glass-forming binary hard-sphere mixture. *Physical Review E* **83**, 051501 (2011).

[300] Waldow, D. A., Ediger, M., Yamaguchi, Y., Matsushita, Y. & Noda, I. Viscosity dependence of the local segmental dynamics of anthracene-labeled polystyrene in dilute solution. *Macromolecules* **24**, 3147 (1991).

[301] Cicerone, M. T. & Ediger, M. Photobleaching technique for measuring ultraslow reorientation near and below the glass transition: tetracene in o-terphenyl. *Journal of Physical Chemistry* **97**, 10489 (1993).

[302] Debye, P. J. W. *Polar Molecules* (Chemical Catalog Company, Incorporated, 1929).

[303] Jose, P. P., Chakrabarti, D. & Bagchi, B. Complete breakdown of the debye model of rotational relaxation near the isotropic-nematic phase boundary: Effects of intermolecular correlations in orientational dynamics. *Physical Review E* **73**, 031705 (2006).

[304] Fischer, E., Donth, E. & Steffen, W. Temperature dependence of characteristic length for glass transition. *Physical Review Letters* **68**, 2344 (1992).

[305] Zangi, R., Mackowiak, S. A. & Kaufman, L. J. Probe particles alter dynamic heterogeneities in simple supercooled systems. *Journal of Chemical Physics* **126**, 104501 (2007).

[306] Mackowiak, S. A., Noble, J. M. & Kaufman, L. J. Manifestations of probe presence on probe dynamics in supercooled liquids. *Journal of Chemical Physics* **135**, 214503 (2011).

[307] Hall, D. B., Deppe, D. D., Hamilton, K. E., Dhinojwala, A. & Torkelson, J. M. Probe translational and rotational diffusion in polymers near t_g: roles of probe size, shape, and secondary bonding in deviations from debye–stokes–einstein scaling. *Journal of Non-crystalline Solids* **235**, 48 (1998).

[308] Qin, D., Xia, Y. & Whitesides, G. M. Soft lithography for micro-and nanoscale patterning. *Nature Protocols* **5**, 491 (2010).

[309] Rogers, J. A. & Nuzzo, R. G. Recent progress in soft lithography. *Materials Today* **8**, 50 (2005).

[310] Xia, Y. & Whitesides, G. M. Soft lithography. *Annual Review of Materials Science* **28**, 153 (1998).

[311] Quake, S. R. & Scherer, A. From micro-to nanofabrication with soft materials. *Science* **290**, 1536 (2000).

[312] Xia, Y. *Soft lithography: micro- and nanofabrication based on microcontact printing and replica molding*. Ph.D. thesis, Harvard University (1996).

[313] Zhao, X.-M., Xia, Y. & Whitesides, G. M. Soft lithographic methods for nano-fabrication. *Journal of Materials Chemistry* **7**, 1069 (1997).

[314] Kumar, A. & Whitesides, G. M. Features of gold having micrometer to centimeter dimensions can be formed through a combination of stamping with an elastomeric stamp and an alkanethiol "ink"followed by chemical etching. *Applied Physics Letters* **63**, 2002 (1993).

[315] Zhao, X.-M., Xia, Y. & Whitesides, G. M. Fabrication of three-dimensional micro-structures: Microtransfer molding. *Advanced Materials* **8**, 837 (1996).

[316] Kim, E., Xia, Y., Whitesides, G. M. *et al.* Polymer microstructures formed by molding in capillaries. *Nature* **376**, 581 (1995).

[317] Kim, E., Xia, Y., Zhao, X.-M. & Whitesides, G. M. Solvent-assisted microcontact molding: A convenient method for fabricating three-dimensional structures on surfaces of polymers. *Advanced Materials* **9**, 651 (1997).

[318] Rogers, J. A., Paul, K. E., Jackman, R. J. & Whitesides, G. M. Using an elastomeric phase mask for sub-100 nm photolithography in the optical near field. *Applied Physics Letters* **70**, 2658 (1997).

[319] Chou, S. Y., Krauss, P. R. & Renstrom, P. J. Imprint of sub-25 nm vias and trenches in polymers. *Applied Physics Letters* **67**, 3114 (1995).

[320] Terris, B. *et al.* Nanoscale replication for scanning probe data storage. *Applied Physics Letters* **69**, 4262 (1996).

[321] Masuda, H. & Fukuda, K. Ordered metal nanohole arrays made by a two-step replication of honeycomb structures of anodic alumina. *Science* **268**, 1466 (1995).

[322] Clarson, S. J. & Semlyen, J. A. *Siloxane Polymers* (Prentice Hall, 1993).

[323] Zhang, J. *et al.* Template-directed convective assembly of three-dimensional face-centered-cubic colloidal crystals. *Applied Physics Letters* **81**, 3176 (2002).

[324] Stöber, W., Fink, A. & Bohn, E. Controlled growth of monodisperse silica spheres in the micron size range. *Journal of Colloid & Interface Science* **26**, 62 (1968).

[325] Zhang, L. *et al.* Hollow silica spheres: synthesis and mechanical properties. *Langmuir* **25**, 2711 (2009).

[326] Zou, D. *et al.* Model filled polymers. i. synthesis of crosslinked monodisperse polystyrene beads. *Journal of Polymer Science* **28**, 1909 (1990).

[327] Shim, S.-E., Cha, Y.-J., Byun, J.-M. & Choe, S. Size control of polystyrene beads by multistage seeded emulsion polymerization. *Journal of Applied Polymer Science* **71**, 2259 (1999).

[328] Yi, G.-R. *et al.* Colloidal clusters of silica or polymer microspheres. *Advanced Materials* **16**, 1204 (2004).

[329] Goodwin, J., Hearn, J., Ho, C. & Ottewill, R. Studies on the preparation and characterisation of monodisperse polystyrene latices. *Colloid & Polymer Science* **252**, 464 (1974).

[330] Rubinstein, M. & Colby, R. H. *Polymer Physics* (Oxford University Press: New York, 2003).

[331] Crocker, J. C. & Grier, D. G. Methods of digital video microscopy for colloidal studies. *Journal of Colloid & Interface Science* **179**, 298 (1996).

[332] Zhang, Z. & Lagally, M. G. Atomistic processes in the early stages of thin-film growth. *Science* **276**, 377 (1997).

[333] Cho, S.-Y., Jeon, H.-J., Kim, J.-S., Ok, J. M. & Jung, H.-T. Hierarchical ordering of quantum dots and liquid with tunable super-periodicity into high aspect ratio moiré superlattice structure. *Advanced Functional Materials* **24**, 6939 (2014).

[334] Chen, Z. *et al.* Two-dimensional crystallization of hexagonal bilayer with moiré patterns. *Journal of Physical Chemistry B* **116**, 4363 (2012).

[335] Zheng, H., Lee, I., Rubner, M. F., Hammond, P. T. *et al.* Two component particle arrays on patterned polyelectrolyte multilayer templates. *Advanced Materials* **14**, 569 (2002).

[336] Cheng, Z., Russel, W. B. & Chaikin, P. Controlled growth of hard-sphere colloidal crystals. *Nature* **401**, 893 (1999).

[337] Dziomkina, N. V. & Vancso, G. J. Colloidal crystal assembly on topologically patterned templates. *Soft Matter* **1**, 265 (2005).

[338] Wang, D. & Möhwald, H. Template-directed colloidal self-assembly− the route to 'top-down' nanochemical engineering. *Journal of Materials Chemistry* **14**, 459 (2004).

[339] Kalischewski, F. & Heuer, A. Dynamic effects on the loss of control in template-directed nucleation. *Physical Review B* **80**, 155421 (2009).

[340] Haas, G. *et al.* Nucleation and growth of supported clusters at defect sites: Pd/mgo (001). *Physical Review B* **61**, 11105 (2000).

[341] Kim, M., Anthony, S. M. & Granick, S. Activated surface diffusion in a simple colloid system. *Physical Review Letters* **102**, 178303 (2009).

[342] Genzer, J. Surface-bound gradients for studies of soft materials behavior. *Annual Review of Materials Research* **42**, 435 (2012).

[343] Kramb, R., Zhang, R., Schweizer, K. & Zukoski, C. Glass formation and shear elasticity in dense suspensions of repulsive anisotropic particles. *Physical Review Letters* **105**, 055702 (2010).

[344] Latka, A. *et al.* Particle dynamics in colloidal suspensions above and below the glass-liquid re-entrance transition. *Europhysics Letters* **86**, 58001 (2009).

[345] Kaufman, L. J. & Weitz, D. A. Direct imaging of repulsive and attractive colloidal glasses. *Journal of Chemical Physics* **125**, 074716 (2006).

[346] Simeonova, N. B. *et al.* Devitrification of colloidal glasses in real space. *Physical Review E* **73**, 041401 (2006).

[347] Puertas, A. M., Fuchs, M. & Cates, M. E. Comparative simulation study of colloidal gels and glasses. *Physical Review Letters* **88**, 098301 (2002).

[348] Arfken, G. B. & Weber, H. J. Mathematical methods for physicists (1999).

[349] Narumi, T., Franklin, S. V., Desmond, K. W., Tokuyama, M. & Weeks, E. R. Spatial and temporal dynamical heterogeneities approaching the binary colloidal glass transition. *Soft Matter* **7**, 1472 (2011).

[350] Han, Y. *et al.* Brownian motion of an ellipsoid. *Science* **314**, 626 (2006).

[351] Donati, C., Glotzer, S. C., Poole, P. H., Kob, W. & Plimpton, S. J. Spatial correlations of mobility and immobility in a glass-forming lennard-jones liquid. *Physical Review E* **60**, 3107 (1999).

[352] Keys, A. S., Abate, A. R., Glotzer, S. C. & Durian, D. J. Measurement of growing dynamical length scales and prediction of the jamming transition in a granular material. *Nature Physics* **3**, 260 (2007).

[353] Brambilla, G. *et al.* Probing the equilibrium dynamics of colloidal hard spheres above the mode-coupling glass transition. *Physical Review Letters* **102**, 085703 (2009).

[354] Shen, T., Schreck, C., Chakraborty, B., Freed, D. E. & O'Hern, C. S. Structural relaxation in dense liquids composed of anisotropic particles. *Physical Review E* **86**, 041303 (2012).

[355] Sheu, A. & Rice, S. A. Depletion interaction in a quasi-two-dimensional binary colloid mixture: Monte carlo simulations. *Physical Review E* **72**, 011407 (2005).

[356] Cuesta, J. & Frenkel, D. Monte carlo simulation of two-dimensional hard ellipses. *Physical Review A* **42**, 2126 (1990).

[357] Cicerone, M. T. & Ediger, M. Relaxation of spatially heterogeneous dynamic domains in supercooled ortho-terphenyl. *Journal of Chemical Physics* **103**, 5684 (1995).

[358] Xia, X. & Wolynes, P. G. Microscopic theory of heterogeneity and nonexponential relaxations in supercooled liquids. *Physical Review Letters* **86**, 5526 (2001).

[359] Zhang, Z., Yunker, P. J., Habdas, P. & Yodh, A. Cooperative rearrangement regions and dynamical heterogeneities in colloidal glasses with attractive versus repulsive interactions. *Physical Review Letters* **107**, 208303 (2011).

[360] Mishra, C. K., Nagamanasa, K. H., Ganapathy, R., Sood, A. & Gokhale, S. Dynamical facilitation governs glassy dynamics in suspensions of colloidal ellipsoids. *Proceedings of the National Academy of Sciences* **111**, 15362 (2014).

[361] Puertas, A. M., De Michele, C., Sciortino, F., Tartaglia, P. & Zaccarelli, E. Viscoelasticity and stokes-einstein relation in repulsive and attractive colloidal glasses. *Journal of Chemical Physics* **127**, 144906 (2007).

[362] Mishra, C. K., Sood, A. & Ganapathy, R. Site-specific colloidal crystal nucleation by template-enhanced particle transport. *Proceedings of the National Academy of Sciences* **113**, 12094 (2016).

[363] Mishra, C. K., Rangarajan, A. & Ganapathy, R. Two-step glass transition induced by attractive interactions in quasi-two-dimensional suspensions of ellipsoidal particles. *Physical Review Letters* **110**, 188301 (2013).

[364] Mishra, C. K. & Ganapathy, R. Shape of dynamical heterogeneities and fractional stokes-einstein and stokes-einstein-debye relations in quasi-two-dimensional suspensions of colloidal ellipsoids. *Physical Review Letters* **114**, 198302 (2015).

[365] Flenner, E. & Szamel, G. Fundamental differences between glassy dynamics in two and three dimensions. *Nature Communications* **6** (2015).

Appendix A

Publications

Publications from the Thesis

- Chandan K Mishra, A K Sood, and Rajesh Ganapathy, Site-specific Colloidal Crystal Nucleation by Template-enhanced Particles Transport, *Proceedings of National Academy of Sciences USA,* ***113(43)****, 12094−12098 (2016).*

- Chandan K Mishra, Amritha Rangarajan, and Rajesh Ganapathy, Two-Step Glass Transition Induced by Attractive Interactions in Quasi-Two-Dimensional Suspensions of Ellipsoidal Particles, *Physical Review Letters,* ***110****, 188301 (2013).*

- Chandan K Mishra and Rajesh Ganapathy, Shape of Dynamical Heterogeneities and Fractional Stokes-Einstein and Stokes-Einstein-Debye Relations in Quasi-Two-Dimensional Suspensions of Colloidal Ellipsoids, *Physical Review Letters,* ***114****, 198302 (2015).*

Publication from collaborative work

- Chandan K Mishra, K Hima Nagamanasa, Rajesh Ganapathy, A K Sood, and Shreyas Gokhale, Dynamical facilitation Governs Glassy Dynamics in Suspensions of Colloidal Ellipsoids, *Proceedings of National Academy of Sciences USA,* ***111(43)****, 15362−15367 (2014).*